High-Resolution Study of Human Neurovascular Coupling in the Retina Using Adaptive Optics

Pierre Senée

université PARIS-SACLAY

High-Resolution Study of Human Neurovascular Coupling in the Retina Using Adaptive Optics

Étude du couplage neurovasculaire rétinien humain à haute résolution par optique adaptative

Thèse de doctorat de l'université Paris-Saclay

École doctorale n° 572, Onde et matière (EDOM)
Spécialité de doctorat : Physique
Graduate School : Physique. Référent : Faculté des sciences d'Orsay

Thèse préparée au **DOTA (ONERA, Université Paris-Saclay)**, sous la direction de **Serge MEIMON**, directeur de recherches, la co-direction de **Michel PAQUES**, professeur des universités-praticien hospitalier et le co-encadrement de **Pedro MECÊ**, chargé de recherches

Thèse soutenue à Paris, le 22 novembre 2024, par

Pierre SENEE

Composition du Jury

Membres du jury avec voix délibérative

Alexandra FRAGOLA Professeure, ISMO, Université Paris-Saclay	Présidente
Stephen A. BURNS Professor (équiv. HDR), School of Optometry, Indiana University	Rapporteur & Examinateur
Karsten PLAMANN Professeur, ENSTA, Palaiseau	Rapporteur & Examinateur
Serge CHARPAK Directeur de recherches, Institut de la vision, Paris	Examinateur
Delphine DÉBARRE Chargée de recherches, LIPhy, Université Grenoble Alpes	Examinatrice

THESE DE DOCTORAT
NNT : 2024UPASP130

université PARIS-SACLAY | ÉCOLE DOCTORALE Ondes et matière (EDOM)

Titre: Étude du couplage neurovasculaire rétinien human à haute résolution par optique adaptative

Mots clés: Rétine, Optique adaptative, Couplage neurovasculaire, Ophtalmologie, Imagerie, Système vasculaire

Résumé: L'œil, grâce à sa transparence, permet d'observer la rétine de manière non invasive via des méthodes optiques, en faisant un organe privilégié pour l'étude du couplage neurovasculaire, un mécanisme clé qui régule l'apport sanguin afin de satisfaire les besoins énergétiques des neurones. Ce processus, essentiel au bon fonctionnement cérébral, peut être altéré dans certaines pathologies oculaires et systémiques. Ainsi, le développement de systèmes d'imagerie de la rétine permettant de caractériser finement le couplage neurovasculaire grâce à une imagerie à haute résolution spatiale et temporelle du réseau vasculaire rétinien pourrait faciliter le diagnostic, la prévention et la compréhension de ces maladies.

Les systèmes d'imagerie plein champ corrigés par optique adaptative (AO), tels que le banc ECUROeil développé par l'ONERA, offrent des avantages considérables pour l'étude du couplage neurovasculaire à haute résolution. Ils permettent une imagerie à la limite de diffraction (2 µm) avec un large champ et une haute cadence d'imagerie. Toutefois, la lumière diffusée par les différentes couches de la rétine réduit le contraste des images. Tout l'enjeu de ma thèse est de trouver un moyen d'améliorer ce contraste. Une piste pour cela est venue de l'utilisation d'une matrice de micromiroirs (DMD) pour projeter une illumination par motifs dans la rétine. Il a été démontré que cette technique améliore le contraste dans les zones éclairées et révèle, par contraste de phase dans les zones non éclairées, les parois des vaisseaux sanguins ainsi que les globules rouges.

En s'appuyant sur ce principe, tout en conservant une imagerie à champ large et à haute vitesse, essentielle pour l'étude du couplage neurovasculaire, j'ai contribué à l'implémentation d'un nouveau système d'imagerie haute résolution : l'AO-CRSO (Confocal Rolling Slit Ophthalmoscope). Ce système projette une fine ligne d'illumination qui est balayée sur la rétine et synchronisée avec l'obturateur (« rolling shutter ») d'une caméra. En ajustant le décalage entre l'illumination et la détection, nous avons réussi à obtenir des images à contraste de phase sans distorsion, permettant ainsi de visualiser les vaisseaux sanguins et les globules rouges à 200 Hz sur un champ de 2,5° x 4°.

Mon travail a ensuite consisté à adapter ce système pour l'étude de la dilatation des vaisseaux sanguins par couplage neurovasculaire au cours d'une stimulation lumineuse. Une voie de stimulation permettant de réaliser des tests « flicker », où une lumière visible est projetée dans l'œil pour stimuler les neurones de la rétine, a été intégrée dans le système. Ensuite, en utilisant des données empiriques acquises à la fois avec les systèmes DMD et AO-CRSO, j'ai optimisé les paramètres d'exposition et le décalage entre l'illumination et la détection, afin de maximiser le contraste des parois des vaisseaux sanguins. J'ai également développé un algorithme me permettant de traiter les images acquises pour mesurer automatiquement le diamètre des vaisseaux imagés. Cette méthode m'a permis de mesurer de manière robuste le diamètre des vaisseaux avec une précision de 0,1 µm toutes les 0,1 secondes sur des séquences d'imagerie de plusieurs minutes.

Ce protocole a été mis en œuvre dans une étude clinique réalisée sur huit sujets sains, visant à étudier le couplage neurovasculaire avec une haute résolution spatio-temporelle. Nous avons observé une dilatation moyenne significative de 5,2 % des artères en réponse à la stimulation lumineuse. De plus, pour la première fois, nous avons pu visualiser la dynamique de dilatation des artères sous l'action simultanée du rythme cardiaque, de la vasomotion et du couplage neurovasculaire. Ces résultats ouvrent ainsi de nouvelles perspectives vers une caractérisation plus fine du couplage neurovasculaire in vivo.

Title: High resolution study of human retinal neurovascular coupling using adaptive optics

Keywords: Retina, Adaptive Optics, Neurovascular Coupling, Ophthalmology, Imaging, Vascular System

Abstract: The eye, due to its transparency, allows for non-invasive observation of the retina through optical methods, making it an ideal site for studying neurovascular coupling, a key mechanism that regulates blood flow to meet the neurons' energy demands. This process, essential for proper brain function, can be impaired in some ocular and systemic pathologies. Thus, the development of retinal imaging systems capable of finely characterizing neurovascular coupling through high spatial and temporal resolution imaging of the retinal vascular network could greatly facilitate the diagnosis, prevention, and understanding of these diseases. Full-field adaptive optics (AO) imaging systems, such as the ECUROeil bench developed by ONERA, offer significant advantages for studying neurovascular coupling at a high resolution. They enable diffraction-limited imaging (2 µm) on a wide field of view and at a high imaging rate. However, light scattered by the different retinal layers reduces image contrast. The main challenge of my thesis was to find a way to enhance this contrast. A solution to improve the contrast came from the use of a digital micromirror device (DMD) to project patterned illumination onto the retina. It has been shown that this technique improves bright field contrast in illuminated areas and reveals translucent structures such as the walls of blood vessels and red blood cells in the non-illuminated areas.

Building on this principle, while maintaining a large field of view and high-speed imaging, which is essential for studying neurovascular coupling, I contributed to the implementation of a new high-resolution imaging system: the AO-CRSO (Confocal Rolling Slit Ophthalmoscope). This system projects a thin line of illumination that is scanned across the retina and synchronized with the rolling shutter of a 2D camera. By adjusting the offset between illumination and detection, we were able to obtain phase contrast images without distortion, allowing us to visualize blood vessels and red blood cells at 200 Hz over a 2.5° x 4° field of view.

My work then focused on adapting this system to study blood vessel dilation due to neurovascular coupling during light stimulation. A stimulation channel allowing for 'flicker' stimulation, where visible light is projected into the eye to stimulate retinal neurons, was integrated into the system. Then, using empirical data acquired with both the DMD and AO-CRSO systems, I optimized the exposure parameters and the offset between illumination and detection to maximize the contrast of blood vessel walls. I also developed an algorithm to process the acquired images and automatically measure the diameter of the imaged vessels. This method allowed me to reliably measure vessel diameters with a precision of 0.1 µm every 0.1 seconds in imaging sequences lasting several minutes.

This protocol was implemented in a clinical study conducted on eight healthy subjects, aiming to study neurovascular coupling with high spatial and temporal resolution. We observed a significant average dilation of 5.2% in the arteries in response to light stimulation. Furthermore, for the first time, we were able to visualize the full dynamics of arterial dilation influenced by heart rate, vasomotion, and neurovascular coupling. These results open new perspectives for a more detailed characterization of retinal neurovascular coupling in the retina.

Remerciements / Acknowledgments

Ce travail est le fruit d'une collaboration entre plusieurs instituts et de nombreuses personnes qui ont marqué ces trois années. Ces quelques pages leur sont dédiées, en signe de reconnaissance pour leur soutien et leurs contributions.

Tout d'abord, je tiens à exprimer ma profonde gratitude aux membres du jury. Un grand merci à Steven Burns et Karsten Plamann, qui ont accepté d'être rapporteurs de ce manuscrit, ainsi qu'à Alexandra Fragola, Serge Charpak et Delphine Debarre, qui m'ont honoré par leur présence en tant qu'examinateurs.

Je souhaite remercier chaleureusement mes encadrants qui m'ont permis de mener à bien cette thèse. En premier lieu, un grand merci à Serge Meimon, mon directeur de thèse, pour m'avoir confié un sujet aussi stimulant et pour son accompagnement tout au long de ces trois années. Merci pour tes idées novatrices, parfois un peu extravagantes qui ont permis de faire avancer mon projet. Merci surtout pour ton enthousiasme que je retrouvais notamment tous les jeudis quand je présentais les derniers résultats de CNV, cet enthousiasme a été un véritablme moteur de motivation, m'encourageant à aller plus loin.

Je souhaite également adresser mes plus sincères remerciements à Pedro Mecê, mon co-encadrant, qui a suivi de près mes travaux tout au long de cette thèse. Pedro, ta rigueur scientifique, ta patience et ton enthousiasme ont été d'une aide précieuse à chaque étape de ce projet. D'ailleurs, je suis convaincu que cette thèse ne serait jamais allée aussi loin sans tes sessions de traitement de données "pour le fun", un concept qui, je dois l'avouer, m'échappe encore un peu, mais dont les résultats ont été indéniablement efficaces. Travailler avec toi a été une expérience enrichissante et inspirante, et je te suis profondément reconnaissant pour ces trois années.

Mes remerciements s'adressent également aux membres du groupe Paris Eye Imaging et de l'hôpital des XV-XX. Merci à Michel Paques pour son expertise autour du couplage neurovasculaire. Merci à Kate pour l'organisation des séminaires, et à Maxime, mon voisin de manip, pour tes conseils avisés ainsi que pour m'avoir généreusement prêté ton œil pour mes expériences. Merci à Jimmy et Josselin, dont l'étude clinique sur les mouvements oculaires m'a permis de prendre en main le banc ECUROeil. Merci à tous les autres membres du groupe, notamment Nate, Elena, Celine, Ysé, Kyoko, Michael, Daniela, Julia, Clementine : merci pour votre accueil chaleureux et vos discussions enrichissantes.

Je remercie également l'équipe R&D de Quantel Medical. J'adresse tout particulièrement mes remerciements à Caroline Venet pour son encadrement bienveillant, sa disponibilité et ses

précieux conseils, notamment lors de la rédaction. J'ai également apprécié nos séances de manip LDH, même si je dois avouer que je ne comprenais pas toujours ce que l'on faisait... Merci aussi pour m'avoir fait découvrir la choucroute clermontoise ! Enfin, je tiens à exprimer ma profonde gratitude à David Pureur, Benjamin Weismer ainsi qu'à l'ensemble de l'équipe pour leur disponibilité, la pertinence de leurs conseils et la richesse des échanges qui ont jalonné ces années.

Un grand merci également à l'équipe HRA pour son accueil. Nicolas, Aurélie, Laurent, Cyril, Vincent, Laurie, Joseph : vos conseils et votre expertise ont été des atouts précieux tout au long de cette thèse. Aux doctorants de l'équipe : Pablo, Mahawa, Maxime, Arnaud, Timothée, Yann, Alix, Antoine, Hugo, Mathieu, Alberto, Perrine, Hiyam et tous les autres, merci pour les moments de partage, votre bonne humeur, et cette ambiance chaleureuse qui a rendu ces trois années si agréables. Une mention spéciale pour mes voisins de bureau : Alix, ton énergie et ton talent pour chanter en travaillant ont illuminé mes journées, et Florian, merci pour ta bonne humeur (et ton amour/fascination pour l'escalade !). Je tiens à exprimer toute ma reconnaissance à Léa Krafft, sans qui ce travail n'aurait tout simplement pas été possible. Léa, dès mon arrivée, j'ai tout de suite été à l'aise de travailler avec toi, ce qui m'a permis d'entamer cette thèse dans les meilleures conditions. J'ai énormément apris grace à toi et nos nombreuses séances d'alignement de Minsky resteront gravées dans ma mémoire. Je dois d'ailleurs avouer que sans ta patience et ton calme, je serais sans doute devenu fou après autant de réalignements.

Je tiens à exprimer ma gratitude aux membres de l'Institut Langevin, dont l'énergie et la convivialité ont rendu ces trois années aussi enrichissantes qu'agréables. Merci à Olivier Thouvenin pour son aide précieuse sur les codes de synchronisation du Minsky, ainsi qu'à Yao pour nos échanges scientifiques... et gastronomiques, autour de notre passion commune pour le poulet. Un grand merci également à l'équipe des jeudis fous: Jad, Inès, Jimmy et Clément, dont la bonne humeur ont été une véritable bouffée d'air frais dans la thèse. Enfin, une mention très spéciale pour Inès, merci d'avoir été ma responsable technique de soutenance. Merci aussi pour le prêt de ton œil et de ton couplage neurovasculaire, sans lesquels mes résultats auraient sans doute été bien moins convaincants ! Mais surtout, merci pour ta bonne humeur légendaire, qui rendait chaque journée au labo plus agréable.

Je tiens bien entendu à remercier ma famille pour son soutien tout au long de mon parcours et pour les moments partagés, qui m'ont permis de me ressourcer et de décompresser. Un grand merci également à mes amis du 14e : Louise, Clara, Stan, Clément et Marie, pour tous les bons moments passés ensemble dans notre "colocation" étendue. Enfin, un merci tout particulier à Ombeline, non seulement pour son aide précieuse dans l'organisation du pot de thèse, mais surtout parce qu'elle me fait rire au quotidien.

Enfin, avoir de nombreux sites de travail signifie également avoir de multiples lieux de restauration. Il serait donc impensable de conclure ces remerciements sans évoquer les cantines qui ont été de véritables bases de vie tout au long de cette thèse. Merci à la cantine de l'ONERA, au CROUS de Jussieu (et son poulet rôti inoubliable), et à la cantine des XV-XX pour ses généreux plateaux. Ces lieux auront nourri autant mon corps que mon esprit.

Résumé en Français

La rétine est un tissu essentiel à la vision, chargé de capter les signaux lumineux et de les transmettre au cerveau sous forme d'impulsions nerveuses. Pour accomplir cette fonction, elle s'appuie sur un ensemble complexe de cellules photosensibles, de neurones, et sur un réseau vasculaire qui garantit son oxygénation et son bon fonctionnement. Unique par sa transparence, l'œil offre un accès optique direct à la rétine, en faisant la seule partie du système nerveux central pouvant être observée de manière non invasive. Un des mechanisme essentiel au bon fonctionnement à la fois du cerveau et de la rétine est le couplage neurovasculaire (CNV), un mécanisme clé qui régule l'apport sanguin afin de satisfaire les besoins en énergie et en oxygène des neurones.

Des altérations du CNV peuvent survenir dans des pathologies oculaires telles que la rétinopathie diabétique ou le glaucome, mais aussi dans des maladies systémiques comme Alzheimer. Ces anomalies du CNV dans la rétine peuvent précéder l'apparition des premiers symptômes cliniques de ces maladies, en faisant un biomarqueur potentiel d'intérêt. Ainsi, développer des systèmes d'imagerie rétinienne capables de caractériser finement le CNV pourrait ainsi faciliter le diagnostic, la prévention et la compréhension de ces maladies.

Dans la rétine, le couplage neurovasculaire se traduit par une dilatation des vaisseaux sanguins et une augmentation du flux sanguin en réponse à une stimulation lumineuse. Pour caractériser ce phénomène, il est nécessaire de pouvoir mesurer ces variations avec une haute résolution spatiale et temporelle. Une haute résolution spatiale est nécessaire pour détecter des dilatations de l'ordre de quelques microns, tandis qu'une haute résolution temporelle est indispensable pour suivre la dynamique du couplage neurovasculaire. Cela permet également de distinguer ce phénomène d'autres variations naturelles, comme celles dues au cycle cardiaque ou à la vasomotion, qui influencent le diamètre des vaisseaux même en l'absence de stimulation. Mon objectif au cours de cette thèse à été de développer un tel système puis de l'exploiter pour étudier le couplage neurovasculaire in vivo.

Mon travail a débuté par l'utilisation d'un système plein champ corrigé par optique adaptative (AO), le banc ECUROeil développé par l'ONERA. Ce dispositif offre une imagerie à la limite de diffraction (résolution de 2 µm) sur un champ large (4° x 4°) et à une cadence élevée (100 Hz). Cependant, avec ce type de système, la lumière est multidiffusée par les différentes couches de la rétine, ce qui a pour conséquence une réduction du contraste des images, rendant nécessaire le moyennage de plusieurs images pour mesurer le calibre des vaisseaux. Cette contrainte limite significativement la résolution temporelle du système, constituant ainsi un frein à l'étude du couplage neurovasculaire.

Dans le premier chapitre de cette thèse, j'ai exploré la piste consistant à utiliser une matrice de micromiroirs (Digital Micromirror Device ou DMD) pour projeter une illumination par motifs dans la rétine sur le banc ECUROeil. Il a été démontré dans des travaux précedents que quand un motif est projeté dans la rétine à l'aide du DMD, on visualise, par contraste de phase, des structures transparentes telles que les parois des vaisseaux sanguins ou les globules rouges. Ce contraste de phase apparait dans les zones du champ qui ne sont pas éclairées directement par le motif d'illumination. Ainsi, il est possible de projeter une ligne fine d'illumination puis de sélectionner numériquement en post traitement, seulement les pixels en bordure de la ligne d'illumination, contenant le contraste de phase. En scannant cette ligne sur l'ensemble du champ, il a été mis en place une méthode permettant d'obtenir des images à contraste de phase sur l'entièreté du champ de vue.

Dans le chapitre 2, en s'appuyant sur le même principe qu'avec le DMD, tout en conservant une imagerie à haute vitesse, essentielle pour l'étude du couplage neurovasculaire, j'ai contribué à l'implémentation d'un nouveau système d'imagerie haute résolution : l'AO-RSO (Rolling Slit Ophthalmoscope). Ce système permet la projection d'une fine ligne d'illumination qui est balayée sur la rétine et synchronisée avec l'obturateur (« rolling shutter ») d'une caméra. En ajustant le décalage entre l'illumination et la détection, nous avons réussi à obtenir des images à contraste de phase sans distorsion, permettant ainsi de visualiser les vaisseaux sanguins et les globules rouges à haute cadence (200 Hz) sur un grand champ (2,5° x 4°).

Dans le chapitre trois, mon travail a ensuite consisté à adapter ce système pour l'étude de la dilatation des vaisseaux sanguins de la rétine par couplage neurovasculaire au cours d'une stimulation lumineuse. Une voie de stimulation permettant de réaliser des tests « flicker », où une lumière visible est projetée dans l'œil pour stimuler les neurones de la rétine, a été intégrée dans le système. Ensuite, en utilisant des données empiriques acquises à la fois avec les systèmes DMD et AO-RSO, j'ai optimisé les paramètres d'exposition et le décalage entre l'illumination et la détection, afin de maximiser le contraste des parois des vaisseaux sanguins. Enfin, J'ai développé un algorithme me permettant de traiter les images acquises pour mesurer automatiquement le diamètre des vaisseaux imagés. Cette méthode m'a permis de mesurer en continu le diamètre des vaisseaux avec une précision de 0,1 µm toutes les 0,1 secondes sur des séquences d'imagerie de plusieurs minutes.

Dans le quatrième chapitre, les méthodes développées au cours de cette thèse ont été appliquées dans le cadre d'une étude clinique menée sur huit sujets sains. Le diamètre de leurs artères a été mesuré en continu lors d'acquisitions de 50 secondes, avec et sans stimulation. Nous avons ainsi pu observer, avec une haute résolution spatiale et temporelle, l'effet d'une stimulation lumineuse sur le diamètre des artères rétiniennes. Cette stimulation a entraîné une dilatation significative des artères, en moyenne de 5%. De plus, pour la première fois, nous avons réussi à visualiser l'évolution temporelle de ce diamètre sous l'influence conjointe du rythme cardiaque, de la vasomotion et du couplage neurovasculaire. Enfin, l'analyse des données collectées sous différentes conditions de stimulation a permis d'obtenir des résultats préliminaires prometteurs, ouvrant des perspectives vers une meilleure compréhension du couplage neurovasculaire, aussi bien chez des sujets sains que pathologiques.

Contents

General introduction

The importance of neurovascular coupling in healthy brain function

The human brain is widely regarded as one of the most complex structures in the animal kingdom. It consists of approximately 86 billion neurons interconnected by trillions of synapses [1]. The brain orchestrates an astonishing number of functions: from basic survival instincts to the highest forms of human cognition and creativity. However, the workings of the human brain remain an open question.

At the heart of the brain's functionality lies a sophisticated network of neurons that communicate through electrical and chemical signals. However, the efficient operation of this neural network is dependent on an efficient and dynamic supply of oxygen and nutrients, delivered via the brain's vascular system. This interdependence between neural activity and blood flow is controlled by a process known as neurovascular coupling.

The work of Roy and Sherrington [2] in the late 19th century laid the foundation for the field of neurovascular coupling, demonstrating that changes in neural activity are accompanied by changes in blood flow in the brain. Over the following century, advancements in imaging technologies, particularly functional magnetic resonance imaging (fMRI)[3], have provided powerful tools for studying neurovascular coupling *in vivo*, offering new insights into the dynamic processes underlying brain function [4]. However, fMRI is a time-consuming and costly technology with limited accessibility, restricting its widespread use. Moreover, its millimeter-scale spatial resolution is much lower than the micrometer-scale of individual cells [5], making it insufficient for measuring neurovascular coupling at the cellular level.

Deregulation of neurovascular coupling is observed in various neuropathological conditions, including ischemic stroke [6], Alzheimer's Disease [7], and cognitive impairments stemming from hypertension [7]. This emphasizes the importance of understanding neurovascular coupling to identify new biomarkers for disease progression monitoring and to design therapeutic strategies targeting aberrant blood flow control mechanisms following these disorders [8].

Accessing neurovascular coupling through the eye at the micrometer scale

Interestingly, the principles of neurovascular coupling are not confined to the brain. The retina is an extension of the central nervous system and provides a unique and accessible window for studying these dynamics [9]. Indeed, the neurons at the core of visual information processing can be easily activated using light. Simultaneously, the effect of the stimulation on the vascular

system of the retina can be assessed using optical imaging modalities.

There are two main advantages of using this approach as compared to classical brain imaging techniques. First, optical modalities can achieve lateral resolutions at the micrometer scale, enabling the visualization of interactions between neuronal cells and the vascular network *in vivo*, potentially down to the level of individual cells. This capability could provide valuable insights into the cellular mechanisms underlying neurovascular coupling, enhancing our understanding of brain function. Additionally, many vision-related and systemic degenerative diseases, such as diabetic retinopathy and Alzheimer's disease, exhibit early disruptions in neurovascular coupling [10, 11]. As a result, the eye could serve as a source of biomarkers for these conditions, potentially allowing for earlier detection than conventional neuroimaging or clinical examinations [12]. This potential is further reinforced by the fact that *in vivo* imaging using optical modalities is typically fast and non-invasive, making it a promising tool for disease screening.

In response to a flickering visible light, neurons of the inner retinal layers are activated. This stimulus triggers the dilation of primary arterioles on the retinal surface, leading to enhanced blood flow throughout arteriolar, capillary, and venular networks within the retina [9]. Therefore, to study neurovascular coupling, one must be able to measure the dilation of blood vessels or the changes in blood flow as a response to light stimulation. To date, numerous techniques have been used to study neurovascular coupling, either by measuring changes caused by light stimulation in blood vessels diameter, for instance with the retinal vessel analyzer [13, 14, 15] or by measuring changes in blood flow with laser Doppler velocimetry [16, 17, 18].

Although these techniques have given precious information about the global and broad working of neurovascular coupling, a system able to measure neurovascular coupling at a high spatial and temporal resolution would be very beneficial to better understand this phenomenon: the dilation of blood vessels in response to light stimulation is minimal, typically only a few micrometers, requiring a system with high resolution and contrast for accurate measurement. Additionally, neurovascular coupling is a dynamic process that demands continuous monitoring and high temporal resolution to track changes in vessel diameter or blood flow over time.

Recent advancements in eye imaging technologies have addressed some of these challenges. Notably, adaptive optics (AO), a technique that corrects dynamic eye aberrations in real-time, first demonstrated in 1997 for retinal imaging, enables the visualization of individual retinal cells [19]. Over the next decades, AO technology advanced further with the development of the Adaptive Optics Scanning Laser Ophthalmoscope (AO-SLO) [20], which enhances image contrast by spatially filtering out multiply-scattered photons. Additionally, "offset aperture" techniques were introduced, slightly offsetting the detection pinhole to allow phase contrast imaging of translucent retinal structures such as ganglion cells, red blood cells, and blood vessel walls [21, 22, 23].

Although adaptive optics offers high spatial resolution, achieving both high spatial and temporal resolution on a large field of view remains challenging. Indeed, AO-SLO systems include a scanning element which results in a trade off between temporal resolution and field of view with this technique. On the other hand, camera-based, full-field adaptive optics systems have a large field of view and high temporal resolution but suffer from low contrast due to multiply scattered photons in the different layers of the retina.

Our approach: developing tools to study neurovascular coupling in the human retina at a high spatial and temporal resolution.

The environment of the Paris eye imaging group in which my PhD thesis was conducted is composed of various innovative imaging instruments directly located at Paris's 15-20 hospital, in proximity with patients and ophthalmologists. The goal of my PhD thesis was to take advantage of this environment to implement a system able to study neurovascular coupling at a high spatial and temporal resolution and then to apply it in a clinical environment.

Before the beginning of my PhD, the group of Serge Meimon has developed a high loop rate AO-Flood Illumination Ophthalmoscope which possesses many of the desirable qualities for studying neurovascular coupling: large field of view, high frame rate, no distortion, and high resolution. However, its primary limitation is the lack of contrast due to noise from multiply scattered photons detected by the camera. To overcome this limitation and improve the system contrast, previous PhD students [24, 25] have incorporated a Digital Micromirror Device (DMD) into the system. With this addition, the illumination can be modulated with high-resolution patterns. It has been demonstrated that using a checkerboard pattern can enhance contrast in the bright areas [26]. Inversely, translucent, phase structures, such as vessel walls and red blood cells, become visible in the non illuminated areas at the edges of the illuminated patterns.

Building on this observation, the concept of the Adaptive Optics-Confocal Rolling Slit Ophthalmoscope (AO-CRSO) was developed during the PhD thesis of Lea Krafft [25]. This system scans the retina with a thin line and utilizes the rolling shutter of a 2D camera for detection, enabling both bright-field and phase contrast imaging across the entire field of view. During my thesis, I focused on implementing this new system with a particular emphasis on high-speed phase contrast imaging to study neurovascular coupling.

The implementation of this system for studying neurovascular coupling involved several key steps. Initially, the DMD-integrated AO-FIO system was employed as a pathfinder to determine the optimal parameters for achieving phase contrast in a full-field camera-based imaging setup, as detailed in **chapter 2**. Next, **chapter 3** presents the implementation of the AO-CRSO system, outlining the technical aspects of its development with an emphasis on phase contrast imaging. **chapter 4** focuses on the work that was conducted in order to use this system to measure the size of blood vessels, including the specific settings of the AO-CRSO system to achieve maximal phase contrast of blood vessel walls and the implementation of an image processing algorithm to measure the caliber of blood vessels from the recorded images. Finally, in **chapter 5** this system was used to measure the effect of flickering light stimulation on the blood vessel diameter of healthy subjects at a high spatial and temporal resolution.

Part I

Introduction

Chapter 1

Studying neurovascular coupling through optical eye imaging

1.1 Clinical significance of studying retinal neurovascular coupling *in vivo*

The retina is optically accessible unlike the rest of the central nervous system. This unique window into both neuronal and vascular system allows for valuable insights into both ocular and systemic diseases. Specifically, neurovascular coupling can be observed *in vivo* in the retina using optical imaging devices. Monitoring retinal neurovascular coupling could potentially allow for earlier diagnosis and intervention, therefore carrying significant clinical implications. As neurovascular coupling is a key physiological mechanism in the healthy brain, alterations of this mechanism perturb the delivery of nutrients to active brain cells and impair the removal of potentially deleterious by-products of cerebral metabolism, which could accelerate or contribute to brain dysfunction [7].

Many neurological pathologies have displayed evidence of alteration of neurovascular coupling, for instance: Alzheimer's disease [10], multiple sclerosis [27], ischemic stroke, [7] or diabetic retinopathy [11]. Due to their age dependence and lack of effective treatments, neurodegenerative diseases are predicted to grow to epidemic proportions over the next several decades [28]. Alzheimer's disease for instance is projected to affect 131 million people by 2050 according to Alzheimer's disease international [29]. Biomarkers of Alzheimer's disease can be found in the retina [30] and some evidence of neurovascular coupling reduction can be found in the early stages of the diseases [31]. Studying neurovascular coupling in the retina might therefore provide new biomarkers for early diagnosis of Alzheimer's disease and for monitoring the progression of the disease.

A further example is glaucoma. Glaucoma is an age-related disease of the visual system and a leading cause of irreversible blindness worldwide, responsible for the blindness of 7.7 million people according to the world health organization [32]. The disease is associated with damages of the optic nerve and a progressive degeneration of ganglion cells. In glaucoma, neurovascular coupling is reduced which can lead to insufficient blood supply to the optic nerve head and retina, exacerbating neuronal damage and contributing to the progression of the disease [33]. Understanding the mechanisms of neurovascular coupling in glaucoma could guide the development of new therapies to preserve neurovascular coupling in order to slow the progression of the disease.

Another example is diabetic retinopathy, one of the leading global causes of irreversible blindness and the main cause of blindness in adults of working age. This disease causes structural changes in the retinal microvasculature that can be used to monitor the disease. However, some of studies indicate that alterations in flicker-induced vasodilatation can be observed at early stages of diabetes with no or minimal diabetic retinopathy [11, 34, 35] making it a promising diagnosis method.

In summary, studying retina neurovascular coupling is motivated by the potential to improve our understanding of brain function, enhance diagnostic and therapeutic strategies in a variety of retinal and systemic conditions.

1.2 Anatomy of the human eye

1.2.1 Optics of the eye

The eye is a complex organ allowing visual perception, its role is to focus light on the retina to form images. It is a complete optical system composed of refractive elements (the cornea and the crystalline lens), an aperture pupil (the iris) and a photodetector (the retina). Figure 1.1 A) provides a schematic representation of the eye, while figure 1.1 B) illustrates the various refractive elements of the eye and the distances between them.

When light first enters the eye, it passes through the cornea, a transparent, dome-shaped surface that provides approximately two-thirds (40-45 diopters) of the eye's total refractive power. Then, light goes through the aqueous humor, a clear fluid filling the anterior chamber, which helps maintain intraocular pressure and provides nutrients to the avascular cornea and lens. The light then reaches the pupil, an adjustable aperture controlled by the iris. The iris's dilator and sphincter muscles modulate the pupil size between 2 and 7 mm in diameter, adapting the amount of light entering the eye. Then, the light is further focused by the lens, a flexible biconvex structure located posterior to the iris, provides the remaining third of the refractive power of the eye (15 diopters) and refines the focus of light through accommodation. This process involves the ciliary muscles altering the lens's shape, increasing its curvature for near vision and flattening it for distance vision [36]. Light then passes through the vitreous humor a transparent, gel-like substance that fills the vitreous chamber before being focused on the retina.

At the retina, the incident light is detected by photoreceptor cells: rods and cones. The retina then performs initial image processing, converting light into electrical signals via a phototransduction cascade. These electrical signals are then relayed to the brain through the optic nerve where they are interpreted as visual perception.

1.2.2 Aberrations

For an imaging system, the resolution is set by the numerical aperture (NA) of the system.

$$NA = n \sin(\theta)$$

Where NA is the numerical aperture, n is the index of refraction of the medium, and θ is half-angle of the maximum cone of light that can enter the system. In the case of the eye, this angle is limited by the size of the pupil. The maximum value of NA for the eye is about

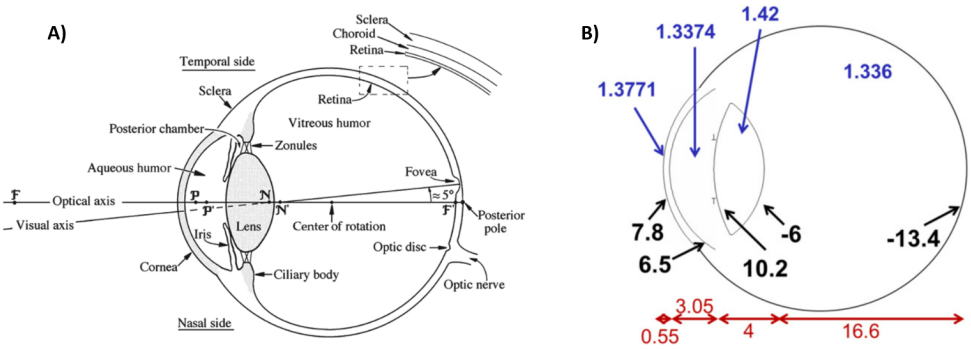

Figure 1.1: A) Horizontal cross-section of the right eye as seen from above, adapted from [37] B) Schematic representation of the eye with the main geometrical and optical information. Refractive indices (blue), curvature radii (black), and distances (red) in mm. Adapted from Artal et al. [38].

0.23, for a pupil diameter of 8 mm. Then, the theoretical optical resolution according to the Rayleigh criterion is given by the following equation:

$$r = \frac{0.61\lambda}{NA}$$

For near-infrared wavelengths, this results in a theoretically achievable lateral resolution of 2 µm with a fully dilated pupil. However, the human eye is not diffraction-limited due to aberrations caused by imperfections in its refractive elements. The impact of these aberrations can be visualized by examining the point spread function (PSF) of a typical emmetropic (normal) eye, as shown in figure 1.2. As the pupil size increases, the PSF is significantly affected by ocular aberrations, thereby limiting resolution. Typically, ocular aberrations limit the resolution of imaging systems to about 10 µm [39].

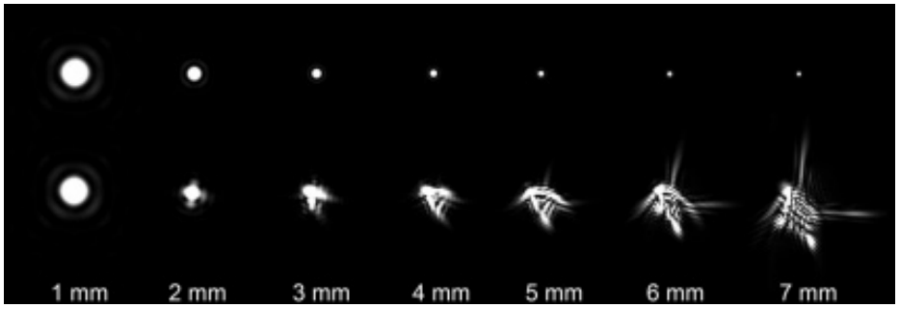

Figure 1.2: The top row shows the point spread function (PSF) of an eye with no aberrations. As the pupil size increases the PSF decreases in size, resulting in higher lateral resolution. The lower row shows the point spread functions for an eye with typical aberrations. Aberrations, particularly for the larger pupil sizes, cause the PSF to increase in size, limiting lateral resolution. Adapted from Roorda et al. [40].

Eye aberrations, can be categorized into three main types: static, dynamic, and chromatic aberrations.

- **Static aberrations** are constant over time and include common refractive errors such

as myopia, hyperopia, and astigmatism. These aberrations are typically corrected with spectacles or contact lenses. They result from permanent irregularities in the shape of the cornea or lens [41] [42].

- **Dynamic aberrations** change over time due to variations of the tear film or the accommodation process by the crystalline lens [39] [43]. These dynamic changes are often more pronounced with eye fatigue.

- **Chromatic aberrations** arise from the wavelength-dependent refraction properties of the crystalline lens. The most common type is longitudinal chromatic aberration, where different wavelengths of light are focused at different distances from the lens, leading to multiple focal planes. This results in color fringing and can affect overall visual sharpness and color perception. [44]

Ocular aberrations are typically represented using Zernike polynomials represented in figure 1.3, which are a series of orthogonal mathematical functions defined over a unit circle. Any wavefront profile can thus be expressed as a weighted sum of these polynomials [45]. The low order terms corresponding to a defocus (myopia or hyperopia) and astigmatism can be translated into the common sphere and cylinder notations used in optometric fields. Higher-order terms describe aberrations such as coma, trefoil, and spherical aberration and necessitate more complicated methods such as adaptive optics to be corrected.

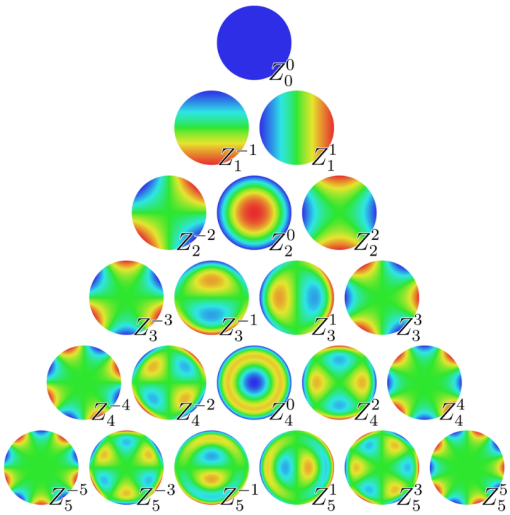

Figure 1.3: The first 21 zernike polynomials, ordered vertically by radial degree and horizontally by azimuthal degree.

1.2.3 Fixational eye movements

Eye movements are critical for visual perception, enabling to track moving objects or shift our gaze rapidly between two points, ensuring a smooth visual experience despite having only a very small area of sharp vision at the fovea. These movements are ensured by 6 extraocular muscles that are represented on figure 1.4.

Furthermore, even during fixation, small displacements of the eyeballs can be observed. These fixational eye movement are essential to vision because they ensure that vision does not

fade due to neural adaptation [46]. Three types of fixational movements can be observed and are depicted on figure 1.4. Tremors are high frequency (40 to 100 Hz) but low amplitude (5 μm) periodic movements. Drift are slow and random movements that occur simultaneously with tremors they are slow motions of the eye of the retina with large amplitudes (5 to 40 μm). Finally, microsacades are fast (about 40 Hz) and jerky movements with a large amplitudes (150 μm) [47, 46].

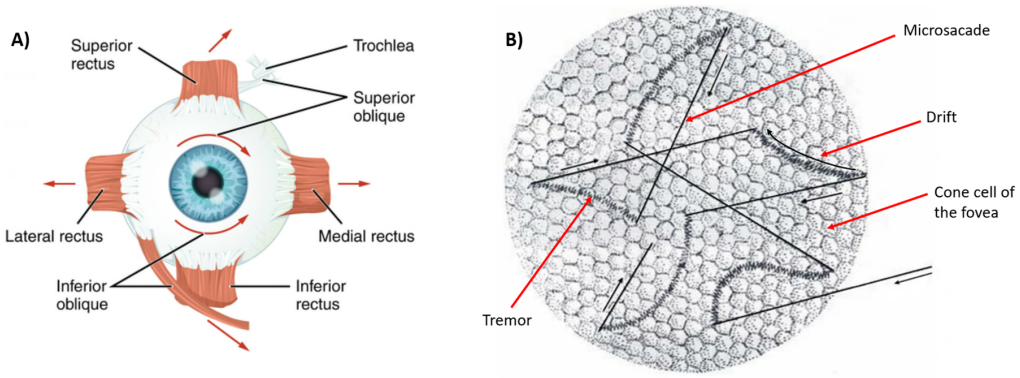

Figure 1.4: A) schematics of the 6 extraocular muscles responsible for eye movements B) illustration of the fixational eye movements, adapted from Pritchard 1961 [48].

Fixational eye movements negatively affect high-resolution retinal imaging. In full-field imaging systems, these movements induce motion blur, whereas in scanning systems, such as scanning laser ophthalmoscopes, they result in intra-frame distortion [49, 50]. A high framerate imaging system (more than 100 Hz framerate) can mitigate motion artifacts, except for those caused by microsaccades [49]."

1.2.4 The retina

1.2.4.1 General structure

The retina is a multi-layered, photosensitive tissue lining the inner surface of the eye, responsible for converting light into neural signals. It is composed of several types of neuronal cells that work together to detect and process visual information, as well as a network of blood vessels that ensure adequate oxygen and nutrient supply to these cells. The visual information detected by the retina are transmitted to the brain via the nerve fibers (axons of the ganglion cells), which converge at the optic nerve head and form the optic nerve.

The anatomy of the retina can be appreciated in figure 1.5. The central region of the retina, the macula, is an area 5-6 millimeters in diameter that is responsible for high-acuity central vision and color perception. Within the macula, a smaller, vessel-free spot called the fovea, measuring about 1.5 millimeters in diameter, contains the highest concentration of photoreceptors, making it the area responsible for the sharpest vision in the human retina. Located approximately 4.5-5 mm from the fovea, the optic nerve head is a circular region measuring about 2 x 2 mm. The visual signals detected by the retina are transmitted by nerve fibers which converge at the optic nerve head, they then travel through the optic nerve, and reach the brain. The major blood vessels of the retina also radiate from the optic nerve head [39]

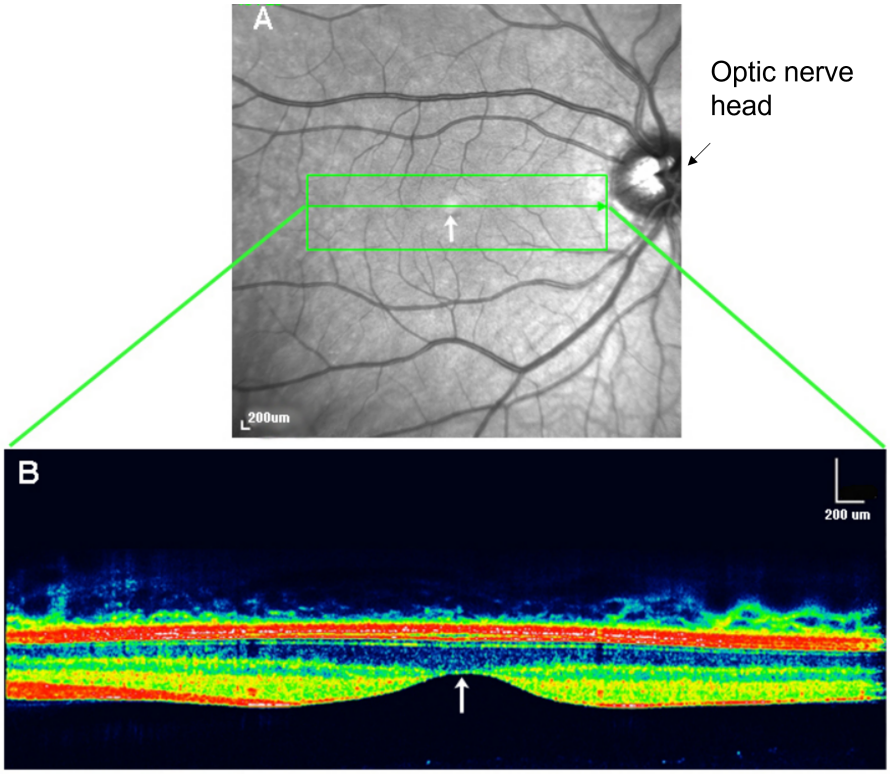

Figure 1.5: A) Fundus photography of a normal human retina B) Optical coherence tomography (OCT) image showing a cross section of the area in the green box. The foveal pit is visible (arrow) and the multiple layers of the retina can be seen. Blue cells are the photoreceptors, primarily cones, packed above the foveal pit. From Helga Kolb at al. [51].

1.2.4.2 Cellular organisation

The neuronal retina is composed of neurons, interneurons, and ganglion cells (see figure 1.6). It is a highly stratified tissue, organized into distinct layers of cells and neuronal synapses: the Ganglion Cell Layer (GCL), Inner Plexiform Layer (IPL), Inner Nuclear Layer (INL), Outer Plexiform Layer (OPL), Outer Nuclear Layer (ONL) and photoreceptor Outer Segments (OS).

The light-sensitive rod and cone photoreceptors convert incoming light into electrical signal in the photoreceptor outer segments (OS) in contact with the retinal pigment epithelium (RPE) cells. Subsequently, bipolar and amacrine cells transmit signals from the photoreceptors to the ganglion cells, which convey visual information to the brain via the optic nerve [52].

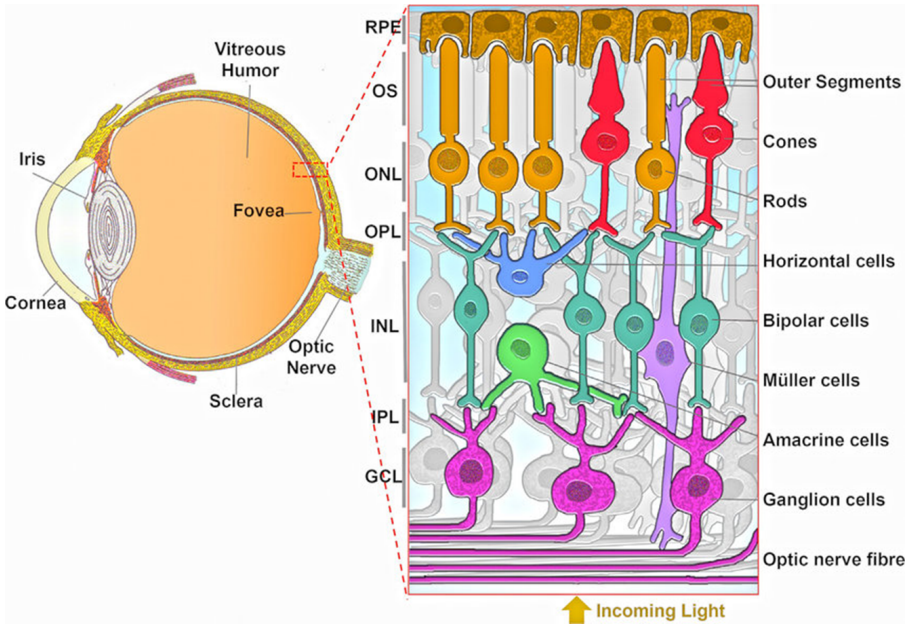

Figure 1.6: Schematics of the different layers and cells of the retina. The different layers of the retina are represented: the Ganglion Cell Layer (GCL), Inner Plexiform Layer (IPL), Inner Nuclear Layer (INL), Outer Plexiform Layer (OPL), Outer Nuclear Layer (ONL) and photoreceptors outer segment (OS). Illustration adapted from Karali et al. [53].

1.2.4.3 Photoreceptors: cones and rods

Photoreceptors are specialized cells in the retina that detect light. They contain photopigments, which absorb photons and initiate a series of electrochemical reactions ending in the creation of electrical signals sent by the ganglion cells towards the brain where it is interpreted as vision. This process is known as phototransduction.

The human retina contains about 125 million photoreceptors, including approximately 120 million rods and 5 million cones [54]. Photoreceptors are divided into rods and cones, each tailored to specific aspects of light perception (represented in figure 1.7 A)). Rods are narrow and primarily distributed in the peripheral retina, they are good at detecting low light levels, thus facilitating night vision and peripheral vision. They are highly sensitive, making them responsible for vision in very low light conditions (scotopic vision). In contrast, cones function optimally in bright light and are responsible for color vision and high spatial acuity. There are three types of cones: blue (S), green (M), and red (L) [55, 56] each sensitive to different parts of the light spectrum, allowing for sharp and colorful vision in well-lit conditions (photopic vision). As observed in figure 1.7 B), the distribution and size of rods and cones is dependent on the eccentricity. Cones, with a diameter of 1-4 µm, are highly concentrated in the fovea (hence the high visual acuity with central vision), and increase to over 4 µm outside the fovea. Rods, on the other hand, have a diameter of approximately 1 µm. Their density peaks around 6 mm from the center of the retina and gradually decreases towards the periphery. [57]

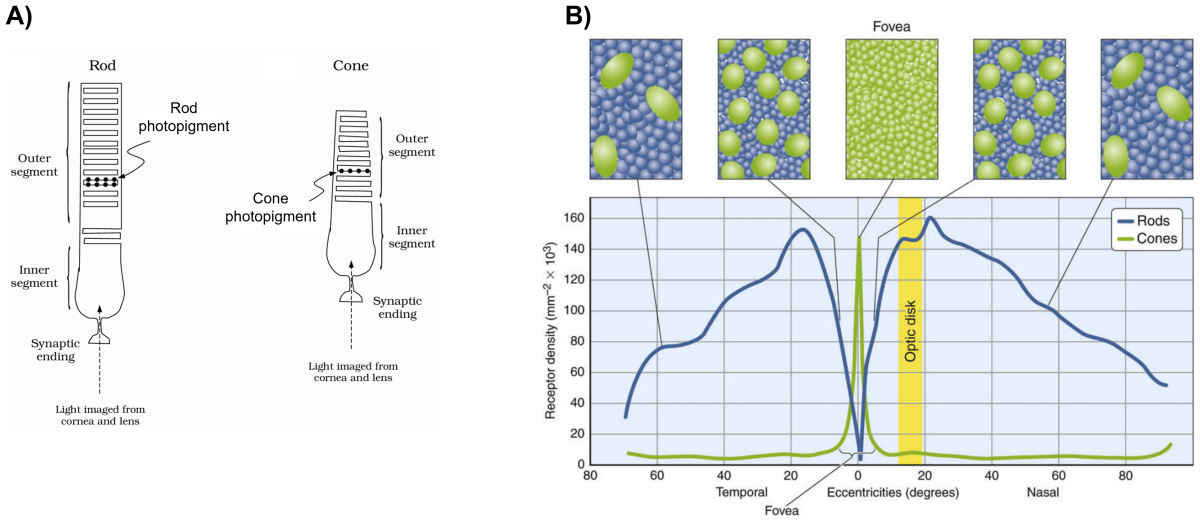

Figure 1.7: A) Schematic of a rod and a cone photoreceptors. Adapted from Baylor et al. [58]. B) Distribution of cones and rods in the human retina. From Mustafi et al. [57]

1.2.4.4 Perfusion of the retina

The retina is the organ with the highest metabolic rate of the human body [59]. To satisfy these elevated needs in oxygen and nutrients, the central retinal artery and the choroidal blood vessels are the two sources of blood, supplying the human retina. The largest blood flow is provided by the choroid (65-85%) [60] and maintain principally the outer retina, and photoreceptors in particular. The central retinal artery provides the rest of the blood flow (20-30%) and enters the optic disc through the lamina cribrosa, where it branches into four principal intra-retinal arteries supplying the inner layers. These two systems are depicted in figure 1.8.

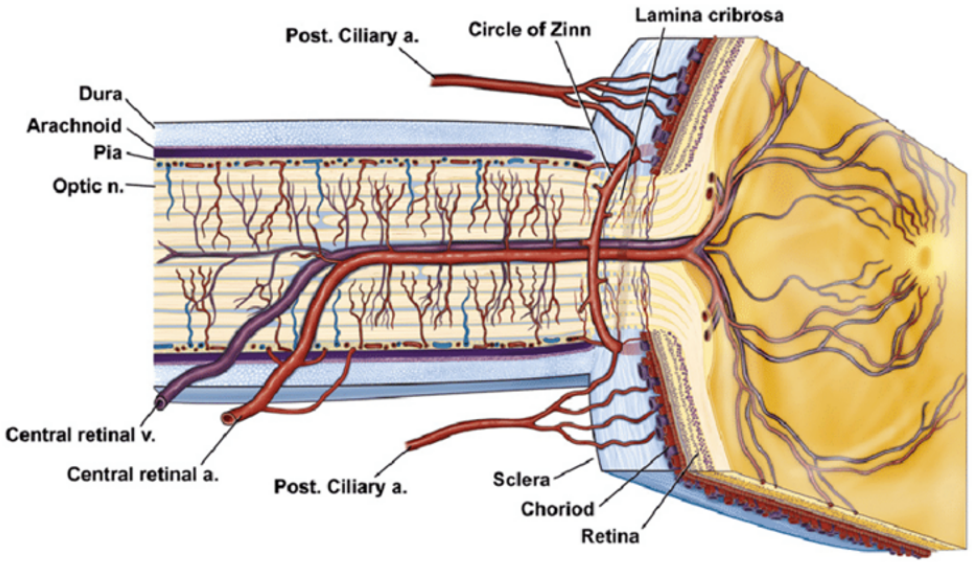

Figure 1.8: Anatomy of ocular circulation. Cut away drawing along the superior–inferior axis of the human eye through the optic nerve, showing the vascular supply to the retina and choroid. Drawing from Anand et al. [61].

These arteries bifurcate to form smaller arteriole branches and terminal arterioles, which feed into capillary beds. Retinal capillaries are organized in an interconnecting three-layer network, depicted in figure 1.9. A first superficial vascular plexus is located in the nerve fiber and ganglion cell layers, a second plexus, the intermediary capillary plexus is located above the inner nuclear layer, finally, the deep capillary plexus lies deeper, in the inner nuclear and outer plexiform layers. The superficial plexus, contains arterioles, venules, and capillaries, while the intermediary and deep vascular bed consists predominantly of capillary-sized vessels [62, 63].A 4th plexus, known as the radial peripapillary capillaries (RPCs), is located in the nerve fiber layer in a small rim surrounding the optic nerve head. These RPCs are located superficially around the optic nerve head, where the nerve fiber bundles are thickest, prior to exiting the retina [64].

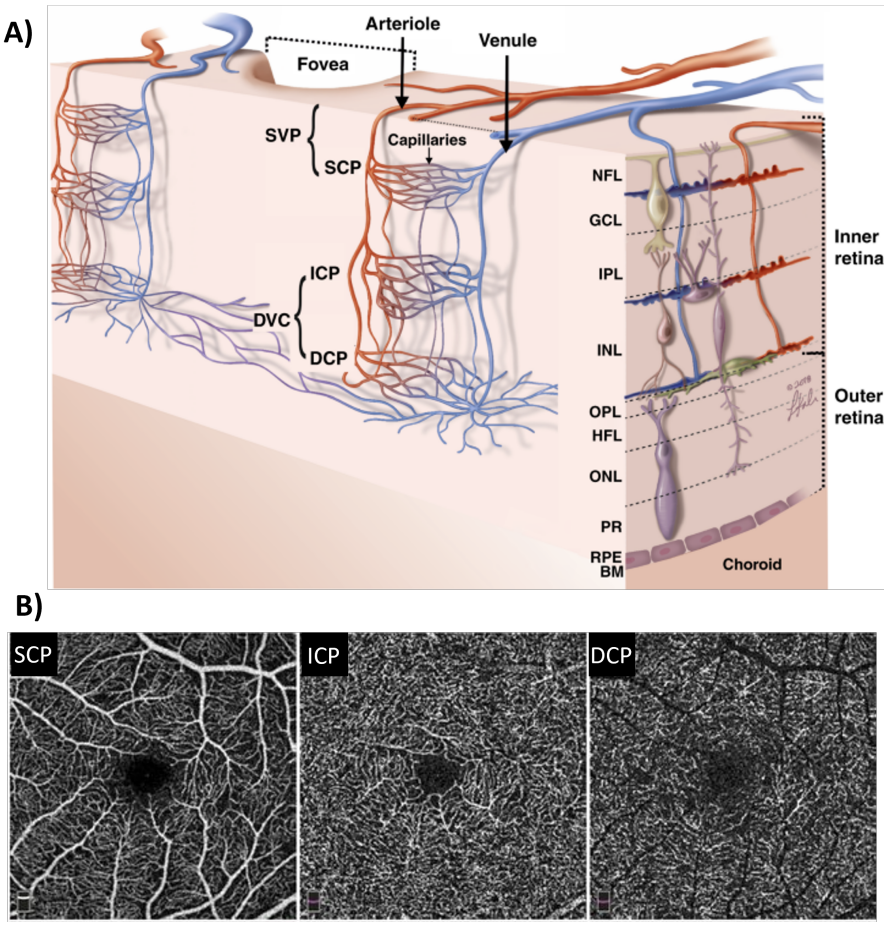

Figure 1.9: A) Illustration of connectivity and configuration of the three retina plexuses. From Sampson et al [65] and adapted from Nesper et al [66]. B) Visualization of three retinal capillary plexuses in optical coherence tomography angiography. Top row: en face OCTA. Bottom row: cross-sectional OCTA with red and green segmentation boundaries (A) Full retinal thickness, (B) superficial capillary plexus, (C) middle capillary plexus, and (D) deep capillary plexus.[67].

1.2.4.5 Structure of retinal vessels

Figure 1.10 illustrates the structure of the arteries, veins, and capillaries in the retina. Blood flows through the hollow interior of the vessels which is called the lumen. The vessel walls are composed of three distinct layers:

- The adventitia or tunica externa which provides structural support and shape to the vessel.
- The tunica media or a middle layer composed of elastic and muscular tissue which regulates the internal diameter of the vessel.
- The tunic intima or an inner layer consisting of an endothelial lining which provides a frictionless pathway for the movement of blood.

There are several morphological differences between arteries, veins and capillaries: Arteries have thick, muscular walls, their tunica media is particularly well-developed, consisting of smooth muscle and elastic fibers, allowing arteries to withstand and regulate the high pressure of blood being pumped from the heart. In the retina, the walls of the largest arterioles have a tunica media with up to seven layers of smooth muscle cells, after several branchings of the vascular network, the number of layers diminishes to just one or two in the retinal periphery [59]. By contracting or relaxing their smooth muscle cells, they can change their tone and play an active role in blood flow regulation.

Veins are responsible for returning oxygen pour blood to the heart, they have thin walls and less developed tunica media than arteries because they don't have to sustain high blood pressure. Their lumen is also large in comparison to arteries which means that they are usually wider and carry more blood volume (120-150 μm for the largest arteries of the retina vs 135-170 μm for the largest veins [68]).

Capillaries are thin-walled vessels consisting of a single endothelial layer. They are encased by pericytes, which are contractile cells that contribute to capillary stability and regulate microcirculatory blood flow [69]. The retinal microvasculature is notable for its uniquely high density of pericytes with more than 90% pericytes coverage in human retina capillaries [70].

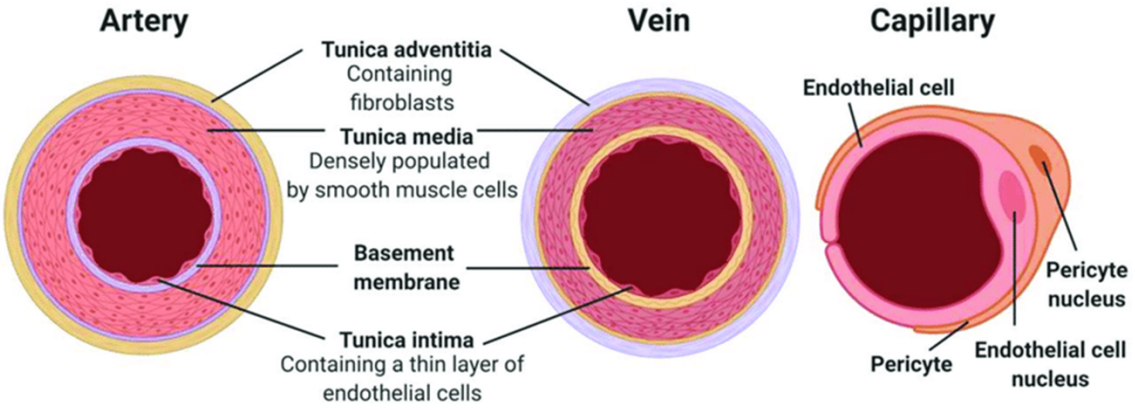

Figure 1.10: Schematic representation of the structure of arteries, veins and capillaries, from Jouda et al [71].

1.3 Retinal neurovascular coupling

When the brain is presented with a sensory stimulus or cognitive task (reading or problem solving for example), the increase in neural activity across various regions are accompanied by local dilation of arteries and veins, resulting in enhanced blood flow, blood volume, and oxygenation in the activated regions. This increase in blood flow in response to heightened neural activity is known as neurovascular coupling. It is a complex process, which involves a dynamic interplay between neurons, glial cells, and the vasculature. It is mediated by multiple signaling molecules. Interestingly, neurovascular coupling is also observable in the retina, where it manifests as flicker-induced hyperemia: when the retina is exposed to a flickering light (a stimulation turning on and off in rapid succession) an increase in blood flow can be observed.

1.3.1 Manifestation in the retina: flicker induced hyperemia

When a flickering visible light stimulus is presented into the eye of a subject, two effects can be observed: blood vessels dilate and blood flow increases in the retina. After administrating a flicker stimulation, usually defined by an approximately 10 Hz flickering visible light for 20 seconds , the primary arterioles on the retina surface dilate by 3-8% [13, 14, 15]. This dilation is driven by the smooth muscle cells of arterioles and has a short latency (less than one second). Veins also dilate by the same 3-8% range but the time course of dilation between arteries and veins can be quite different, as can be observed in figure 1.11.

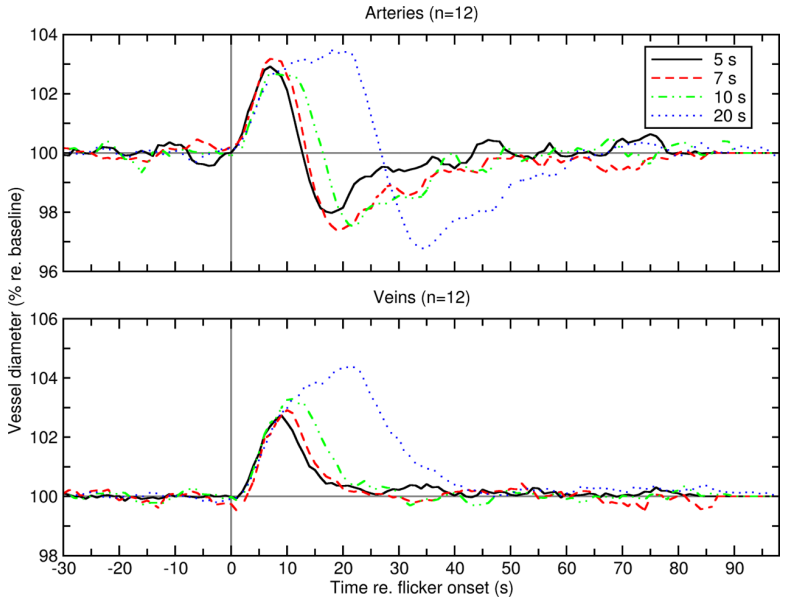

Figure 1.11: Time course of dilation for different flicker durations, from Heitmar et al [72]. The top graph illustrates the response of an arteriole to stimulation, showing an initial dilation of 3% following the onset of stimulation, followed by a brief contraction after the stimulation ends, and finally a return to the baseline diameter. The bottom graph depicts the response of a venule, demonstrating a dilation of 4% post-stimulation, then returns to baseline diameter.

Regarding blood flow, an increase of around 50% in blood flow was also observed in large arterioles of the human retina following a flicker stimulation [73, 74] and an increase in blood flow of 30-50% in the optic nerve head was also measured by Riva et al [75, 17]. In capillaries, an increase in blood flow due to a flicker test can also be observed in the three capillary plexuses of the mouse, as demonstrated by OCT angiography by Liu et al. [76]. Duan et al. [77] has also demonstrated significant dilation of capillaries in the perifoveal region in humans in response to flicker stimulation.

One important aspect of the functional hyperemia response is its localized nature: Studies in the brain have shown that activation of specific brain regions results in an increase in blood flow restricted to that region [4]. In the same manner, the retinal vasculature is also able to control blood flow locally in response to light stimulation. For instance Srienc et al [78] has shown that, when the rat retina is stimulated focally with a flickering spot, blood velocity increases are greatest near the stimulated region. In humans, Zhong et al [79] have demonstrated that a local flicker stimulation increases blood velocity specifically in the arteries upstream of the stimulated regions.

1.3.2 Mechanism of retinal neurovascular coupling

Neurovascular coupling in the retina is a complex and coordinated process. It involves a dynamic interplay between neurons, glial cells, and vascular cells. The cells involved in this process are commonly called part of the neurovascular units, represented in figure 1.12.

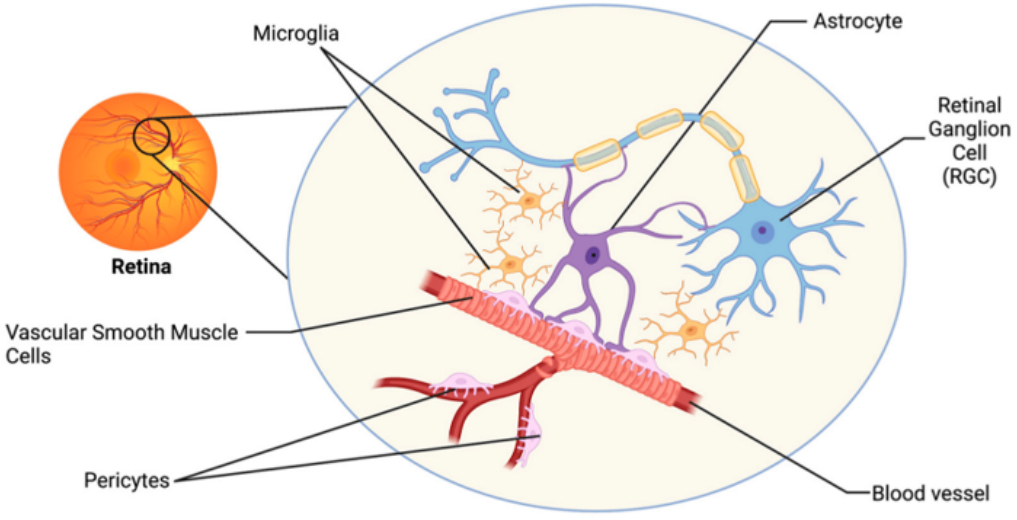

Figure 1.12: The retinal neurovascular unit. The retinal neurovascular unit consists of three main cell types: neurons (retinal ganglion cells and amacrine cells), glial cells (astrocytes and microglia), and vascular cells (endothelial cells, vascular smooth muscle cells, and pericytes) adapted from Haider et al. [80].

The process of neurovascular coupling in the retina involves various vasoactive agents that are produced by neurons and glial cells in response to light stimulation. The mechanisms mediating neurovascular coupling in the retina remain unclear [59]. However, it is believed that multiple neurovascular coupling mechanisms operate concurrently to produce functional hyperemia [9]. Detailing all the proposed mechanisms is out of the scope of this manuscript. However, a simplified mechanism of neurovascular coupling in the retina can be described as such:

1. **Neuronal activation**: When photoreceptors detect light, they generate electrical signals that are transmitted to bipolar cells and then to ganglion cells. This increased neuronal activity leads to an increased demand for oxygen and nutrients.

2. **Release of neurotransmitters and signaling molecules by neurons**: Active neurons (amacrine and ganglion cells) release neurotransmitters and vasoactive substances. This release is detected by neighboring glial cells. These glial cells (Astrocytes and muller cells) also release vasoactive substances.

3. **Vasodilation and blood flow regulation**: Vasoactive substances released by neurons and glial cells act on the smooth muscle cells of arterioles and pericytes around capillaries, causing vasodilation.

4. **Feedback mechanisms**: Neuronal activity leads to a drop in energy reserves in active neurons and to the generation of metabolic byproducts, for CO_2, that can dilate nearby blood vessels.

5. **Retrograde propagation**: The activated site generates a vascular response that propagates to the upstream vascular segments supplying the activated region. This backward transmission ensures a coordinated dilation of the vessels upstream of the stimulated region.

1.4 Imaging neurovascular coupling in the retina

To study neurovascular coupling in the human retina *in vivo*, it is necessary to either measure blood vessel diameter to assess dilation in response to light stimulation or to detect changes in blood flow triggered by such stimulation. Below is a non-exhaustive list of imaging techniques available for measuring these effects:

1.4.1 The retinal vessel analyser (RVA)

The gold standard method to measure the effect of light stimulation on the caliber of vessels of the retina is the Retinal Vessel Analyser (RVA) (Imedos Systems UG, Jena, Germany). This system assesses retinal vessel diameter by analysing the brightness profile of the vessel using video sequences obtained with a conventional fundus camera. This system can measure the dilation of large blood vessels of the retina during a flicker test ([11, 14, 72]) where 3%-8% dilation have been reported. However, because of its limited transverse resolution, the vessel walls are not visible with this technique and measurement relies on light absorption by the erythrocytes. Furthermore, its applicability is primarily restricted to large vessels (diameter>90 µm) [81].

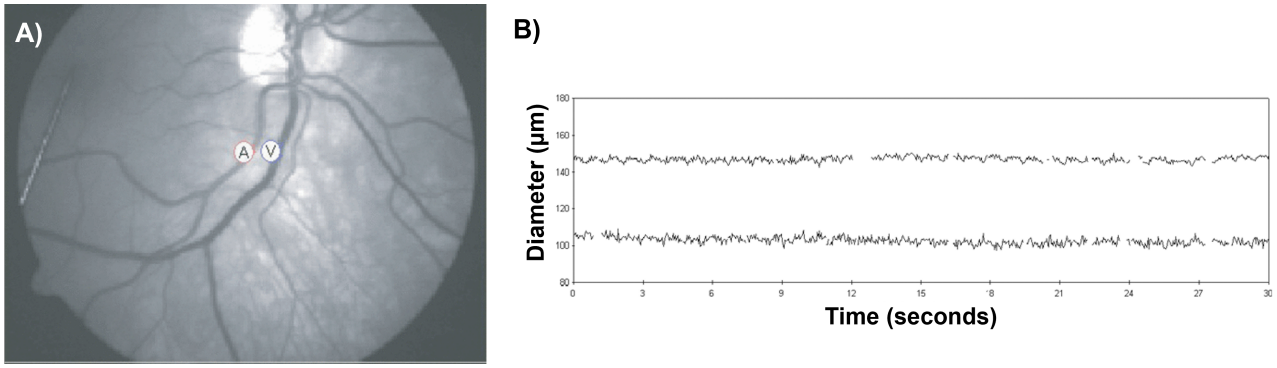

Figure 1.13: Example of vessel diameter measured with the RVA. A) Ocular fundus observed on the retinal vessel analyzer monitor. Retinal arteries (A) and veins (V) can be selected for measurement. B) Typical reading from the retinal vessel analyzer software showing retinal vessel diameters over time. The upper curve represents the diameter of a retinal vein, while the lower curve represents the diameter of a retinal artery. Adapted from Garhofer et al. [81].

1.4.2 OCT-angiography (OCT-A)

OCT was invented in 1991 [82] and has become an essential tool for ocular imaging in clinics. The principle of OCT is close to that of the Michelson interferometer. The light of a low coherence source is split by a beam splitter into two channels. The first beam is reflected on a mirror (the reference channel) and the second is directed towards the retina (the sample channel). The beam reflected from the retina is combined with the reference beam, creating an interference pattern. This pattern is analyzed to detect path length differences between the reference and sample beams, therefore determining the depth of the different layers of the retina. To scan the depth of the retina, the axial position of the reference mirror can be modulated (Time-Domain OCT) or the wavelength of the light source can be modulated (Spectral-Domain OCT).

OCT-angiography (OCT-A) was introduced to produce images of the retinal vasculature based on the fluctuations due to the circulation of erythrocytes in the retina. Repeated scans of the retina are taken at the same location, while flowing red blood cells causes more variation in the OCT signal between repeated scans than static tissue. Using this principle, OCT-A can produce blood flow contrasted volumes revealing arteries, veins and capillaries on quite a large field of view ($\approx 10^\circ$ x 10°). Some groups have used OCT-A to study neurovascular coupling. For instance Liu et al. [76] have demonstrated an increase in capillary density in the three capillary plexuses of the mouse retina when exposed to a flicker stimulation.

However, while OCT-A can provides binarized images of the vasculature, it lacks the ability to offer quantitative information on blood velocity. Additionally, the method has a limited temporal resolution, as capturing an angiographic volume requires several seconds [83].

1.4.3 Laser Doppler Flowmetry (LDF)

Laser Doppler flowmetry is a technique where blood flow is measured from the self interference of the light backscattered by the eye on a photodiode [16, 17, 18]. A monochromatic laser is focused on the retina, it is then considered that a part of the backscattered light is doppler shifted by static diffuseurs while another part of the light has been scattered by moving erythrocytes thus creating a Doppler frequency shift. The theoretical developments derive metrics from the Doppler power spectrum density measurement, such as the local velocity and volume of blood [18]. This method has been used extensively in conjunction with a flicker stimulation to measure increase in blood flow in the optical nerve head [17, 84] and in retinal blood vessels [75, 73]. However, the main limitation of this technology is that blood flow can only be monitored at a single point.

1.4.4 Adaptive optics (AO)

Adaptive optics (AO), initially developed by astronomers, uses a deformable mirror to correct optical aberrations caused by the Earth's atmosphere, thereby increasing the resolution of images captured by ground-based telescopes. This principle was first applied to eye imaging in 1997 [19], where dynamic eye aberrations were corrected in real time using a deformable mirror within a fundus camera imaging system. This innovation led to the first cellular-resolution images of the retina.

Figure 1.14 illustrates the principle of adaptive optics applied to retinal imaging. A beacon light source used for wavefront correction is focused on the retina (Not represented on the figure). The light backscattered by the retina now has a distorted wavefront. It is reflected by the deformable mirror then detected by the wavefront sensor (WFS). Deformation of the wavefront is measured by the WFS. In retinal imaging, the most commonly used is the Shack-Hartmann WFS. It is composed of an array of micro-lenses that are conjugated with the pupil of the eye and a sensor, located at the focal plane of the micro-lenses. A control computer drives the DM in real time to correct the wavefront from the aberrations detected by the WFS [85]. The light from the imaging source, is reflected by the deformable mirror before being collected by a detector, where a high-resolution image is formed.

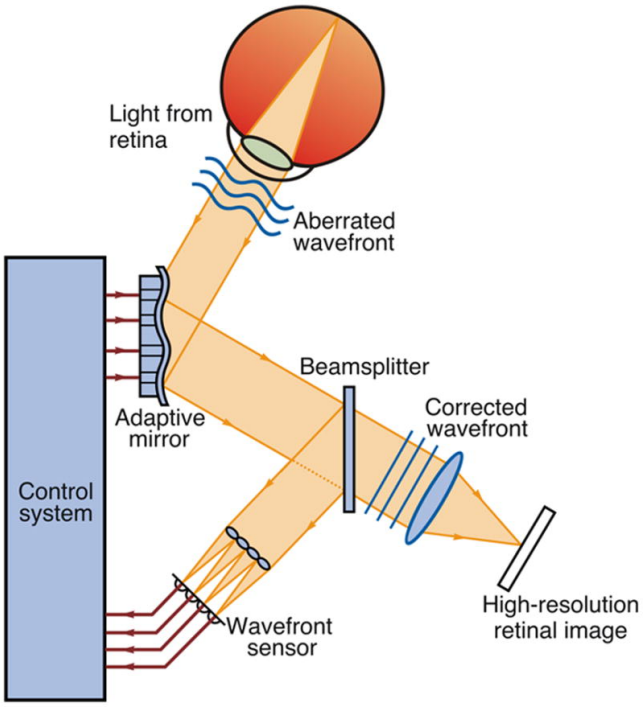

Figure 1.14: Schematic representation of an adaptive optics system applied for the correction of ocular aberrations.

1.4.4.1 Adaptive optics - Flood Illumination Ophthalmoscope (AO-FIO)

In the first generation of adaptive optics retinal imaging system, the near infrared imaging light was sent in a full field configuration, hence "Flood Illumination", in the same way as a fundus camera. This type of system has the advantage of having a relatively large field of view (typically 4°x4°) and a fast acquisition rate of a few milliseconds [86]. With adaptive optics, a diffraction limited transverse resolution of 2 µm can be achieved when using near infrared light [87].

Work using AO-FIO system have been carried out to study neurovascular coupling at a high transverse resolution, notably using the rtx1 from Imagine Eyes (Imagine Eyes, Orsay, France) a commercial AO-FIO device [88, 89, 90]. Work from Duan et al [77] have also shown dilation of capillaries in the perifoveal regions in humans due to flicker stimulation by using a visible light AO-SLO.

The limitations of this system include the lack of optical sectioning and the low contrast of images caused by multiply scattered photons from out-of-focus retinal layers. This reduced contrast requires image averaging to accurately measure blood vessel diameter, which in turn compromises temporal resolution (For instance, the rtx1 need to average 1 sec of images to measure the diameter of a blood vessel). This limitation may explain why no group has characterized the temporal behavior of flicker induced vasodilation with AO-FIO, instead opting to measure vessel diameter only before, during and after flicker stimulation.

1.4.4.2 Adaptive optics - Scanning Laser Ophthalmoscope (AO-SLO)

The adaptive optics - Scanning Laser Ophthalmoscope (AO-SLO) was proposed in the early 2000's [20]. This systems, derived from confocal microscopy, consist of illuminating the retina with a focused laser beam and collecting the backscattered light though a pinhole in front of a detector thus filtering the out of focus photons. As a result, this system provides an enhanced contrast and axial resolution as compared to AO-FIO [85, 91]

An alternative way of using the AO-SLO is by slightly offsetting the detection pinhole of the system. By doing this, the light directly backscattered is blocked and the light coming to the detector has been multiply scattered in the retina before coming back to the displaced aperture, similarly to dark field microscopy. This technique called "offset aperture" enable the visualization of phase objects that were otherwise invisible [22, 92, 23, 21].

This technique is particularly interesting for imaging the retinal vasculature as it provides excellent contrast for blood vessels [22] and mural cells [92] as can be appreciated in figure 1.15. Moreover, offset aperture AO-SLO also provide a good contrast on erythrocytes making it possible to resolve individual red blood cells moving in capillaries [21, 22]

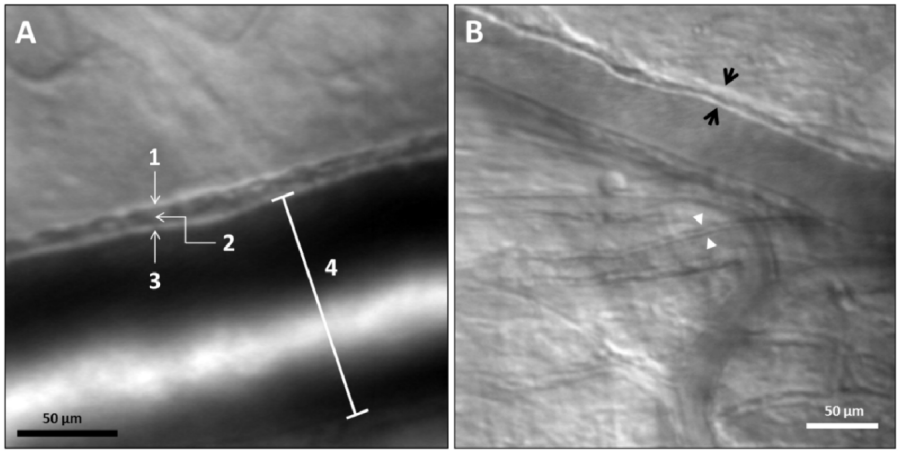

Figure 1.15: AO-SLO offset aperture images of blood vessels from Chui et al. [22]. A) Image of a 110 µm lumen diameter arteriole, the three layers of the arteriole wall can be observed 1: Tunica adventitia; 2: Tunica media (smooth muscle); 3: Tunica intima. B) Image if a 40 µm lumen diameter arteriole.

This imaging modality has been used in conjunction with a flicker stimulation to study neurovascular coupling at a high resolution in the retina. For instance Zhong et al. [79] have measured local blood velocity changes due to flicker stimulation in arteries of the retina and demonstrated that the functional hyperemia response was spacially related to the location and size of the flicker stimulus. Raymond L. Warner et al [93] have measured blood flow and diameter for capillaries, venules and arterioles of the retina before, during and after a wide field flicker stimulation.

Although this technique offers high resolution and contrast, the need to scan the entire field of view in both vertical and horizontal directions creates a trade-off between field of view and imaging speed. AO-SLO systems typically have a small field of view and a low frame rate (1-3° at 20-30 Hz [39]). Furthermore, this system is susceptible to image distortion due to eye movements happening during the scanning of the retina.

1.4.5 Comparative overview of the different techniques

	RVA	OCT-A	LDF	AO-FIO	AO-SLO
Blood flow measurement	No	No	Yes	Yes	Yes
Vessel size measurement	Yes	Yes	No	Yes	Yes
Prone to motion artifacts	No	Yes	No	No	Yes
Spatial resolution	-	+	-	++	++
Contrast	-	++	N/A	-	++
Temporal resolution	++	--	+	++	-
Field of view	++	++	--	+	-

Figure 1.16: Summary of the performances of the ophthalmic instrument used to study neurovascular coupling presented in this section, subjectively appreciated.

There is a wide range of ophthalmic instruments that can be used to study neurovascular coupling either by measuring blood flow or by measuring blood vessel diameter. As we can see from the overview of these systems (see table 2.11), each instrument offers unique capabilities, but they also come with trade-offs. A new instrument that minimizes these compromises could significantly benefit the field by providing more comprehensive data, thereby advancing our understanding of neurovascular coupling.

Regarding high resolution techniques, AO-FIO and AO-SLO, present opposite challenges. AO-FIO offers a high frame rate and a broad field of view, which are advantageous for capturing rapid changes across large retinal areas, but it suffers from its low contrast. On the other hand, AO-SLO provides highly contrasted images of the blood vessels but is limited by a slower frame rate and a narrower field of view due to its scanning element. A system that could integrate the strengths of both AO-FIO and AO-SLO, delivering both high spatial resolution and high temporal resolution would be a great tool for monitoring flicker-induced vasodilation in the retina.

Moreover, in the case of blood flow imaging, there is a lack of an instrument capable of quantitatively measuring blood flow across a large field of view. Existing instruments either focus on measurement of blood flow on a small area (such as LDF, or AO-SLO) or non quantitative measurement over a large field of view (OCT-A). Developing an instrument that can assess blood flow quantitatively over a large field of view would fill this gap, offering new insight into neurovascular coupling.

Part II

Instrumental development

Introduction to part II

As discussed in Chapter 1, a variety of imaging systems are available to study neurovascular coupling, each with their own strengths. However, there is a significant gap in the availability of a high-resolution system that combines both high spatial and high temporal resolution across a large field of view. The primary aim of my PhD thesis was to develop such a system, capable of probing neurovascular coupling in the retina at the micrometer and millisecond scales. To achieve this goal, I considered three imaging systems:

- The DMD-integrated AO-FIO, a system capable of projecting high-resolution patterns onto the retina.
- The Adaptive Optics - Confocal Rolling Slit Ophthalmoscope (AO-CRSO), a high resolution imaging system, using a scanning line illumination and the rolling shutter of a 2D camera to achieve high speed phase contrast imaging.
- A Laser Doppler Holography (LDH) system, a promising solution for quantifying blood flow in the retina, currently in extensive use with patients at Paris's 15-20 hospital.

In this second part of the manuscript, I will present the instrumental developments I carried out on both the DMD-integrated AO-FIO and the AO-CRSO to create an imaging system capable of studying flicker-induced vasodilation in the retina with high spatial and temporal resolution. Although I also explored the Laser Doppler Holography system, due to time constraints, my focus remained on the first two systems. Preliminary work on the Laser Doppler Holography system is included in Appendix A.

Chapter 2

The DMD-integrated AO-FIO: a pathfinder towards a clinical instrument for studying neurovascular coupling

To investigate neurovascular coupling in the retina at a high spatial and temporal resolution, it is essential to use an imaging system that can either track erythrocytes to measure blood flow or resolve blood vessel walls to assess their dilation in response to light stimulation. Such a system must combine high transverse resolution with a high frame rate and a large field of view, while also providing sufficient contrast to clearly visualize the structures of interest. A system that accomplishes many of these requirements is the Digital Micromirror Device (DMD)-integrated Adaptive Optics (AO) Flood Illumination Ophthalmoscope (FIO), which is described in this chapter.

The DMD-integrated AO-FIO is a subsystem of the ECRUROeil bench. Developed during previous PhD theses with ONERA [24] [94] [25], this system allows for the projection of high resolution patterns in the retina. Paired with the high frame rate, large field of view and distortion-free imaging provided with AO-FIO, this system has been used for applications such as visual psychophysics (see appendix A), super resolution imaging [94] and maximizing bright field contrast using partial field imaging [26]. Owing to this high frame rate and resolution, this imaging modality is a promising solution to study neurovascular coupling. Consequently, at the beginning of my PhD, I first pursued the idea of using the DMD-integrated AO-FIO to measure the dilation of blood vessel in response to light stimulation.

The first step towards that goal was to enhance the system's usability. Stable imaging over extended periods is crucial for accurately monitoring dynamic changes in blood vessel diameter in response to light stimulation. Therefore, improvements were made to ensure the system's stability, reliability, and ease of use. These improvements are detailed in section 2.2.

Secondly, the development of a high-resolution, camera-based instrument for the study of neurovascular coupling requires addressing the challenge of enhancing the contrast of blood vessel walls and erythrocytes. The system's ability to project various patterns allows for the exploration and optimization of the different types of contrast techniques that can be achieved in the retina on a camera-based system. Through this flexibility, we gain valuable insights into the most effective methods for achieving a high contrast on blood vessel walls and erythrocytes. This work is detailed in section 2.3.

Finally in section 2.4, we looked at the possibility of using this system to study neurovascular

coupling in the retina.

2.1 Description of the ECUROeil Bench

The ECUROeil bench (Étude et Conception de systèmes Ultra Résolus pour l'OEIL, or Study and Design of High-Resolution Systems for the Eye), was the primary system that I used throughout my PhD. Originally implemented during Jessica Jarosz's thesis in 2015 [95], this system was initially conceived as a high loop rate AO-FIO system, providing in-vivo cellular resolution imaging with a wide field of view (4°x4°) and a high frame rate (100 Hz). Since then, the ECUROeil bench has evolved into a platform for enhancing full-field retinal imaging by varying the system's illumination geometry. Notable work include the retinal goniometer [24] modality, which enables control over the angle of incidence of the illumination on the retina. The introduction of a Digital Micromirror Device (DMD) for projecting patterned illumination on the retina has also led to many applications. For instance, during Yann Lai Tim's thesis, the ability to project fringes on the retina was used to achieved Structured Illumination Microscopy (SIM) imaging in the retina, which enhanced both contrast and resolution [94]. Additionally, the capacity to project illumination patterns on the retina was used during the thesis of Elena Gofas [24] and Léa Krafft [25] to increase bright-field contrast in partially illuminated regions [26].

2.1.1 The DMD-integrated AO-Flood Illumination Ophthalmoscope: optical setup

The optical setup of the DMD-integrated AO-Flood Illumination Ophthalmoscope is represented in figure 2.1. The adaptative optics correction module is composed of a Shack-Hartmann wavefront sensor as well as a deformable mirror enabling a close loop correction at 30 Hz [50]. A superluminescent diode emitting at 750 nm and with a spectral bandwidth of 20 nm is used for the beacon source and a 860 nm superluminescent diode with a bandwidth of 60 nm is used for the imaging source. The image is formed on a CMOS camera (ORCA-Fusion, Hamamatsu) which is mounted on a translation stage used to translate the camera on the right imaging plane.

To project illumination patterns onto the retina, a Digital Micromirror Device is employed. This device consists of an array of square mirrors, each mirror can be individually toggled ON (reflecting light into the optical system) or OFF (deflecting light away from the system). The DMD is positioned at a focal plane conjugate to the retina. Additionally, the imaging light passes through the deformable mirror before reaching the retina. This ensures that the patterns projected by the DMD are pre-compensated by the DM, allowing for the delivery of high-resolution illumination patterns.

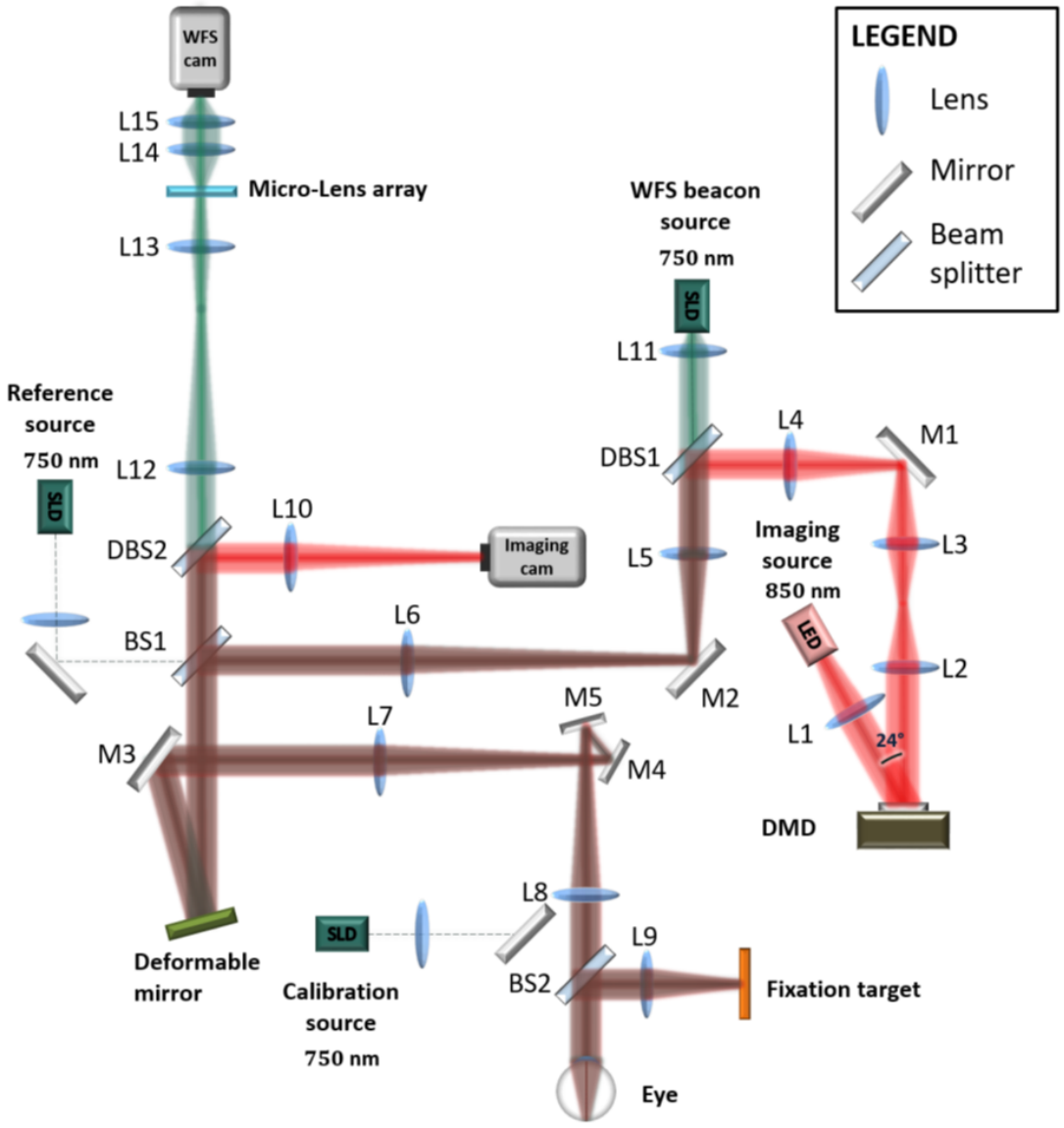

Figure 2.1: Experimental set-up of the the DMD-integrated AO-FIO. The use of a digital mirror device (DMD) enables the projection of high resolution illumination patterns in the retina.

2.2 Improvement of the clinical usability of the ECUROeil bench

To study neurovascular coupling, it is essential to have a system that not only produces high-quality images but is also easy to use and reliable. Furthermore, the capability to perform prolonged imaging sessions is important for monitoring dynamic processes and long-term changes in neurovascular coupling. This requires an easy to operate and robust system that can maintain performance over extended periods of time. During my thesis, I first contributed to improve this aspect of the system.

2.2.1 Implementation of a 3 axis motorized chinrest

One aspect of improving the usability of the system involved implementing a better chinrest. In its initial implementation, the chinrest of the system could be moved along three axes, but only the x-axis was motorized (see figure 2.2). While this setup was sufficient for imaging the retinas of cooperative subjects which were familiar with the system, it proved inconvenient to use with patients. Specifically, the manual control of the y-axis, which was located close to the subject, made adjustments during acquisitions quite inconvenient. This posed a significant issue as proper alignment of the subject with the system is crucial, requiring constant adjustments of both the x and y axes.

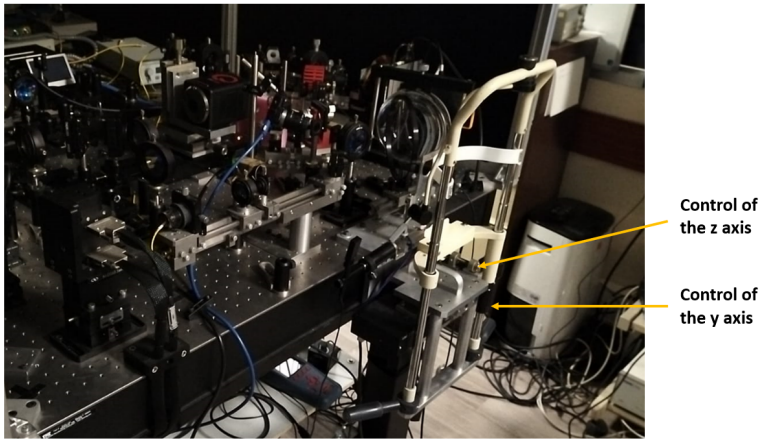

Figure 2.2: Picture of the old chinrest of the ECUROeil bench.

To address this issue, a new chinrest with three motorized axes was designed during Antoine Odobert's master thesis internship at ONERA. Due to space constraints on the optical bench and the need to leave room for the subjects being imaged, three sturdy motorized axes were relocated to the left side of the table. A custom-made chinrest piece was then attached to the y-axis using an aluminum piece (see figure 2.3).

2.2.2 Installation of a light-blocking cloth

To improve patient comfort and reduce external light interference during acquisitions, a light-blocking cloth was installed around the chinrest (figure 2.3). This setup ensures that patients are in a dark environment during imaging sessions, which minimizes distractions and helps

maintain their focus, this is particularly important considering that we ultimately want to do light stimulation on our subjects.

Figure 2.3: On the left, a representation of the new chinrest with 3 motorized axis installed on the system. On the right, a picture of the light-blocking installed on the system.

2.2.3 Data Acquisition software

For image recording, the Holovibes software [96] was selected, originally designed for laser Doppler holography applications. This software leverages the capabilities of graphics processing units (GPU), (Nvidia GTX Titan Xp in our case), to enable real-time image visualization and several image processing features such as band pass filtering or image averaging. Additionally, Holovibes supports high-throughput imaging without any frame drops.

Using Holovibes instead of the camera manufacturer's software (Hamamatsu, ORCA Fusion) significantly enhances the system's usability. With Holovibes, images can be visualized in real-time, and the contrast or filtering can be adjusted on the rendered image, facilitating the identification of retinal structures and the adjustment of imaging parameters. Moreover, the only constraint on acquisition duration is the computer's disk space, allowing for continuous recording of several minutes of imaging without any frame drops. This capability ensures extended and uninterrupted imaging sessions, which are very interesting for studying neurovascular coupling.

After implementing these improvements, the clinical readiness of the system was improved dramatically. A single operator can easily fully operate the system, simultaneously adjusting the chinrest position to keep the right pupil alignment throughout data acquisition while also controlling imaging and AO loop settings. These advancements in clinical usability have made it possible to employ this system in a clinical trial aimed at studying the dynamics of micro-eye movements to identify biomarkers of Age-Related Macular Degeneration (AMD).

2.2.4 Clinical application: studying the dynamics of micro-eye movements to identify biomarkers of retinal diseases

A thorough description of this work can be found in an article published by Jimmy Murari et al in Ophthalmology, which can be found in the first appendix A. Briefly, the goal of this

work was to analyze ocular movements in both control populations and populations with early AMD while the subjects performed psychophysical tests using patterns projected through the DMD-integrated AO-FIO. An example of a pattern projected for a fixation task is represented in figure 2.4.

These tests were conducted using patterns projected by the DMD, which allowed for tracking ocular movements while imaging the photoreceptors of the retina at 800 Hz. To link alterations in eye movements with structural changes in the retina, particularly the presence of drusen, the central retina of the patients was also imaged using gaze-dependent imaging [97]. Participants were recruited from the SilverSight Cohort [98] and divided into three groups: young controls, older controls, and preclinical AMD subjects. Among these subjects, microsaccade amplitude, drift diffusion coefficient, and ISOline Area (ISOA) were found to be significantly larger in patients with foveal drusen compared to controls. This provides compelling evidence of both functional and structural signs of early age-related changes in the retina.

The success of this clinical study, using the DMD-integrated AO-FIO, even in patients with reduced visual acuity, eye opacity, or pupil dilation, highlights the system's robustness and its suitability for clinical investigations.

Figure 2.4: Example of pattern projected with the DMD-integrated AO-FIO used for a visual psychophysics fixation task.

2.3 Enhancing the contrast of blood vessels walls and erythrocytes on a camera-based system

When a pattern illumination is projected into the retina instead of a full field illumination, the contrast of retinal structures varies significantly. Notably, phase contrast can be observed in the non-illuminated regions surrounding the pattern. This effect has been documented in previous work by Elena Gofas [24] and Lea Krafft [25]. My approach was to use empirical data in which illumination patterns of various sizes and forms had been used, to understand how to enhance the contrast of blood vessel walls and erythrocytes on a camera-based adaptive optics system.

2.3.1 Full field illumination versus projection of patterns in the retina

Full field imaging:

When the micro mirrors of the DMD are all switched ON, the entire field of view is illuminated, akin to a standard flood illumination ophthalmoscope. The full-field illumination of the retina results in multiply scattered photons, contributing to significant background noise. Consequently, hypo-reflective structures become invisible or obscured by the diffuse background.

A typical averaged image of the nerve fiber layer with this configuration can be observed on figure 2.5 A). In this image, the blood vessels exhibit their characteristic appearance, including a bright central strip attributed to strong specular reflection from their upper surface. However, the vessel walls exhibit poor contrast, and distinguishing the different layers of these walls is challenging. Additionally, to enhance the signal-to-noise ratio, image averaging is necessary, complicating the imaging of dynamic features such as erythrocytes.

Pattern projection:

When a pattern is projected onto the retina, the structures located outside the projected area exhibit a contrast that is reminiscent of phase contrast images that can be obtained with offset aperture AO-SLO. [92] [22]. As can be observed in figure 2.5, the contrast of the vessel walls is increased as compared to full field illumination (figure: 2.5 B1), Some capillaries also become visible right outside of the projected pattern (figure:2.5 B2).

A similar effect is observed with erythrocytes. In videos of registered frames, the flow of erythrocytes at the edges of projected static patterns can occasionally be detected. A frame from one of these example is presented in figure 2.6 where individual red blood cells moving within a capillary are visible (Orange arrow in figure 2.6).

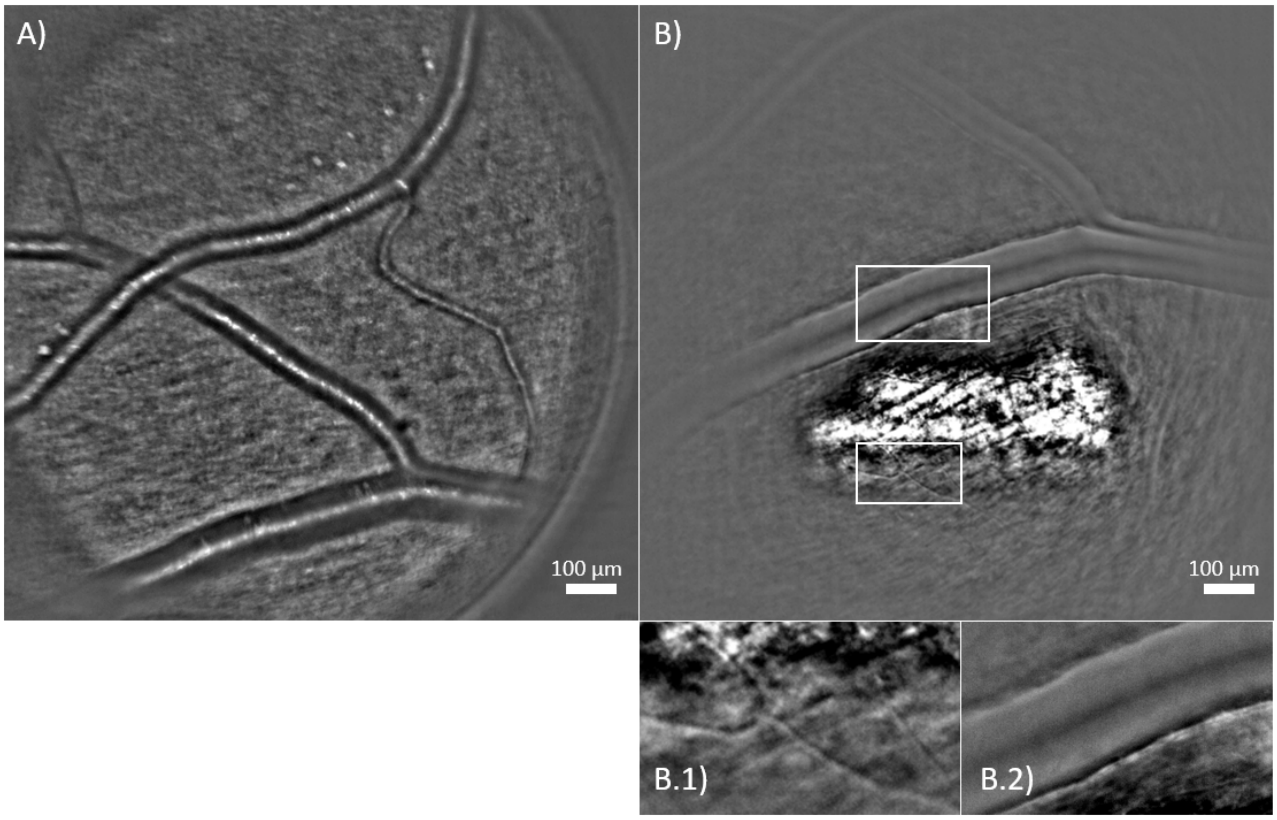

Figure 2.5: A) full field image B) image were a 100 µm x 500 µm rectangular pattern is projected in the retina. B1) and B2) are magnified regions of the image showing respectively phase contrast of a capillary and the vessel walls of a large vessel.

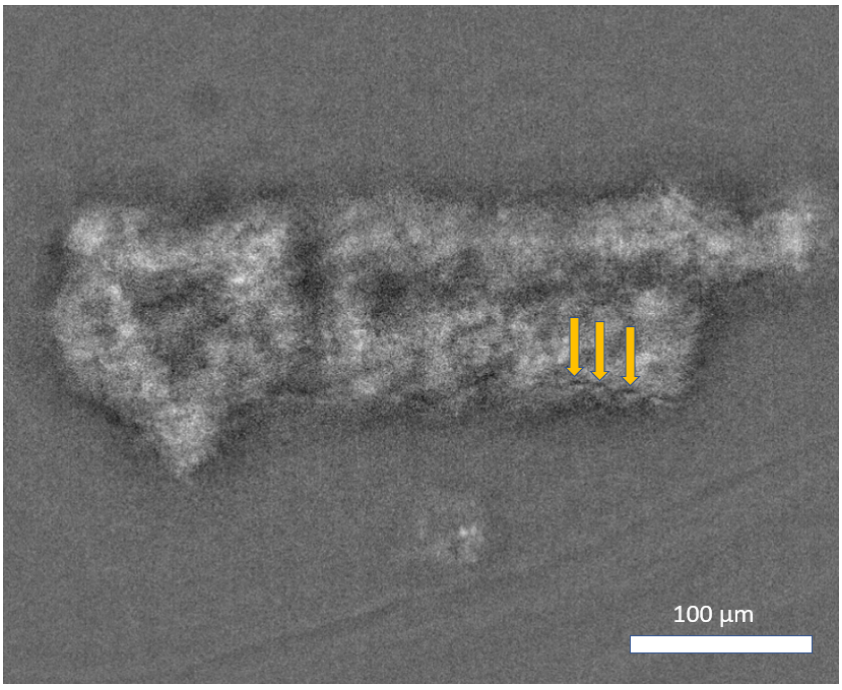

Figure 2.6: Image showing how red blood cells can be imaged at the edge of projected patterns.

The mechanism underlying this contrast is complex, encompassing diffraction, refraction, absorption and scattering. Some studies have tried to simulate phase contrast imaging in the case of AO-SLO systems, notably Guevara-Torres et al. [99]. In our case, which is the case of a full field imaging system, the observed contrast seems similar as what is described in the oblique back-illumination model described in microscopy by Ford, Chu and Mertz [100]. In this model, a lateral offset between the illumination and the object is imposed and a camera-based detector is used. The light is first backscattered by the scattering medium then refracted by the phase object, finally pupil filtering produces the phase gradient contrast.

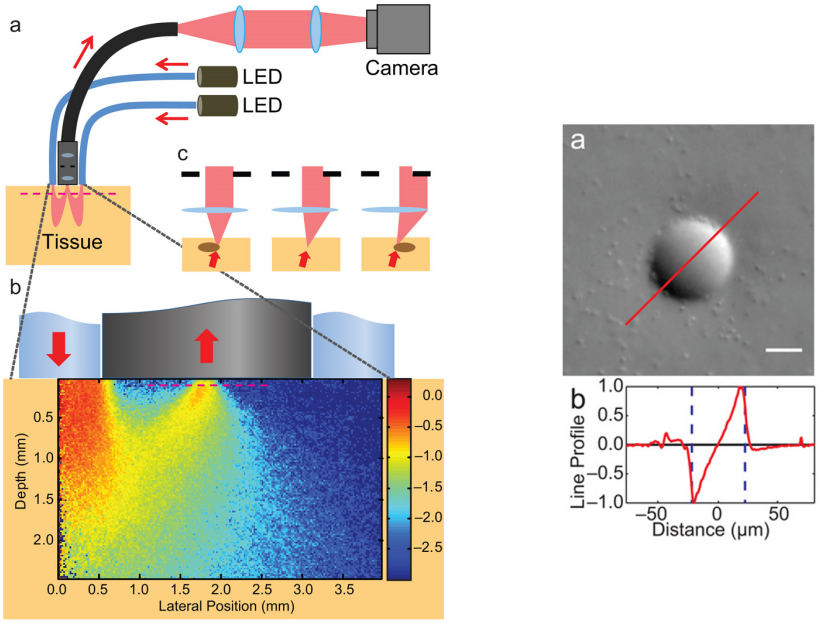

Figure 2.7: Schematic description of the oblique back-illumination microscope system introduced by Ford et al. for phase contrast imaging of thick scattering samples. From Ford et al. [100].

Simulation work in the form of a Monte Carlo simulation is underway in our group to better understand how this phase contrast appears in the case of the retina. However, for the practical purpose of developing a system capable of measuring neurovascular coupling in the retina, I focused on empirical evidence to understand the behavior of this contrast and how it can be optimized for imaging blood vessel walls and erythrocytes.

2.3.2 Empirical characteristics of phase contrast

2.3.2.1 Aspect of the phase contrast

In figure 2.8 two images where patterns have been projected in the retina to elicit phase contrast are presented. These examples highlight how phase contrast looks like for circular structures such as photoreceptors or erythrocytes and for non-circular structures such as blood vessels.

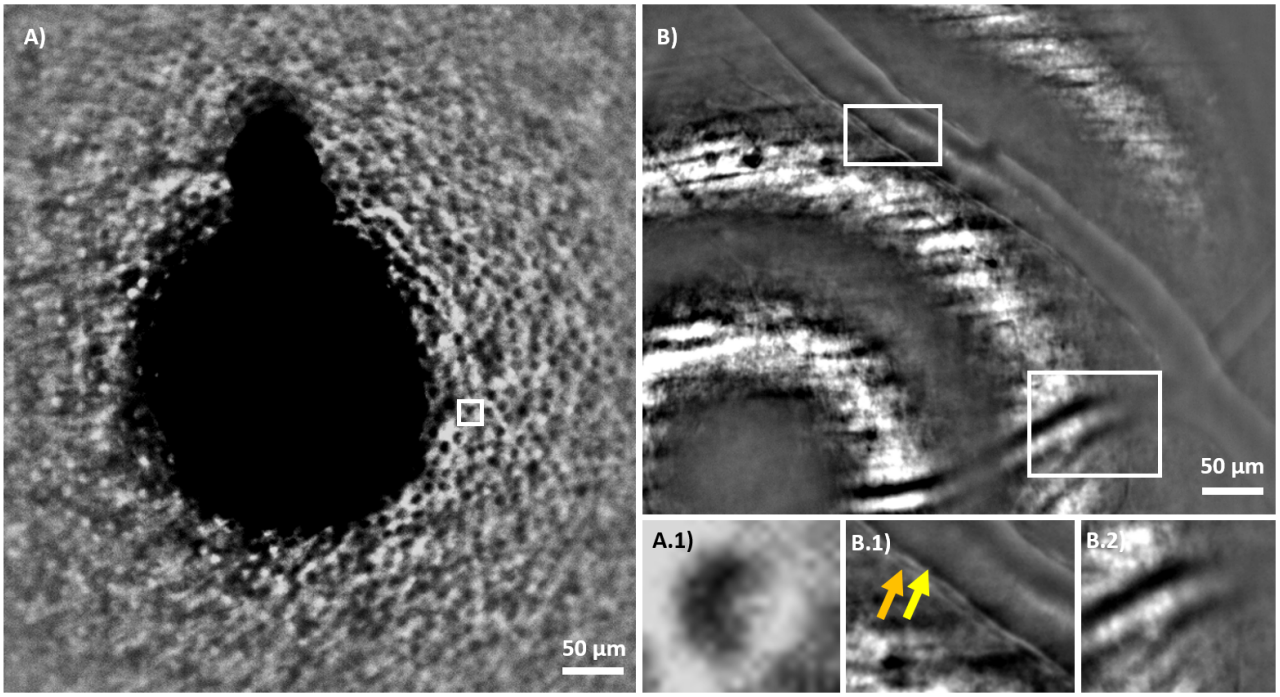

Figure 2.8: Aspect of the phase contrast in the non illuminated regions of the field of view. A) a circular illumination pattern was projected on the retina while the system was focused on the photoreceptor layer. A circular mask was placed on the illumination region to highlight the phase contrast aspect of the photoreceptor. A.1) Shows a magnified photoreceptor, showing its phase gradient aspect. B) Concentric rings were projected on the retina while the system was focused on the nerve fiber layer to show the aspect of blood vessels at the edge of the projected pattern. B.1) shows a magnified view of a blood vessel at the edge of a projected pattern showing the highly contrasted vessel wall. The orange and yellow arrows point respectively at the tunica adventitia and the tunica intima of the blood vessel. B.2) is a magnified image of a blood vessel inside the illuminated region, the vessel wall is not visible.

2.3.2.2 Circular structures: photoreceptors and erythrocytes

Figure 2.8 A) shows a circular pattern projected while focusing on the photoreceptor layer. The pattern was masked during post-processing to better visualize the photoreceptor inner segments revealed by phase contrast. These circular and translucent structures exhibit a contrast gradient, with the side closest to the illumination appearing darker and the side furthest from the illumination appearing brighter, as shown in the magnified image (figure 2.8 A.1). The same appearance is observed for erythrocytes as shown in figure 2.6. This contrast gradient is very similar to what was described by Ford et al. [100] (See figure 2.7).

2.3.2.3 Non-circular structures: blood vessels

Figure 2.8 B) depicts the projection of an illumination pattern near a blood vessel. The vessel wall near the projected pattern exhibit a high contrast. The tunica externa appears as a thin dark layer, indicated by the orange arrow in figure 2.8 B.1). Similarly, the tunica intima appears as a thin dark layer, indicated by the yellow arrow. The tunica media, located between the tunica intima and tunica externa, is visible as a white layer.

2.3.2.4 Direction of the pattern with respect to the structure

For non centro-symmetrical structures such as vessels, there is an important impact of the orientation of the illumination pattern with respect to the vessel. Indeed when the vessel is in the same direction as the pattern for instance in figure 2.8 B.1) ,the vessel wall exhibits strong contrast. Conversely, when the vessel is perpendicular to the pattern, as illustrated in figure2.8 B.2), the vessel wall is not visible.

2.3.2.5 Size of the illuminated region

The further the structure is from the illumination patch, the less contrasted it is. Therefore for a given amount of incident photons, the best strategy is to concentrate all the photons close to the structure that we want to image. With the DMD-integrated AO-FIO however, this is not possible as the size of the illuminated area is proportional to the number of incident photons.

2.3.2.6 Projection of a single pattern compared to multiple patterns

When multiple separated patterns are projected with the DMD-integrated AO-FIO, a significant decrease in phase contrast at points which are surrounded by illuminated regions can be observed. This effect can be seen for instance in figure 2.9 B) where the area at the center of the projected four circles exhibit very low phase contrast. The remaining contrast at the center of the four circles is interpreted as absorption contrast. In the same manner, projecting multiple parallel lines as in figure 2.9 A) results in reduced phase contrast in regions with equal distance to two illumination lines. This is due to cross talk effects between the phase contrast caused the opposing projected pattern causing opposing contrast gradients on the structure.

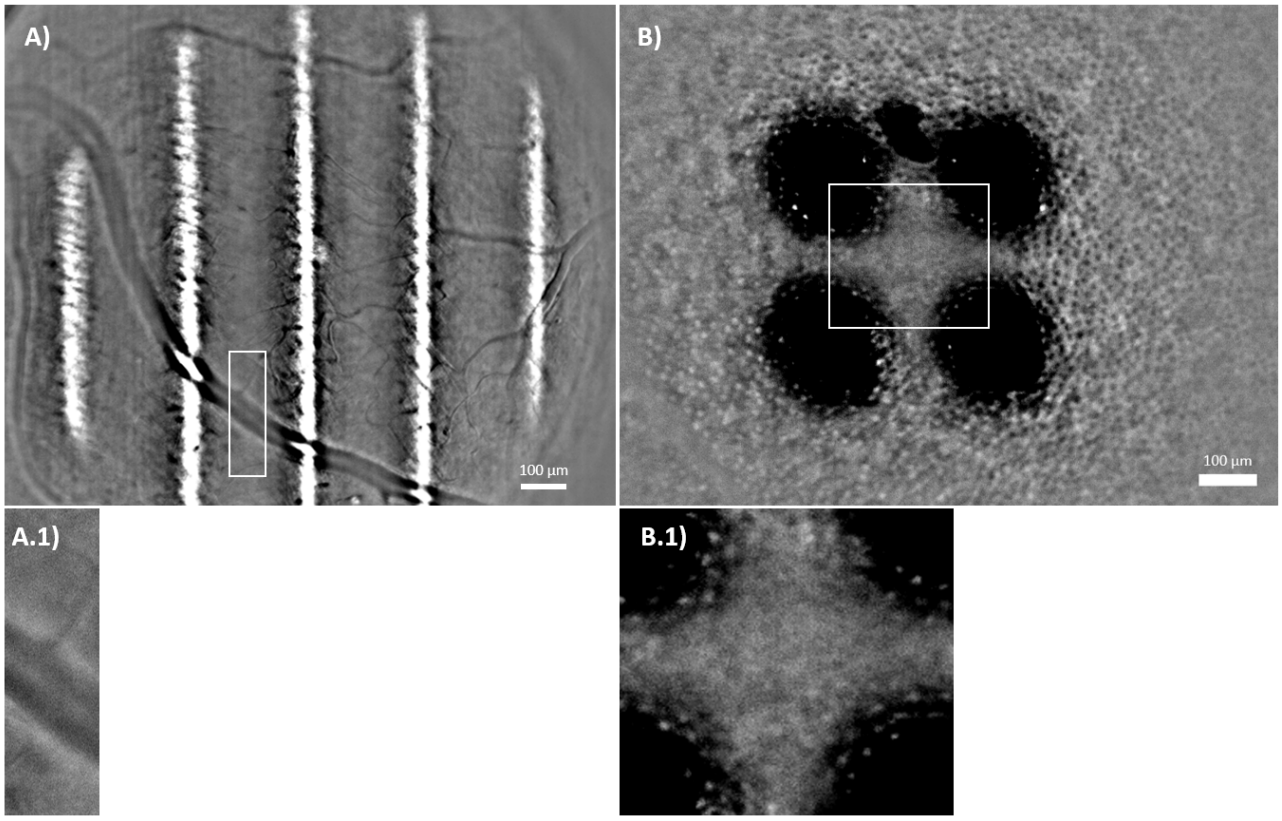

Figure 2.9: Effect of pattern symmetry on phase contrast. A) Thin periodic lines were projected onto the retina while focusing on the nerve fiber layer. A loss of phase contrast is evident in the region with approximately equal distances between two lines. A.1) A magnified view highlighting this loss of phase contrast. B) Four small circles were projected onto the retina while focusing on the photoreceptors. The contrast of the photoreceptors' inner segments between the four circles is very low, as shown in B.1).

2.3.2.7 Extension of phase contrast

When a pattern is projected near a structure of the retina, the phase contrast seems to be the strongest near the projected pattern and to decay with the distance between the projected pattern and the structure. The rate of this decay is different depending on the observed structure of the retina. These differences can be explained by their differences in size, shape, optical index and depth in the retina. In figure 2.10, illumination patterns were projected near various retinal structures to determine the maximum distance with which good phase contrast is conserved.

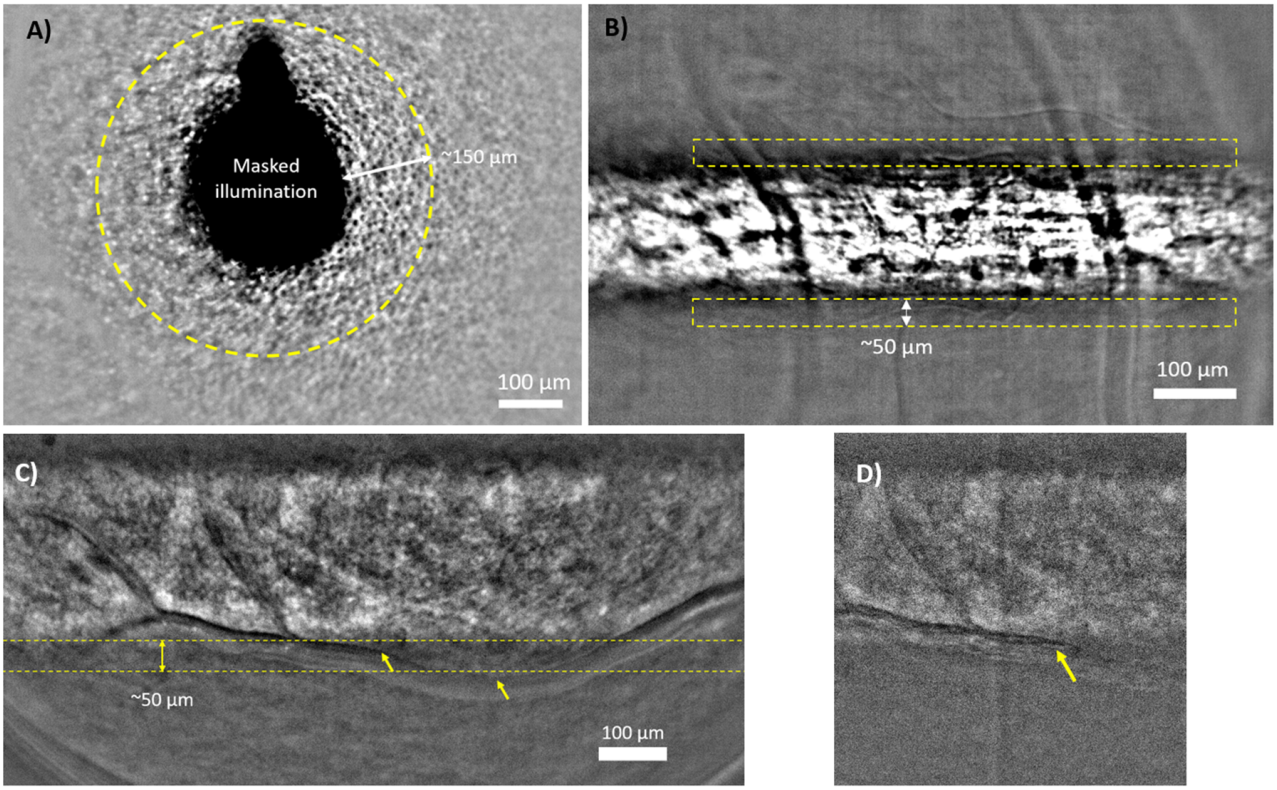

Figure 2.10: Observed extension of phase contrast for different structures of the retina. The yellow dashed area represents the area of good phase contrast for each structure A) A circular pattern was projected with the system focused on the photoreceptor layer. Outside the pattern, the photoreceptors' inner segments are visible, extending approximately 150 µm. B) A rectangular shape was projected with the system focused on the nerve fiber layer. Capillaries are visible, extending 50 µm around the projected rectangle. C) A rectangular pattern was projected near a blood vessel with the system focused on the nerve fiber layer. Two orange arrows highlight a well-contrasted vessel wall (left arrow) and a vessel wall outside the area of good phase contrast (right arrow). D) Image captured from a video of the same area shown in C). Erythrocytes are visible at the edge of the projected pattern, as indicated by the orange arrow.

Photoreceptors
When the system is focusing on the photoreceptor layer and a pattern is projected, the photoreceptor's inner segment is visible outside of the pattern with an extension of approximatelly 150 µm as annotated in the yellow dashed circular area in figure 2.10 A).

Blood vessel walls
For large blood vessels, the vessel wall is visible quite far from the projected pattern as observed in figure 2.5 where the vessels can be seen on almost the entire field of view of the image. However, the different layers of the wall are visible no more than 100 µm away from the illumination pattern (figure 2.8 B.1)). For smaller blood vessel however, the extension of phase contrast is around 50 µm as we can see in figure 2.5 where the area further than 50 µm from the edge of the projected rectangular pattern exhibit significant reduction in the contrast of the vessel wall.

Capillaries
For capillaries, as exemplified in figure 2.10 the extension of good phase contrast seems to also be 50 µm. It is however interesting to note that some capillaries are still visible further from this distance, most of them are only visible in the rectangular dashed orange area.

Erythrocytes
For erythrocytes, the only time when we were able to see them using the DMD-integrated AO-FIO was when they were right on the edge of a projected pattern in the way depicted in figure 2.6.

Our observations regarding the extension of phase contrast can be summarized in the following table:

	Photoreceptors' inner segment	Blood vessel wall	Capillaries	Erythrocytes
Extension of phase contrast	150 µm	50 µm	50 µm	30 µm

Figure 2.11: Observed extension of phase contrast for different structures

2.3.3 Application: Developing a strategy to optimize phase contrast imaging of blood vessels and erythrocytes

To achieve full field phase contrast imaging, one can project complementary patterns in the retina, select numerically the area outside of the projected pattern which exhibit phase contrast and reconstruct the total field of view. The observed characteristics of phase contrast from the previous section can help us find the best strategy to do so:

Choice of the pattern: As outlined in the previous section, the projection of multiple complementary patterns leads to regions within the field of view exhibiting reduced phase contrast due to cross-talk effects. Therefore, employing a single monoblock shape is a more effective strategy than projecting multiple complementary patterns. Then to make a full field image, this monoblock shape must be scanned across the entire field of view. A shape that meets these requirements particularly well is a line. Ideally, this line should be thin and capable of concentrating as much energy as possible within the eye safety limit.

Area of detection: As discussed in the previous section, the phase contrast extension for vessel walls and capillaries is 50 µm, and for erythrocytes, it is 30 µm. This extension defines the area surrounding the projected line to be selected for maximizing phase contrast on these structures

Direction of the scan: Using a scanning line, the retina can either be scanned horizontally or vertically. For blood vessels, given their non-centrosymmetric nature, the projected line must be parallel to the vessels to achieve maximum phase contrast. Considering the vascular structure of the retina, a vertical scan would provide access to a greater number of vessels compared to a horizontal scan.

Post processing: The entire retina can be scanned from top to bottom by projecting a vertically moving line. Then, on each recorded image, the entirety of the image is masked numerically except the non illuminated region just above the line. By combining all these images, a full field image is obtained, this image named "offset 1". By doing the same procedure but this time by masking numerically the entirety of the images except the area beneath the projected line we get the "offset 2" image. Given the observed phase contrast characteristics, which exhibit a gradient from dark to bright, the offset 1 and offset 2 images display opposite contrast gradients. A final phase contrast image can be obtained by subtracting the offset 1 and offset 2 images, effectively canceling out the background and enhancing the phase contrast. The same principle, applied in AO-SLO systems through a technique known as split-detection, has proven effective for imaging phase objects [21]

2.3.4 Optics letter: Multimodal high-resolution retinal imaging using a camera-based DMD-integrated adaptive optics flood-illumination ophthalmoscope

This strategy was carried out in the following article published in Optics Letter to demonstrate full field phase contrast high-resolution imaging using the DMD-integrated AO-FIO. My main contributions to this work are the peripheral improvements presented in section 1, the collection of the data for this article and analysing the empirical data taken from the DMD to find the best strategy to improve phase contrast imaging of erythrocytes and blood vessels.

Optics Letters

Multimodal high-resolution retinal imaging using a camera-based DMD-integrated adaptive optics flood-illumination ophthalmoscope

Léa Krafft,[1,2] Pierre Senée,[1,2] Elena Gofas,[2] Olivier Thouvenin,[3] Michael Atlan,[2,3] Michel Paques,[2] Serge Meimon,[1,2,3,†] and Pedro Mecê[2,3,†*]

[1] DOTA, ONERA, Université Paris Saclay F-91123 Palaiseau, France
[2] Paris Eye Imaging Group, Centre d'Investigation Clinique 1423, Quinze-Vingts National Ophthalmology Hospital, DGOS, INSERM, Paris, France
[3] Institut Langevin, ESPCI Paris, CNRS, PSL University, Paris, France
[†] These authors contributed equally to this work.
*pedro.mece@espci.fr

Received 15 May 2023; revised 28 June 2023; accepted 28 June 2023; posted 30 June 2023; published 11 July 2023

We demonstrate the feasibility of a multimodal adaptive optics flood-illumination ophthalmoscope, able to provide both bright-field and dark-field images (such as phase contrast). The multimodality was made possible by integrating a digital micromirror device (DMD) at the illumination path to project a sequence of complementary high-resolution patterns into the retina. Through a versatile post-processing method that digitally selects backscattered or multiply scattered photons, we were able: (1) to achieve up to four-fold contrast increase of bright-field images when imaging the photoreceptor mosaic and nerve fibers; and (2) to visualize translucent retinal features such as capillaries, red blood cells, vessel walls, ganglion cells, and photoreceptor inner segments through phase contrast.

https://doi.org/10.1364/OL.495515

The adaptive optics scanning laser ophthalmoscope (AO-SLO) [1] has become the primary technique to achieve *in vivo* cellular resolution retinal imaging. In bright-field mode, highly contrasted images from photoreceptors (PR) and nerve fiber layer (NFL) can be obtained owing to the use of a confocal pinhole, filtering out multiply scattered photons and detecting backscattered photons [1]. Additionally, the lateral displacement of the detection position compared with the illumination in AO-SLO made possible off-axis detection schemes revealing translucent retinal structures such as PR inner segment, red blood cell, vessel walls, capillaries, and ganglion cells [2–4]. Such dark-field techniques explore multiple scattering and forward scattering photons to generate contrast from phase gradient [2,5].

Although AO-SLO has proven its value, it is prone to image distortion due to its slow scanning speed relative to eye motion [6]. Reducing the image field-of-view (FOV) is a common strategy to mitigate intra-frame distortion. However, the typical image rate is still slow to track dynamic processes in the retina such as blood flow in capillaries. Conversely, camera-based adaptive optics flood-illumination ophthalmoscope (AO-FIO) systems have demonstrated immunity to motion-induced artifacts across the FOV owing to their high throughput [7]. Nevertheless, AO-FIO has not been favored over AO-SLO because of its lack of confocal gating, deteriorating the image contrast in bright-field mode. Moreover, dark-field techniques have not been so far fully explored and demonstrated in AO-FIO, apart from preliminary results restricted to obtaining such contrast in a narrow portion of the FOV [8,9], consequently most of the translucent retinal features seen in AO-SLO are still not visible in AO-FIO.

Recent works have demonstrated that spatial filtering could be implemented in AO-FIO to enhance the imaging contrast on bright-field mode while still benefiting from the distortion-free images [10,11]. Those works build on the use of programmable pattern projections with a digital micromirror device (DMD). The patterns generated by the DMD partially illuminate the FOV, decreasing the total number of detected multiply scattered photons [10]. Then, spatial filtering was possible by putting to zero value the camera pixels corresponding to non-illuminated areas. Finally, images acquired with complementary patterns were recombined to form a full-field image with enhanced contrast. Lee *et al.* reported up to three-fold contrast improvement compared with conventional AO-FIO images at a frame rate of 250 Hz [11]. However, all these works only focused on exploring backscattered photons coming from illuminated areas to generate bright-field photoreceptor mosaic imaging in a narrow FOV. Here, we demonstrate the capability of a DMD-integrated AO-FIO to not only generate large FOV contrast-enhanced bright-field images but also to reveal translucent retinal features, not yet visible in AO-FIO through phase and absorption contrasts.

The DMD-integrated AO-FIO platform was previously described in detail elsewhere [10]. High-resolution illumination patterns generated by the retina-conjugated DMD were projected on the retina after being pre-compensated for ocular aberrations by the deformable mirror (DM). Hence, the double pass on the DM allowed for diffraction-limit resolution for both illumination (for patterns projection) and imaging. Projected

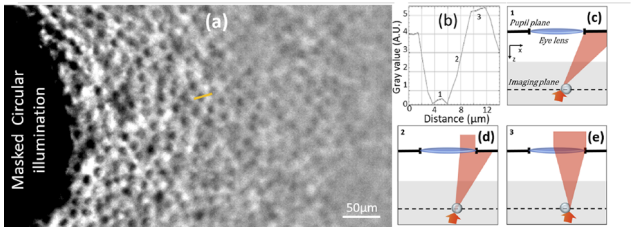

Fig. 1. (a) Cropped phase contrast image of PRs after masking the illumination area (black region). Note that the contrast starts to decline for PRs located around 0.5° away from the illuminated area. (b) Intensity profile across one photoreceptor (orange line) outlining the diphasic aspect. Labels 1–3 refer to the contrast mechanism described in (c)–(e), which is inspired by the model presented in Ref. [14].

patterns consisted of binary images generated by custom-built Python software. We used the manufacturer software EasyProj to upload patterns and control the DMD, enabling us to project static patterns or a sequence of patterns.

To demonstrate the multimodal ability of the system, we designed two different sequences of patterns: one favoring a higher contrast for bright-field imaging (named "Pattern sequence 1"), and another to favor a better contrast in phase contrast imaging (named "Pattern sequence 2"). Patterns spacing was based on the observation described in Fig. 1(a), while the width was empirically determined by experiment prior to image acquisition. A schematic of the patterns can be found in Figs. 2(a) and 3(a). Pattern sequence 1 consisted of periodic vertical lines with a width of 28 μm, and spaced by 252 μm over 3.5° FOV. To illuminate different areas of the retina, the pattern was successively shifted by 55 μm at 30 Hz. For a full cycle of illumination, four patterns were needed. Pattern sequence 2 consisted of a single horizontal line with a width of 100 μm over 3.5° FOV. Then, 24 patterns were generated, each one subsequently shifted by 50 μm.

Images were acquired on four healthy subjects. Written informed consent was obtained from all participants in accordance with institutional guidelines. The experimental procedures adhered to the tenets of the Declaration of Helsinki. The participants were seated in front of the system, while their head was stabilized with a forehead and chin rest. A fixation target was used to guide their line of sight during the imaging session. Eye drops were used for pupil dilation. The total irradiance for the imaging and AO light sources was, respectively, 1700 μW and 2.8 μW, which is below the ocular safety limits stipulated by the International Organization for Standardization (ISO) standards for group 1 devices.

Before image acquisition, a calibration step consisted of matching the focal planes of the camera and the DMD by moving a translation stage where the camera was mounted. Then, a final step before starting image acquisition consisted of using the DM to place the camera/DMD focal plane at the retinal layer of interest. The camera acquired images of 2048×2048 pixels at 100 Hz (10 ms exposure, which is sufficient to avoid motion blur [12]), while the illumination field-of-view, without any pattern projection, was as large as $3.5° \times 3.5°$. Before acquiring images with Pattern sequences 1 and 2, an image sequence without any pattern (equivalent to a conventional AO-FIO image, and named here full-field illumination) composed of 100 frames was acquired and served as a reference for image processing. The DMD projected the sequence of patterns at 30 Hz and was not synchronized with the camera acquisition (see Visualization 1 for examples of image sequences using Patterns 1 and 2). Because of the lack of synchronization, one-third of raw images presented artifacts originated from the transient states of the DMD micro-mirrors and needed to be discarded. To

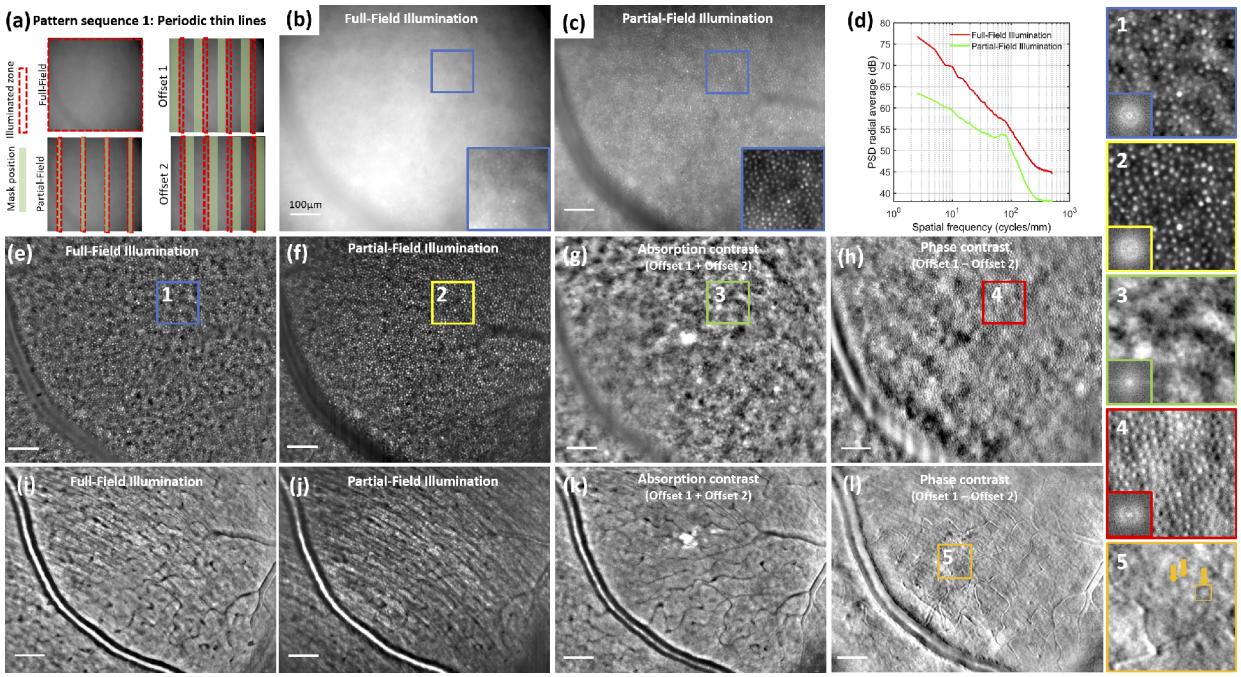

Fig. 2. (a) Pattern sequence 1 detection schemes. (b),(c) Full-field and partial-field images highlight the contrast gain, respectively. (d) Power spectral density from (b) and (c). (e),(f) Full-field and partial-field images after applying a digital high-pass filter, respectively. (g),(h) Absorption and phase contrast images of PRs, respectively. (i)–(l) Full-field, partial-field, absorption, and phase contrast for NFL imaging, respectively. (1)–(5) are magnified images and their respective Fourier transforms. Yellow arrows indicate ganglion cells, and yellow box delineates a single one. Scale bar: 100 μm.

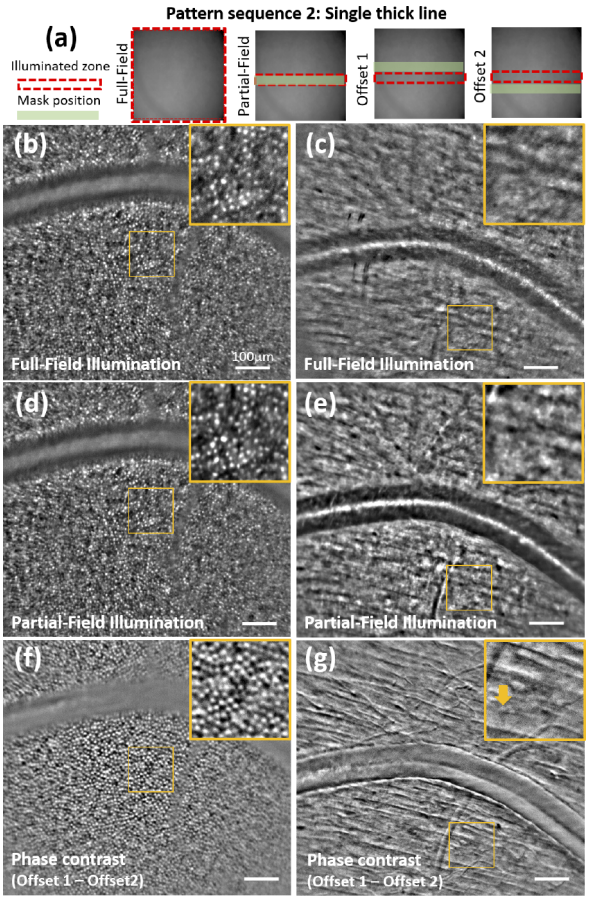

Fig. 3. (a) Pattern sequence 2 detection schemes. (b),(c) Conventional AO-FIO images of (b) PRs and (c) NFL. (d),(e) Contrast-enhanced bright-field images of PRs (d) and NFL (e). (f),(g) Phase contrast images of (f) PRs and (g) NFL. Yellow arrow indicates ganglion cells. Scale bar: 100 µm.

illuminate the same retinal area at least 50 times, image acquisition consisted of 500 and 3000 frames for Pattern sequences 1 and 2, respectively, enabling the reconstruction of full-field images. Images were acquired using custom-made open-source Holovibes software, allowing to apply a high-pass filter to eliminate multiply scattered haze in real-time [7]. This software was particularly convenient for fine positioning of the imaging plane and DMD patterns at the retinal layer of interest.

After the acquisition, each image sequence was processed as follows. First, the reference sequence (without any pattern) was averaged after registering them using a custom-built high-spatial frequency-based phase correlation algorithm adapted to noisy AO-FIO images [13]. Then, the reference averaged image was used as a global reference to register (i.e., align) patterned images using the same registration algorithm. To generate the different image contrasts, by selecting photons detected in and out of illumination zones, we converted the binary patterns generated for the DMD into masks at the camera plane. Image shifts previously measured to correct eye motion were also applied to the masks. Then, we used the masks to do digital filtering (putting pixels outside the zone of interest to zero value), enabling us to generate the following contrasts: (1) near-confocal bright-field imaging (henceforth denominated as partial-field illumination [10]); (2) absorption contrast; and (3) phase contrast. Partial-field imaging consisted of putting to zero value all the pixels outside the zone of illumination, favoring the detection of back-scattered ballistic photons, in a similar manner as previous DMD-integrated AO-FIO works [10,11] and confocal AO-SLO. To generate absorption and phase contrasts, we summed and subtracted two "offset" images [4,5] generated with the partial-field masks shifted into two different directions, respectively. For example, in the case of Pattern sequence 2, Offset images 1 and 2 were, respectively, generated by putting to zero all pixels except those at the top (for Offset 1) or the bottom (for Offset 2) part just outside the illumination zone for a given number of pixels, here 100 (see Fig. 3).

Figure 1 highlights the ability of DMD-integrated AO-FIO to generate dark-field imaging. When projecting a static circular pattern, while focusing at the photoreceptor layer, a gradient contrast varying from dark to bright can be noticed in individual PRs located outside the illuminated zone. Such contrast is the hallmark of phase-gradient images seen in AO-SLO systems [5,15]. In the case of AO-FIO, the principle can be explained as follows: multiply scattered photons, originating from the illuminated area at a deeper layer, are refracted by a retinal feature, and filtered out by the eye's pupil. The part of the retinal feature close to the illumination will refract light out of the eye's pupil [Fig. 1(c)] generating a dark contrast [label 1 in Fig. 1(b)]. On the other hand, the part of the retinal feature far from the illumination will refract light inside the eye's pupil [Fig. 1(e)], generating a bright contrast [label 3 in Fig. 1(b)]. Such behavior has a strong similarity with oblique back-illumination microscopy [14]. Another interesting observation in Fig. 1(a) is that the farther the photoreceptor is from the illuminated area, the lower the phase contrast. By taking advantage of these observations, we created two different pattern sequences to demonstrate the capability of DMD-integrated AO-FIO to achieve multimodal imaging, through post-processing selection of ballistic and multiply scattered photons.

Figures 2(b) and 2(c) present a comparison of images generated with full-field and partial-field illumination [see Fig. 2(a) for the detection schemes] at the same retinal eccentricity when imaging the PR layer. Thanks to the spatial filtering in partial-field image, the haze generated by the detection of multiply scattered photons is decreased, hence the image presents a better contrast. We measured an averaged Michelson contrast of 6.6% and 26.6% for full-field and partial-field illumination, respectively, for a four-fold improvement. Further image improvement can be seen through the power spectral density of both images [Fig. 2(d)]. Owing to the spatial filtering, not only the haze low-spatial frequency energy decreases, but the spectral signal-to-noise ratio increases from 17.1 to 37.6. These observations are in accordance with previous publications using DMD-based AO-FIO [10,11]. Nevertheless, here, with our designed pattern, we were able to reconstruct an image with a larger field-of-view ($3.1° \times 2.6°$ against $0.7° \times 0.7°$), higher contrast gain (4 against 3) [11] and without any reconstruction artifacts [10]. In full-field illumination, it is common practice to filter out the multiply scattered haze with digital filtering [7]. Even after digital filtering, it is possible to notice an improvement in partial-field images compared with full-field [Figs. 2(e), 2(f), 2(i), and 2(j)]. In both PRs and NFL imaging, better optical sectioning can be noticed. In the case of PRs imaging, optical sectioning leads to the disappearance of a medium-spatial frequency probably coming from out-of-focus choriocapillaris, and make vessel located posterior to PRs darker, as it is typically seen in high optical sectioning imaging systems, e.g., in AO-SLO [3] or

in full-field optical coherence tomography (OCT) [16]. These changes also help to considerably increase photoreceptor mosaic contrast even after digital filtering. The increase of contrast is even more evident in the case of NFL imaging, where individual nerve fiber bundles become much more visible and contrasted, with the disappearance of capillary structures.

The same image sequence used to generate partial-field images can be processed to generate absorption and phase contrast images. To do so, we used the masks designed for Offset 1 and 2 [Fig. 2(a)]. By summing Offset images 1 and 2, one can generate absorption contrast images of PRs and NFL [Figs. 2(g) and 2(k), respectively]. For PRs, putative retinal pigment epithelium (RPE) [17] cells start to become visible, while PRs contrast decreases. In a similar manner, for NFL, nerve fibers disappear while previously rejected capillaries can be visualized. Finally, by subtracting Offset 1 from Offset 2, one can generate phase contrast images of PRs and NFL [Figs. 2(h) and 2(l), respectively]. In this case, for PRs, photoreceptor mosaic is again visible, but with phase gradient contrast similar to the one obtained using split-detection AO-SLO [3,5], which has been shown to correspond to the photoreceptor inner segment [3]. Now, for NFL, vessel and capillary walls have become highly contrasted, and putative ganglion cells (size: 10–12 μm) have started to be visible, in a similar manner and consistent size as it was previously shown for multi-offset AO-SLO [4,5].

The thinner lines composing Pattern sequence 1 favor partial-field imaging to the detriment of phase-contrast one. Indeed, with a thinner line fewer photons reach the retina, meaning that fewer photons will be multiply scattered to contribute to the phase contrast. Moreover, using a periodic multi-line pattern with a short inter-line distance leads to a competition of opposite phase gradient (or cross talk), decreasing or canceling out phase contrast. To favor phase contrast image, we designed and used Pattern sequence 2, composed of a single thicker line, increasing the number of photons being multiply scattered, and avoiding contrast cross talk. Figure 3 shows the results obtained with full-field (conventional AO-FIO), partial-field, and phase contrast imaging using Pattern sequence 2. For the partial-field case, the contrast presents a lower improvement compared with Pattern sequence 1 (2.9 against 4 for PRs case) and some PRs are not completely visible. On the other hand, phase contrast images of PRs and NFL are more contrasted. For PRs, we measured a Michelson contrast of 47% against 19% for Pattern sequence 1. Such an increase of contrast helps us to better appreciate the photoreceptor inner segment mosaic, where unseen PRs in bright-field mode can now be seen, as well as vessel walls, capillaries, individual fibers, and putative ganglion cells (size: 11 μm). One interesting fact about phase-contrast images is their directional dependence according to the illumination pattern. Indeed, one can see that the contrast gradient is oriented orthogonally to the direction of the line illumination (see PRs insets in Figs. 2 and 3).

One limitation of the presented system is the low effective frame rate, which is shown to be suitable to image static retinal features. However, to visualize retinal dynamic features, such as red blood cells, also commonly visualized in phase-contrast using AO-SLO [2], one can use static patterns and be again limited by the camera frame rate (see Visualization 2 and Visualization 3). Another very interesting asset of the DMD-integrated AO-FIO is its versatility, as photons selection to generate all different contrasts can be done in post-processing. Such a tool can be helpful to design the most suitable masks to visualize a given retinal feature. Two examples of this versatility can be found in Visualization 4 and Visualization 5. Visualization 4 shows that phase gradient contrast decreases as the detected areas are located farther away from the illumination zone. This observation is in accordance with Fig. 1(a). Finally, the strategy presented here to generate multimodal images and enhance SNR bright-field imaging can also be applied to flood-illumination interferometric imaging techniques such as full-field OCT [16].

In this Letter, we proposed a DMD-integrated AO-FIO system able to generate multimodal retinal imaging, such as bright-field and dark-field (absorption and phase contrasts) images. The multimodal configuration was made possible by projecting a sequence of complementary patterns and by selecting in post-processing the image area where image reconstruction should take place. Owing to the given system, and the proposed acquisition/processing pipeline, we were able, at the same time, to: (1) obtain up to four-fold contrast improvement in bright-field modality when imaging highly scattered structures such as PRs and NFL; and (2) to visualize, through phase contrast images, translucent retinal features such as capillaries, red blood cells, vessel walls, ganglion cells, and PRs inner segment.

Funding. Office National d'études et de Recherches Aérospatiales (PRF TELEMAC); Agence Nationale de la Recherche (ANR-18-IAHU-0001, ANR-22-CE19-0010-01).

Disclosures. The authors declare no conflicts of interest.

Data availability. All data is available upon request.

REFERENCES

1. A. Roorda, F. Romero-Borja, W. J. Donnelly III, H. Queener, T. J. Hebert, and M. C. Campbell, Opt. Express **10**, 405 (2002).
2. T. Y. Chui, D. A. VanNasdale, and S. A. Burns, Biomed. Opt. Express **3**, 2537 (2012).
3. P. Mecê, E. Gofas-Salas, M. Paques, K. Grieve, and S. Meimon, Biomed. Opt. Express **11**, 4069 (2020).
4. E. Gofas-Salas, Y. Rui, P. Mecê, M. Zhang, V. C. Snyder, K. V. Vienola, D. M. Lee, J.-A. Sahel, K. Grieve, and E. A. Rossi, Biomed. Opt. Express **13**, 117 (2022).
5. P. Mecê, E. Gofas-Salas, Y. Rui, M. Zhang, J.-A. Sahel, and E. A. Rossi, Opt. Lett. **46**, 1085 (2021).
6. A. E. Salmon, R. F. Cooper, C. S. Langlo, A. Baghaie, A. Dubra, and J. Carroll, Trans. Vis. Sci. Tech. **6**, 9 (2017).
7. E. Gofas-Salas, P. Mecê, C. Petit, J. Jarosz, L. M. Mugnier, A. M. Bonnefois, K. Grieve, J. Sahel, M. Paques, and S. Meimon, Appl. Opt. **57**, 5635 (2018).
8. S. Meimon, E. G. Salas, P. Mecê, K. Grieve, J. A. Sahel, and M. Paques, Investig. Ophthalmol. Vis. Sci. **59**, 4641 (2018).
9. E. Gofas-Salas, P. Mecê, L. Mugnier, A. M. Bonnefois, C. Petit, K. Grieve, J. Sahel, M. Paques, and S. Meimon, Biomed. Opt. Express **10**, 2730 (2019).
10. L. Krafft, E. Gofas-Salas, Y. Lai-Tim, M. Paques, L. Mugnier, O. Thouvenin, P. Mecê, and S. Meimon, Appl. Opt. **60**, 9951 (2021).
11. S. Lee, S. S. Choi, R. K. Meleppat, R. J. Zawadzki, and N. Doble, Opt. Lett. **48**, 791 (2023).
12. J. Lu, B. Gu, X. Wang, and Y. Zhang, PLoS One **12**, e0169358 (2017).
13. P. B. de Mecê, "4D exploration of the retina for adaptive optics-assisted laser photocoagulation," Ph.D. thesis, Université Sorbonne Paris Cité (2018).
14. T. N. Ford, K. K. Chu, and J. Mertz, Nat. Methods **9**, 1195 (2012).
15. A. Guevara-Torres, D. Williams, and J. Schallek, Opt. Lett. **45**, 840 (2020).
16. J. Scholler, K. Groux, K. Grieve, C. Boccara, and P. Mecê, Opt. Lett. **45**, 5901 (2020).
17. D. Scoles, Y. N. Sulai, and A. Dubra, Biomed. Opt. Express **4**, 1710 (2013).

2.4 Is the DMD-integrated AO-FIO suitable for studying neurovascular coupling ?

In the following section, I evaluated whether of not the different possible configurations of the DMD-integrated AO-FIO could be used to study neurovascular coupling at a high spatial and temporal resolution by being capable of measuring the diameter of the blood vessels or for imaging erythrocytes.

2.4.1 Full field illumination

The first possible configuration is simply to image the blood vessels using full field illumination. In figure 2.12 a first attempt at measuring flicker induced vasodilation with this method is presented. A simple wide field stimulation target was used to project a 10 Hz flickering light into the retina of a healthy volunteer and the lumen diameter of an artery was measured manually every 0.5 seconds.

The full-field illumination of the retina results in multiply scattered photons, contributing to significant background noise. Consequently, hypo-reflective structures such as vessel walls become invisible or obscured by the diffuse background. Due to this phenomenon 50 images were averaged (hence a measurement every 0.5 sec) to try to increase the signal to noise ratio for the measurement. Even with this averaging, the wall of the artery was not well contrasted as can be seen in 2.12 with the red arrow pointing to a wall where the delimitation between the lumen and the tunica media of the vessel is hard to interpret. This resulted in a very imprecise measurement of the vessel wall that can be appreciated in the plotted diameter of the vessel in 2.12. Moreover this imprecision of the measurement is greater than the expected 3-5% vasodilation due to a flicker stimulation. [9]

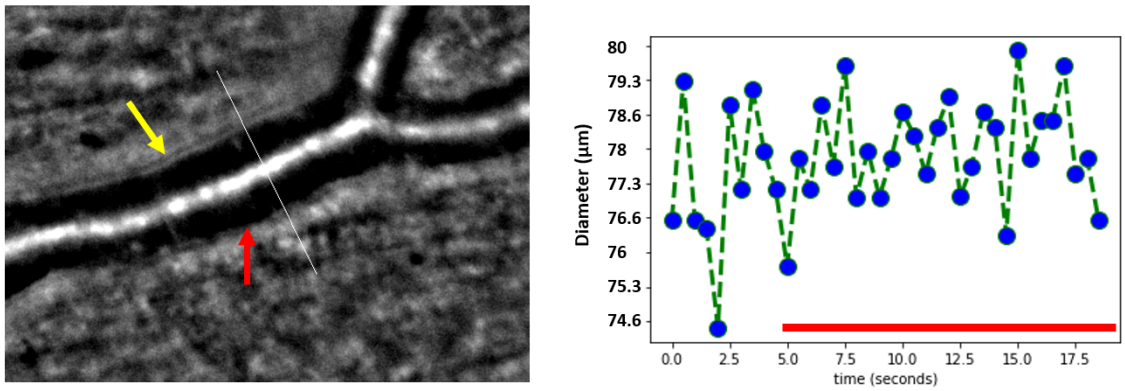

Figure 2.12: Attempt to measure the diameter of a retinal artery using the DMD-integrated AO-FIO, The whole field of view was illuminated, and the lumen diameter of the artery was manually measured on averaged images taken every 0.5 seconds. The measurements, taken at the section indicated by the white line, are plotted in the graph on the right. The artery wall exhibits low contrast: the three layers of the artery wall are barely visible on one side (indicated by the yellow arrow) and are not visible on the other side (indicated by the red arrow).

2.4.2 Static pattern projection

This method involves projecting a static pattern onto the retina and to position this pattern in such a way that a blood vessel is located right outside of the projected pattern. To evaluate the possibility of using this technique to measure NVC, a simple wide field stimulation target was used to project a 10 Hz flickering light into the retina of a healthy volunteer. At the same time images of the retina of the subject were recorded using the DMD-integrated AO-FIO which was projecting a static rectangular pattern in the retina of the subject. Some images from this initial experiment are presented in figure 2.13.

This method however quickly revealed impractical because eye movement would change the relative position of the projected pattern with the blood vessel, thereby resulting in varying contrast of the vessel. This can be observed in figure 2.13 by comparing the magnified regions A.3 and B.3 or A.2 and B.2. In both cases the distance between the vessel and the illumination pattern has changed between the two images, as a consequence the effect of the light stimulation is hard to interpret. Consequently, for acquisitions of more than a few seconds where the subject cannot maintain perfect fixation , this method does not work.

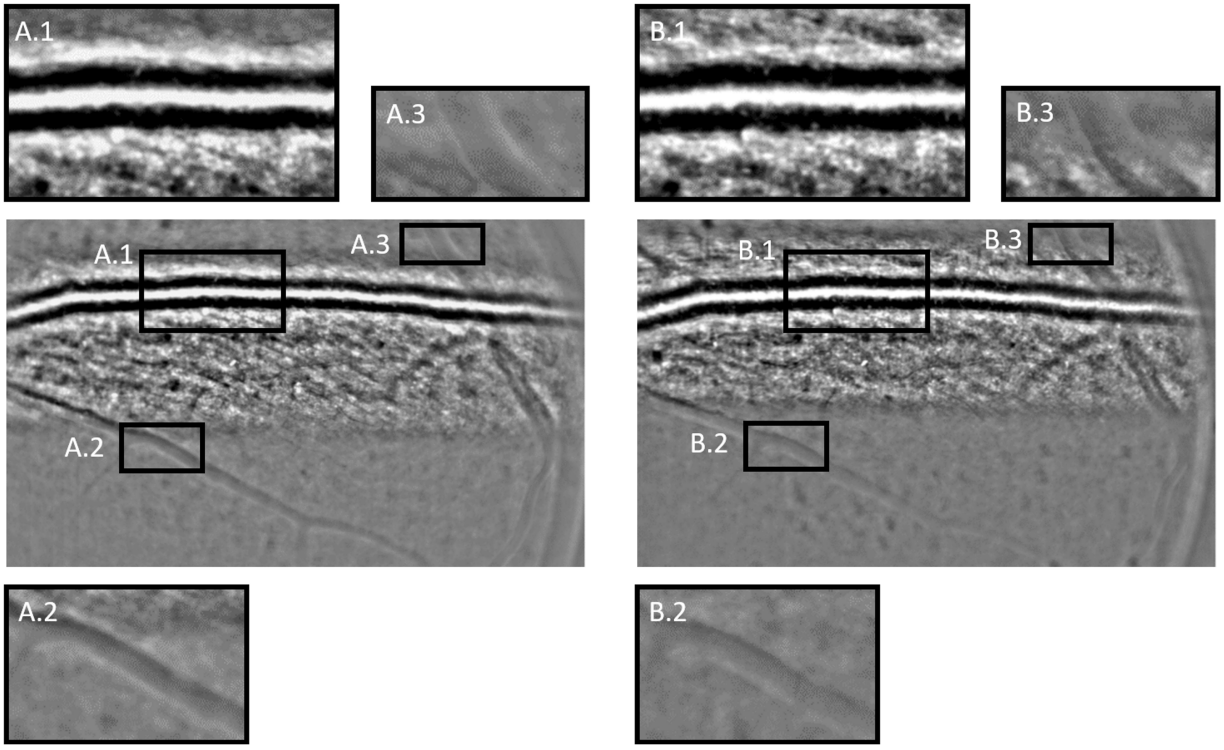

Figure 2.13: Flicker test using the DMD-integrated AO-FIO projecting a static rectangular pattern. A) before stimulation B) After stimulation. The flaws of this method are clearly visible: the contrast is changing between the two images because the position of the illuminated rectangle has changed due to eye movements.

2.4.3 Dynamic pattern projection

Alternatively, using the method presented in section 2.3.3 allows for full-field phase contrast images. For instance, the images of the nerve fiber layer presented in the previous section (Section 2.3.4) exhibit well-contrasted vessel walls, clearly separating the different layers of the wall. This facilitates unambiguous measurement of the lumen and wall diameters of blood vessels, as demonstrated in figure 2.14.

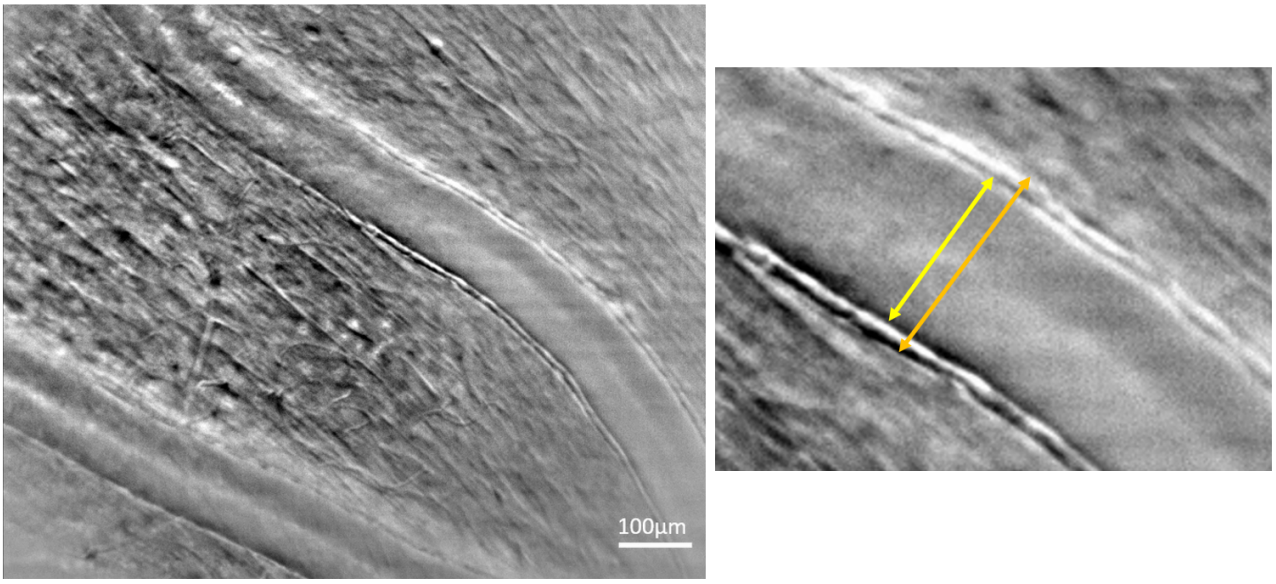

Figure 2.14: Phase contrast image of the nerve fiber layer using the DMD-integrated AO-FIO (following the method described in 5.1, employing a scanning thick line). Two large blood vessels are visible in the image, with the lower vessel being a vein and the upper vessel being an artery. A magnified region of the artery highlights the clear visibility of the different layers of the vessel wall. The lumen diameter (indicated by the yellow arrow) and the wall diameter (indicated by the orange arrow) can be easily measured.

While this method is effective for imaging static retinal features by averaging multiple images, it is less suitable for capturing dynamic retinal structures such as red blood cells and blood vessels. This limitation arises because the number of incident photons in the retina are proportional to the area of the illuminated patch, making the DMD-integrated AO-FIO quite photon-inefficient and resulting in a low effective frame rate. For instance, the effective frame rate with the thick line method described in 5.1 is approximately one image per second (24 patterns projected at 30 Hz to scan the entire image). Due to this limitation, and with the goal of achieving high-speed measurements of neurovascular coupling, a more efficient system based on the same principle was developed in the next chapter.

In many aspects, the work that was done on this system marks a significant step toward developing a high-resolution clinical instrument for studying neurovascular coupling. First, it represents a pivotal transition for the ECUROeil bench, evolving from an instrument usable on cooperative subjects to a robust system ready for clinical studies on patients. Secondly, it enhances our understanding of how phase contrast imaging can be achieved with a camera-based system, allowing us to optimize this contrast for visualizing erythrocytes and blood vessel walls.

Conclusion of the chapter: Reaching the end of this chapter, I demonstrated that:

- I improved the usability of the ECUROeil bench, making it possible to use it in the context of data acquisition on patients.
- The DMD-integrated AO-FIO proves suboptimal for studying neurovascular coupling, using both static pattern projection due to eye movements and using a scanning line pattern due to the resulting low effective frame rate.
- The DMD-integrated AO-FIO was a pathfinder toward the development of a more efficient system. By using the system's ability to project various patterns, I gained valuable empirical insights into optimizing phase contrast for blood vessel walls and erythrocytes. In addition, an effective method for achieving high contrast across a wide field of view was established: projecting a scanning line pattern and detecting only the non-illuminated regions above or below the line.

Chapter 3

Implementation of an optimized multimodal imaging platform with phase contrast capabilities: the Adaptive Optics - Confocal Rolling Slit Ophthalmoscope (AO-CRSO)

In Chapter 2, we demonstrated that partial illumination of the field of view using a Digital Micromirror Device (DMD) can achieve phase contrast in a camera-based flood illumination imaging system. Furthermore, we established that it is possible to obtain full-field phase contrast images by projecting a scanning line onto the retina and to reconstruct the total image with offline spatial filtering. The method presented in chapter 2 is effective for imaging static features of the retina. However, because of its low effective temporal resolution, it falls short in tracking erythrocytes and measuring the subtle changes in the lumen diameter of blood vessels at a high temporal resolution.

Building on the insights gained from the DMD-integrated AO-FIO, a proof-of-concept for a more efficient system was proposed. By projecting a scanning thin line into the retina and spatially filtering directly using the rolling shutter of a 2D camera, enhanced bright field contrast as well as high speed phase contrast imaging is possible, making it a promising solution to study neurovascular coupling.

This chapter is dedicated to the presentation of this new system and is organized in the following manner:

In section 3.1, the system is introduced, focusing on the practical aspects of its implementation, particularly the implementation and fine-tuning of phase contrast imaging.

In section 3.2, the finalized system is described in detail, as presented in an article currently in preparation. This section includes the specifications of the various system components and the different imaging modalities that can be achieved with the system.

Concept of the system

The Adaptive Optics - Confocal Rolling Slit Ophthalmoscope (AO-CRSO) is the second subsystem of the ECUROeil bench. The optical layout of this system is shown in figure 3.1. A new illumination module was integrated into the ECUROeil bench, consisting of an 850 nm SLED that projects a thin horizontal line onto the retina using a Powell lens. This line is then scanned vertically across the retina using a galvanometer mirror. Detection is achieved with a 2D camera (ORCA-Fusion, Hamamatsu) operating in rolling shutter mode, where the camera's rolling shutter is synchronized with the galvanometer mirror's scanning motion via a custom MATLAB software. The camera's rolling shutter functions as a horizontal physical slit, with its width adjustable by modifying the pixel exposure time. By controlling the offset between illumination and detection, it is possible to operate in either bright field mode, where the illumination and detection lines overlap, or in phase contrast mode by introducing an offset between the illumination line and the camera's rolling shutter. The use of a 2D camera's rolling shutter for retinal imaging was previously demonstrated by Muller et al. [101] for confocal imaging. However, their approach employed a digital light projector for line-scan illumination, whereas we use a Powell lens in our system. Furthermore, to the best of our knowledge, this is the first demonstration of this principle on an adaptive optics system.

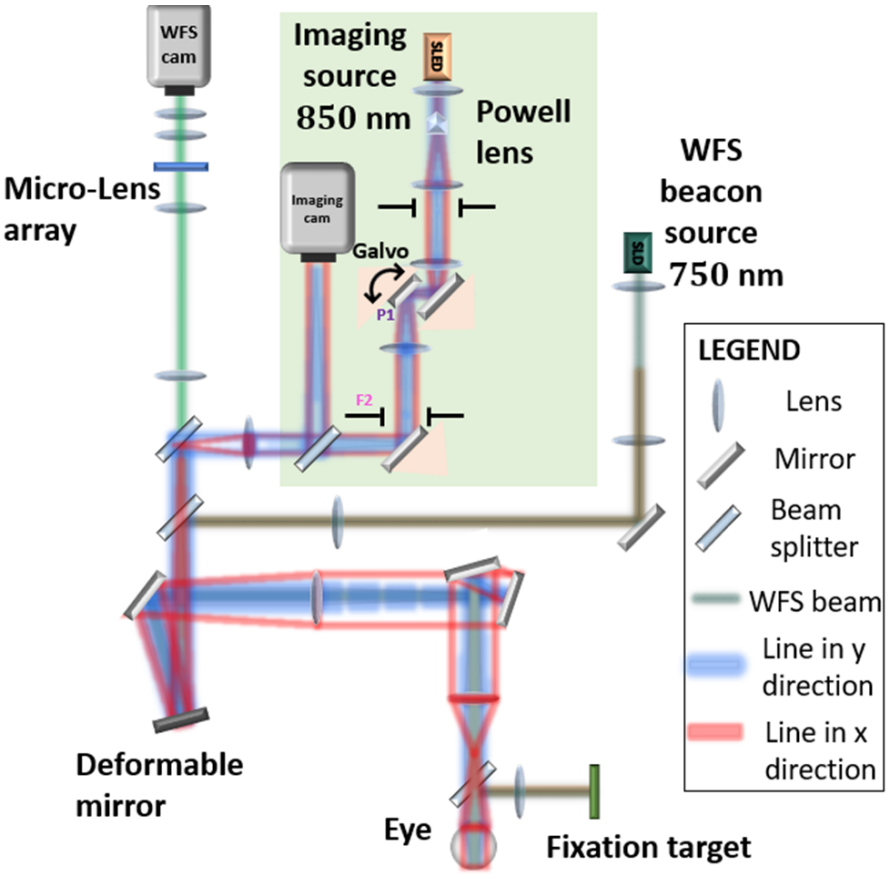

Figure 3.1: Optical layout of the AO-CRSO system.

3.1 Practical implementation of phase contrast imaging on the AO-CRSO

Implementing phase contrast imaging on the AO-CRSO required the application of principles established for phase contrast in the DMD-integrated AO-FIO, as detailed in chapter 2. Specifically, this involved introducing an offset between the illuminated line and the detection "slit" of the camera's rolling shutter. However, implementing phase contrast on this system first required further optimization of the overall system which are first briefly described. Then a fine tuning of the synchronization between the illumination and the detection was important in achieving phase contrast imaging.

3.1.1 Optimization of the total transmitted optical power of the system

Optimizing the total optical power of any imaging system was important to increase the signal to noise ratio of the final images. One key element to achieve images of high quality when implementing the AO-CRSO system was optimizing the total transmitted power of the system.

The ISO 15004-2:2007 standard, which sets illumination limits for ophthalmic instruments, was used for the design of the system. For this system, this standard imposed a limit of approximately 3 mW ([25]). According to this standard, remaining under this limit ensures that the system can be safely used by anyone, including non-specialists, without any risk. Despite the source having a maximum output power of 20 mW, in the first iteration of the system, the maximum power that we could measure at the cornea was only 0.97 mW moreover the output power was unstable and depended on the bending and coiling of the source fiber.

This was due to the polarization of the source used for the system. Indeed superluminescent led (SLD) such as the one we are using are partially polarized with extinction ratios of around 8-9 db. Although this extinction ratio was not specified for our SLD (Thorlabs SLD850S-A20W). Due to this phenomenon, some orientation of this polarization caused substantial loss of power when passing through elements of the system with polarization dependent transmission or reflection such as the beamsplitter separating the illumination beam and the collection of the light by the camera.

As a result, substantial power loss was happening due to the varying polarization of the source. Simply moving the fiber of the source could change the measured power at the cornea from 0.3 mW to 0.9 mW and vibrations of the system would also cause the power to drift due to this phenomenon. To solve this issue, a custom SLD source including a polarization maintaining fiber was ordered. With this modification the output power was completely stable and could be maximized at 1.4 mW.

3.1.2 Improvement of the quality of the projected line

Ensuring the quality of the projected line is essential for achieving optimal system performance both in bright field or with phase contrast modalities. This requires meeting several criteria:

- **Thickness of the line**: Because the gain in bright field contrast is inversely dependent on the area of the projected pattern in the retina [26]. In order to effectively increase bright field contrast, the line projected with the Powell lens needs to have a width of 10 pixels.
- **Uniformity of the line**: The intensity distribution of the line must be uniform to avoid non-uniformity in the final image. This criterion was optimized by adjusting the injection of the source into the Powell lens.
- **Sharpness of the edges of the line**: This is important to have the right contrast, most importantly, it is important for phase contrast imaging. This criterion is largely dependent on the adaptive optics pre-compensation of the projected line.
- **Straightness of the line**: If an angle between the projected line and the horizontal rolling shutter "slit" remains, the contrast might vary over the field of view. For example while trying to have a bright field image, the center of the image will be well contrasted, but the corners of the images will not be contrasted due to mismatch between illumination and detection. This criterion was optimized by adjusting the orientation of the powell lens.

One more thing to take into consideration was stray reflections by the lenses of the system which required adding some tilt to some lenses of the system. To visualize the aspect of the projected line over the field of view and therefore adjusting the previously mentioned criteria, an artificial eye was used, as demonstrated in figure 3.2.

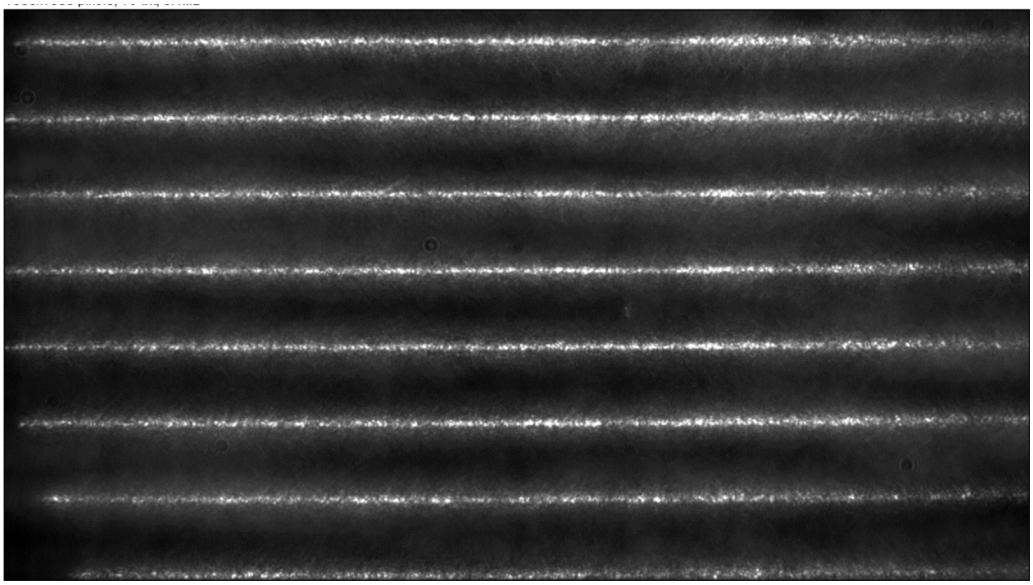

Figure 3.2: Profile of the projected line on the whole field of view, visualized using an artificial eye. An artificial eye was used to adjust the projected line. 10 accumulated images are superimposed thus displaying the aspect of the illumination line at various points within the field of view.

3.1.3 Setting up the synchronization for phase contrast imaging

Proper synchronization between the rolling shutter of the camera and the galvanometer mirror is essential for the system to function correctly in both bright field and phase contrast configurations. This section details the methods used to establish synchronization, first for bright field imaging and then for phase contrast imaging.

3.1.3.1 The user interface and its effect on the synchronization state of the system

The synchronization between the rolling shutter of the camera and the galvanometer mirror is controlled by a custom matlab software: an analog sawtooth signal is generated via Matlab and conditioned by a National Instrument DAQ-mx card to drive the galvanometer mirror. While a TTL signal is sent to the the camera to begin the acquisition of a frame. The shape of the sawtooth signal as well as the delay between the TTL signal and the sawtooth signal are controlled via the Matlab software which provides a user interface for controlling the synchronization state of the system. This software is depicted in figure 3.3. On the main window of this user interface, the TTL and sawtooth signal are represented. On the right side of the user interface, the three parameters that can be modified on this user interface are Vmin, Vmax and the delay between the TTL and the sawtooth signals.

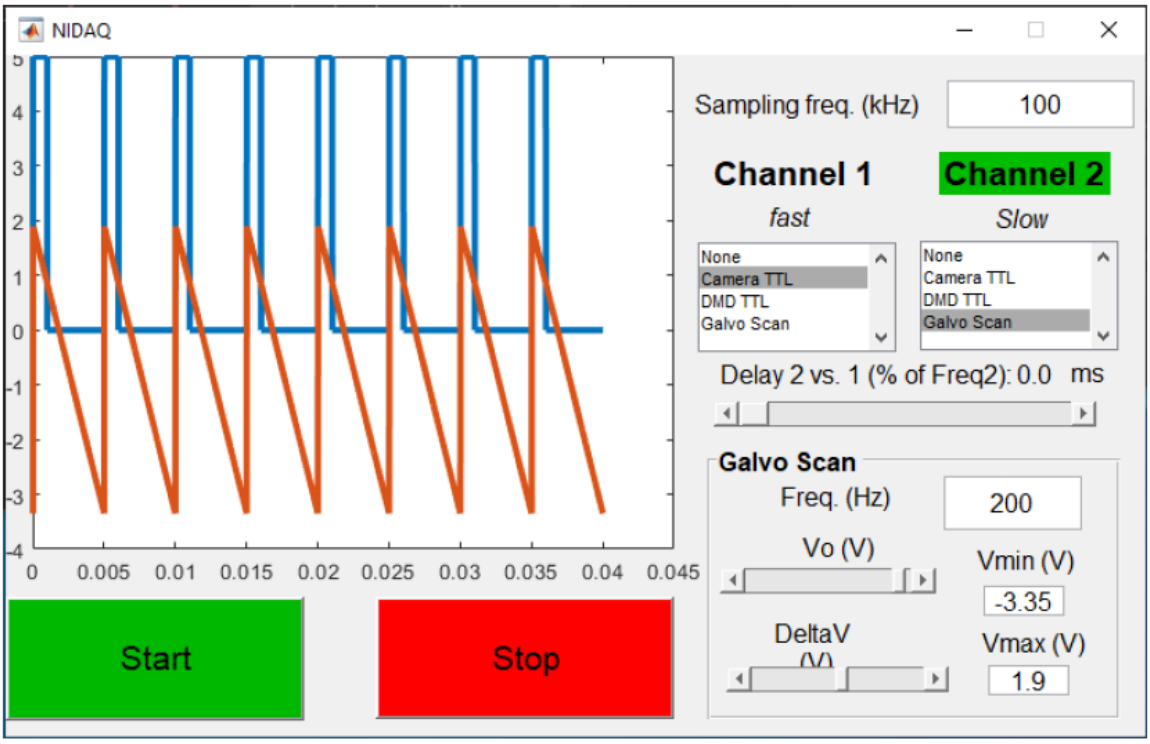

Figure 3.3: Matlab user interface controlling the synchronization between the galvanometer mirror and the rolling shutter of the camera. The TTL signal sent to the camera is represented in blue and the sawtooth signal sent to the galvanometer mirror is represented in red.

Figure 3.4 illustrates the impact of these parameters on the synchronization state of the system. The parameters V_{max} and V_{min} determine the maximum and minimum positions of the galvanometer mirror, respectively. The "delay" parameter controls the interval between the start of the TTL signal and the initiation of the sawtooth signal, which in turn determines the offset between the detection "slit" and the illumination line. Finally, an important parameter is the exposure time of each pixel line, which dictates the width of the detection "slit". 5 µs of exposure time correspond to a detection "slit" of 1 pixel in retinal space. Finding the correct synchronization state for the system means finding the value of these four parameters for bright field and for phase contrast imaging.

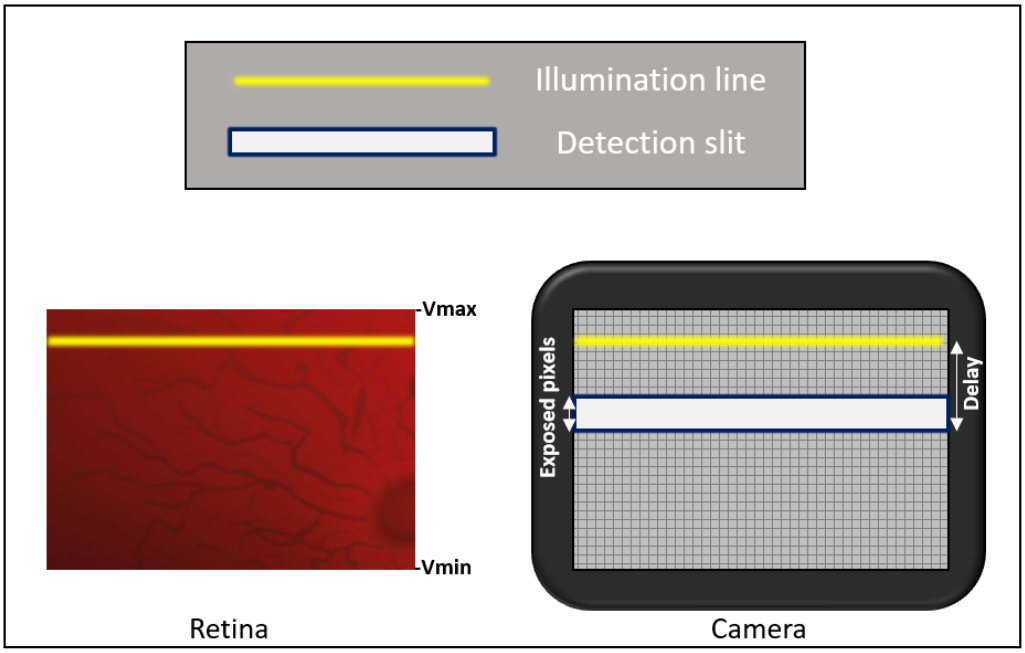

Figure 3.4: Representation of the laser line projected in the retina and the effect of varying the exposure time and the delay in the camera space.

3.1.3.2 Finding the synchronization parameters for bright field imaging

The first step towards determining the right parameters for phase contrast imaging is to find the right bright field synchronization. This is because in bright field configuration, the exposure time is fixed which makes one less variable to determine. Indeed, for bright field, the exposure time is fixed at 50 µs so that the detection slit in the retinal space matches the 10 pixel width of the projected line.

At this stage, the remaining variables to determine are V_{min}, V_{max}, and the delay. V_{min} and V_{max} respectively define the minimum and maximum positions of the galvanometer mirror during the duration of a recorded frame. These two positions are connected linearly throughout the recorded frame duration, meaning the difference between V_{min} and V_{max} sets the scan speed of the galvanometer mirror. Therefore, the gap between V_{min} and V_{max} must be selected to match the speed of the camera's rolling shutter, which is determined by the frame rate (typically 200 Hz for 1000 vertical pixels). The synchronization procedure for bright field is done in three main steps. An artificial eye is imaged with the system to provide feedback on the synchronizations step of the system.

1. Starting from an arbitrary set of V_{min}, V_{max} and delay values, the first step is to roughly adjust V_{min} and V_{max} to appropriate values. To achieve this, the exposure time of the system is set to the inverse of the frame rate (5 ms). This effectively means that the detection "slit" of the system spans the entire field of view, eliminating confocality. By doing so, the illuminated field of view can be directly visualized on the image of the artificial eye, allowing V_{min} and V_{max} to be adjusted so that the entire field of view is illuminated.

2. Next, the exposure time is set to 50 µs. Because the initial V_{min}, V_{max} , and delay values are not precisely correct, only a partial overlap of the illumination line and the detection slit is observed at this stage (see figure 3.5). On the camera, this results in a portion of the field of view displaying high intensity while the rest remains dark. To address this issue, the difference between V_{min} and V_{max} is incrementally adjusted to improve signal uniformity. Once the correct difference between V_{min} and V_{max} is determined, the signal is uniform over the entire field of view which means that the the galvanometer speed matches the camera rolling shutter speed.

3. When the signal is uniform over the field of view, a delay between the illumination line and the detection slit might still be present (For instance, as displayed in figure 3.5 D) The next step is to maximize the bright field intensity of this signal by either adjusting V_{min} and V_{max} by the same value or by changing the delay value.

When the signal is maximal and uniform over the field of view, the correct synchronization parameters have been found.

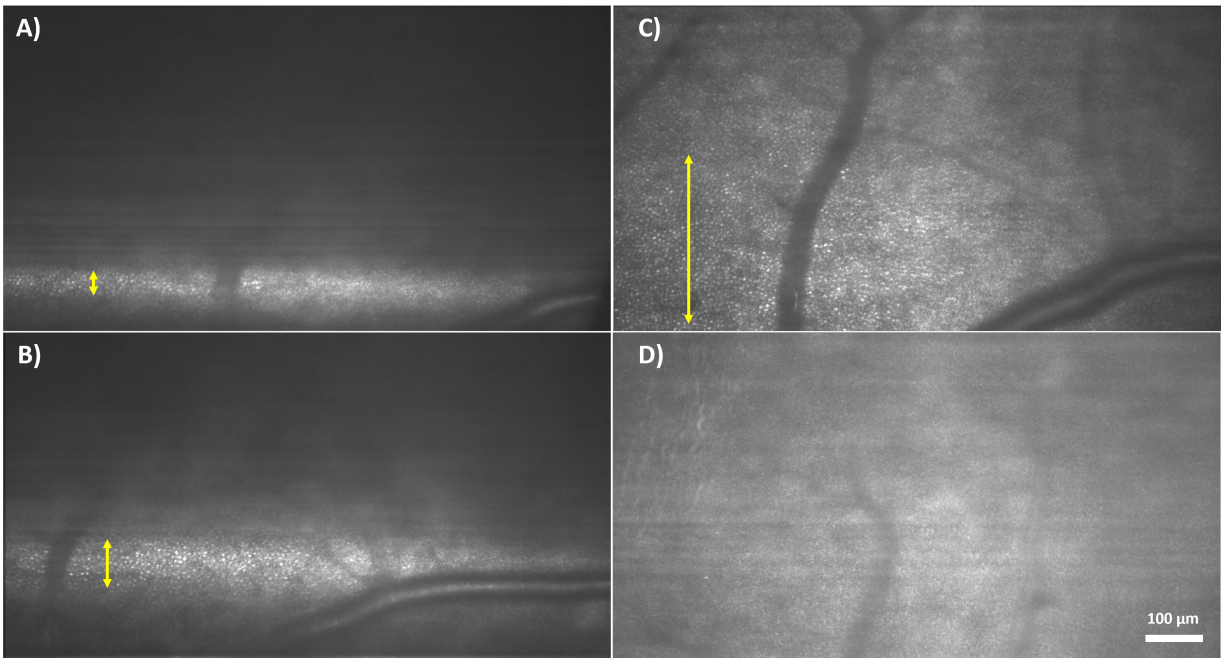

Figure 3.5: Example of images taken at different steps of the synchronization setting up process. The system was focused on the photoreceptors layer. A) Starting from a random set of V_{min} and V_{max} values, the speed of the galvanometer scan does not match the speed of the camera's rolling shutter. This mismatch results in only a partial overlap of the illumination line and the detection "slit" in each image. B) The overlap is gradually increased by adjusting the difference between V_{min} and V_{max}. C) The overlap reaches nearly the full extent of the field of view. The photoreceptors at the top of the image are not visible, indicating that the overlap is still not perfect. The extent of the overlap is indicated by the yellow arrow in images A, B, and C. For A,B and C, the extension of the overlap has been represented with a yellow arrow. D) The image is uniform over the field of view, however, a delay between the illumination and detection is present (as can be witnessed with the low visibility of the photoreceptors).

3.1.3.3 Implementation of phase contrast imaging

Once V_{min}, V_{max} and delay values have been found for the bright field configuration. Phase contrast imaging is obtained by increasing the size of the detection slit by changing the exposure time value and putting an offset between illumination and detection. The optimal value of offset and exposure time varies depending on the structure that we want to image. For blood vessels, an empirical approach detailed in chapter 4 was employed to find the best set of offset and exposure time.

As detailed in the following article 3.2, subtracting consecutive positive and negative offset in the same way as with split detection AO-SLO, further increase phase contrast. To implement this differential offset mode on the system, the Matlab user interface was modified (see figure 3.7). When the button 'DF sequence' is pressed, the sawtooth signal sent to the galvanometer mirror alternated between a signal where the "delay" value is increased by a specified "offset 1" value and a signal where the "delay" value is decreased by a specified "offset 2" value. The effect of these changed sawtooth signals on the synchronization of the system can be appreciated on figure 3.6.

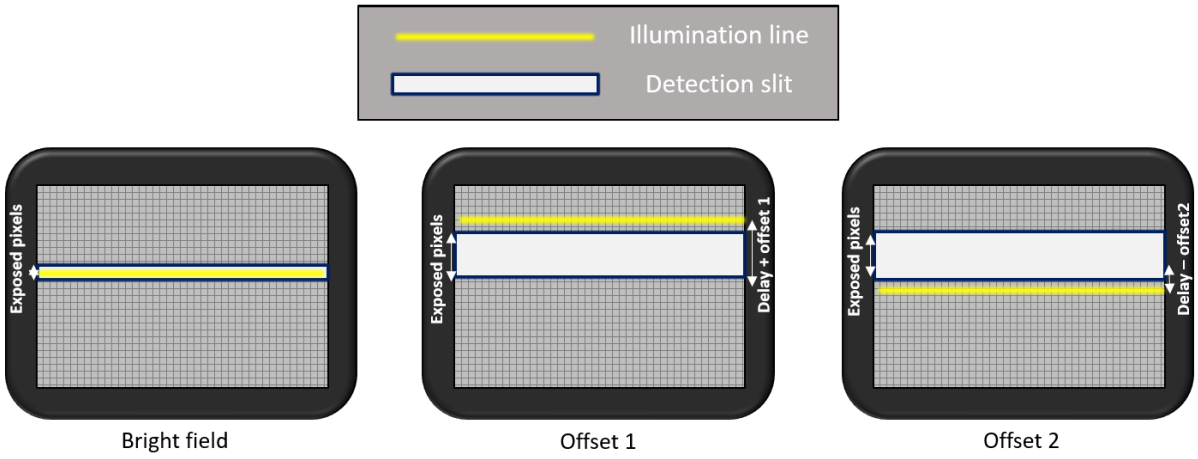

Figure 3.6: Schematic representation of bright field mode, Offset 1, and Offset 2. In bright field mode, the pixel exposure time is set so that the width of the rolling shutter matches the width of the illumination line, and the "Delay" parameter is set to ensure overlap between illumination and detection. In Offset 1 and Offset 2 modes, the pixel exposure time is extended, with the "Delay" value either increased by a specified "Offset 1" or decreased by a specified "Offset 2" value.

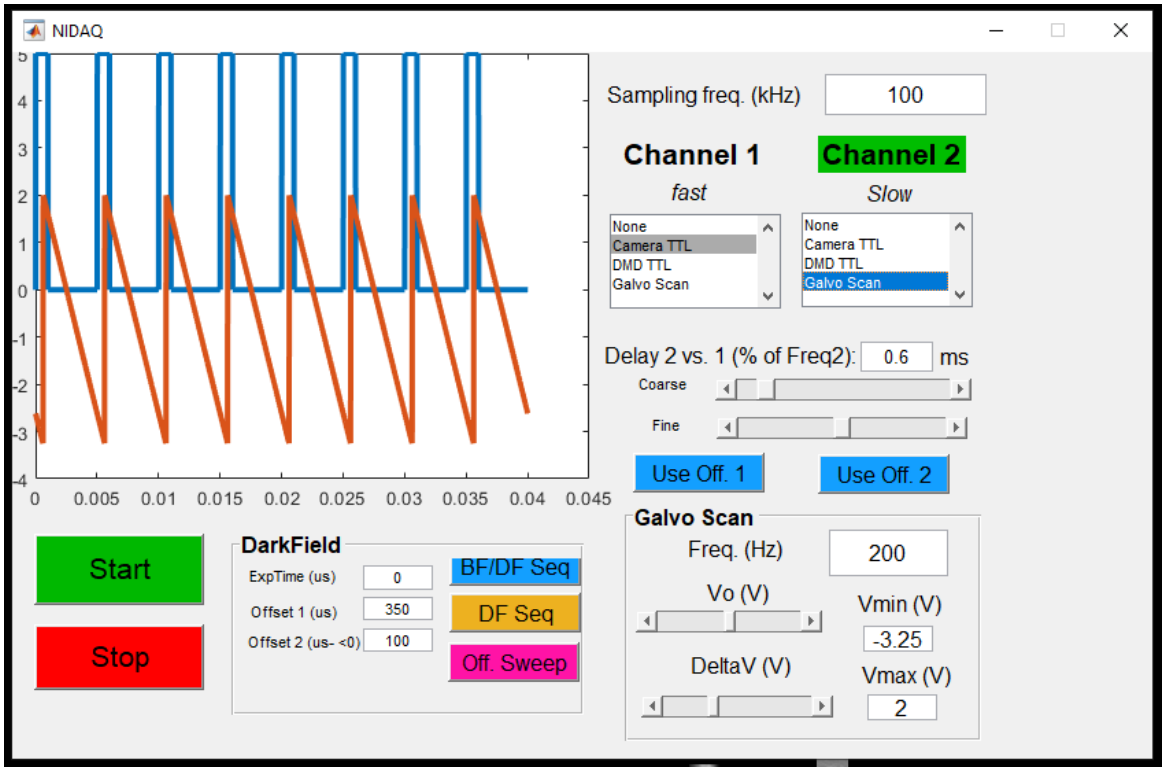

Figure 3.7: New version of the Matlab user interface for the galvo-rolling shutter synchronization, allowing to switch between bright field and phase contrast imaging mode. By clicking on "DF Seq", the galvanometer mirror alternates between offset 1 and offset 2 every image.

3.1.3.4 Fine tuning the synchronization for differential offset imaging

In practice, differential offset imaging requires very fine adjustments of the delay between the illumination and detection otherwise the offset 1 and offset 2 images can be unbalanced (with one offset being brighter than the other). To finely adjust this delay, the positive and negative offset images are visualized using the button "Use off.1" and "Use off.2" in the new user interface (figure: 3.7). The delay can then be finely tuned using the fine delay cursor to balance the two offsets. For example raw images from offset 1 and 2 displaying a balanced aspect are presented in figure 3.8. Once the synchronization parameters have been set, they can be saved for later acquisitions.

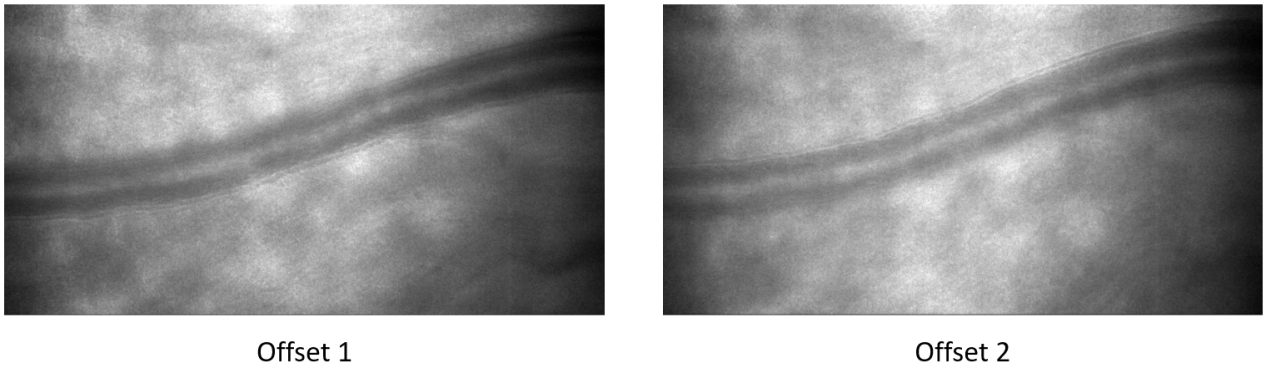

Figure 3.8: Example of offset 1 and offset 2 images displaying a balanced aspect. The overall brightness of the two images are the same

3.2 *Proceeding*: High contrast and high speed multimodal imaging platform: the adaptive optics-confocal rolling slit ophthalmoscope (AO-CRSO)

The AO-CRSO system is described in detail in the following proceedings. A co-authored article, in which I will be the first author alongside Léa Krafft (equal contribution), is currently under preparation and will present the same content as this proceeding.

Contribution: The system was originally conceptualized by Léa Krafft during her PhD thesis [25], and I contributed to its implementation. My main contribution involved integrating the phase contrast modality into the system, as presented in the previous section.

HIGH CONTRAST AND HIGH SPEED MULTIMODAL IMAGING PLATFORM: THE ADAPTIVE OPTICS - CONFOCAL ROLLING SLIT OPHTHALMOSCOPE (AO-CRSO)

Lea Krafft[1,2], Pierre Senee[1,2,3], Olivier Thouvenin[4], Daniela Castro Farias[2,5], Michel Paques[2,5], Pedro Mecê[2,4,+], and Serge Meimon[1,2,+,*]

[1]DOTA, ONERA, Université Paris Saclay F-91123 Palaiseau, France
[2]Paris Eye Imaging Group, Centre d'Investigation Clinique 1423, Quinze-Vingts National Ophthalmology Hospital, DGOS, INSERM, Paris, France
[3]Quantel Medical, Cournon d'Auvergne, France
[4]Institut Langevin, ESPCI Paris, CNRS, PSL University, Paris, France
[5]Quinze-Vingts Hospital, Paris, France
[+]These authors equally contributed to this work

ABSTRACT

Adaptive optics imaging techniques are invaluable for cellular-level retina visualization. While AO Flood illumination ophthalmoscopes provide distortion-free, high-speed images, they lack contrast. On the other hand, AO scanning laser ophthalmoscopes offer highly contrasted images due to point by point illumination and spatial filtering but suffer from low pixel throughput and distortion artifacts. Our recent advancements, using a DMD integrated AO-FIO, show that we can illuminate and capture multiple spatially separated zones, achieving contrast close to the one of a confocal microscope. Our theoretical framework emphasizes that each zone must be smaller than 100 μm in both directions or smaller than 10 μm in only one direction to minimize the diffuse light component. Building upon these results, we developed a cutting-edge confocal rolling slit ophthalmoscope, able to achieve brightfield contrast similar to a confocal ophthalmoscope, along with phase contrast images. We utilize a classical sCMOS camera with a rolling shutter synchronized with the line source scanning of the field of view. The system makes use of all the incident photons that can be collected, whether singly, multiply scattered or absorbed. Easy digital switching between the darkfield and brightfield, as well as modification of the size and offset of the detection aperture, enhances the adaptability and versatility of this multimodal imaging system, allowing for fine-tuning of imaging modalities and comprehensive exploration of the retina.

Keywords: Retinal imaging, scattering, microscopy, phase contrast, adaptive optics

1. INTRODUCTION

Adaptive optics breakthrough has allowed to reach the diffraction limited resolution and to observe the retinal cells, in-vivo. Achieving detailed visualization of retinal features poses yet a challenge due to the optical complexity of the retina, which is a multilayered organ, situated above the highly scattering choroidal and scleral layers. Multiple scattering that drowns the structures in a diffuse background, making them scarcely noticeable has indeed been a significant hurdle. This challenge prompted a transition from full-field illumination and camera-based detection, as seen in adaptive optics flood illumination ophthalmoscopes (AO-FIO), to the point-by-point scanning approach employed by adaptive optics confocal scanning laser ophthalmoscopes (AO-SLO). The spatial filtering performed by its detection aperture that physically blocks the multiply scattered photons

Further author information: (Send correspondence to S.M.)
S.M.: E-mail: serge.meimon@onera.fr, Telephone: +33 1 46 73 47 83
L.K.: E-mail: lea.krafft@onera.fr, Telephone: +33 1 46 73 47 86

has demonstrated its ability to provide highly contrasted retinal images of the most reflective structures. However, the previously mentioned techniques lack the capability to visualize the weakly scattering retinal features such as vessel walls or capillaries. The signal from neighbouring highly reflective structures indeed eclipses the latter. In order to circumvent this issue and observe these otherwise imperceptible objects, AO-SLO devices have incorporated an offset aperture configuration. Unlike conventional AO-SLO and AO-FIO, which utilize reflectance contrast by collecting singly backscattered light from the illuminated regions in brightfield mode, the offset aperture AO-SLO technique diverges by employing multiply scattered light. This approach provides contrast originating from phase gradients in a complementary darkfield imaging mode, inspired by oblique back-illumination microscopy.[1–3] Usually performed by adding an offset between the focused illumination beam and the detection aperture, this offset aperture AO-SLO successfully demonstrated high contrast visualization of translucent cells, such as vessel walls, mural cells, photoreceptor inner segments, ganglion cells.[2,4–7]

Despite the complementary brightfield and darkfield imaging modes, the spatial filtering capability provided by AO-SLO detection aperture, comes with a trade-off. As this method involves a point-by-point imaging approach, 2D scanning is required for comprehensive reconstruction of the field of view. The mechanical scanners implemented in AO-SLO present speed limitations compared to fixational eye movements. Consequently, the resulting images are susceptible to distortion artifacts. Limiting the reconstructed field of view is a common trade-off to increase the pixel rate and thus mitigate motion-induced artifacts. For instance, acquisition rates higher than $120Hz$ can be achieved on cropped fields.[8]

Higher pixel throughput can also be achieved by sacrificing confocality in one direction by using a line instead of a point to illuminate the retina with a Line Scanning Laser Ophthalmoscope (LSLO).[9–11] Then, the illumination is scanned over one dimension and the back scattered light is commonly detected with a line camera that spatially filters out the multiply scattered noise. The LSLO first introduced by Hammer et al.[9] could reach a frame rate of $30Hz$. Despite a notable increase in imaging speed, further enhancements are necessary to prevent the impact of eye motion on acquired images. With reported eye movement frequencies reaching up to $100Hz$,[12,13] the Nyquist theorem suggests a minimum imaging rate of $200Hz$ to avoid motion artifacts. Lu et al. achieved retinal imaging at $200Hz$ within a 1.2 deg by 1.2 deg field of view using a high-speed LSLO.[10] Notably, increasing the imaging frame rate by constraining the field of view has shown effectiveness for imaging blood flow in capillaries, as illustrated by Gu et al.[11] They successfully conducted retinal imaging at a rate of $800Hz$ within a field of view measuring 1.2 deg by 0.3 deg using a high-speed LSLO.

Yet, ensuring both high imaging rate and wide field of view is necessary for detecting subtle changes or abnormalities across a larger area as well as for studying blood flow and thus contributing to effective diagnostics and monitoring.

For this reason, developing an AO-FIO with spatial filtering to allow both high contrast brightfield imaging and phase contrast capabilities as opposed to AO-SLO, would definitely be a valuable contribution in retinal imaging. This approach has been initiated by using a digital micro-mirror device (DMD) for partially illuminating the retina with projected patterns and digitally filtering out the detected signal with masks.[14–16] Although this technique serves as a valuable pathfinding tool, the effective frame rate for generating full-field high-contrast images is restricted. In Krafft et al., we reported an effective frame rate up to $25Hz$.[16] This limitation arises because the technique requires multiple image acquisitions to reconstruct the field of view. Additionally, spatial filtering is applied in post-processing to each image of the sequence. Moreover, the process of shaping the illumination in reflection, as executed by the DMD, involves notable power loss.

In this work, we tackle these limitations to demonstrate how an adaptive optics camera-based ophthalmoscope is capable of multimodal, high-speed retinal imaging. We opted for a line illumination, shaped in transmission by line-generating lens for optimal power illumination. High throughput imaging was achieved by synchronizing the scanning of the line with the exposed arrays of pixels of a sCMOS camera, operating in the rolling shutter mode. The rolling shutter enables spatial filtering of the backscattered signal at the acquisition rate, resulting either reflectance contrast similar to that of an AO-SLO in brighfield mode, or phase-contrast images, in darkfield mode. The resulting setup, named the adaptive optics confocal rolling slit ophthalmoscope (AO-CRSO), demonstrates remarkable detection flexibility. It allows for real-time digital switching between darkfield and brightfield modes and provides precise control over the temporal offset between the line and the exposed pixels, as well as pixel exposure time. These capabilities are particularly valuable for enhancing phase contrast.

2. METHOD

2.1 General description of the method

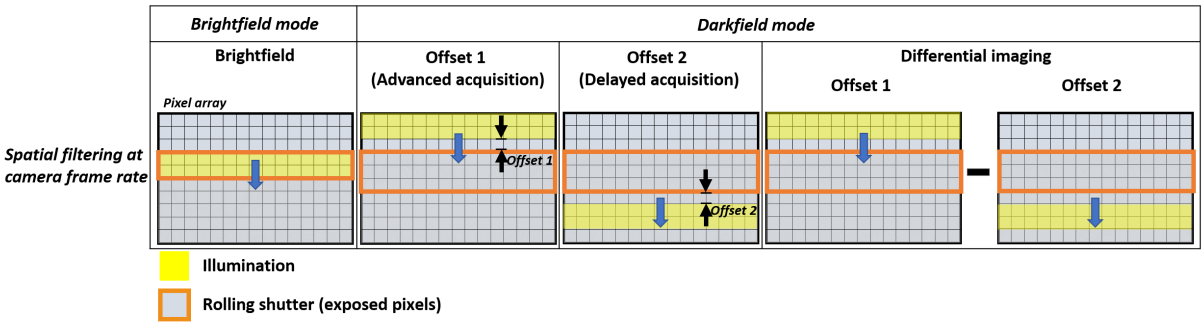

Figure 1. Schematic description of multimodal imaging with the CRSO. Both brightfield and darkfield modes can be generated by adjusting the aperture size of the rolling shutter and its offset relatively to the line illumination.

Figure 2 illustrates the acquisition modes enabled by the CRSO for achieving the multiple contrasts. It relies on a fine monitoring of the detection aperture size and offset relative to the illuminated region during the scan. In practice, the detection aperture corresponds to the electronic rolling shutter of the camera. In brightfield mode, effective spatial filtering of multiply scattered light and out-of-focus light is accomplished by overlapping the center of the backscattered line with the rows of camera pixels which are being exposed. In order to maximize the signal to noise ratio, the size of the detection aperture is chosen to match the size of the line illumination. In darkfield mode, which includes offset 1, offset 2 and differential imaging, the offset is fine-tuned to ensure that the light collected by the pixel rows being exposed comes from non-illuminated regions. Both aperture size of the rolling shutter and offset between the line illumination and the rolling shutter are meticulously adjusted to maximize the contrast of the structures of interest.
The imaging mode as well as the detection parameters are monitored through a customized graphical user interface (GUI) developed in Matlab. The GUI incorporates features to facilitate the configuration of optimal detection parameters and acquisition methods for maximizing contrast. It allows manual adjustment of the offset and aperture size while simultaneously visualizing the contrast of structures on the camera display in real-time. Moreover, it allows to systematically change the delay between illumination and the detection aperture at regular intervals. For high-speed differential imaging, consecutive images are acquired with alternating delays, corresponding to one offset followed by its opposite. Lastly, incorporating brighfield acquisition into this sequence enables to get reflectance and phase contrast information within a single acquisition. Further details on the synchronization can be found in the section 2.3.

2.2 Optical setup

Figure 2-a describes the experimental setup of the system. The AO-FIO platform located at the Paris Quinze-Vingts National Ophthalmology Hospital has been described in previous work.[14,16,17] It was adapted to integrate the CRSO module. The latter benefits from the adaptive optics subsystem to operate as a standalone imaging module of the AO-FIO plateform. Briefly, the illumination systems consists of a fibered broadband Superluminescent Diode (SLD) that emits at 850 nm with a spectral bandwidth of 55 nm and an output power of 20 mW ($SLD850S - A20W$, Thorlabs). The low temporal coherence length of the light source helps mitigating speckles[18] that can originate from interferences between the scattered wavefronts in a disordered medium. The SLD output fiber is directly connected to a collimator. The resulting $0,60mm$ diameter collimated beam is then faned out in one dimension to generate a line source using a Powell lens with a fan angle of 30 deg (♯43 − 473, Edmund Optics).[19] Instead of the non uniform Gaussian laser beam that would be produced by cylindrical lenses, Powell lenses provide an homogeneous illumination distribution in the direction of the line, as shown in its intensity profile along the line, in Fig. 3-c. Its use yet requires to limit the illumination field in the direction of the line in order to minimize power loss. For this reason, the beam is refocused in that direction with an

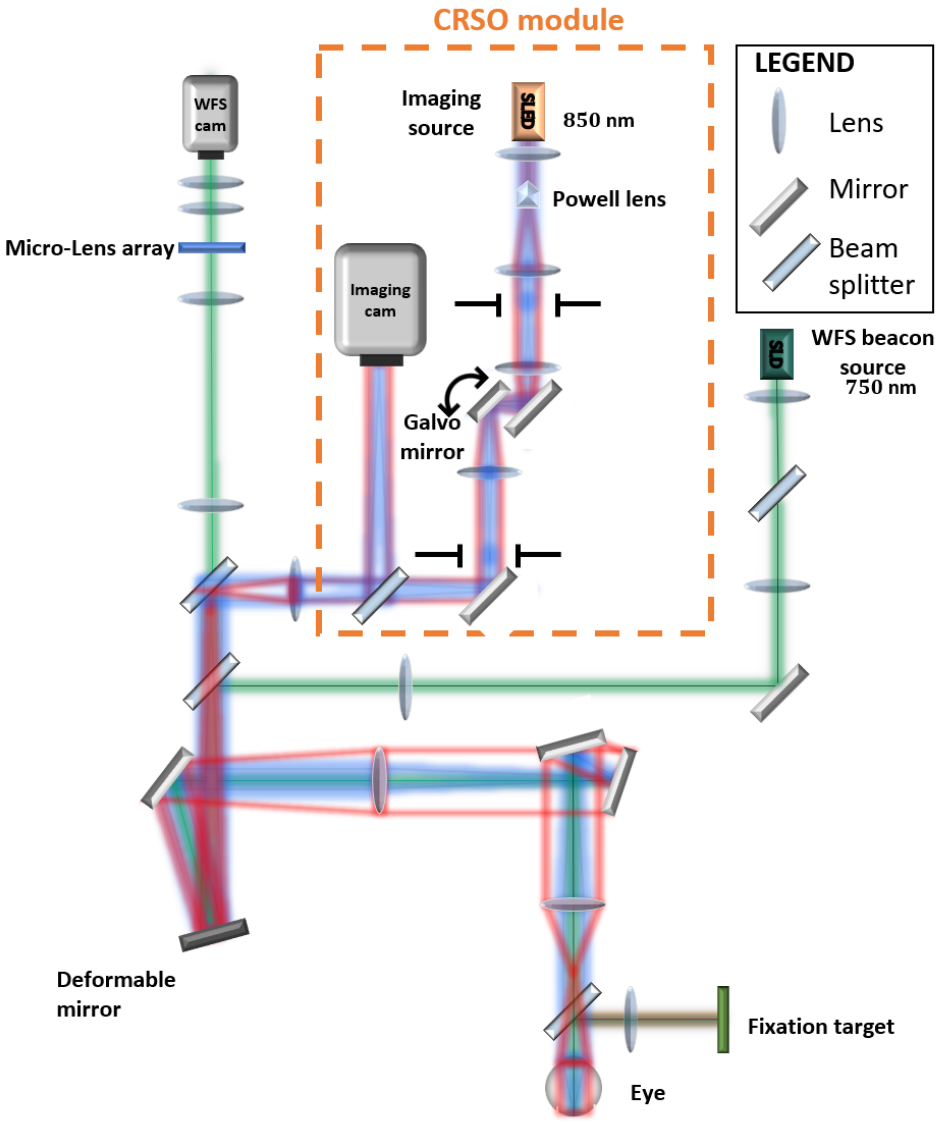

Figure 2. Schematic drawing of the CRSO module (orange rectangle). The length of the line is modelled in red, while its width is depicted in blue. The setup is integrated to the Paris Eye Group AO-FIO plateform, with its adaptive optics module represented in green.

achromatic doublet with a short focal lens. The focal planes of both the Powell and the following doublet were superposed so that the object line is formed on the image focal plane of the lens. The image of the line on the retina is shown in Figure 3-a. Its length covers 4 deg lateral field of view ($1.2mm$ on the retina) of the imaging system. In designing the system, careful consideration was given to set the appropriate thickness of the line illumination to minimize multiple scattering for spatially filtered brightfield images. Guided by theoretical studies[20] and supported by experimental work,[14] the thickness has been set at $10\mu m$ ($7\mu m$ FWHM).
To scan the line across the retina, an achromatic doublet is used to relay the light beam to a galvanometer mirror ($6210H$, Cambridge technology). The galvanometer mirror is optically conjugated with the pupil of the eye. This ensures that the light beam remains stationary at the pupil plane and scans across the retinal plane.

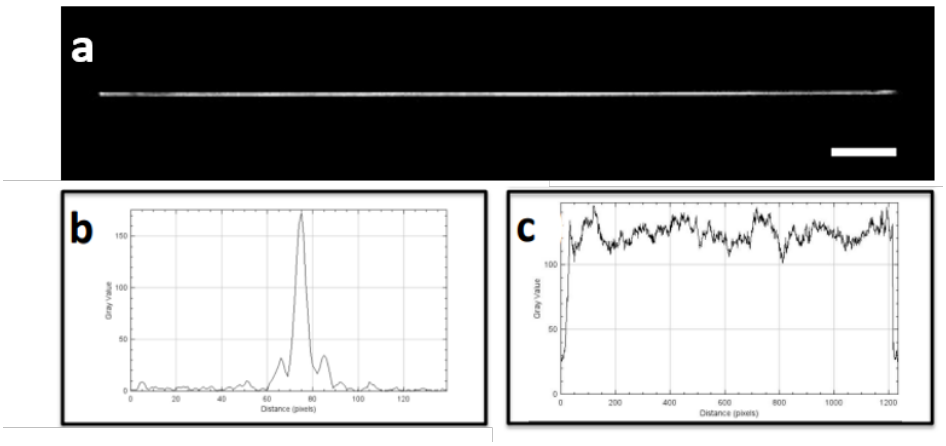

Figure 3. Image (a) and intensity profile of the line illumination on the retina, along its length (b) and its width (c). The width of the line is estimated at $7\mu m$ (FWHM) and its length $1200\mu m$. Scalebar: $100\mu m$.

Additionally, the galvanometer mirror is conjugated with the deformable mirror.
The illumination beam is relayed to the deformable mirror through a telescope setup composed of the two achromatic lenses. The line is focused on the DM along the direction of its length, while the its thickness remains collimated. The incident power is thus distributed over an elongated spot towards the vertical direction. The incoming flux and the size of the beam on the cornea and the retina is be measured to ensure ocular safety, according to the standards. Light is then delivered to the eye by additional relay optics. A beamsplitter located between the two achromatic lenses of the telescope transmits fifty percent of the light power through the rest of the optical system to the deformable mirror before reaching the eye. The backscattered light from the retina propagates in the reverse direction along the incoming path until it reaches the beamsplitter. Half of the incident light is reflected and directed onto the imaging camera (ORCA-Fusion Digital CMOS Camera, Hamamatsu). The camera is monitored with Holovibes software.[21]
The amplitude of the scan can be adjusted to achieve a specified vertical field of view. The scanning speed of the galvanometer mirror is suitable for capturing full-field images over the maximum field of view of 5 deg (approximately 2000 by 2000 pixels) at a rate of $100Hz$ and over half of the field of view (2000 by 1000 pixels) at $200Hz$. The results presented in this work were obtained at $200Hz$ with a scan amplitude covering roughly half of the total field of view.
The imaging camera is equipped with 2304 by 2304 pixels, with a pixel pitch of $6.5\mu m$. It is operated in rolling shutter mode to synchronize the electronic shutter of the camera with the scanning of the galvanometer mirror when acquiring AO-CRSO images. The camera achieves an imaging rate of 200 frames per second (fps) for a region of interest measuring 2048 by 1000 pixels.

2.3 Synchronisation

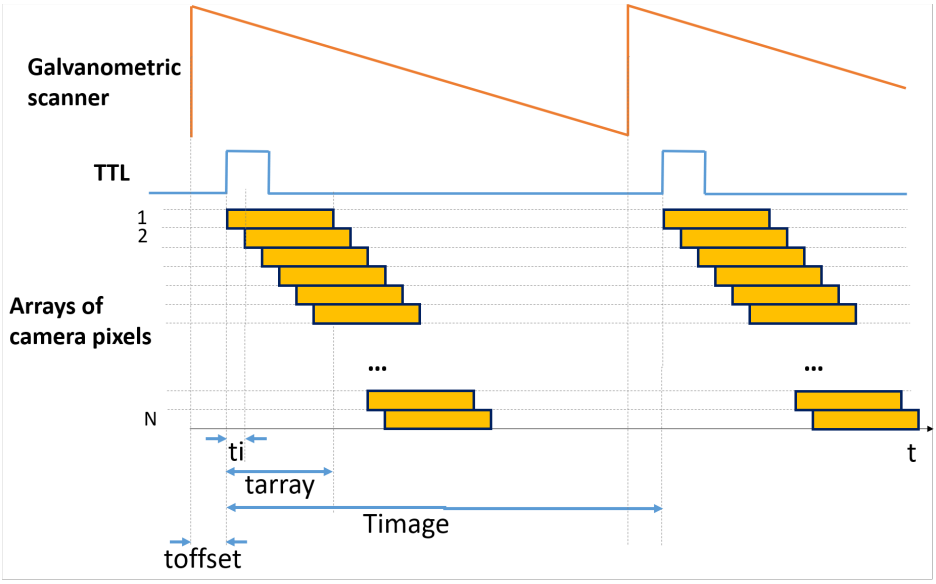

Figure 4. Chronogram of the synchronization between the galvanometer mirror and the sCMOS camera. ti corresponds to the time between the exposure of two consecutive arrays of pixels. $tarray$ is the exposure time of a pixel array. $Timage$ is the period of the TTL signal, namely the time between the start of two consecutive frames. $Toffset$ corresponds to the delay between the scan of the galvanometric mirror and the array of pixels being exposed. The latter is thus set to $0\mu s$ for brightfield acquisitions.

The synchronization between the rolling shutter of the imaging camera and the galvanometric scanner is achieved by transmitting an electronic transistor-transistor logic signal (TTL) to the camera, simultaneously with the application of an analog sawtooth signal to the galvanometer mirror conditioned by the National Instrument DAQ-mx card. The synchronization chronogram is depicted in Figure 4. The TTL signal generated by the computer and sent to the camera thanks to a National Instrument DAQ card.The analog sawtooth signal is generated using a custom-made Matlab code. The trigger signal sent to the camera defines the starting time of the acquisition of a frame. The camera is configured in the "Edge trigger" sub-mode of the External trigger mode. This ensures that the acquisition of a new frame initiates on the rise of the TTL signal. Consequently, the TTL signal defines the frame rate of the imaging sequence. A frame grabber, Active Silicon Frame Grabber (FireBird BASEBOARD 2xCXP662) allows to transfer the images to the system memory.
As depicted in Fig.4, each pixel array is exposed during tarray. At a defined time, as multiple arrays are exposed one can define the width of the camera rolling shutter as the number of pixel arrays exposed. The variable ti represents the time between the exposure of two consecutive arrays. Therefore, it also indicate the period during which the rolling shutter shifts down with a one-array step or its speed per pixel array. Drawing this parallel between temporal considerations of synchronization and an equivalent spatial detection aperture, one can observe the similarity between the offset aperture approach of AO-SLO and the AO-CRSO. Additionally, the variable toffset, representing the delay between the scan of the galvanometric mirror and the exposure of the pixel array, is equivalent to a spatial shift of the detection aperture relative to the line illumination. We consider acquisitions of frames of 1000 arrays of pixels at a rate of $200Hz$, corresponding to $5ms$ exposure time per frame. In order to scan the entire field of view, the speed of the galvanometric mirror is $5\mu s$ per line.
In brightfield images, to maximize the signal-to-noise ratio, it is crucial to maintain the exposure of each pixel array while the scanning line aligns with the array of pixels. Given that the thickness of the line illumination corresponds to 10 pixel arrays, it also aligns with the width of the rolling shutter, resulting in an exposure time of $50\mu s$ per pixel array.
For darkfield images, both the exposure time and the temporal offset (delay or advance) are set within a range

from typically $50\mu s$ to $400\mu s$. In other words, both the aperture size of the rolling shutter and the offset between the line illumination and the expose pixels are set from $7\mu m$ to $59\mu m$.

2.4 Processing

Images of both photoreceptor layer and nerve fiber layer were acquired with the AO-CRSO module at different eccentricities. To compensate for ocular motion, the image stacks went under a registration process before being averaged. This involved adapting to full-field AO-CRSO images a custom-made high-spatial frequency-based phase correlation algorithm, implemented in Matlab and detailed in.[22] Image processing first consists in discarding the blurred frames and those affected by eye blinking. Subsequently, a reference frame is selected from the stack, and the vertical and horizontal shifts resulting from ocular movements are estimated by computing phase correlation maps between each frame and the chosen reference frame. The images presented in the following section were averaged across a stack comprising several hundreds of registered images. For figure 5, AO-SLO images, corresponding to acquisitions of the same region were also performed with the multimodal AO retinal imager (MAORI) (Physical Sciences, Inc., Andover, MA, USA) at the Quinze Vingts Hospital in Paris, described in.[23]

2.5 Image acquisition

In-vivo retinal images were captured from a single healthy young participant.The participant followed institutional guidelines and adhered to the tenets of the declaration of Helsinki. After an explanation of the study's nature and potential outcomes, the subject provided informed consent.
The participant underwent pupil dilation with a 1% tropicamide solution (Mydriaticum, tropicamide 0.5%). Seated in front of the AO-full-field ophthalmoscope and securely stabilized using a chin and forehead rest, the participant was fixating on a yellow crosshair. This target served only to guide the subject's gaze, facilitating exploration of the retina.
The powers of the AO beacon source was $3.7\mu W$ and the imaging source was $0.9mW$. The irradiance of the illumination remained lower than the maximum permissible radiant exposure set by ISO standards (ISO 15004-2 (2007)) for devices classified under group 2.

3. RESULTS

3.1 Brightfield comparison with conventional AO-FIO and AO-SLO

The distinctive attribute of the CRSO lies in its ability to effectively reject multiply scattered photons. To evaluate its spatial filtering capabilities, we conducted a comparative analysis between brightfield CRSO images and those obtained using AO-FIO and confocal AO-SLO, on the same region of the subject.
For a meticulous comparison, we opted to use the same CRSO imaging path for acquiring both AO-FIO and brightfield AO-CRSO images. For AO-FIO images, all the camera pixels were exposed from the start of the acquisition until the exposure time of a single frame of $5ms$. The raw AO-FIO and AO-CRSO images then underwent the same processing algorithm as detailed above. Similar illumination between these images highlights the effect of the rolling shutter on the imaging contrast. The raw AO-FIO, AO-CRSO and AO-SLO images were averaged in order to get similar light irradiance.

	AO-FIO	AO-CRSO	AO-SLO
Michelson contrast	0,17	0,72	0,86
Photoreceptor SNR	5	35	45

Table 1. Comparative measurements of the Michelson contrast and photoreceptor signal-to-noise ratio, conducted among AO-FIO, AO-CRSO, and AO-SLO. These measurements were performed on the data presented in Fig. 5.

Figure 5 shows this comparison in the photoreceptor layer, on a region close to the fovea. 4 deg by 2.4 deg AO-FIO (A) and AO-CRSO (B) images were successfully acquired at $200Hz$. The comparative AO-SLO image (C) was acquired at $30Hz$ over a field of view of 2.2 deg by 1.9 deg. The scattering haze, predominant in the AO-FIO

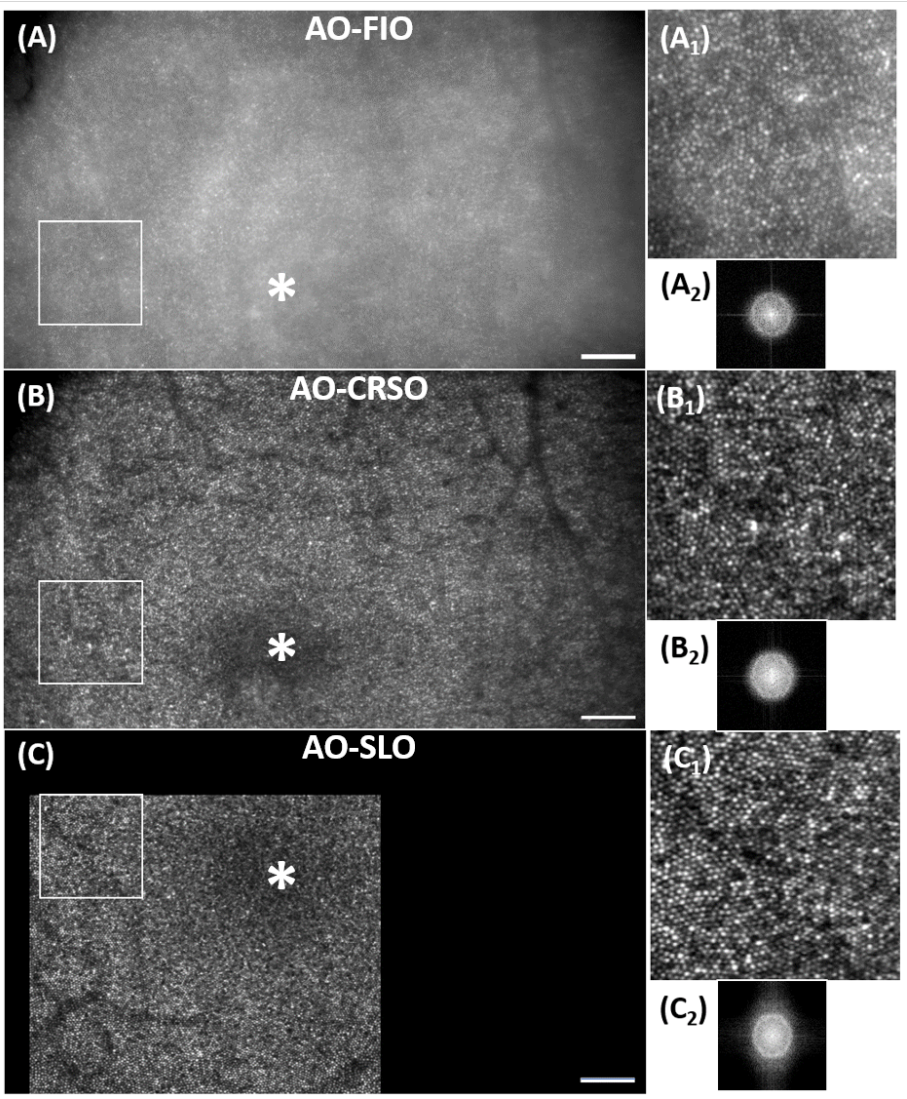

Figure 5. Images of photoreceptor cells near the fovea. 4 deg by 2.4 deg average images acquired with the AO-CRSO with an exposure time of $5ms$ per array (equivalent to global shutter mode) (A), with an exposure time of $50\mu s$ per array (B). 2.2 deg by 1.9 deg confocal AO-SLO image acquired at the same region (C). The white star indicates the center of the fovea. Scale bar: $100\mu m$. Zoom of the same region of 0.6 deg by 0.6 deg (A1, B1 and C1) and their Fourier transform images (A2, B2 and C2). Scale bar: $50\mu m$.

image (A), has been significantly reduced in the AO-CRSO image, making the contrast of the photoreceptors closer to the one in the AO-SLO image (C). This observation is further validated by images (A1, B1, and C1), which represent zoomed-in views of the same retinal region measuring 0.6 deg by 0.6 deg.

The enhancement of contrast is further evident when analyzing the frequency content of the images. The power density spectra depicted in (A2), (B2), and (C2) were obtained by computing the Fourier Transform of (A1), (B1), and (C1). Our specific interest is driven towards how bright the Yellot's ring, which represents the frequency footprint of photoreceptors, gradually increases from the AO-FIO to the AO-SLO

To quantify this improvement, table 1 displays the photoreceptor SNR computed from power density spectra (A2), (B2), and (C2) and the Michelson contrast measured directly on the images (A), (B), and (C). It highlights a 4 fold improvement in Michelson contrast or a 7 fold increase in photoreceptor SNR achieved through the spatial filtering

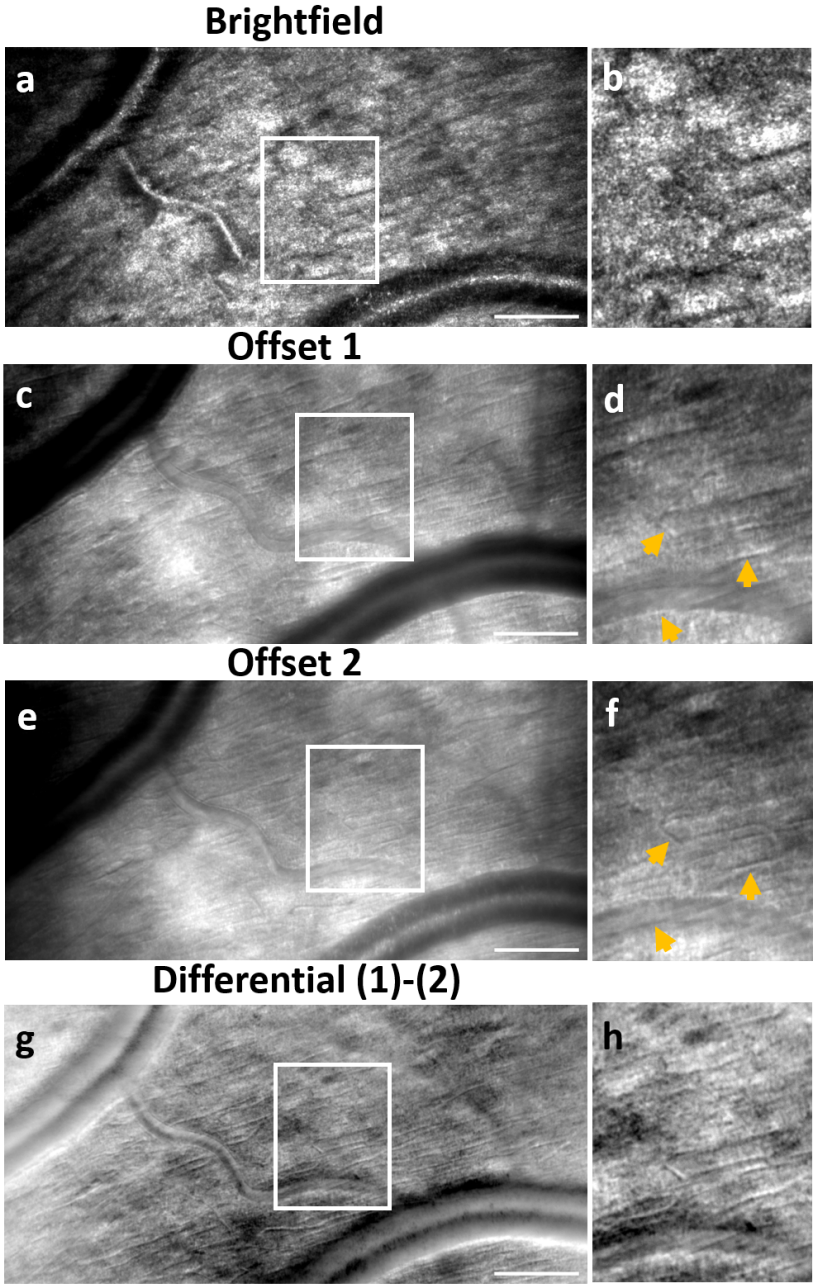

Figure 6. Multimodal imaging with the AO-CRSO reveals images of the nerve fiber layer at the peripheral retina (at 9 temporal degrees). Average images of 4.1 deg by 2.0 deg were acquired with the AO-CRSO in both brightfield (a) and darkfield modes, including offset 1 (c), offset 2 (e), and live differential (g) images. The average live phase contrast images were obtained by sequentially acquiring offset 1 and offset 2 images and subtracting them in real-time. Magnified views of 0.4 deg by 0.5 deg are shown for each acquisition mode (b), (d), (f), (h). In brightfield mode, the exposure time is set to $50\mu s$ per array. In phase contrast mode, the exposure time is adjusted to $300\mu s$ with a delay of $100\mu s$ (approximately $15\mu m$). The yellow arroheads in offset 1 and offset 2 images highlinght the typical inverted contrast between both offsets. Scale bar: $100\mu m$.

of the AO-CRSO (0.72 Michelson contrast and 35 photoreceptor SNR), compared to the AO-FIO (Michelson contrast of 0.17 and photoreceptor SNR of 5). With such enhancements, the AO-CRSO reaches approximately 80% of both the Michelson contrast and photoreceptor SNR of the AO-SLO (0.86 and 45, respectively).

3.2 Multimodal imaging

To advance this proof-of-concept of AO-CRSO towards high-throughput multimodal imaging, we executed imaging sequences that alternated between brightfield and offset 1 and 2 acquisitions, on the nerve fiber layer, at 9 temporal degrees. The resulting images from the same sequence, acquired at $200Hz$ after registration and averaging for each imaging mode (brightfield (a), offset 1 (c), offset 2 (e), and differential (g) images), are presented in Figure 6.

Similar to AO-SLO offset aperture images, the brightfield image (a), (b) favors the strong specular reflection from nerve fibers and the upper external part of blood vessels.[5] By shifting the detection aperture equivalent to $15\mu m$ from the illumination, we effectively filtered out the reflective signal, revealing capillaries, as depicted in (c), (d), (e), and (f).
Magnified views of offset 1 and 2 images (d) and (j) particularly highlight their inverted contrasts, reminiscent of observations in offset aperture AO-SLO,[4,24,25] as indicated by the yellow arrowheads. The vessel contrast is further improved in the differential image (g).
Expanding this study to another retinal eccentricity, Fig. 7 presents two distinct views of the same regions for the photoreceptor layer and the nerve fiber layer.
Effects of spatial filtering clearly visible in the photoreceptor layer. The brightfield mode renders the photoreceptor cells highly contrasted and bright, while the vessels in neighboring layers are optically sectioned and appear dark. The orange arrowheads in Fig. 7-(c) are pointing towards rods. This demonstrates that implementing the CRSO module to the Paris Eye group AO-FIO has not affected the lateral resolution (of $2\mu m$). In phase contrast mode (see Fig 7-(b) and (d)), the differential image reveals the photoreceptor inner segments, akin to the AO-SLO split detection technique.[2] Their precise visualization, whether the outer segment exhibits strong backscattering or not, has proven to be beneficial in the follow-up of gene therapy,[26] blindness, AMD, and glaucoma.[27]
The change in frequency content between the two acquisition modes (a) and (b) can be examined with the power spectral density (PSD) of images (a) and (b) through their Fourier Transform computation. The resulting images (e) and (f) display the frequency footprint of the photoreceptor cells, known as Yellot's ring, in both images.
While the PSD of the brightfield image shows an isotropic distribution of the photoreceptor signal's energy, the PSD of the differential image reveals a preferential energy distribution towards a vertical direction. This direction corresponds to the asymmetric axis, which matches the direction of the offset between the scanning line illumination and the pixel arrays. This observation aligns with multi-offset aperture images, as detailed in Mecê et al.[28]

In the images of the nerve fiber layer, the fiber bed, initially covering the entire field of view in Fig.7-(g), vanishes in Fig.7-(h). This phenomenon resembles the results reported by Chui et al. when utilizing a large aperture with an offset.[4] In the differential image, the capillaries that are hardly visible in the brightfield image, become notably discernible (blue arrowheads).

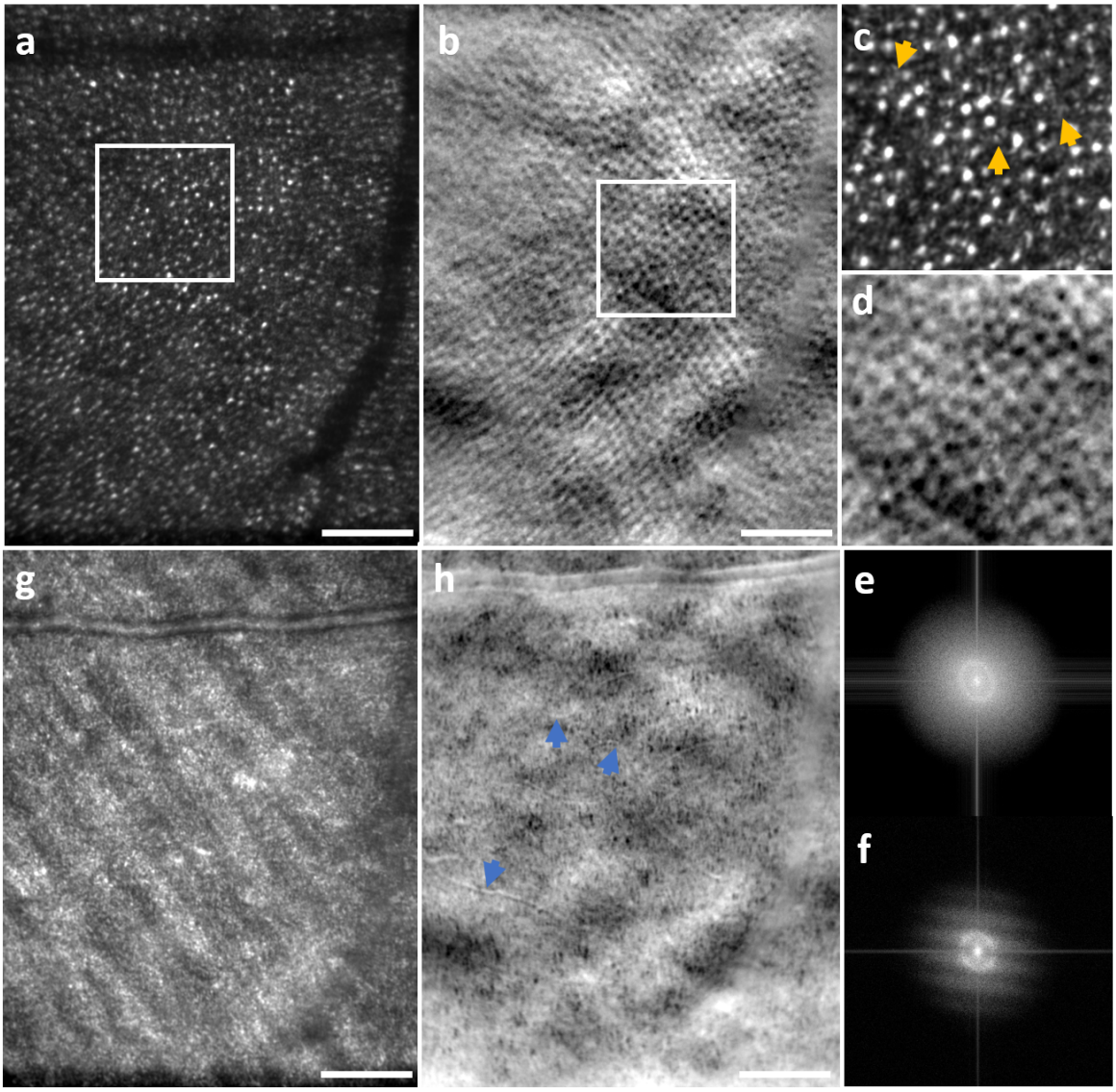

Figure 7. 1.5 deg by 2.0 deg brightfield (a), (g) and differential (b), (h) AO-CRSO images of the same region on both the photoreceptor (a), (b) and the nerve fiber (g), (h) layers, at 9 temporal degrees. 1.0 deg by 1.0 deg magnified views of photoreceptors are shown in brightfield (c) and differential imaging (d) modes, as well as the corresponding power density spectra (g) and (h) computed from (a) and (b). The blue arrowheads in the differential image of the nerve fiber layer (h) point towards capillaries. The orange arrowheads in the magnified view of the photoreceptors in brightfield (c) point towards rods. Scale bar: $100\mu m$.

4. DISCUSSION

This study demonstrates the flexibility and efficiency of the AO-CRSO in tailoring the imaging process to specific contrast requirements. To evaluate this capacity even further, we conducted a parametric study to evaluate the contrast evolution when varying the offset between the line illumination while keeping the same exposure time of $300\mu s$ per line (corresponding to an aperture size of $44\mu m$). In Fig. 8, we observe a gradual change in contrast of differential images in the the nerve fiber layer with increasing offsets. Smaller offsets enhance the contrast

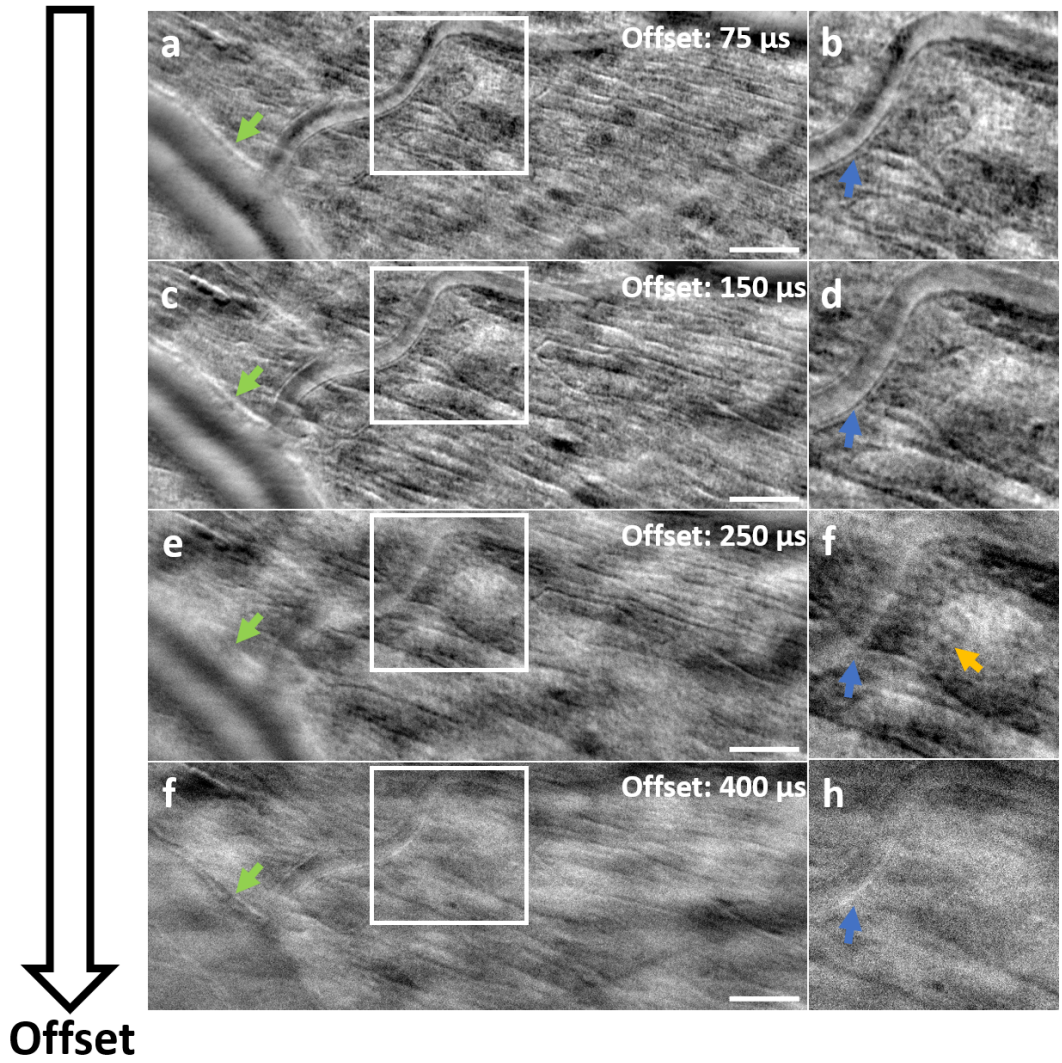

Figure 8. 3.2 deg by 1.2 deg differential images of the nerve fiber layer, as the delay between the illumination and the rolling shutter increases, at a constant exposure time of $300\mu s$. The delays were set at $75\mu s$ (a), $150\mu s$ (b), $250\mu s$ (c), and $400\mu s$ (d). The corresponding offsets are $11\mu m$ (a), $22\mu m$ (b), (c), (d). The green arrowheads highlight the same large vessel for each offset. The blue arrowheads in the magnified views show the same vessel under different offsets. The yellow arrowhead in (f) points towards putative ganglion cells. Scale bar: $100\mu m$.

of capillaries and vessel walls. This contrast begins to dissipate at $250\mu m$ (equivalent to $37\mu m$). The altering appearance of the vessel wall indicated by the blue arrowhead illustrates this trend. Larger features, such as the vessel pointed out by the green arrowhead, remain visible at larger offsets before fading at $400\mu s$ (equivalent to $60\mu m$). Notably, putative ganglion cells (size: 10–$12\mu m$) become visible with a consistent size and in a manner similar to images previously demonstrated in multi-offset AO-SLO,[7] at an offset of $250\mu s$ ($37\mu m$), as indicated by the yellow arrowhead in the magnified view. Achieving high precision in offset settings is crucial to observe these cells, as they become obscured at the subsequent offset of $400\mu s$.

In Fig. 8, we observe a gradual change in contrast as the offset increases. While the smallest offsets favor the contrast of capillaries and vessel walls, their contrast beging to dissipate at $250\mu m$ (equivalent to $37\mu m$). The varying aspect of the vessel wall pointed by the blue arrowhead illustrates this tendency. Bigger features as

the vessel pointed by the green arrowhead are visible at bigger offsets before fading. Particularly interesting, at offset $250\mu s$, ($37\mu m$), displays putative ganglion cells (size: 10–$12\mu m$ as pointed by the yellow arrowhead on the magnified view.
Along with the system's versatility, these results also highlight the ability of the AO-CRSO to perform imaging with spatial filtering similarly to AO-SLO technique but with an asset of being at the camera pixel rate.
This marks a notable evolution from conventional camera-based pattern projection multimodal retinal imaging approaches.[16] Specifically, the AO-CRSO's rolling shutter camera eliminates the need for additional digital filtering in post-processing required with the pattern projection approach. What adds further value for clinical practice is its capability for direct visualization of the retina in the desired mode and synchronization settings during eye examinations.
Additionally, the ability to switch detection modes within a single acquisition, without affecting the frame rate enables the system to perform rapid multimodal imaging. In comparison to offset aperture AO-SLO, the AO-CRSO cannot achieve simultaneous bright and darkfield imaging. However, with the alternating acquisition modes, the delay between consecutive raw brightfield and offset images can be reduced to one frame, that is $5ms$ at $200Hz$. Consequently, complementary data in brightfield and differential imaging modes can be obtained at an effective rate of approximately $67Hz$ for a field of view of 4 deg by 2.4 deg.
More particularly, high throughput phase contrast imaging, represents a valuable asset of the AO-CRSO. Offset aperture acquisitions alternating advanced and delayed detection with the same offset, allows to get direct visualization of the blood flow in the microvasculature. Giving access to a quantitative counting of erythrocytes provides a distinctive benefit for the in-depth examination of vascular disease over time in humans.[11]
Narrowing the field of view to 1 deg by 4 deg, we successfully captured individual red blood cells within capillaries at a rapid imaging rate of $400Hz$. Figure 9 depicts the perfusion map of the area where red blood cell flow was captured, computed from differential images. Reslicing the $400Hz$ video along the selected capillary's direction enabled to create the kymograph in (b). This technique, previously used on brightfield images,[29] allowed us to retrieve blood cell speed within vessels. Using the same method, blood flow in the capillary was estimated from $0.68mm/s$ to $1.35mm/s$, consistent with ranges presented in prior work. Additionally, by reslicing perpendicularly to the same capillary, blood flow was measured by counting individual red blood cells, employing a technique demonstrated in mice.[30–32] The corresponding kymograph in (c) indicates a blood flow of 40 to 100 red blood cells per second, aligning with in vivo measurements in human retinal capillaries presented in.[32]

Adapting the image processing method would help improve the imaging quality over the entire field of view bringing a more accurate estimation of potential biomarkers such as blood flow. In fact, imaging fine dynamic functional processes such as moving red blood cells over the full field and the entire imaging sequence makes the imaging quality even more sensitive to registration performances at subpixel level. Implementing to our processing scheme stripe-based image registration method seem particularly adapted to this challenge.[33,34] In fact, the precision of the registration relies on the reference frame, which must be carefully selected to be with minimum distortion. High-speed imaging enabled by the AO-CRSO may facilitate better and easier generation of a reference frame with minimal intra-frame distortion.

5. CONCLUSION

The AO-CRSO has demonstrated its ability to utilize both directly scattered and multiply scattered photons to image various structures such as fibers, vessels, capillaries, or photoreceptors, employing both brightfield and phase contrast modes. Successful image acquisition has been demonstrated across different regions of both the foveal and peripheral retina.
Proof-of-concept images exhibit a notable contrast enhancement compared to AO-FIO images, approaching the contrast levels of images obtained at lower rates with confocal systems. This enhancement has been achieved while maintaining a resolution sufficient for observing the structures of the smallest cells, such as foveal center cones and rods.
Notably, features observed in offset images closely resemble those seen in phase contrast images acquired with offset aperture AO-SLO, suggesting significant potential for enhancing visibility and broadening the range of structures revealed by this technique.

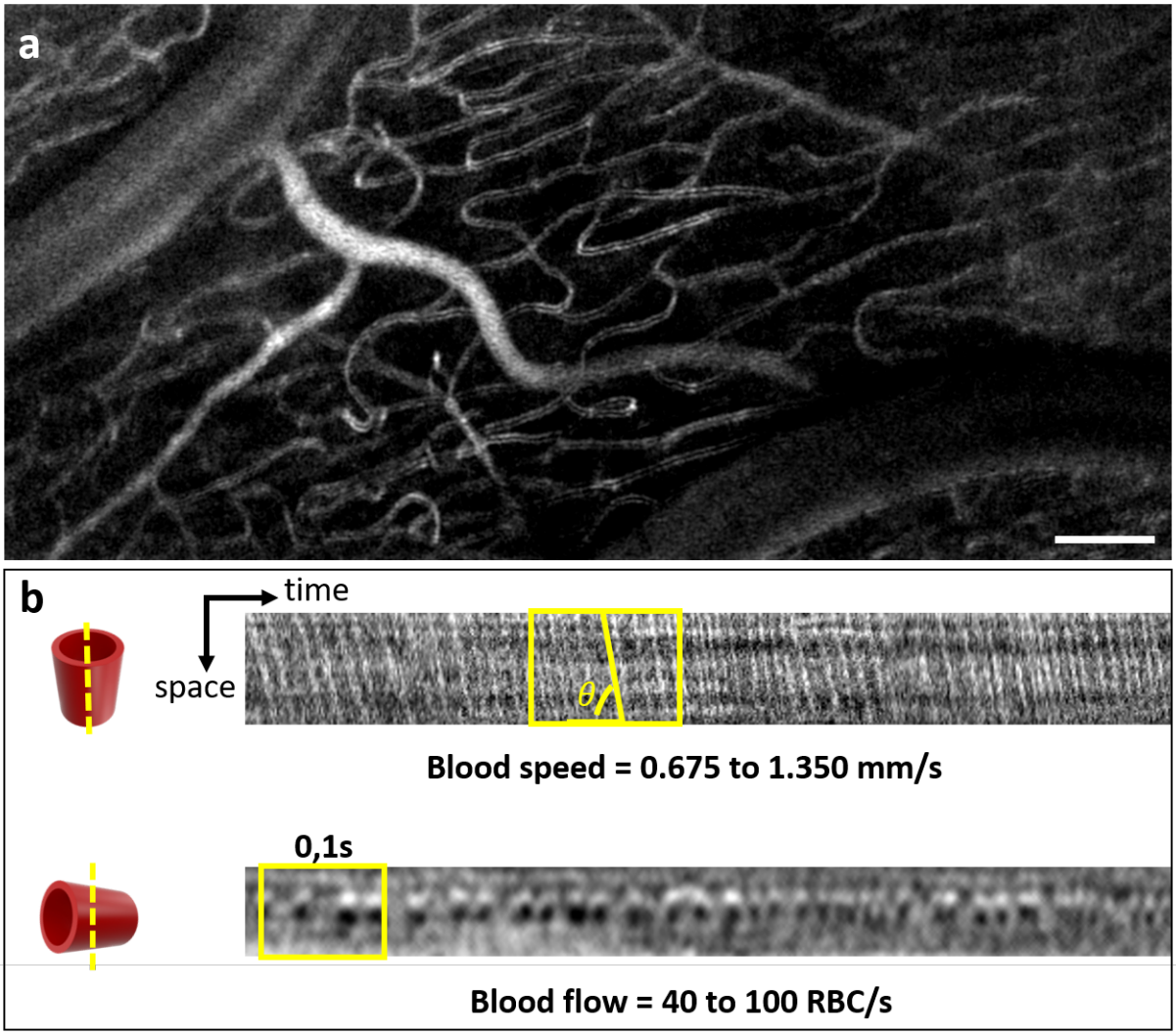

Figure 9. Red blood cell counting is performed on the motion contrast differential image. The 3.9 deg by 1.9 deg motion contrast image (a) is generated from the same image sequence as in Fig. 7-(g). The kymograph of the red blood cell flow is computed by reslicing the capillary section (in yellow) from the $400Hz$ image sequence in the direction of the capillary ((b) first row). Blood flow is measured using a kymograph of the red blood cell flow from the same capillary section through perpendicular reslicing for counting individual red blood cells ((b) second row). Scalebar: $100\mu m$.

Furthermore, the demonstrated flexibility to adjust the detection offset for optimizing imaging contrast on specific structures underscores the versatility of the AO-CRSO. The capability to acquire images using the alternating acquisition modes minimizes intra-frame motion-induced artifacts, opening new perspectives for functional imaging such as blood flow measurements and the study of retinal diseases.

ACKNOWLEDGMENTS

The authors would like to thank Elena Gofas and Kate Grieve for their the fruitful discussions and for providing the AO-SLO dataset. We also want to thank Michael Atlan for his technical support on Holovibes software.

Office National d'études et de Recherches Aérospatiales (PRF TELEMAC); Agence Nationale de la Recherche (ANR-18-IAHU-0001, ANR-22-CE19-0010-01).

REFERENCES

[1] Ford, T. N., Chu, K. K., and Mertz, J., "Phase-gradient microscopy in thick tissue with oblique back-illumination," **9**(12), 1195–1197.

[2] Scoles, D., Sulai, Y. N., Langlo, C. S., Fishman, G. A., Curcio, C. A., Carroll, J., and Dubra, A., "In vivo imaging of human cone photoreceptor inner segments," **55**(7), 4244.

[3] Laforest, T., Künzi, M., Kowalczuk, L., Carpentras, D., Behar-Cohen, F., and Moser, C., "Transscleral optical phase imaging of the human retina," **14**(7), 439–445.

[4] Chui, T. Y. P., VanNasdale, D. A., and Burns, S. A., "The use of forward scatter to improve retinal vascular imaging with an adaptive optics scanning laser ophthalmoscope," **3**(10), 2537.

[5] Chui, T. Y. P., Gast, T. J., and Burns, S. A., "Imaging of vascular wall fine structure in the human retina using adaptive optics scanning laser ophthalmoscopy," **54**(10), 7115.

[6] Sulai, Y. N., Scoles, D., Harvey, Z., and Dubra, A., "Visualization of retinal vascular structure and perfusion with a nonconfocal adaptive optics scanning light ophthalmoscope," **31**(3), 569.

[7] Gofas-Salas, E., Rui, Y., Mecê, P., Zhang, M., Snyder, V. C., Vienola, K. V., Lee, D. M. W., Sahel, J.-A., Grieve, K., and Rossi, E. A., "Design of a radial multi-offset detection pattern for in vivo phase contrast imaging of the inner retina in humans," **13**(1), 117.

[8] Burns, S. A., Elsner, A. E., Sapoznik, K. A., Warner, R. L., and Gast, T. J., "Adaptive optics imaging of the human retina," **68**, 1–30.

[9] Hammer, D. X., Ferguson, R. D., Ustun, T. E., Bigelow, C. E., Iftimia, N. V., and Webb, R. H., "Line-scanning laser ophthalmoscope," **11**(4), 041126.

[10] Lu, J., Gu, B., Wang, X., and Zhang, Y., "High-speed adaptive optics line scan confocal retinal imaging for human eye," **12**(3), e0169358.

[11] Gu, B., Wang, X., Twa, M. D., Tam, J., Girkin, C. A., and Zhang, Y., "Noninvasive in vivo characterization of erythrocyte motion in human retinal capillaries using high-speed adaptive optics near-confocal imaging," **9**(8), 3653.

[12] Ezenman, M., Hallett, P., and Frecker, R., "Power spectra for ocular drift and tremor," **25**(11), 1635–1640.

[13] Riggs, L. A., Armington, J. C., and Ratliff, F., "Motions of the retinal image during fixation*," **44**(4), 315.

[14] Krafft, L., Gofas-Salas, E., Lai-Tim, Y., Paques, M., Mugnier, L., Thouvenin, O., Mecê, P., and Meimon, S., "Partial-field illumination ophthalmoscope: improving the contrast of a camera-based retinal imager," **60**(31), 9951.

[15] Lee, S., Choi, S. S., Meleppat, R. K., Zawadzki, R. J., and Doble, N., "Programmable, high-speed, adaptive optics partially confocal multi-spot ophthalmoscope using a digital micromirror device," **48**(3), 791–794.

[16] Krafft, L., Senée, P., Gofas, E., Thouvenin, O., Atlan, M., Paques, M., Meimon, S., and Mecê, P., "Multimodal high-resolution retinal imaging using a camera-based DMD-integrated adaptive optics flood-illumination ophthalmoscope," **48**(14), 3785.

[17] Gofas-Salas, E., Mecê, P., Petit, C., Jarosz, J., Mugnier, L. M., Montmerle Bonnefois, A., Grieve, K., Sahel, J., Paques, M., and Meimon, S., "High loop rate adaptive optics flood illumination ophthalmoscope with structured illumination capability," **57**(20), 5635.

[18] Halpaap, D., García-Guerra, C. E., Vilaseca, M., and Masoller, C., "Speckle reduction in double-pass retinal images," **9**(1), 4469.

[19] Powell, I., "Linear deiverging lens."

[20] Krafft, L., "Spatial filtering for flood illumination ophthalmoscope."

[21] "Holovibes."

[22] Mecê, P. B., "4d exploration of the retina for adaptive optics-assisted laser photocoagulation."

[23] Hammer, D. X., Daniel Ferguson, R., Mujat, M., Patel, A., Plumb, E., Iftimia, N., Chui, T. Y. P., Akula, J. D., and Fulton, A. B., "Multimodal adaptive optics retinal imager: design and performance," **29**(12), 2598.

[24] Rossi, E. A., Granger, C. E., Sharma, R., Yang, Q., Saito, K., Schwarz, C., Walters, S., Nozato, K., Zhang, J., Kawakami, T., Fischer, W., Latchney, L. R., Hunter, J. J., Chung, M. M., and Williams, D. R., "Imaging individual neurons in the retinal ganglion cell layer of the living eye," **114**(3), 586–591.

[25] Guevara-Torres, A., Williams, D. R., and Schallek, J. B., "Origin of cell contrast in offset aperture adaptive optics ophthalmoscopy," **45**(4), 840.

[26] Pang, J.-j., Deng, W.-T., Dai, X., Lei, B., Everhart, D., Umino, Y., Li, J., Zhang, K., Mao, S., Boye, S. L., Liu, L., Chiodo, V. A., Liu, X., Shi, W., Tao, Y., Chang, B., and Hauswirth, W. W., "AAV-mediated cone rescue in a naturally occurring mouse model of CNGA3-achromatopsia," **7**(4), e35250.

[27] Jackson, G. R., Owsley, C., and Curcio, C. A., "Photoreceptor degeneration and dysfunction in aging and age-related maculopathy," **1**(3), 381–396.

[28] Mecê, P., Gofas, E., Rui, Y., Zhang, M., Sahel, J.-A., and Rossi, E. A., "Spatial frequency-based image reconstruction to improve image contrast in multi-offset adaptive optics ophthalmoscopy."

[29] Joseph, A., Guevara-Torres, A., and Schallek, J., "Imaging single-cell blood flow in the smallest to largest vessels in the living retina," **8**, e45077.

[30] Guevara-Torres, A., Joseph, A., and Schallek, J. B., "Label free measurement of retinal blood cell flux, velocity, hematocrit and capillary width in the living mouse eye," **7**(10), 4228.

[31] Dholakia, K. Y., Guevara-Torres, A., Feng, G., Power, D., and Schallek, J., "In vivo capillary structure and blood cell flux in the normal and diabetic mouse eye," **63**(2), 18.

[32] Gu, B., Sarraf, D., Ip, M., Sadda, S. R., and Zhang, Y., "In vivo measurement of the lineal density of red blood cells in human retinal capillaries using high speed adaptive optics ophthalmoscopy," **46**(14), 3392–3395.

[33] Vogel, C. R., Arathorn, D. W., Roorda, A., and Parker, A., "Retinal motion estimation in adaptive optics scanning laser ophthalmoscopy," **14**(2), 487–497.

[34] Zhang, M., Gofas-Salas, E., Leonard, B. T., Rui, Y., Snyder, V. C., Reecher, H. M., Mecê, P., and Rossi, E. A., "Strip-based digital image registration for distortion minimization and robust eye motion measurement from scanned ophthalmic imaging systems," **12**(4), 2353.

Conclusion of the chapter: Reaching the end of this chapter, I demonstrated that:

- I implemented an imaging system capable of high speed, high resolution, distortion-free imaging on a large field of view, both in bright field and with phase contrast modalities: the Adaptive Optics - Confocal Rolling Slit Ophthalmoscope (AO-CRSO).
- By employing the differential offset phase contrast modality with this system, blood vessels and capillaries are well contrasted, enabling the measurement of blood vessel diameter.
- Owing to the high imaging speed, resolution and contrast, erythrocytes can be individually imaged within capillaries, making it possible to measure erythrocyte speed and blood flow.

Part III

Clinical application

Introduction to part III

In Chapter 3, we introduced the AO-CRSO, an imaging system that offers high spatial and temporal resolution across a wide field of view in both bright field and phase contrast modalities, enabling high contrast imaging of blood vessel walls and erythrocytes. This third part of the manuscript focuses on the clinical application of this system for studying neurovascular coupling. My goal was to specifically adapt this system for measuring the effect of flicker stimulation on the diameter of retinal blood vessels at a high spatial and temporal resolution. This work is detailed in Chapter 4. Subsequently, the system was applied on a cohort of healthy patients. The results of this clinical investigation are presented in Chapter 5.

Chapter 4

Adapting the AO-CRSO for measuring flicker induced vasodilation at a high spatial and temporal resolution

Adapting the AO-CRSO to measure the effect of flicker stimulation on blood vessel tone involves focusing on three main aspects:

The first step is to integrate a stimulation channel into the system to activate retinal neurons. This stimulation channel must be optimized to ensure effective triggering of neurovascular coupling. This process is detailed in section 4.1.

In section 4.2, once the capability for light stimulation is established, the parameters of the AO-CRSO must be tuned to measure blood vessel size, with particular emphasis on enhancing the contrast of vessel walls. For this step, finding the appropriate offset and exposure time settings of the system is crucial.

Finally, to analyze the images captured by the system, an image processing method capable of precisely measuring changes in vessel diameter in response to light stimulation is required. This method needs to be as automatic as possible. This work is presented in section 4.3

4.1 Implementation of a stimulation channel to trigger neurovascular coupling

Neurovascular coupling in the retina can be observed by administering a flickering light stimulus to the eye, which describes an illumination alternating in brightness usually with a frequency in the 5-20 Hz range. This type of stimulus increases the activity of amacrine cells and ganglion cells in the inner retinal layers leading to the dilation of primary arterioles by the relaxation of smooth muscle cells [59] and enhanced blood flow throughout arteriolar, capillary, and venular networks of the retina. To provoke neurovascular coupling in the retina, a stimulation channel was designed and implemented within the system. Designing this channel started with reviewing literature to find the best light stimulation configuration to favor a strong NVC response. In the following section, the different requirements in terms of intensity, frequency, wavelength, and size of the stimulation are discussed.

4.1.1 Requirements of the stimulation channel to trigger neurovascular coupling.

Wavelength: Neurovascular coupling is driven in the retina by the increased activity of amacrine and ganglion cells [59]. The role of ganglion cells is to transmit image-forming visual information from the retina to the brain in the form of action potentials [102]. Therefore, any visible light that can be detected by the retina has the potential to increase the activity of ganglion cells and therefore to trigger functional hyperemia. Some evidence in cats from Riva et al [17] have shown that blood flow increase in the optic nerve head in response to flicker stimulation closely follow the scotopic luminous sensitivity curve when an area of the retina presenting predominantly rods was stimulated. Following the same principle, to stimulate the central human retina, monochromatic light with a wavelength close to the photopic peak sensitivity of the eye should work the best.

In humans, different flicker wavelengths have successfully induced functional hyperemia. Alternating yellow and green/blue light has been used on the RVA [13, 14, 73] as well as yellow light (530-600 nm) [15, 31, 72].

Frequency: The effect of flicker stimulation frequency on blood flow at the optical nerve head has been assessed using laser doppler flowmetry in both cats and humans [75]. For both studies, a band-pass response was found with a significant increase in blood flow between 2 and 30 Hz. The effect of flicker frequency on retinal blood vessel dilation has also been measured on humans [14]. Vasodilation of retinal arteries was observed with flicker frequencies between 2 and 64 Hz. However, flicker frequencies in the range 4 to 16 Hz provoked the strongest responses in both arteries and veins.

Stimulation intensity: A wide range of stimulation intensities has been used in the literature to elicit a functional hyperemia response in the eye. The RVA, commonly used to measure flicker-induced hyperemia, employs a flicker stimulation intensity of approximately 260 lx [73]. Some studies have also utilized lower intensities; for instance, Zhong et al. [79] successfully used an illuminance of 6.6 lx. Using a low illuminance might be interesting as it results in a more comfortable stimulation for the patient.

Area of stimulation: It has been established in prior research both on animals [103],[104] and in humans [79] that neurovascular coupling in the retina is a location-specific process. Meaning that blood vessels dilate in order to bring more blood specifically to the regions where neurons have been activated. Consequently, to get a maximum functional hyperemia response, the area of stimulation should be as broad as possible, centered on the fovea and should encompass photoreceptors downstream of the imaged blood vessel.

Final choice of flicker parameters: Considering the available amoled screen for delivering the stimulation, the final flicker parameters are detailed in figure 4.1. A wide-field green light with a wavelength centered at 530 nm and a FWHM (Full Width at Half Maximum) of 40 nm was selected. The stimulation was delivered with an illuminance of 7 lx and a flicker frequency of 10 Hz, using square wave modulation at a 50% duty cycle. The area of stimulation in the retina was of 25° × 20°.

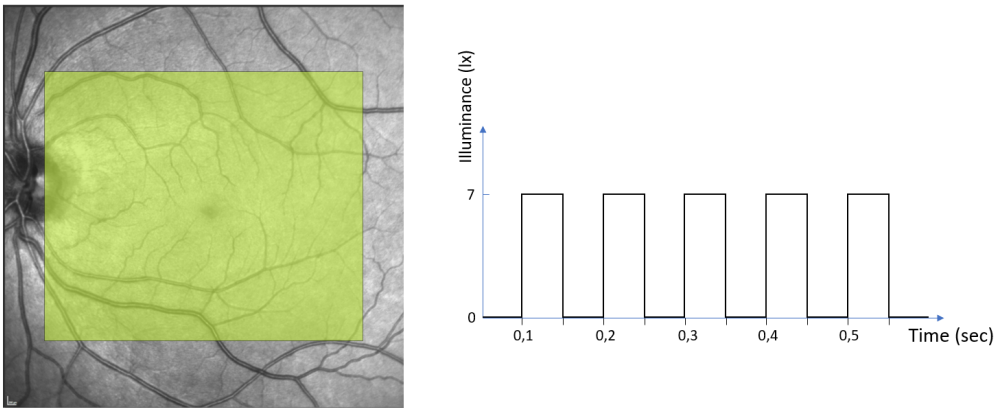

Figure 4.1: Parameters of the flicker stimulation. The stimulation region, is represented as a 20° x 25° rectangle on a retinal fundus image. The temporal profile of the stimulation follows a square wave modulation with a 50% duty cycle at 10 Hz.

4.1.2 Practical implementation of the fixation target

To deliver the stimulation, a 136x66 mm amoled screen (Waveshare, China) also used as a fixation target was chosen. The screen was set on a translation stage (see figure: 4.2) so that the distance from the lens to the screen could be adjusted to compensate for spherical refractive error of the imaged eye. An image of the screen was formed on the retina using a 150 mm lens and a pellicle beam splitter was used to separate the stimulation path and the imaging path (see figure: 4.2). To ensure a wide field of stimulation and fixation, a large 4 inches lens and a 4 inches beamsplitter had to be used in our setup. As a result, a final 25°x 20° rectangular region of stimulation could be obtained.

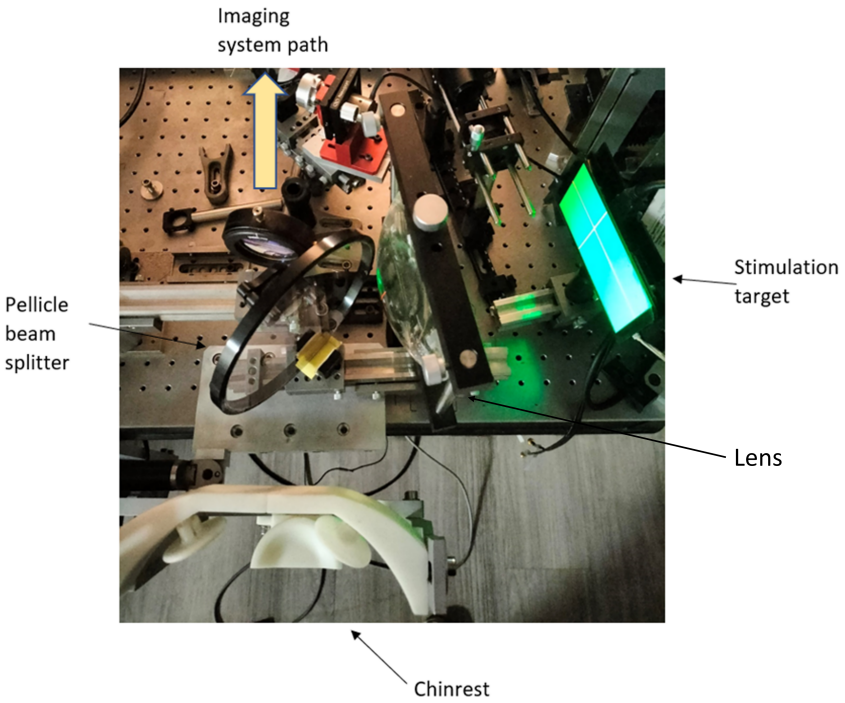

Figure 4.2: Practical implementation of the stimulation target.

4.1.3 Control of the fixation target

To control the fixation target and the stimulation channel, I developed a Python software. With the custom developed software, the operator can select the position of the fixation target and activate the stimulation sequence. Figure 4.3 shows the control window of this software.

Control over the flicker parameters, including the frequency, color, and timing of the flicker, is possible through the use of this software. During the flicker sequence, a countdown is displayed for the operator to provide spoken indications to the subject. This is particularly useful to prevent the subject from being surprised by the stimulation therefore ensuring that fixation is maintained by the imaged subject.

The start of the stimulation sequence was also synchronized with the start of the recording by the imaging system. This synchronization was achieved by implementing a double-click algorithm: the click to start the flicker sequence automatically triggered the 'start recording' button in the imaging system window. This method does not ensure perfect synchronization. To verify the precision of the synchronization, the target was placed directly in front of the imaging camera to determine the recorded image at which the flicker starts. With this method, a 100 ms precision on the synchronization between the flicker stimulation and the imaging system was measured.

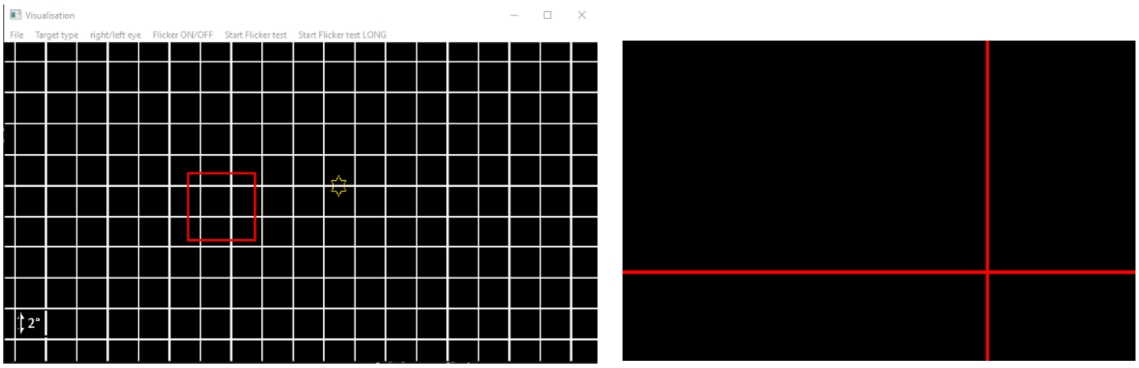

Figure 4.3: Control of the fixation/stimulation target. On the left, the window to control the fixation target and start the flicker stimulation sequences is shown. On the right, a view of the target projected onto the screen used for stimulation and fixation is depicted.

4.2 Choosing the best imaging parameters to image vessel walls

As discussed in the previous chapter, the AO-CRSO system is capable of phase contrast imaging, a modality particularly effective at revealing blood vessel walls. To investigate the effect of flicker stimulation on the lumen diameter of retinal blood vessels, we must determine the optimal system parameters, specifically in terms of exposure time and offset to reveal blood vessel walls.

With the AO-CRSO system, phase contrast imaging is achieved by introducing an offset between the illumination line and the detection rolling shutter of the camera. To optimize phase contrast, two key variables can be adjusted: the exposure time of each line of pixels in the camera's rolling shutter (which effectively changes the width of the detection "slit") and the offset between the illumination line and the detection "slit." Identifying the right values for these parameters is essential to maximize phase contrast of the vessel walls.

4.2.1 Optimizing vessel walls contrast: empirical approach

To find, the best parameters for imaging blood vessels, I opted for an empirical approach. The choice of the exposure time was first guided by the results of the work on the DMD-integrated AO-FIO: As we have seen in chapter 2, when projecting an illumination pattern into the retina, the extension of phase contrast was not the same for every structure. For blood vessel walls, the approximate extension of good phase contrast was approximately 50 µm. With this information, we have a good starting point of the exposure time that would optimize vessel walls contrast: 50 µm is equal to approximately 70 pixels in retinal plane (1 pixel = 0.73 micron in retinal plane) which results in an exposure time of around 350 µs for each line of pixels (5 ms of total exposure time for each total frame, with 1000 pixels in the vertical direction).

After setting the exposure time, the system was switched to 'sweep' mode to determine the appropriate offset parameter. In this mode, the delay between the sawtooth signal sent to the galvanometer mirror and the TTL signal sent to the camera is incrementally increased with each frame. This method allows the recorded video to display the varying contrasts achievable

at different offset positions. An example of an image sequence recorded using this method is shown in 4.4.

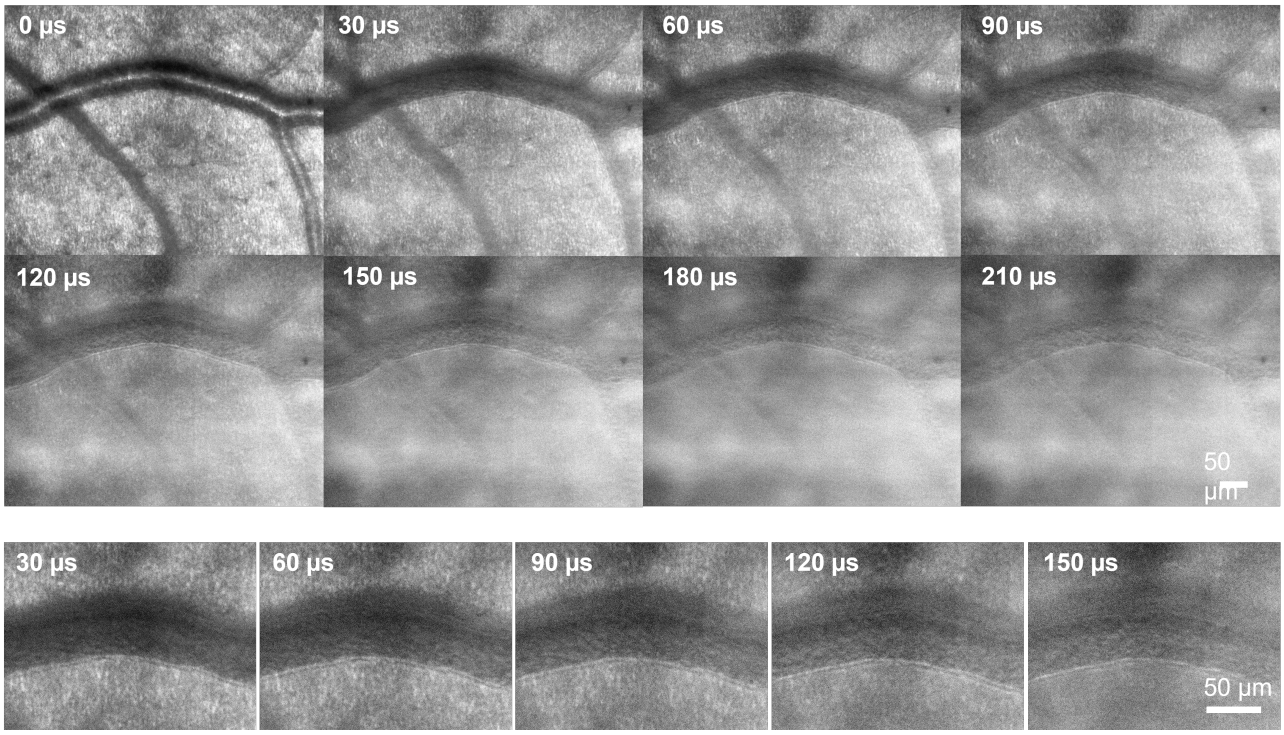

Figure 4.4: Demonstration of a sweep sequence. The system was focused on the nerve fiber layer, with pixel exposure times set to 300 µs. The top row displays 8 images selected with incremental offset values of 30 µs. At a 0 µs offset, we have bright field contrast and the vessel walls are not visible. Good phase contrast for the vessel walls is observed at offset values between 30 µs and 150 µs. The optimal contrast is achieved at offset values of 60 µs, 90 µs, and 120 µs, as shown in the magnified images in the bottom row.

This method was conducted with different exposure times to determine the optimal combination of exposure time and offset. We found that an exposure time of 300 µs provided the best contrast for the vessel walls. Regarding the offset, a wide range of offset values resulted in good contrast, as shown in figure 4.4, where offsets between 30 µs and 150 µs yielded good contrast. I considered that increasing the offset causes high-frequency background features (such as nerve fibers) to disappear. Therefore, I chose an offset value of 50 µs, since maintaining some background features was important for accurately registering the recorded images which would be an important step in the processing of the images.

The final exposure time was set to 300 µs, resulting in a detection 'slit' of 43 µm. The chosen offset parameter of 50 µs created a 7 µm gap between the illumination line and the detection 'slit.' As discussed in previous chapters, subtracting consecutive positive and negative offsets further enhances phase contrast. The final configuration of these positive and negative offsets used for imaging blood vessels is presented in figure 4.5.

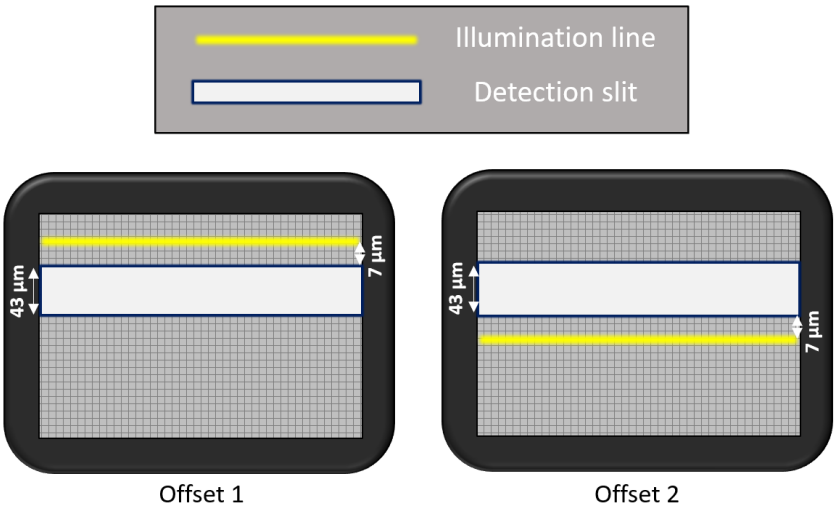

Figure 4.5: Final imaging parameters chosen for phase contrast imaging of blood vessels. An exposure time of 300 µs results in a 43 µm detection 'slit,' and an offset of 50 µs creates a 7 µm gap between the illumination line and the detection slit.

4.2.2 Choice of the field of view and framerate

As discussed in chapter 3 , with the AO-CRSO, the horizontal field of view is fixed by the length of the illumination line which is around 2000 pixels (4.5°) wide. While the vertical field of view depends on the scanning course of the galvanometer mirror which results in a trade-off between the vertical field of view and the total framerate. The following field of view and framerates are possible with the system:

- 4.5° x 4.5° at 100 Hz
- 4.5° x 2.5° at 200 Hz
- 4.5° x 1.25° at 400 Hz

It has been shown by Lu et al. [49] that eye motion artefacts are minimized for frame rates above 200 Hz. For this reason, the 4.5° x 2.5° at 200 Hz configuration was chosen as the default configuration.

4.2.3 Typical images of retinal arteries obtained with these parameters

Figure 4.6 presents examples of phase contrast images (differential offset) of arterioles obtained after optimization of the systems parameters for imaging vessel walls. These images are comparable to those of arterioles captured with split detection AO-SLO ([22], [92]) where the three layers of the arteriole wall can be distinguished (see, for instance, figure 4.6 B).

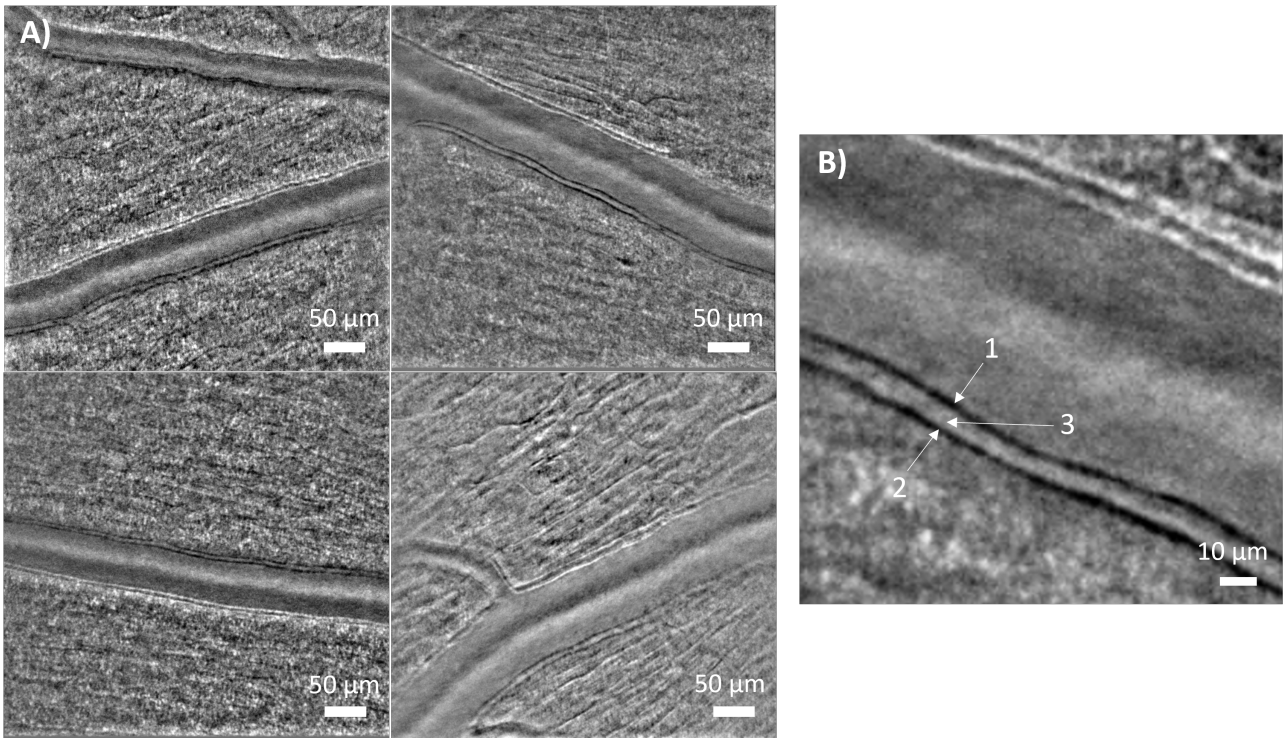

Figure 4.6: Example of phase contrast images taken with this configuration. A) For each example, the system was focused on the nerve fiber layer, and 10 differential images were averaged. B) Magnified image of one example from A, showing the three layers of the artery: 1) tunica intima, 2) tunica media (composed of smooth muscle cells), and 3) tunica adventitia.

4.3 Image processing

As seen in the previous section, the AO-CRSO is capable of high framerate phase contrast imaging. This offers the possibility for measuring neurovascular coupling at a high temporal resolution. However, to measure the diameter of blood vessels with a high sampling rate (at least every 0.1 seconds), measuring manually the size of vessels is not feasible. For instance, a 50 second recording results in approximately 10 000 images. To automatically extract the vessel size at regular intervals from the recorded images, an algorithm was developed. This algorithm consists of 4 main steps: image registration and averaging, manual selection of the zone where vessel wall will be analyzed, detection of the vessel walls, vessel wall diameter computation over time.

4.3.1 Image registration

To correctly measure the size of the vessel, a custom-made registration method was employed using MATLAB. The basis for this method is an algorithm which was originally developed by Pedro Mecê to register AO-FIO images and is detailed in the following paper: [105]. The main steps of this methods are the following: The images are first bandpass filtered to remove high spatial frequency noise (dominated by photon noise) and low spatial frequency (dominated by photons collected from out-of-focus retinal layers and multiply scattering). Then, a phase correlation between the two images is computed by multiplying the reference image FFT with

the other image FFT and taking the real part of this multiplication a correlation map is obtained. The 2D maximum of this correlation map gives the shift between the reference image and the current image. At this step, the shift is only measured pixel wise. To improve the precision of this method, a parabolic fit using the surrounding points vertically and horizontally is employed. From the parabolic fit coefficients, a new maximum is found resulting in a sub-pixel precision. This method is schematically represented in figure 4.7.

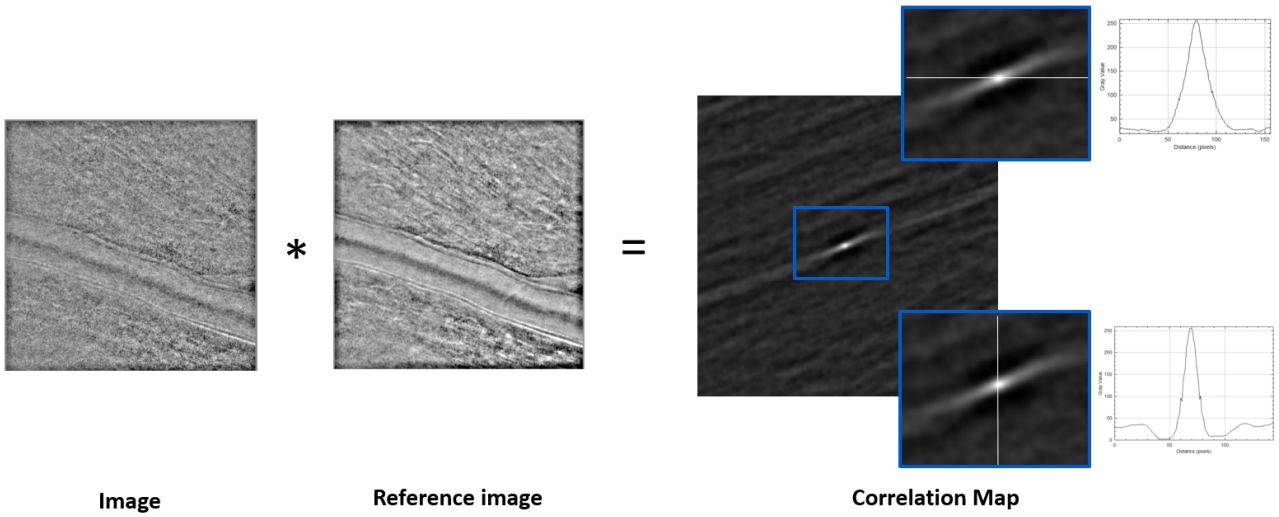

Figure 4.7: Representation of the registration method used. A correlation map is obtained by computing the cross correlation of a reference image and the image to register. The resulting correlation map is represented on the right: the image shift is measured by finding the maximum of the correlation map.

Figure 4.8 is a schematic representation of how I applied this algorithm. To enhance the performance of the registration process, a high signal-to-noise reference image was first generated by averaging the initial 100 images from the stack. These 100 images were registered using the first image of the batch as the reference, after which they were averaged. Before proceeding with the registration of the entire stack of 10,000 images, I visually inspected the resulting reference image to ensure its sharpness. If the reference image was not sharp, for instance in cases where a blink occurred early in the acquisition, a different set of 100 images was selected to create the reference image. Once a high signal-to-noise reference image was obtained, the full stack was registered.

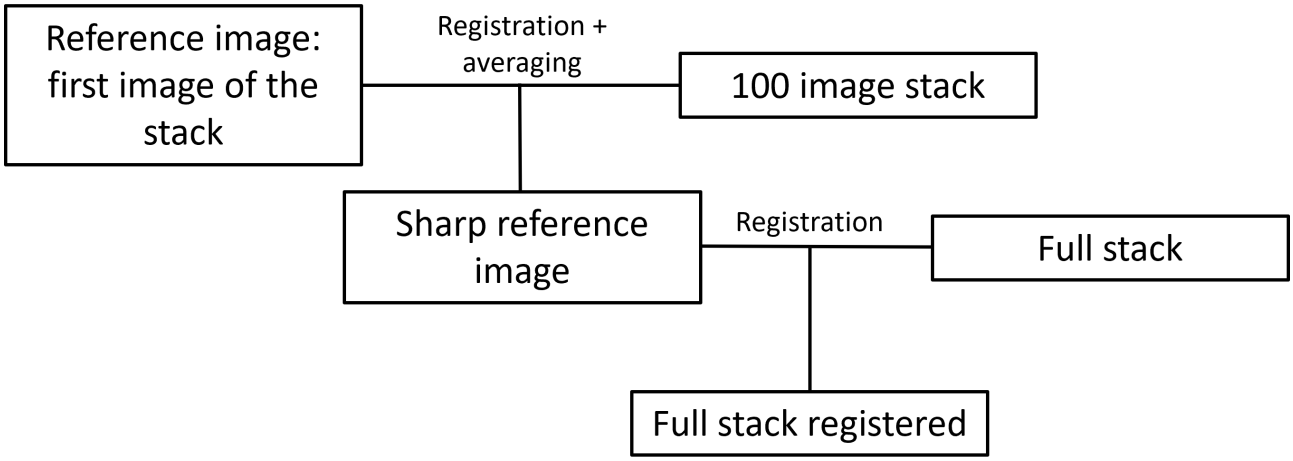

Figure 4.8: Schematic representation of the image registration pipeline

4.3.2 Averaging

The temporal evolution of the diameter of blood vessels is affected by three main mechanisms: The cardiac cycle, vasomotion and neurovascular coupling. To measure the complete dynamics of blood vessels, the fastest process that we have to sample is the cardiac cycle. With every heartbeat, veins and arteries of the retina slightly dilate. This process happens with a frequency of 1-1.7 Hz in healthy subjects (60-100 beats per minute). Therefore, to sample this process, we need at least to measure the vessels size 3 times per seconds.

The AO-CRSO system can acquire differential offset images at 100 Hz on a 2.5°x4.5° field of view. However, depending on the patient being imaged, a single split image can still be noisy. To improve the signal to noise ratio, we chose to average images by groups of 10. The improvement in quality with averaging can be appreciated in figure 4.9.

For most patients, averaging 2-3 images is enough to precisely measure the vessel diameter, however by averaging 10 images we are assured that all patients would yield usable images. Furthermore by averaging 10 images, a final sampling rate of 10 Hz is maintained, which is sufficient for capturing the vessel dynamics down to the effect of the cardiac cycle.

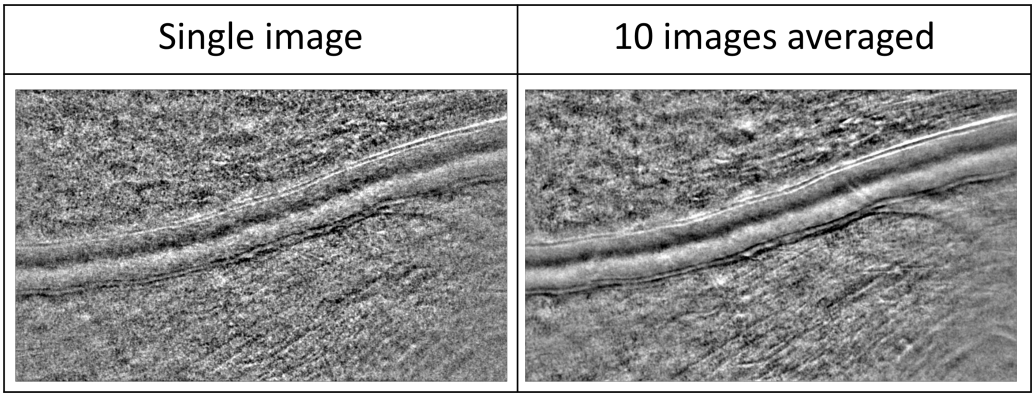

Figure 4.9: Single differential offset image versus 10 differential offset images averaged.

4.3.3 Creation of a "M scan"

Once the images are registered and averaged, a simple semi-automatic algorithm was developed to measure the size of the vessel from each averaged frame of the recorded video. The first step of this algorithm is to construct a “M scan” of the vessel. This M scan is a time-based representation of the cross section of the blood vessel.

To make the M scan, the images are first rotated to make the vessel horizontal (see figure 4.10). This rotation is executed automatically by identifying the vessel's dominant linear features using a Hough transform. Manual fine-tuning of the rotation is also possible. Then, a 30 µm segment of the vessel is chosen (orange rectangle in figure 4.10 B)). This segment is chosen at a location where the vessel walls are well-defined, and the vessel shows minimal tortuosity.

The columns from this 30 µm segment are averaged to produce a high signal-to-noise ratio cross-section of the vessel at each frame of the recorded video. Using excessively long segments (100 µm or more) can be problematic as it decreases the precision of the method. Conversely, very short segments (less than 10 µm) do not sufficiently enhance the signal-to-noise ratio for some subjects. We found that a segment length of 30 µm performed best.

Plotting these averaged cross-sections as a function of time generates the M scan of the vessel, as illustrated in figure 4.10 C. This M scan clearly reveals the temporal evolution of the vessel's wall and changes in the vessel's diameter can be appreciates. Some data loss, due to blinks also appear as vertical grey lines in the M scan, indicating missing data. However, in more than 90% of the recorded frames, the size of the blood vessel can be measured.

This algorithm can be applied to multiple acquisitions without having to adjust any parameters. As long as the fixation target is at the same location, all the frames can be registered with the same reference image and the same rotation angle and vessel segment choice can be applied to all the acquired images. This enables automatic processing of multiple flicker sequences and analysis of the same region of interest among different acquisition at the same eccentricity.

4.3.4 Detection of the vessel walls

A Matlab script was developed to extract the lumen diameter of the vessel from its corresponding recored M-scan. Each column of the M-scan represents the average cross-section of the vessel at a given time. By plotting the pixel intensity of a column of the M-scan, a graph, as shown in figure 4.11 B), is produced.

This profile exhibits two distinct sets of peaks: two positive peaks that we believe corresponds to the tunica intima and adventitia on one side of the vessel, and two negative peaks corresponding to the tunica intima and adventitia on the other side of the vessel.

I defined the lumen diameter of the vessel as the distance between the two internal peaks which represent the tunica intima of the vessel. The position of these two peaks are indicated by red arrows in figure 4.11.

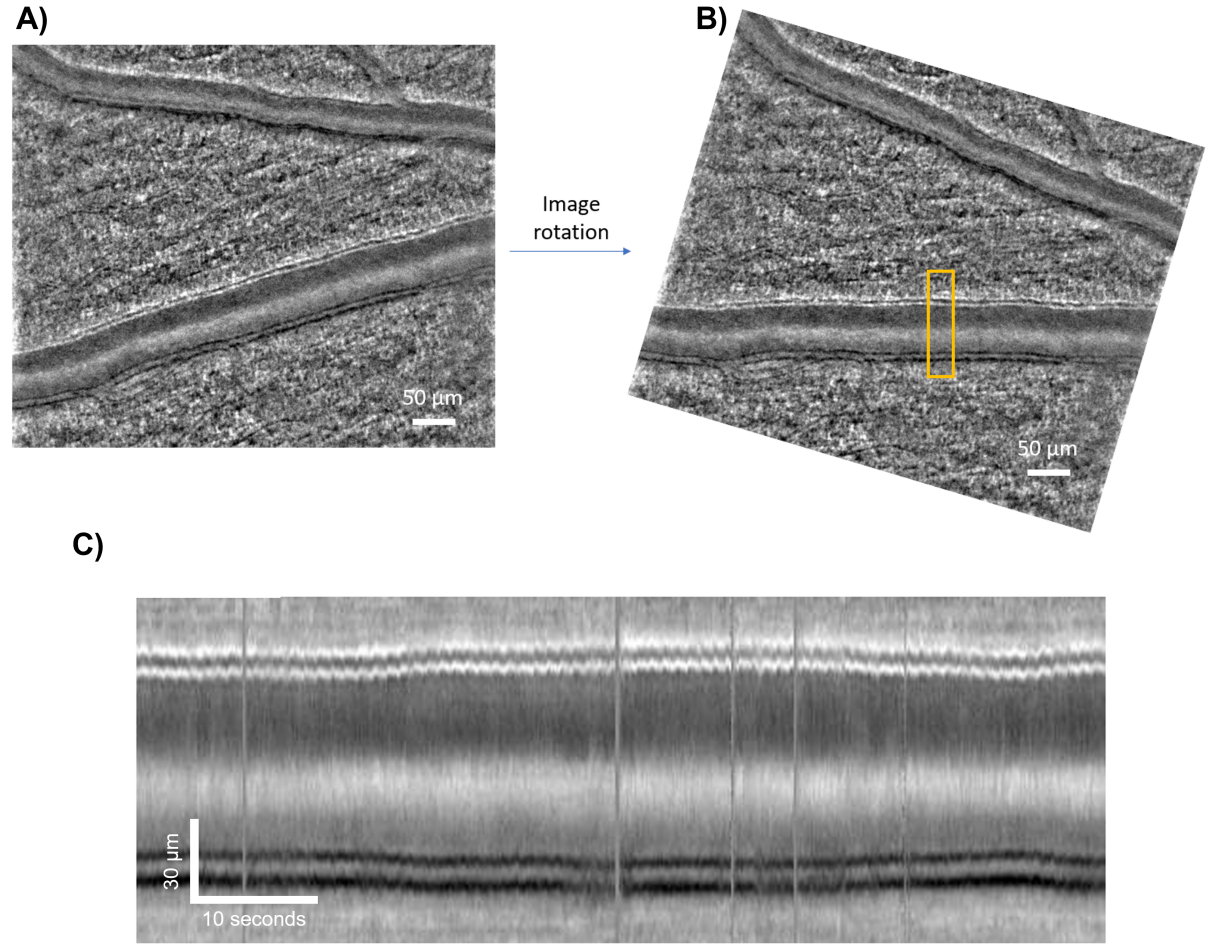

Figure 4.10: Generation of an M scan of a blood vessel from the recorded video. A) Example image of a blood vessel after averaging of 10 recorded split images. B) The images is rotated so the vessel of interest is horizontal, a 30 µm section of the vessel is chosen to make the M scan. C) Resulting M scan of the vessel, each column of the M scan represents the average cross section of the vessel at a given time of the 50 seconds acquisition. The vessel's dilation is clearly visible by looking at this M scan.

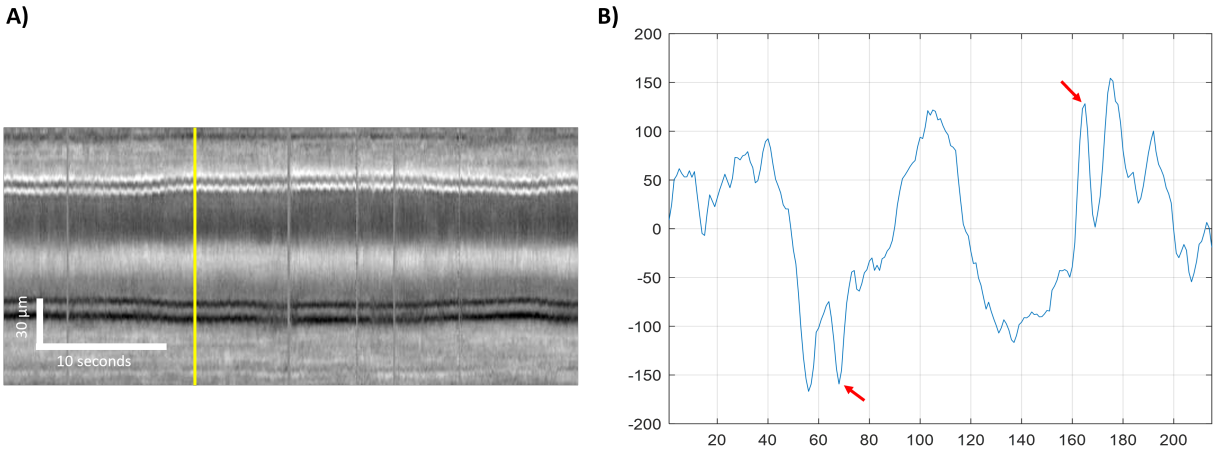

Figure 4.11: Peaks detection from the M-scan. A) M-scan of the vessel. B) Pixel intensity along the yellow line in A, showing two negative peaks and two positive peaks. The red arrows indicate the peaks corresponding to the tunica intima of the vessel.

To reliably detect the lumen diameter with this algorithm, some challenges had to be addressed:

- The patient have to blink during the acquisition, which will result in some data loss. As a result, the M scan exhibits vertical lines where no image of the retina is detected.
- The image quality and global intensity can vary over time. This is due to several factors including dynamic aberrations, head and eye movements.

To reliably measure the correct peaks corresponding to the tunica intima of the vessels and avoid false detection due to noise and blinks, a two-step strategy was employed. First, a pixel intensity threshold was set to detect only peaks above a certain pixel intensity value. Then, the region around which to search for a peak was manually defined. Typically, the vessel's wall moves by only a few microns due to neurovascular coupling; therefore, any detected peaks outside of this specified window were eliminated.

After detecting the position of both peaks, we initially achieve a pixel size precision on the lumen diameter, which in our case is 0.7 µm. To improve precision, a parabolic fit was employed: after locating the pixel corresponding to the detected peak, a sub-pixel estimation was performed by computing the parabolic fit of the pixels surrounding the detected peak. From the parabolic fit coefficients, a new peak position was determined by identifying the location of the parabola's summit. In our case, the parabolic fit was performed using 3 pixels. By examining the detected vessel walls in the M-scan in figure 4.12, the precision of this method can be appreciated. For instance, the displacements of the tunica intima with each heartbeat can be precisely observed.

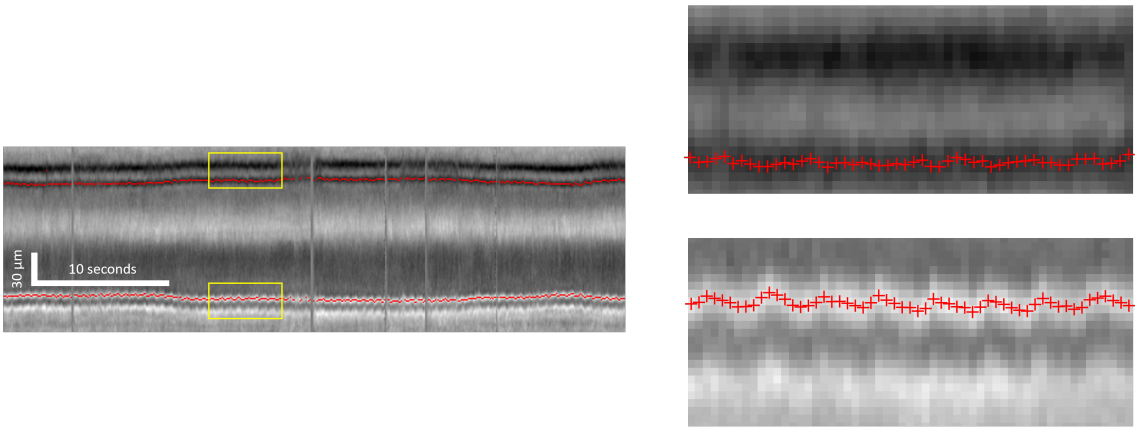

Figure 4.12: Detected position of the vessel's tunica intima. The detected position of the two sides of the tunica intima were represented as red crosses on the M-scan of the vessel. On the right, magnified regions of the M-scan, highlighted by yellow rectangles, are displayed.

Conclusion of the chapter: In this chapter, we have discussed how the AO-CRSO system was adapted to measure flicker-induced vasodilation. Additionally, I presented the image processing pipeline that I developed to extract submicrometer-precision lumen diameter measurements from the captured AO-CROS images:

- I integrated a stimulation channel into the AO-CRSO, designed for wide field flicker stimulation in the retina. I also developed a software to control this stimulation channel therefore having complete freedom on the stimulation parameters.
- Using empirical data both from the DMD-integrated AO-FIO and the AO-CRSO, I tuned the systems parameters, including offset and exposure time, to maximize vessel walls contrast.
- I developed an image processing algorithm to semi-automatically measure vessel lumen diameter at a 0.1 µm precision every 0.1 seconds for acquisitions of up to a few minutes.

Chapter 5

Measuring flicker induced vasodilation at a high spatial and temporal resolution on a healthy subject cohort

It was established in chapter 4 that we optimized the AO-CRSO system in order to make it completely operational to measure how blood vessels of the retina dilate when the retina was exposed to flickering light stimulation. In this chapter, we applied this system on a cohort of healthy subjects. More than 50 flicker tests were done in 8 healthy subjects. Our goal was twofold: First, in section 5.1 we aimed to demonstrate the system's capability to reliably measure flicker-induced vasodilation at high spatial and temporal resolution. Secondly, we explored the effects of various parameters and stimulation, leveraging the system's capabilities to gain deeper insights into the flicker-induced response and the dynamics of blood vessels. The most conclusive results from this part of the work are presented in section 5.1. However, some aspects of this research require further investigation. These preliminary results, which suggest promising directions for future study, are detailed in section 5.2.

5.1 Article in preparation: measuring flicker induced vasodilation at a high spatial and temporal resolution in the human retina

The following section is structured as an article in preparation which aims to demonstrate the system's capability to reliably measure flicker-induced vasodilation at high spatial and temporal resolution.

5.1.1 Article

Measuring flicker induced vasodilation at a high spatial and temporal resolution in the human retina.

Pierre Senée[1,2,3], Léa Krafft[1,2], Daniela Castro Farias[2], Olivier Thouvenin[4], Michael Atlan[2,4], Michel Paques[2], Serge Meimon[1,2] and Pedro Mecê[2,4]

1, DOTA, ONERA, Université Paris Saclay F-91123 Palaiseau, France
2, Paris Eye Imaging Group, Centre d'Investigation Clinique 1423, Quinze-Vingts National Ophthalmology Hospital, DGOS, INSERM, Paris, France
3, Quantel médical, Cournon d'Auvergne, France
4, Institut Langevin, ESPCI Paris, CNRS, PSL University, Paris, France

Significance:

Neurovascular coupling is a fundamental mechanism of the brain which locally regulates blood flow in response to changes in neuronal activity. Here, we show a method to measure *in-vivo* how blood vessels of the retina dilate in response to visible light stimulation of the neurons. By imaging the retina at a high speed and high resolution, this method provides new insight into the inner working of functional blood flow regulation in the retina. Clinically, this method holds promise for improved diagnosis of retina or systemic diseases where active blood perfusion becomes deficient.

Abstract:

Neurovascular coupling (NVC) is a crucial process in which blood flow is dynamically adjusted to meet the metabolic demands of active neurons. In this study, we introduce an innovative method for *in-vivo* imaging of retinal blood vessel dilation in response to visible light stimulation, offering insights into the functional regulation of retinal blood flow. Using high-resolution, high-speed phase contrast imaging, we continuously monitored retinal vessel dynamics in eight healthy subjects, capturing precise temporal and spatial changes in vessel size under both stimulated and baseline conditions. The flexibility of our method also allowed for the exploration of various acquisition and stimulation settings, broadening possibilities for investigating neurovascular coupling in the retina. This work not only enhances our understanding of neurovascular coupling but also has the potential to identify new biomarkers for vision-impairing conditions and neurodegenerative diseases.

Introduction:

Upon activation of specific brain regions, a localized augmentation in cerebral blood flow ensues, facilitating the delivery of oxygen and essential nutrients to meet the increased metabolic demands due to neural activity. This physiological response is known as neurovascular coupling. Neurovascular coupling was first reported more than 100 years ago by Roy and Sherrington [1] and led to a large body of brain research [2], [3] where it is the source of the BOLD signal detected with fMRI [4].

Dysregulation of neurovascular coupling is observed in vision affecting diseases such as Glaucoma [5] and diabetic retinopathy [6], [7] but also in various neuropathological conditions, including ischemic stroke [8], Alzheimer's Disease [9], and cognitive impairments stemming from hypertension [9]. This emphasizes the importance of understanding neurovascular coupling to identify new biomarkers for disease progression monitoring and to devise therapeutic strategies targeting aberrant blood flow control mechanisms following these disorders [10].

Since the retina is part of the central nervous system, neurovascular coupling can also be observed in the human retina. Administering a visible flickering light to the eye activates amacrine cells and ganglion cells in the inner retinal layers. This stimulus triggers the dilation of primary arterioles on the retinal surface, leading to enhanced blood flow throughout arteriolar, capillary, and venular networks within the retina [11].

The retina thereby provides a unique opportunity to study NVC. It shares the same embryological origin as the brain [12], [13] and as such, shares many similarities in term of structure and physiology with it. It is also the only portion of the central nervous system that is optically accessible for *in-vivo* micrometer cellular resolution imaging. Therefore, there exists the possibility that *in-vivo* retinal imaging of NVC can provide useful biomarkers of neurodegenerative disease much earlier in the disease process than conventional neuroimaging methods or clinical examination [14].

However, investigating CNV *in-vivo* remains challenging and many aspects of it are still unknown. Indeed, the dilation of blood vessels in response to light stimulation is minimal, typically only a few micrometers, necessitating a system with high resolution and contrast for accurate measurement. Furthermore, NVC is a dynamic process that requires continuous monitoring to track temporal changes in vessel diameter. Additionally, even without external stimulation, the tone of retinal arterioles is modulated by spontaneous rhythmic fluctuations in blood vessel size due to the cardiac cycle and vasomotion [15], [16], [17]. An imaging system with both a high spatial and temporal resolution would be able to discriminate between the dilation provoked by flicker stimulation and the dilation attributable to intrinsic vasomotion and cardiac pulsations and therefore could be a great tool to gain a deeper understanding of neurovascular coupling.

The Dynamic Vessel Analyser (DVA) (Imedos Systems UG, Jena, Germany) is the gold standard method for assessing the effect of light stimulation on retinal vessels. This system evaluates retinal vessel diameter by analyzing the brightness profile of the vessel through video sequences captured with a conventional fundus camera. It is particularly useful for measuring blood vessel dilation during a flicker test, where studies have reported a dilation of 3%-5% [18], [19], [20]. However, due to the system's limited transverse resolution, the vessel walls are not

visible, and diameter measurements rely on light absorption by the column of erythrocytes. This limitation results in reduced measurement precision, with a reported measurement sensibility of 5-7% for artery diameter (Polak et al. [21]). Moreover, the DVA is only applicable to larger vessels of diameter bigger than 90 µm [22].

OCT techniques, a gold standard in retinal imaging, can also be used to measure the diameter of blood vessels, but they inevitably suffer from time-varying speckle noise, which significantly impact the precision of the measurement [23], [24].

By correcting for eye aberrations, adaptive optics (AO) methods can reach transverse resolution in the retina of up to 2 µm. Owing to this resolution, blood vessel walls can be resolved [25], [26] which makes them ideal to measure the slight widening of vessels when the retina is exposed to light stimulation. The first generation of AO system, AO-Flood Illumination Ophthalmoscopes (FIO) used a full field illumination and a 2D camera [27]. These systems benefit from a high temporal resolution and a large field of view. However, due to the multiply scattered photons being detected by the camera, the images yield a low contrast, which limits their ability to study NVC. Duan et al. [28] have bypassed this issue by using visible light FIO to increase erythrocytes contrast and have measured dilation of capillaries during flicker tests. However, measurement of vessel caliber was only done before and after flicker and the measurement was based on perfusion maps, which is not a direct measurement of the vessel diameter through vessel wall imaging.

Another well established adaptive optics technique is the AO-Scanning Laser Ophthalmoscope (AO-SLO), an application of the confocal microscope in retinal imaging [29]. In the past decade, an alternative way of using this system, by displacing the confocal aperture has enabled the visualization of translucent structures of the retina such as blood vessel walls or erythrocytes with both high contrast and resolution [25], [26], [30]. Warner et al [31], have used such a system to measure the effect of a flicker stimulation on the retinal microvasculature, where both blood velocity and vessel diameter were measured. However, the measurements were done before, during and after the stimulus and not continuously over time.

To address these shortcomings, we developed a method that enables direct visualization of vessel wall of different calibers, arteries, and veins, at a high spatial and temporal resolution. The proposed method is based on the utilization of a line scanning illumination and the use of the rolling shutter of a 2D camera for the detection. By imposing an offset between the illumination line and the rolling shutter of the camera, phase contrast images can be generated enabling the direct visualization of vessel walls.

Using our proposed method, we were able to reliably measure flicker induced vasodilation over time (10 measurements per second) with a spatial precision of 100 nm and a temporal precision of 100 ms respectively. This method was applied to eight healthy subjects, allowing us to investigate various characteristics of the flicker-induced vasodilation response such as the influence of : arterial diameter, flicker stimulus duration, downstream retinal arterial areas, cumulative stimulation effects, and the uniformity of the response along the vessel.

Results and discussion:

Measuring the Dynamics of Retinal Arteries with and without Flicker Stimulation.

To measure the dynamics of retinal arteries in healthy subjects, imaging was conducted under two conditions: first, during a 40-second period with no stimulation, and second, during a flicker test. The flicker test involved 10 seconds without stimulation, 20 seconds with flicker stimulation, and another 20 seconds without stimulation. The flicker stimulation was done inside a wide rectangular 25°x20° region centered on the fovea. A green light flickering at 10 Hz and 50% duty cycle was used for all the presented studies (See material and method for more information).

Figure 1 presents the results for one subject and shows the example of one acquisition with (Fig 1.E,F)) and without (Fig 1.C,D) flicker. An artery perfusing the fovea was chosen for imaging (Fig. 1A)). This was done because the region near the fovea contains a high concentration of ganglion cells [32], therefore a strong response should be observed for an artery directly perfusing this region if exposed to flicker stimulation.

From the recorded images a profile of a line perpendicular to the vessel over time (M scan), representing the evolution of the vessel in time of the vessel can be constructed (Fig. 1C,1E) and the vessel's lumen diameter can be measured in time (Fig. 1D, 1F). The baseline diameter is defined in each acquisition as the average lumen diameter of the vessel during the first 10 seconds without flicker. Without stimulation (Fig 1.D), the vessel's diameter is modulated by two components. First the cardiac cycle, responsible for the rhythmic dilation at approximately 1 Hz can be seen in blue in (Fig 1.D). Secondly, a slower oscillation at around 0.1 Hz can also be observed by looking at the moving average in red (Fig 1.D). We believe this second component to be vasomotion which is described as a spontaneous rhythmic change in the vessel diameter arising from alternating smooth muscle dilation and constriction and has been previously observed *in-vivo* [15], [16], [17]. From our study, we have seen large differences between subjects for both the frequency and the amplitude of vasomotion (see supplementary information).

Fig. 1E,1F shows the evolution of the diameter of an artery during a flicker test. When the stimulation starts (Fig. 1F at t = 20 seconds) the diameter of the artery increases rapidly at around 0.5%-1% of dilation per second for approximately 5 seconds. Then the artery continues to dilate steadily at 0.1%-0.2% of dilation per second until a maximum dilation is reached around the end of the 20 seconds of flicker stimulation. After the end of the stimulation, the artery contracts back to its diameter pre-flicker. On some acquisition, this contraction undershoots under the baseline diameter before dilating back to the baseline diameter (see supplementary information).

This general trend of the vessel's diameter during a 20 second flicker test is consistent with what has been described with fundus camera imaging using the Dynamic Vessel Analyzer DVA [18], [20]. However, owing to our high spatial resolution and high contrasted vessel wall visualization, our approach is not limited to very large vessels and a single acquisition makes it possible for the first time to visualize the effect of the cardiac cycle, vasomotion and neurovascular coupling.

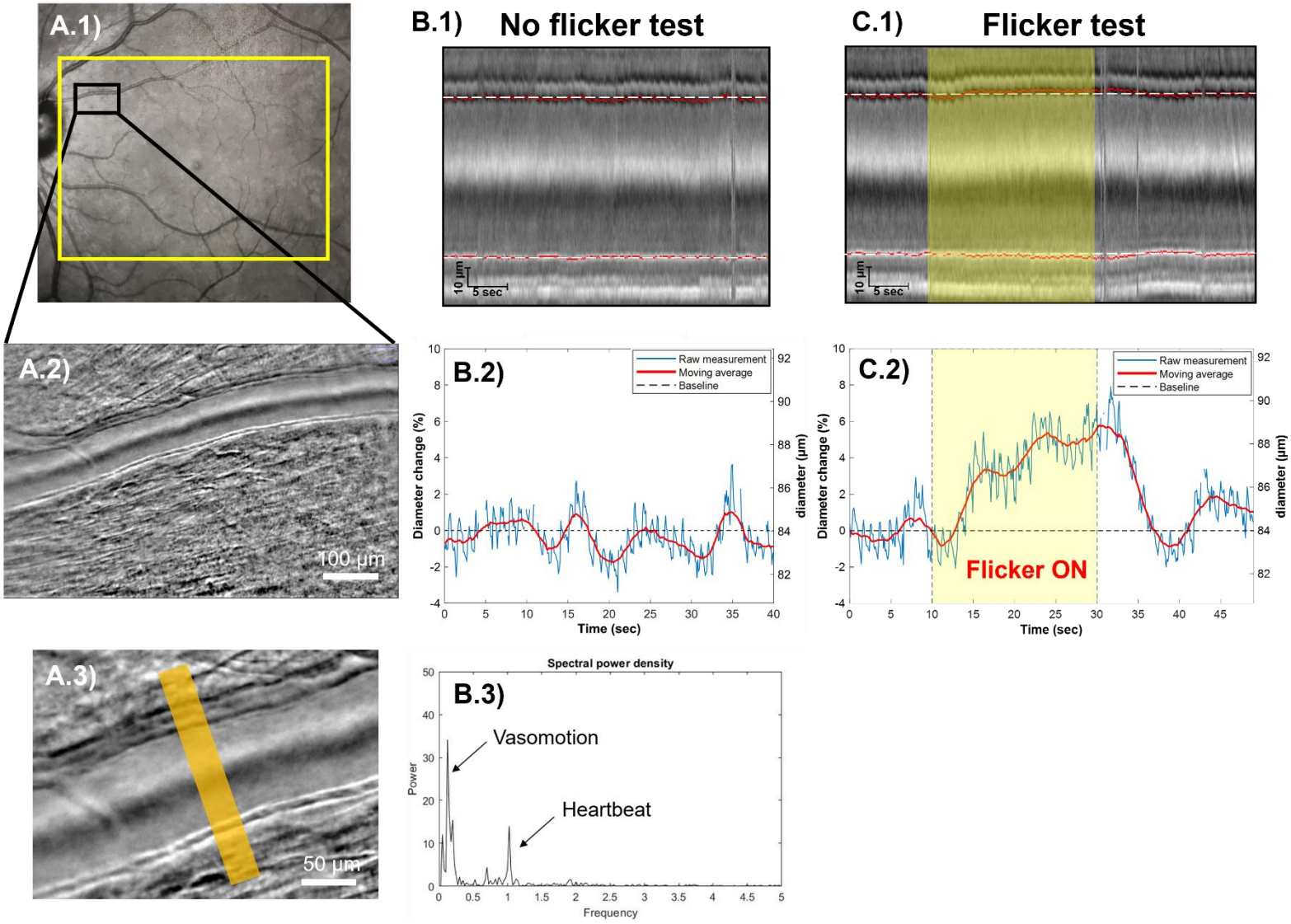

Fig 1 *: A.1) Fundus photography image of the imaged subject, the yellow rectangle represents the stimulated area during the wide field flicker test. The black rectangle represents the imaged area. A.2) 2.5°x4.5° region imaged by the system encompassing an artery upstream of the fovea. A.3) Magnified region of the image of the system, the section of the vessel where the lumen diameter is measured is represented in orange. B.1) M scan of the artery without flicker stimulation representing the profile of the vessel over time, white dashed lines represent the baseline position of the wall (tunica intima) of the vessel. B.2) Plot of the artery's lumen diameter over time without flicker stimulation. B.3) Plot of the spectral power density of the lumen diameter data, two peaks at 0.1 Hz and 1 Hz can be observed. C.1) M scan of the artery with flicker stimulation, the stimulation is represented on the M scan as a yellow rectangle. C.2) Plot of the artery's lumen diameter over time with flicker stimulation.*

Study of the Vascular Diameter response to Flicker Stimulus on 8 Healthy Subjects.

The same protocol as described in the previous section was conducted on 8 healthy subjects. For each subject, 3 acquisitions without stimulation and 3 acquisitions with a flicker stimulation were taken. For each acquisition, the maximum dilation and delay of the dilation was measured. (See fig. 2A)

Fig. 2B and 2C respectively represent the relative and absolute maximum dilation on all the acquisitions on the 8 subjects. For all the subjects, the maximum dilation was significantly higher with the flicker stimulation (red bars in Fig 2B and 2C) than without the flicker stimulation (blue bars in Fig 2B and 2C). A 5.2 % ± 1.6 % (4.4 µm ± 1.3 µm) maximum dilation was recorded during the flicker acquisitions on the 8 subjects. The maximum dilation without flicker stimulation was of 2.5 % ± 1% (2.1 µm ± 0.9 µm). We believe this observed dilation without stimulation to be due to vasomotion. The average and variability of the latency was of 20.4 ± 2.3 sec. On average, the maximum dilation was reached around the end of the 20 seconds of stimulation, which is consistent with work from Riva et al. [33] showing a saturation in the increase in blood flow in the optical nerve head after 20 seconds of stimulation.

By looking at Fig. 2B and 2C we can note for some cases a large variability among subjects as well as a large variability among different acquisitions for a single subject. This large variability can be attributed to two factors : first the effect of vasomotion which is an oscillation of the vessel walls which is not strictly periodic and displays large variability among different acquisitions both in terms of amplitude and frequency. Secondly, flicker induced vasodilatory response varies greatly from one subject to another with some subjects, displaying 8-9 % dilation while other only 2% as a response to flicker stimulation. To get a better understanding of the factors which can determine the strength of this response we investigated in later sections the effect of the size of the artery and the effect of the region perfused by the artery.

A)

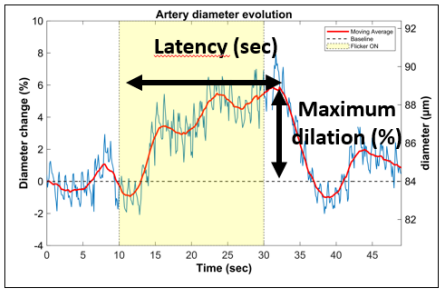

B)

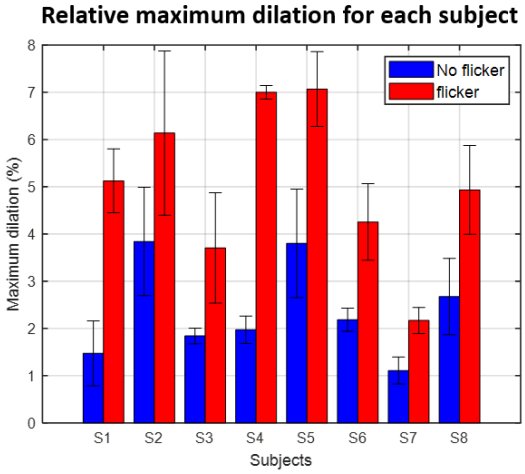

C)

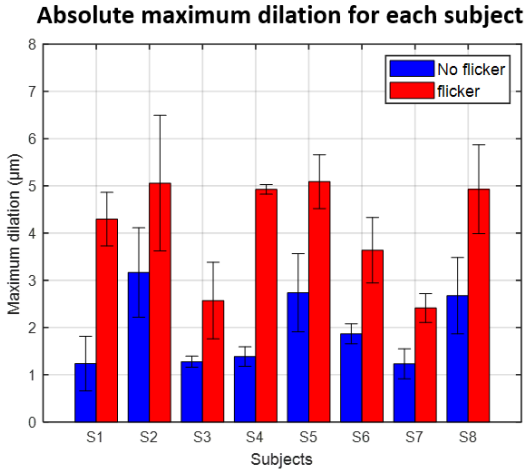

Fig 2 : Maximum dilation and latency for the 8 healthy subjects.

A) For each acquisition, the maximum dilation is defined as the maximum relative dilation of the moving average of the lumen diameter. The delay is defined as the duration between the beginning of the flicker and the time at which maximum dilation is reached. B) Maximum relative (%) dilation for each acquisition without flicker stimulation in blue and with flicker stimulation in red. C) Maximum absolute (µm) dilation for each acquisition without flicker stimulation in blue and with flicker stimulation in red.

Effect of Baseline Arterial lumen Diameter on Flicker Induced Vasodilation.

We investigated the effect of the size of the artery on the response to flicker stimulation. In Fig. 3A are represented the maximum dilation as a function of baseline arterial diameter. A clear trend could be seen where the smaller the artery, the higher the dilation.

To get more insight into the temporal aspect of the dilation depending on the size of the arteries, we separated the subjects into three groups depending on the baseline diameter of the imaged arteries. In Fig. 3B the average curves from the three groups are plotted. Notably, the maximum dilation is most pronounced in the d < 80 µm group and least pronounced in the d > 90 µm group. Moreover, directly after the onset of flicker, in the initial fast dilation phase, the three groups exhibit a drastically different dilation speed. As illustrated in Fig. 3B, the d < 80 µm group dilates at a rate of approximately 1% (0.7 µm) per second, the 80 < d < 90 µm group dilates at a rate of approximately 0.7% (0.55 µm) per second, and the 90 µm < d group dilates at a rate of 0.4% (0.4 µm) per second.

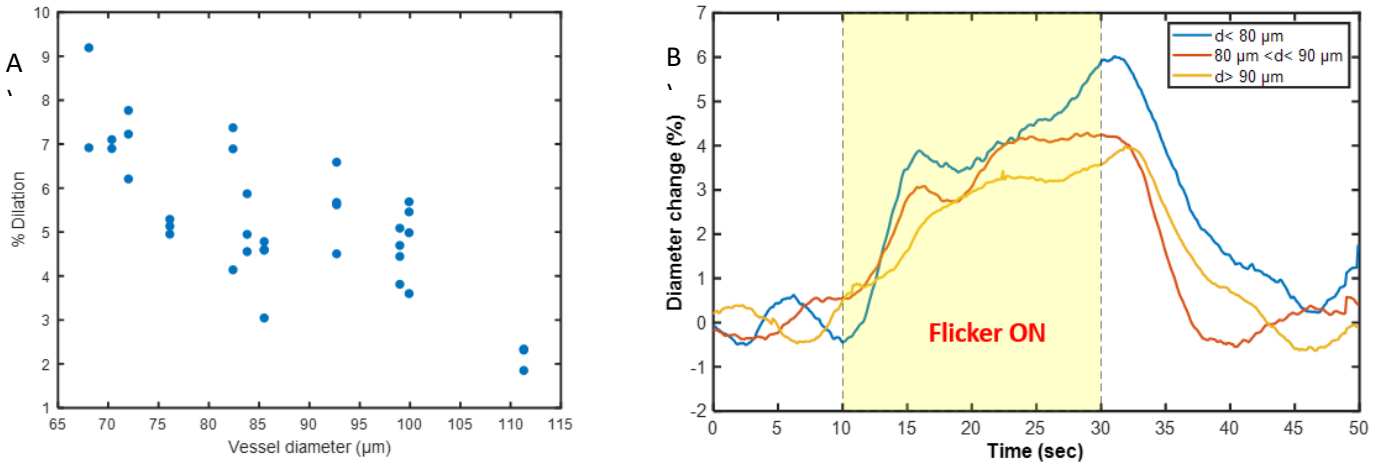

A) Maximum dilation for each flicker stimulation as a function of baseline lumen diameter B) Averaged graph of every flicker test grouped by baseline lumen diameter: blue represents diameters smaller than 80 µm, red represents diameters between 80 and 90 µm, and yellow represents diameters greater than 90 µm.

Studying the Effect of Flicker Duration on one Healthy Subject.

We used our system to study the effect of the duration of the flicker stimulation on flicker induced vasodilation. On the same subject, we conducted flicker test of increasingly longer stimulation times (0,2,5,10,20,40 and 60 seconds).

For each acquisition, the system imaged an artery upstream of the fovea for 10 seconds without stimulation followed by the flicker stimulation, followed by 20 seconds without stimulation. Three acquisitions were taken for each flicker stimulation duration and then averaged. The results from these acquisitions are presented in Fig. 4A.

For very short stimulation durations, although a significant increase in the vessel's diameter can be observed compared to without stimulation, the dilation is less pronounced than with the standard 20 seconds of flicker stimulation. As shown in Fig. 4A, a ~3% maximum dilation for 2 seconds of stimulation was obtained. Moreover, the maximum dilation is reached a few seconds after the end of the stimulation, whereas for a 20-second stimulation, the maximum dilation typically occurs close to the end of the flicker period, with an average delay of 20.5 seconds as shown in Fig. 2.

For very long stimulations, the artery does not dilate more than the maximum dilation reached for 20 seconds of stimulation, as can be seen in Fig. 4B. For 40 and 60 seconds of stimulation, the vessel's diameter reaches a plateau after ~20 seconds, which is reflected in the latency measured in Fig. 4C. For some of these long stimulations, the vessel's diameter starts to slightly decrease even before the end of the stimulation.

This study confirms that stimulation beyond 20 seconds is unnecessary, as this duration is sufficient to achieve maximum vasodilation. Interestingly, the study also found that very brief stimulations of just a few seconds can produce significant vasodilation. This could lead to more comfortable and faster flicker tests for patients.

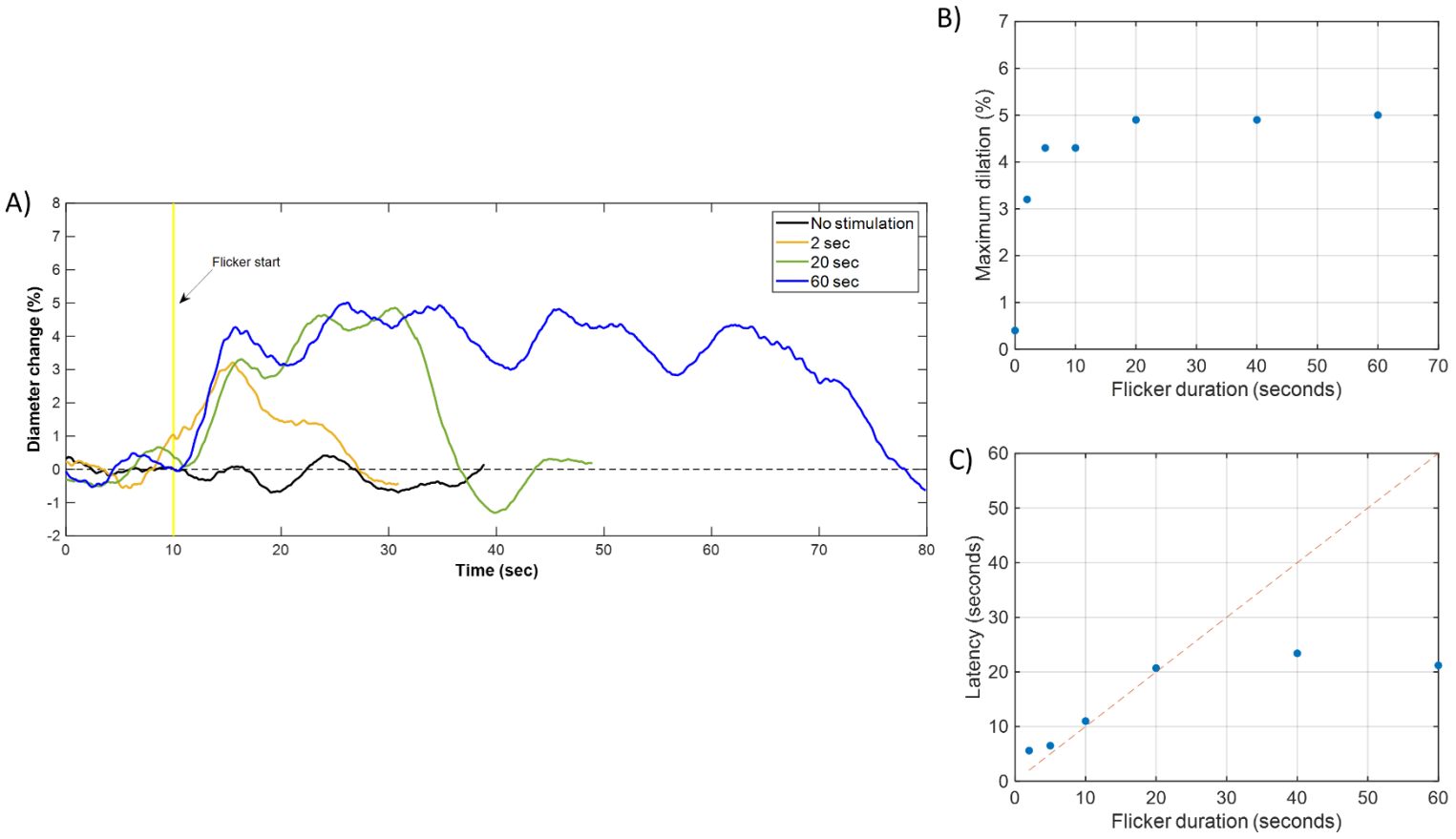

Figure 4: Measurement of lumen diameter response to varying durations of flicker stimulation.

(A) Average lumen diameter curves for different flicker durations, with flicker stimulation starting at t = 10 seconds. The three curves for each condition were averaged. For clarity, only flicker durations of 0, 2, 20, and 60 seconds are represented. (B) Plot showing the average maximum dilation across all flicker duration conditions. (C) Plot showing the average latency of dilation across all flicker duration conditions, the dashed line represents the x=y linear equation.

Using our Large FOV to Simultaneously Measure the Response of One Vein and two Arteries on One Healthy Subject.

We took advantage of our system's large FOV to measure the effect of flicker stimulation on three vessels simultaneously. On one subject, we selected an area of interest where two arteries and one vein could be imaged within a 4.5°x4.5° FOV.

This area was chosen because it contains two large arteries and one large vein. Additionally, the two arteries supply blood to distinct regions. As illustrated in Fig. 5A, artery 1 directly supplies the fovea, whereas artery 3 supplies the peripheral retina. The diameter of the three vessels was measured and the evolution in time of their lumen diameters are represented in Fig. 5.

We can observe that the vasomotion between the two arteries in Fig. 5.1 and 5.3 is mostly synchronized. This resemblance may come from their shared origin as daughter branches of the same artery. However, artery 1, which perfuses directly the fovea, exhibits a notable dilation of 6.2%, while artery 3, supplying the periphery, dilates only up to a maximum of 4.2%. With the ganglion cell layer being thicker near the fovea than it is at the periphery of the retina, this observation is in line with the known phenomenon of neurovascular coupling enhancing blood flow specifically to the activated regions in response to flicker stimulation [34].

However, artery 1 has also a smaller baseline diameter than artery 3. As we have seen in the previous section, small arteries tend to dilate more than larger ones. More investigation needs to be done to understand which effect is predominant.

The temporal evolution of the vein lumen diameter differs significantly from that of the two arteries. The increase in diameter following stimulation appears more gradual and exhibits larger fluctuations compared to the arteries. Additionally, a slight delay in the dilation of veins compared to arteries is observed, which aligns with the arteries' more active role in blood flow regulation, in contrast to the veins' more passive role.

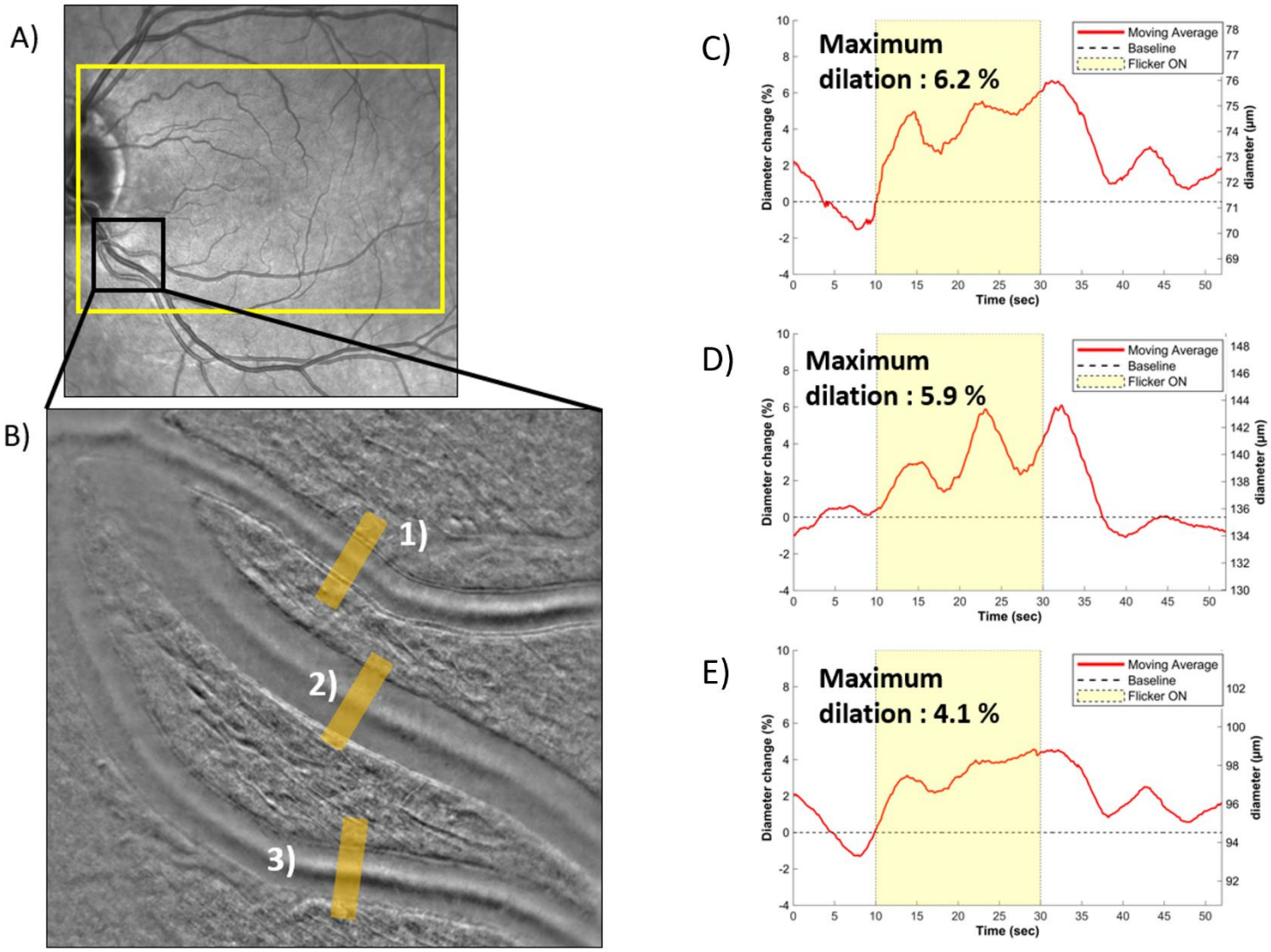

Figure 5: Effect of flicker stimulation on lumen diameter of retinal vessels within a large (4.5°x4.5°) field of view.

(A) Fundus photograph of the subject with the yellow rectangle indicating the stimulation area and the black square showing the imaged area. (B) Averaged image of the 4.5°x4.5° imaged FOV, identifying vessels: arteries (1 and 3) and vein (2). The area where the lumen diameter was measured is represented with an orange rectangle. (C,D,E) Evolution in time of the lumen diameter of vessels 1,2 and 3 respectively.

Material and Method:

Subjects.

Eight subjects, ranging in age from 24 to 33 y (S1 = 24, S2 = 25, S3 = 26, S4 = 25, S5 = 27, S6 = 27, S7 = 28 and S8 = 33 years old) and free of ocular disease, participated in the experiments. All subjects had a spherical equivalent refraction between 0 and −4.5 diopters. All had normal intraocular pressure (IOP), and appearance of optic disk and fundus, as determined by the 15-20 ophthalmology hospital (Paris, France). All procedures on the subjects adhered to the tenets of the Declaration of Helsinki.

Delivery of Flicker Stimulation.

A stimulation screen (Waveshare, China) was integrated into the imaging system. The screen provided a 25°x20° illumination region centered on the fovea. The screen was combined with the imaging system using a pellicle beam splitter. A programmable, stable fixation target was provided for the subject during all stimulus conditions. The flicker stimulation was generated and delivered using a custom Python software allowing the simultaneous start of the recording with the imaging system and the beginning of the flicker test protocol. The full-field flicker stimulus used in this experiment was green (530 nm, 40 nm FWHM) with a square-wave modulation of the entire field at 50 % duty cycle with a maximum illuminance of 7.3 lx and a minimum illuminance of 0 lux. These illuminance intensities and modulation rates were chosen to be similar to previous literature studying neurovascular coupling in the retina in order to induce high metabolic activity [33], [35], [36].

Imaging System.

The system named the Adaptive Optics – Confocal Rolling Slit Ophthalmoscope (AO-CRSO) was described previously by Krafft et al. [37]. It consists of a 2D camera based, non-confocal, split detection AO-line scanning ophthalmoscope. The light emitted from a SLED (Thorlabs) is projected in the retina into a line pattern of 10 µm width using a powell lens. The light backscattered by the retina is then detected using the rolling shutter of the detection camera (ORCA-Fusion, Hamamatsu). The rolling shutter and the galvanometer mirror of the illumination scan are synchronized via a custom Matlab (Mathworks, Natick, MA) software. To achieve phase contrast imaging of the vessel walls, a 10 µm offset between the illumination laser line and the exposed pixels of the rolling shutter is imposed. The exposure time of each line of pixel of the rolling shutter is chosen at 300 µs, thus giving an effective width of the rolling shutter of 50 µm in retinal space. Consecutive positive and negative offset images are alternated and subtracted to achieve split detection imaging, further increasing the phase contrast of images. This system allows high resolution (2 µm), high speed (100 Hz), phase contrast imaging on a large field of view (2.5°x4.5°) without image distortion. Because the line is scanned vertically with this technique. The scanning course of the galvanometric mirror can also be modified resulting in a tradeoff between frame rate and vertical field of view. Although the 2.5°x4.5° for 100 Hz is the configuration that we use the most 4.5°x4.5° for 50 Hz is also possible.

Experimental Design.

All imaging sequences were collected with the room lights off. The subject's eye was cyclopleged and dilated using tropicamide 0.5%. The eye and head were aligned with the imaging system using a chinrest mounted to a motorized XYZ translation stage. Correct imaging focus was realized by optimizing vessel walls contrast using the real-time displayed images. For each subject, an artery upstream of the fovea in the nasal region was selected using fundus camera image of the subject. The imaging region was chosen along the selected artery and at ~8° eccentricity. Once the imaging region was selected, three acquisitions of 40 seconds without stimulation were taken. Then three flicker tests, each consisting of 10 seconds of recording without stimulation, 20 seconds of flicker stimulation and 20 seconds without stimulation were taken. Between each flicker test, a one-minute break was included.

Recording by the imaging system was synchronized with the stimulation channel. The system acquired images continuously during the entirety of each 40-second baseline recording and during each 50-second flicker tests. The system provides phase contrast imaging at 100 Hz on a 2.5 x 4.5° FOV allowing visualization of 1.2 mm sections of horizontal blood vessels and making it possible to keep the vessel of interest inside the imaging field of view despite imperfect eye fixation which is unavoidable during 50 sec acquisitions.

Post Processing.

Images were first registered using a custom Matlab (Mathworks, Natick, MA) phase correlation algorithm [38]. Images were averaged in groups of 10 to enhance signal-to-noise ratio, thereby producing a sharp image of the blood vessels every 100 ms. This approach was employed to enhance signal-to-noise ratio while maintaining the capability to monitor blood vessel's fluctuation in diameter due to the cardiac cycle in all subjects.

Vessel Walls Detection.

From the registered and averaged images, a 30 µm segment of the vessel was chosen. For each averaged image, pixel lines perpendicular to the vessel's direction within the selected segment were averaged. These averaged lines, each representing the cross-sectional average of the vessel in the 30 µm segment, were plotted over time to produce an M-scan of the vessel (Fig. 1C, 1E). From the M-scan, the positions of the vessel's inner and outer wall were measured on each side. A MATLAB peak detection algorithm was used to determine their positions by identifying the two maxima and two minima in each pixel line of the M-scan corresponding to the tunica intima and the tunica externa of both sides of the vessel. The lumen diameter was defined as the distance between the two inner walls of the vessel. A parabolic fit was implemented to achieve a subpixel measurement of the lumen diameter with a precision of 0.1 µm.

Data Representation

To represent the measured diameter, both the raw measurements taken every 0.1 seconds and the moving average were represented. The moving average was chosen on a 3 second window to filter out the effect of the cardiac cycle. For the measurement of the maximum dilation (represented in Fig 2A), the moving average was chosen instead of the raw measurement, this was done to filter out the effect of the cardiac cycle on the lumen diameter which variations don't reflect the effect of neurovascular coupling on the vessel.

Conclusion:

We developed a high resolution, high frame rate, large field of view phase contrast imaging system and applied it to measure the effect of flicker light stimulation on large arteries and veins of healthy subjects. This system was employed to assess the effects of flicker stimulation on the diameter of large arteries and veins, in a cohort of eight subjects. The proposed method enabled reliable measurement of flicker-induced vasodilation with a spatial resolution of 100 nm and a temporal resolution of 100 ms. Additionally, the large field of view and distortion-free imaging provided by the system ensures high robustness, enabling continuous data acquisition for up to four minutes, with data loss occurring exclusively during subjects' blinks.

The complete temporal dynamics of retinal artery diameters were measured in eight healthy subjects, both with and without flicker stimulation. Our imaging system allowed simultaneous observation of the effects of the cardiac cycle, vasomotion, and flicker stimulation on the measured vessel diameter. During flicker stimulation, a significant maximum dilation of 5.2% ± 1.6% (4.4 µm ± 1.3 µm) was observed across all subjects, compared to a maximum dilation of 2.5% ± 1% (2.1 µm ± 0.9 µm) without stimulation. Continuous high-speed measurements revealed the modulation of retinal vessel diameter by both the cardiac cycle and vasomotion, emphasizing the necessity of capturing the full temporal profile of dilation to study neurovascular coupling effectively, rather than relying solely on pre- and post-stimulation diameter measurements, as it is commonly done in retinal neurovascular studies.

Furthermore, various characteristics of the flicker-induced vasodilation response were investigated. Across subjects, a correlation was observed between flicker-induced vasodilation and arterial size, with smaller arteries demonstrating greater maximum dilation compared to larger arteries. The effect of flicker stimulation duration was also evaluated in one subject. For short stimulation durations (<20 seconds), a significant increase in vessel's diameter was noted, although the response was less pronounced compared to the standard 20-second stimulation. Conversely, for stimulation durations longer than 20 seconds, no further dilation was observed beyond the maximum achieved with 20 seconds of stimulation.

The system's large field of view was also used to image two large arteries and one large vein in a single subject, allowing for the simultaneous assessment of vasomotion and flicker-induced vasodilation in vessels perfusing different retinal regions. Interestingly, of the two arteries examined, the one perfusing the fovea exhibited a greater maximum dilation compared to the artery supplying the retinal periphery, suggesting as expected that neurovascular coupling preferentially enhances blood flow to regions of the retina with a higher density of activated neurons.

While additional acquisitions on multiple subjects would be required to establish these characteristics of the flicker induced response, these findings pave the way for further exploration and underscore the versatility of the proposed method.

Supplementary Information

Examples of Acquisitions with and without Stimulation on the 8 Subjects :

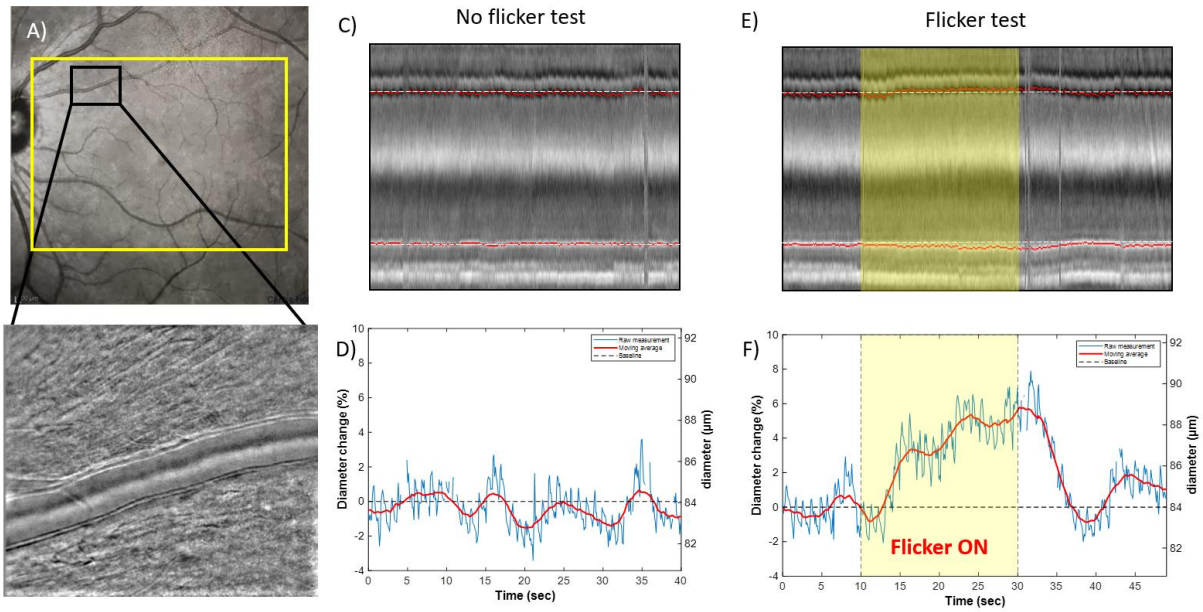

S1 : ILO

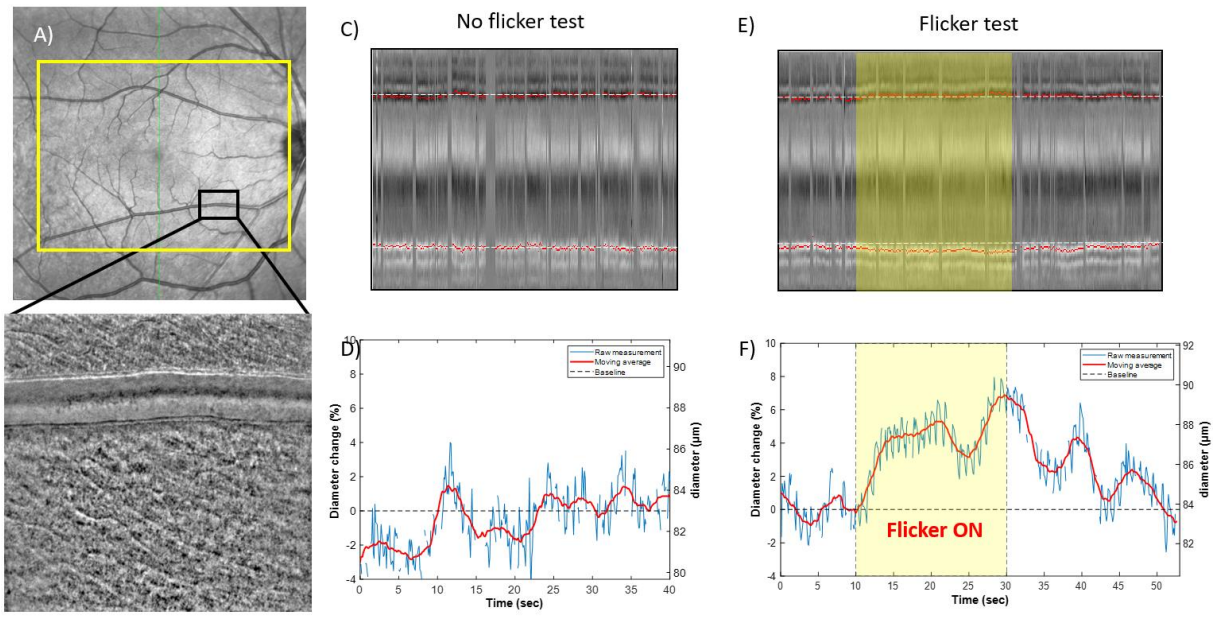

S2 : JMU

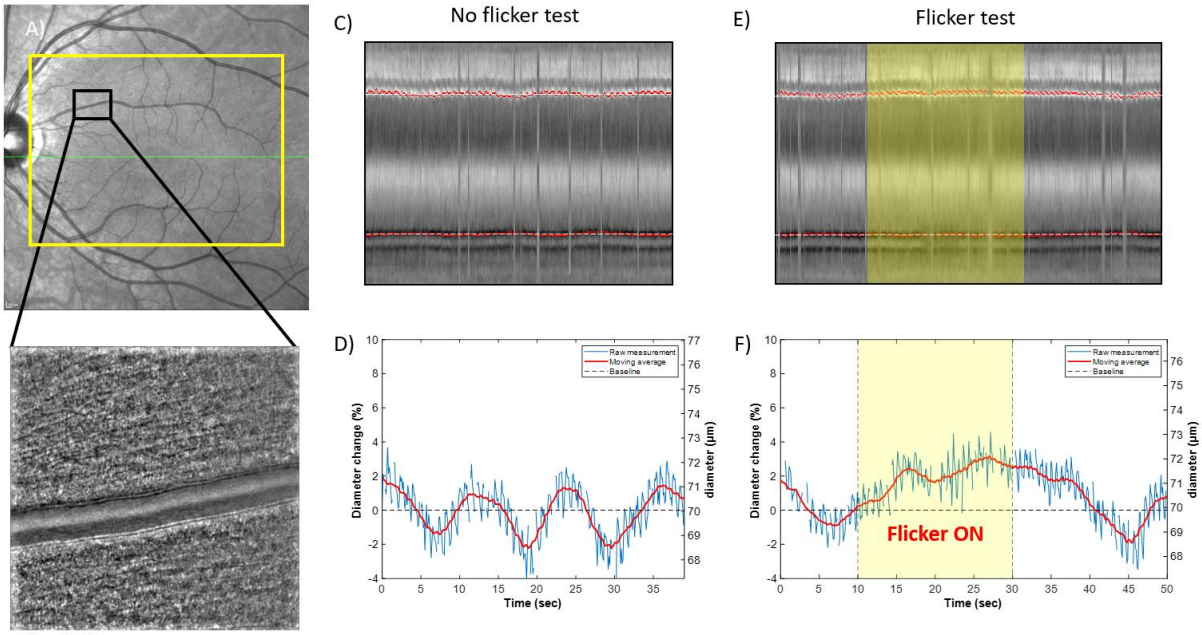
A)
C)
No flicker test
E)
Flicker test
D)
F)
Raw measurement
Moving average
Baseline
Diameter change (%)
diameter (µm)
Time (sec)
Flicker ON

S3 : OMA

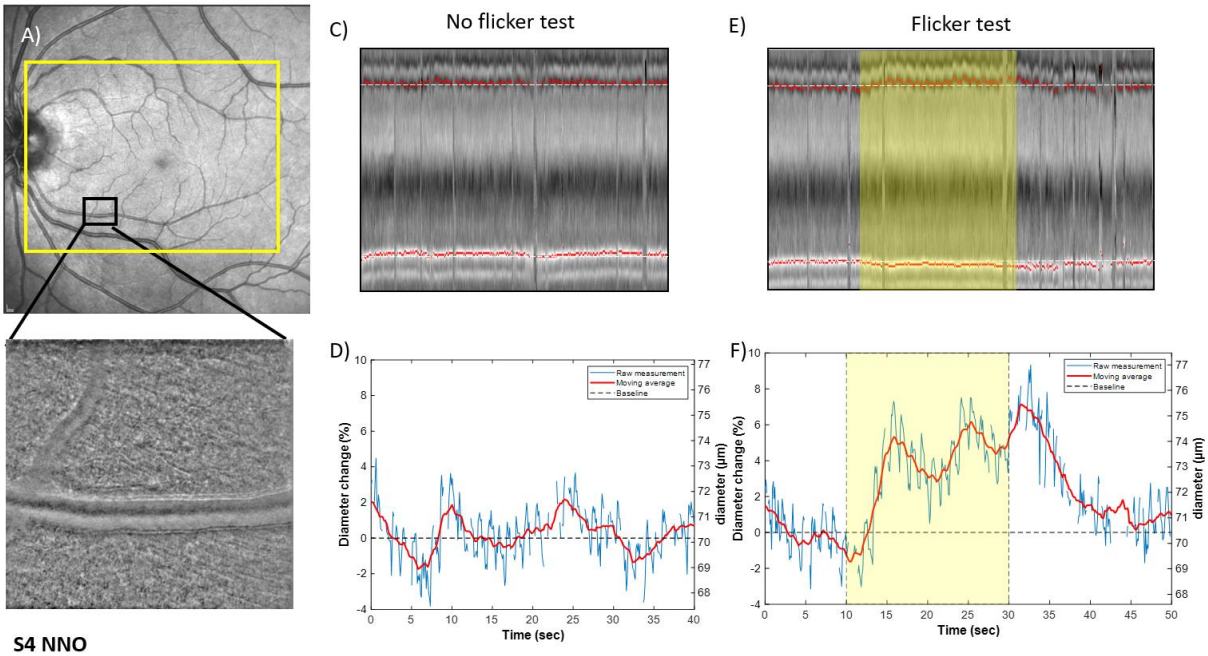
A)
C)
No flicker test
E)
Flicker test
D)
F)
Raw measurement
Moving average
Baseline
Diameter change (%)
diameter (µm)
Time (sec)

S4 NNO

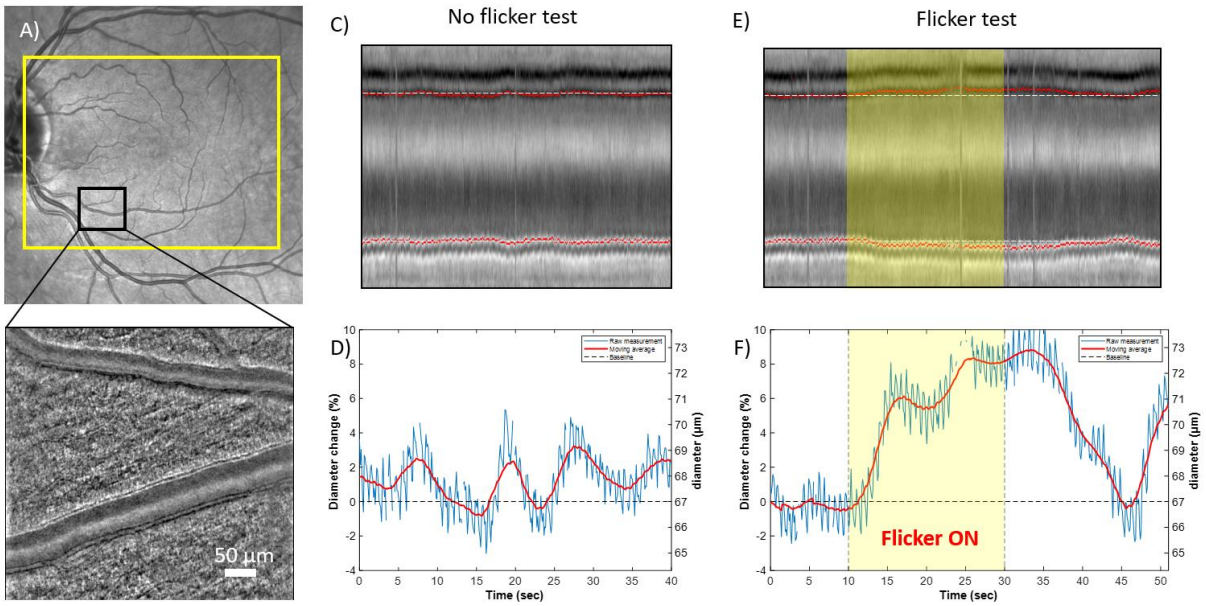
A)
50 µm
C)
No flicker test
D)
Raw measurement
Moving average
Baseline
Diameter change (%)
diameter (µm)
Time (sec)
E)
Flicker test
F)
Flicker ON

S5 : EGO

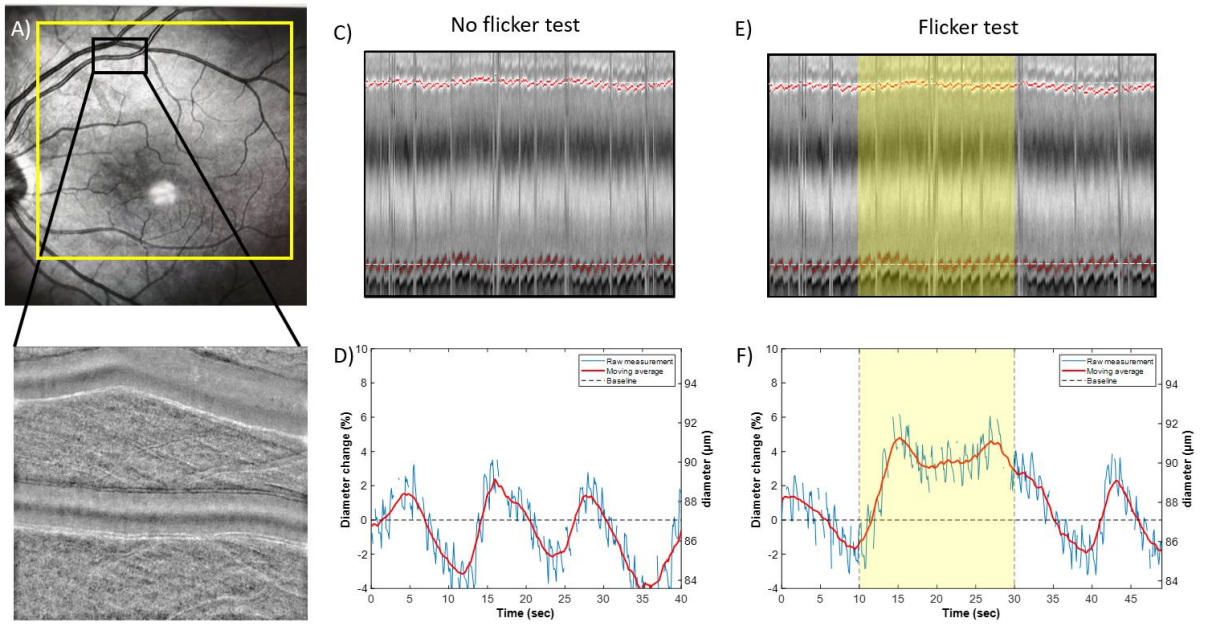
A)
C)
No flicker test
D)
Raw measurement
Moving average
Baseline
Diameter change (%)
diameter (µm)
Time (sec)
E)
Flicker test
F)

S6 : PSE

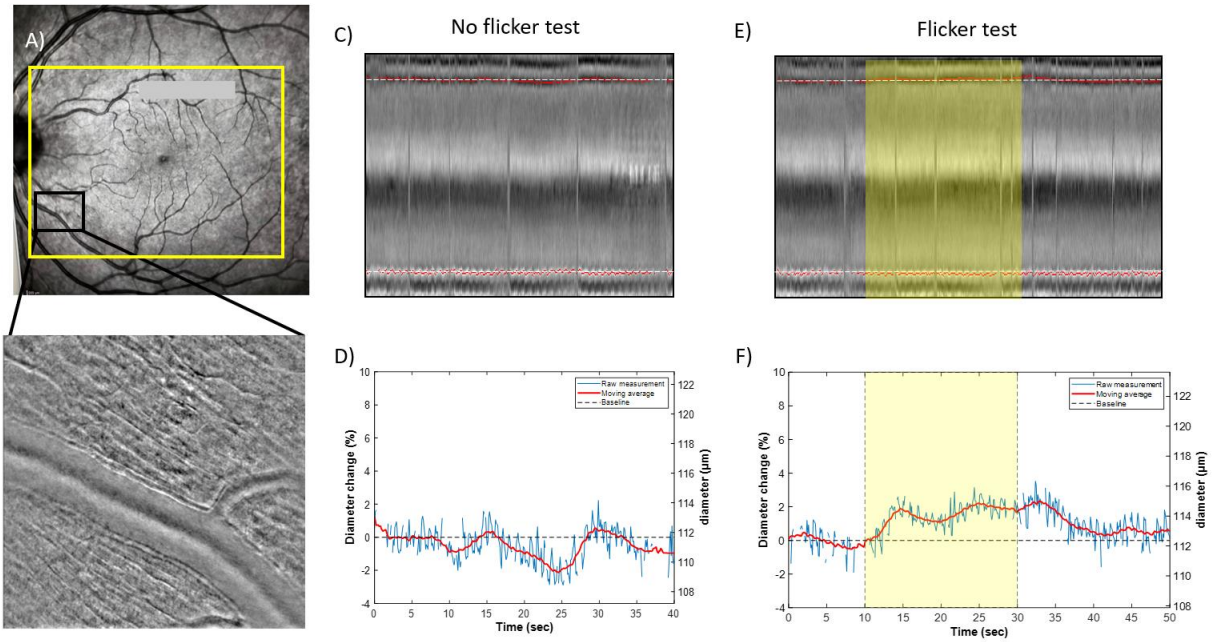
A)
C)
No flicker test
E)
Flicker test
D)
F)
Raw measurement
Moving average
Baseline
Diameter change (%)
diameter (µm)
Time (sec)

S7:LKR

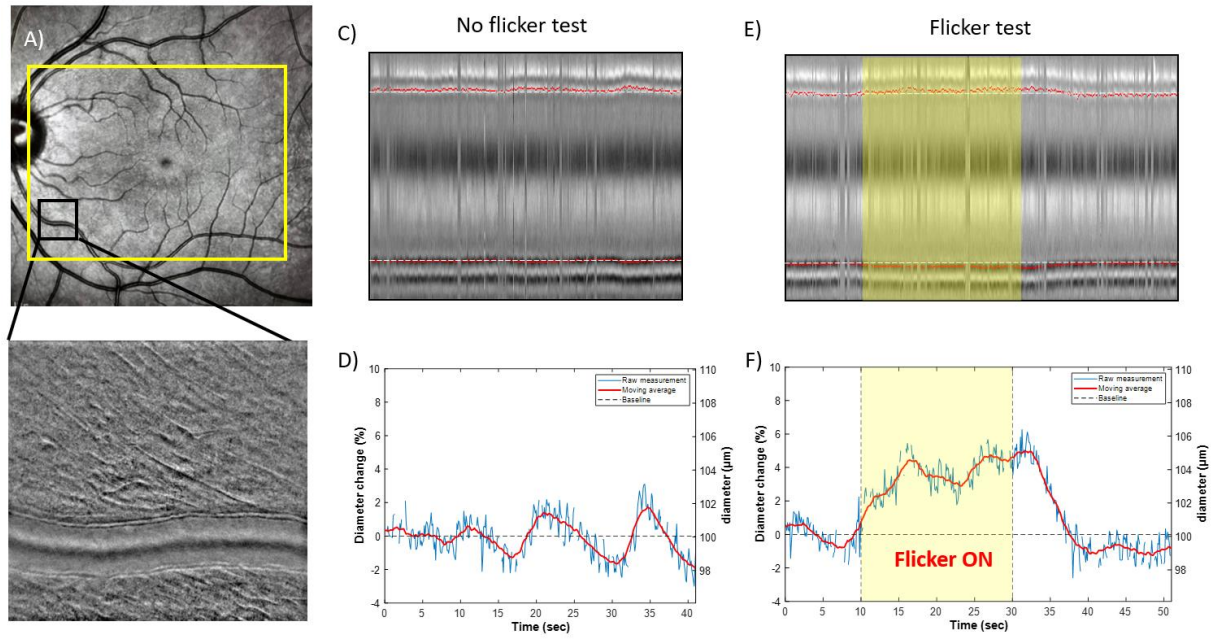
A)
C)
No flicker test
E)
Flicker test
D)
F)
Raw measurement
Moving average
Baseline
Diameter change (%)
diameter (µm)
Time (sec)
Flicker ON

S8 : JGR

Bibliography

[1] C. S. Roy and C. S. Sherrington, “On the Regulation of the Blood-supply of the Brain,” *J. Physiol.*, vol. 11, no. 1–2, pp. 85-158.17, Jan. 1890.

[2] M. R. Metea and E. A. Newman, “Glial Cells Dilate and Constrict Blood Vessels: A Mechanism of Neurovascular Coupling,” *J. Neurosci.*, vol. 26, no. 11, pp. 2862–2870, Mar. 2006, doi: 10.1523/JNEUROSCI.4048-05.2006.

[3] P. G. Haydon and G. Carmignoto, “Astrocyte control of synaptic transmission and neurovascular coupling,” *Physiol. Rev.*, vol. 86, no. 3, pp. 1009–1031, Jul. 2006, doi: 10.1152/physrev.00049.2005.

[4] C. Iadecola, “The Neurovascular Unit Coming of Age: A Journey through Neurovascular Coupling in Health and Disease,” *Neuron*, vol. 96, no. 1, pp. 17–42, Sep. 2017, doi: 10.1016/j.neuron.2017.07.030.

[5] L. K. Wareham and D. J. Calkins, “The Neurovascular Unit in Glaucomatous Neurodegeneration,” *Front. Cell Dev. Biol.*, vol. 8, p. 452, Jun. 2020, doi: 10.3389/fcell.2020.00452.

[6] G. Garhöfer, C. Zawinka, H. Resch, P. Kothy, L. Schmetterer, and G. T. Dorner, “Reduced response of retinal vessel diameters to flicker stimulation in patients with diabetes,” *Br. J. Ophthalmol.*, vol. 88, no. 7, pp. 887–891, Jul. 2004, doi: 10.1136/bjo.2003.033548.

[7] A. Lecleire-Collet *et al.*, “Evaluation of Retinal Function and Flicker Light-Induced Retinal Vascular Response in Normotensive Patients with Diabetes without Retinopathy,” *Invest. Ophthalmol. Vis. Sci.*, vol. 52, no. 6, pp. 2861–2867, May 2011, doi: 10.1167/iovs.10-5960.

[8] C. W. Leffler, D. W. Busija, R. Mirro, W. M. Armstead, and D. G. Beasley, “Effects of ischemia on brain blood flow and oxygen consumption of newborn pigs,” *Am. J. Physiol.-Heart Circ. Physiol.*, vol. 257, no. 6, pp. H1917–H1926, Dec. 1989, doi: 10.1152/ajpheart.1989.257.6.H1917.

[9] H. Girouard and C. Iadecola, “Neurovascular coupling in the normal brain and in hypertension, stroke, and Alzheimer disease,” *J. Appl. Physiol.*, vol. 100, no. 1, pp. 328–335, Jan. 2006, doi: 10.1152/japplphysiol.00966.2005.

[10] D. Attwell, A. M. Buchan, S. Charpak, M. Lauritzen, B. A. MacVicar, and E. A. Newman, “Glial and neuronal control of brain blood flow,” *Nature*, vol. 468, no. 7321, pp. 232–243, Nov. 2010, doi: 10.1038/nature09613.

[11] E. A. Newman, “Functional hyperemia and mechanisms of neurovascular coupling in the retinal vasculature,” *J. Cereb. Blood Flow Metab. Off. J. Int. Soc. Cereb. Blood Flow Metab.*, vol. 33, no. 11, pp. 1685–1695, Nov. 2013, doi: 10.1038/jcbfm.2013.145.

[12] J. R. Cameron *et al.*, “Lateral thinking – Interocular symmetry and asymmetry in neurovascular patterning, in health and disease,” *Prog. Retin. Eye Res.*, vol. 59, pp. 131–157, Jul. 2017, doi: 10.1016/j.preteyeres.2017.04.003.

[13] D. G. Cogan and T. Kuwabara, “Comparison of retinal and cerebral vasculature in trypsin digest preparations.,” *Br. J. Ophthalmol.*, vol. 68, no. 1, pp. 10–12, Jan. 1984, doi: 10.1136/bjo.68.1.10.

[14] A. H. Kashani *et al.*, “Past, present and future role of retinal imaging in neurodegenerative disease,” *Prog. Retin. Eye Res.*, vol. 83, p. 100938, Jul. 2021, doi: 10.1016/j.preteyeres.2020.100938.

[15] L. Petersen, C. Aalkjaer, and T. Bek, “Vasomotion in Retinal Arterioles Is Modified by Exercise and Flicker Stimulation,” *Invest. Ophthalmol. Vis. Sci.*, vol. 63, no. 13, p. 7, Dec. 2022, doi: 10.1167/iovs.63.13.7.

[16] T. Bek, P. Jeppesen, and J. K. Kanters, “Spontaneous High Frequency Diameter Oscillations of Larger Retinal Arterioles Are Reduced in Type 2 Diabetes Mellitus,” *Invest. Ophthalmol. Vis. Sci.*, vol. 54, no. 1, pp. 636–640, Jan. 2013, doi: 10.1167/iovs.12-11182.

[17] L. Zhao, S. Liu, Y. Liu, and H. Tang, “Vasomotion heterogeneity and spectral characteristics in diabetic and hypertensive patients,” *Microvasc. Res.*, vol. 151, p. 104620, Jan. 2024, doi: 10.1016/j.mvr.2023.104620.

[18] G. Garhöfer, C. Zawinka, K.-H. Huemer, L. Schmetterer, and G. T. Dorner, “Flicker Light–Induced Vasodilatation in the Human Retina: Effect of Lactate and Changes in Mean Arterial Pressure,” *Invest. Ophthalmol. Vis. Sci.*, vol. 44, no. 12, pp. 5309–5314, Dec. 2003, doi: 10.1167/iovs.03-0587.

[19] T. T. Nguyen *et al.*, “Correlation of light-flicker-induced retinal vasodilation and retinal vascular caliber measurements in diabetes,” *Invest. Ophthalmol. Vis. Sci.*, vol. 50, no. 12, pp. 5609–5613, Dec. 2009, doi: 10.1167/iovs.09-3442.
[20] R. Heitmar and R. J. Summers, “The Time Course of Changes in Retinal Vessel Diameter in Response to Differing Durations of Flicker Light Provocation,” *Invest. Ophthalmol. Vis. Sci.*, vol. 56, no. 12, pp. 7581–7588, Nov. 2015, doi: 10.1167/iovs.15-17089.
[21] K. Polak *et al.*, “Evaluation of the Zeiss retinal vessel analyser,” *Br. J. Ophthalmol.*, vol. 84, no. 11, pp. 1285–1290, Nov. 2000, doi: 10.1136/bjo.84.11.1285.
[22] G. Garhofer *et al.*, “Use of the retinal vessel analyzer in ocular blood flow research,” *Acta Ophthalmol. (Copenh.)*, vol. 88, no. 7, pp. 717–722, Nov. 2010, doi: 10.1111/j.1755-3768.2009.01587.x.
[23] J. M. Schmitt, S. H. Xiang, and K. M. Yung, “Speckle in optical coherence tomography,” *J. Biomed. Opt.*, vol. 4, no. 1, pp. 95–105, Jan. 1999, doi: 10.1117/1.429925.
[24] D. Goldenberg, J. Shahar, A. Loewenstein, and M. Goldstein, “Diameters of retinal blood vessels in a healthy cohort as measured by spectral domain optical coherence tomography,” *Retina Phila. Pa*, vol. 33, no. 9, pp. 1888–1894, Oct. 2013, doi: 10.1097/IAE.0b013e31829477f2.
[25] T. Y. P. Chui, D. A. VanNasdale, and S. A. Burns, “The use of forward scatter to improve retinal vascular imaging with an adaptive optics scanning laser ophthalmoscope,” *Biomed. Opt. Express*, vol. 3, no. 10, pp. 2537–2549, Oct. 2012, doi: 10.1364/BOE.3.002537.
[26] T. Y. P. Chui, T. J. Gast, and S. A. Burns, “Imaging of Vascular Wall Fine Structure in the Human Retina Using Adaptive Optics Scanning Laser Ophthalmoscopy,” *Invest. Ophthalmol. Vis. Sci.*, vol. 54, no. 10, pp. 7115–7124, Oct. 2013, doi: 10.1167/iovs.13-13027.
[27] J. Liang, D. R. Williams, and D. T. Miller, “Supernormal vision and high-resolution retinal imaging through adaptive optics,” *JOSA A*, vol. 14, no. 11, pp. 2884–2892, Nov. 1997, doi: 10.1364/JOSAA.14.002884.
[28] A. Duan, P. A. Bedggood, B. V. Bui, and A. B. Metha, “Evidence of Flicker-Induced Functional Hyperaemia in the Smallest Vessels of the Human Retinal Blood Supply,” *PLOS ONE*, vol. 11, no. 9, p. e0162621, Sep. 2016, doi: 10.1371/journal.pone.0162621.
[29] A. Roorda, F. Romero-Borja, W. J. D. Iii, H. Queener, T. J. Hebert, and M. C. W. Campbell, “Adaptive optics scanning laser ophthalmoscopy,” *Opt. Express*, vol. 10, no. 9, pp. 405–412, May 2002, doi: 10.1364/OE.10.000405.
[30] Y. N. Sulai, D. Scoles, Z. Harvey, and A. Dubra, “Visualization of retinal vascular structure and perfusion with a nonconfocal adaptive optics scanning light ophthalmoscope,” *JOSA A*, vol. 31, no. 3, pp. 569–579, Mar. 2014, doi: 10.1364/JOSAA.31.000569.
[31] R. L. Warner *et al.*, “Full-field flicker evoked changes in parafoveal retinal blood flow,” *Sci. Rep.*, vol. 10, no. 1, p. 16051, Sep. 2020, doi: 10.1038/s41598-020-73032-0.
[32] C. A. Curcio and K. A. Allen, “Topography of ganglion cells in human retina,” *J. Comp. Neurol.*, vol. 300, no. 1, pp. 5–25, Oct. 1990, doi: 10.1002/cne.903000103.
[33] C. E. Riva, E. Logean, and B. Falsini, “Visually evoked hemodynamical response and assessment of neurovascular coupling in the optic nerve and retina,” *Prog. Retin. Eye Res.*, vol. 24, no. 2, pp. 183–215, Mar. 2005, doi: 10.1016/j.preteyeres.2004.07.002.
[34] Z. Zhong, G. Huang, T. Y. P. Chui, B. L. Petrig, and S. A. Burns, “Local flicker stimulation evokes local retinal blood velocity changes,” *J. Vis.*, vol. 12, no. 6, p. 3, Jun. 2012, doi: 10.1167/12.6.3.
[35] C. E. Riva, E. Logean, and B. Falsini, “Temporal dynamics and magnitude of the blood flow response at the optic disk in normal subjects during functional retinal flicker-stimulation,” *Neurosci. Lett.*, vol. 356, no. 2, pp. 75–78, Feb. 2004, doi: 10.1016/j.neulet.2003.08.069.
[36] K. Polak, L. Schmetterer, and C. E. Riva, “Influence of flicker frequency on flicker-induced changes of retinal vessel diameter,” *Invest. Ophthalmol. Vis. Sci.*, vol. 43, no. 8, pp. 2721–2726, Aug. 2002.
[37] L. Krafft *et al.*, “High-contrast and high-speed multimodal imaging platform: the adaptive optics-confocal rolling slit ophthalmoscope (AO-CRSO),” in *Ophthalmic Technologies XXXIV*, SPIE, Mar. 2024, pp. 9–24. doi: 10.1117/12.3001609.
[38] P. Mece, A. Chen, C. Petit, L. Mugnier, M. Paques, and S. Meimon, “Real-time optical stabilization of retinal motion at micrometer precision using Adaptive Optics Flood-Illumination Ophthalmsocope,” Dec. 28, 2023, *Optica Open*. doi: 10.1364/opticaopen.24907464.v1.

5.2 Supplementary investigation of neurovascular coupling

5.2.1 Cumulative effect

We investigated if repeated exposure to flicker tests, would result in a different response compared to a single exposure. To test this hypothesis, we conducted an experiment following the same procedure detailed in the previous section (5.1). However, instead of a single 20 seconds flicker test, we applied a sequence of five stimulations, each lasting 20 seconds, consecutively. Due to the time-consuming nature, and the potential discomfort for the subjects of this extended protocol ,we limited this experiment to only two participants. The results from these two acquisitions can be seen in figure 5.1 and figure 5.2.

For subject one in 5.1, no influence of consecutive flicker was noticed: the maximum dilation reached at the fifth stimulation was identical to that observed at the first stimulation. For subject 2 in 5.2, the amplitude of the modulation of the vessel diameter (due to vasomotion) seemed to increase after the second stimulation but no cumulative effect was observed. These preliminary results show no evidence of cumulative effect. However, we only collected data on two subjects and more investigation would be required to further understand the effect of repeated exposure to flicker tests.

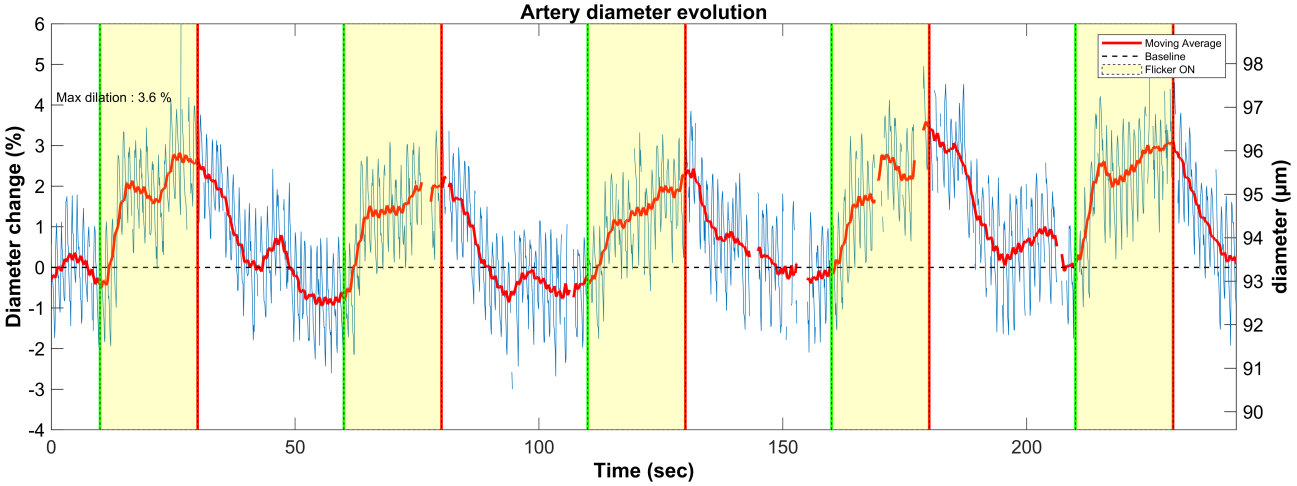

Figure 5.1: Cumulative flicker effect study using five consecutive flickers of 20s and spaced by 30s without flickering for subject 1.

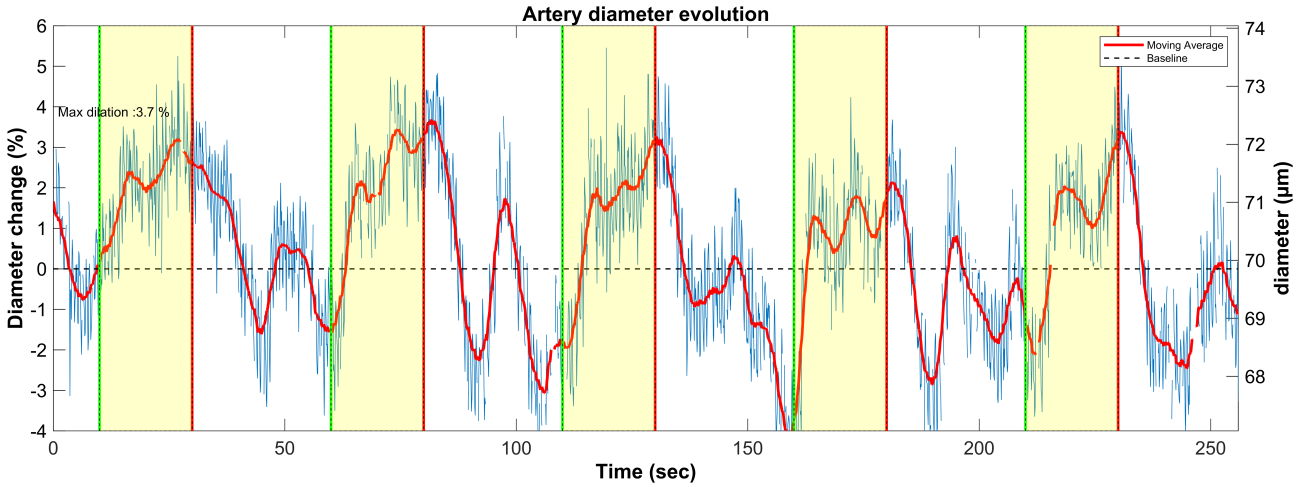

Figure 5.2: Cumulative flicker effect study using five consecutive flickers of 20s and spaced by 30s without flickering for subject 2.

5.2.2 "Placebo" flicker

During each flicker stimulation, a vocal countdown is provided before the start of the stimulation. This ensures that the subject is not startled by the onset of the stimulation and helps maintain good fixation and a stable position on the chinrest, which is crucial for image quality. We aimed to test whether the subject's awareness of the incoming stimulation influenced the vasodilatory response.

We called this test the "placebo flicker", the results on one subject are depicted in figure 5.3: In this experiment, five short flicker stimulations (only 5 seconds of flicker, with the same flicker characteristics as described in section 5.1) were administered successively. A vocal countdown was given before each stimulation. However, during the third and fifth stimulations, a countdown was provided, but no actual stimulation was delivered. The subject was not aware of which of the 5 stimulations were "fake". This approach aimed at assessing the impact of anticipation and the effect of the countdown on the observed response.

As expected, the subject's artery dilates during each of the three real stimulations. A hint of a very small dilation is observed during the first fake stimulation, which could easily be attributed to vasomotion. No dilation is observed during the second fake stimulation. Although this test was conducted on only one subject, it confirms that the observed dilation was indeed caused by the flicker stimulation and was not influenced by the subject's awareness of the incoming stimulation.

Another interesting takeaway from this experiment which was also highlighted in the article 5.1 is the fact that short flicker stimulation much shorter than 20 seconds, can result in an already significant dilation of arteries. In this case, stimulating with a flicker duration of 5 seconds resulted in a maximum dilation of 3.3%.

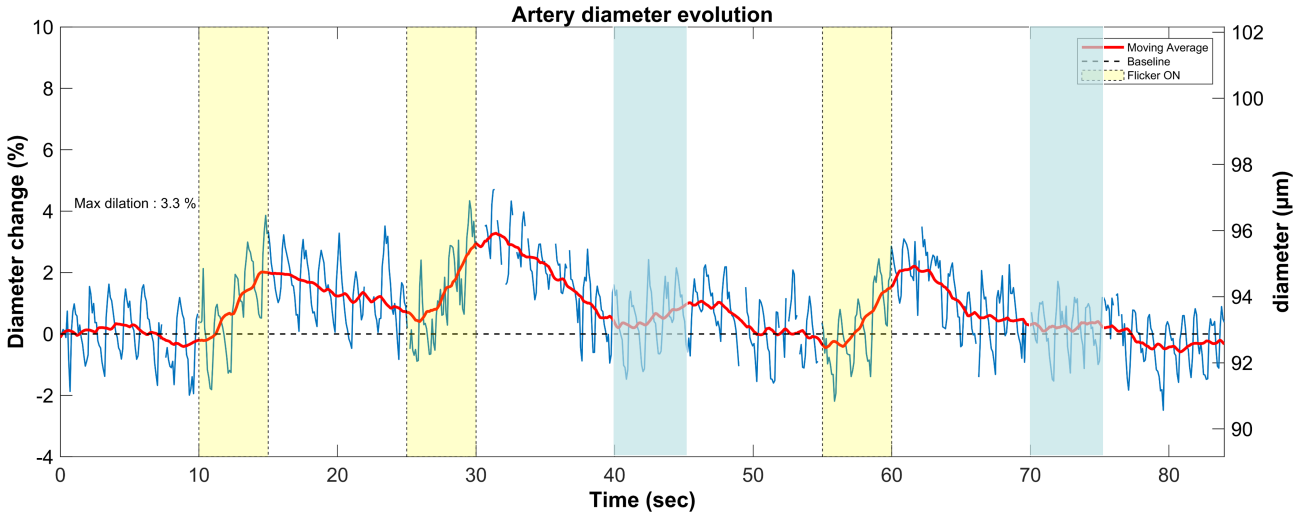

Figure 5.3: "Placebo" flicker test. The yellow bars represent real exposure to flicker stimulation while the grey bars represent "fake" ones where no stimulation is delivered but the subject expected a flicker stimulation. A vocal countdown was given before each real or fake stimulation.

5.2.3 Effect of flicker frequency

We investigated the effect of varying the frequency of flicker stimulation on arterial response. One subject underwent three acquisitions for each flicker frequency condition, with the frequencies tested being 30, 12.5, 5, 2, and 0.5 Hz. For each condition, the three acquisitions were averaged. These averaged curves are presented in Figure 5.4.

Unfortunately, the quality of the data from this session was compromised. The AO spot was positioned directly on the artery which caused inconsistent system focus and significant data loss. Despite these limitations, we were able to observe the overall effect of varying flicker frequencies on arterial response.

Interestingly, flicker stimulation induced significant vasodilation in the patient's artery at all tested frequencies. This was expected to some extent from the literature, where Polak [14] has shown the vasodilation of retinal arteries was observed in response to short wavelength flicker with frequencies between 2 and 64 Hz. However, even with a flicker frequency as low as 0.5 Hz, a smaller but significant vasodilation was observed. (see 5.4)

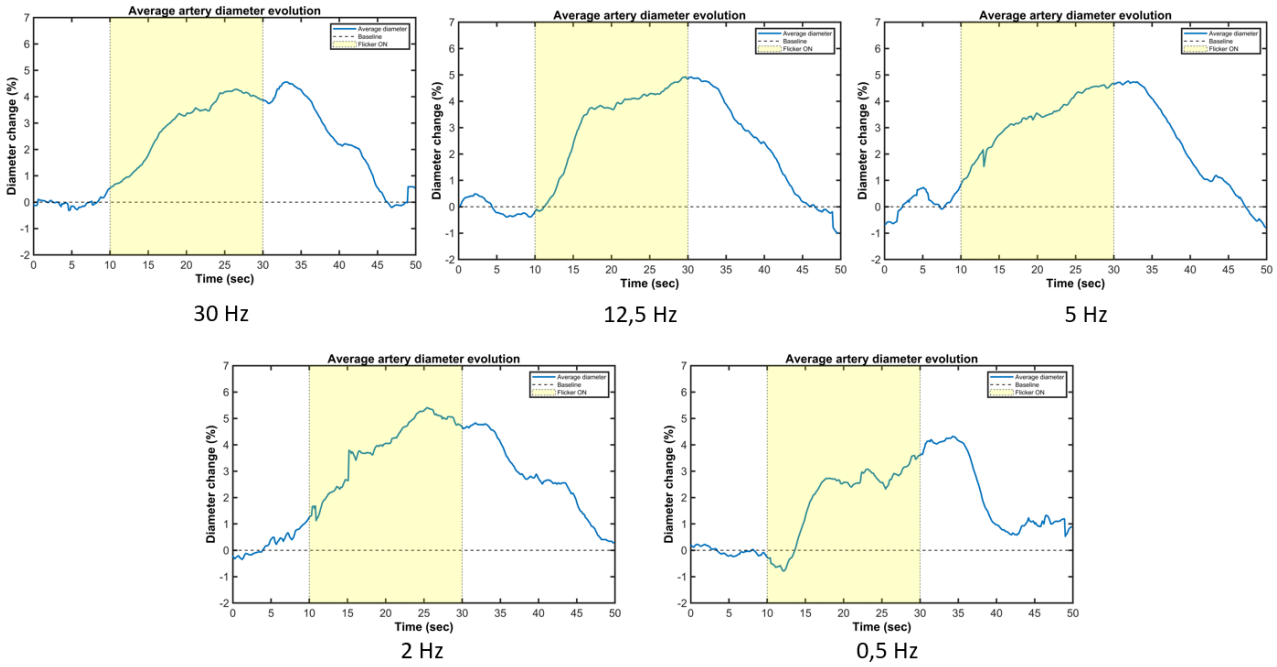

Figure 5.4: Flicker test of varying flicker frequency on one subject.

5.2.4 Variability in vessel dilation observed at different locations

The method I developed during my PhD thesis allows for the generation of phase contrast images over a large field of view and at a high framerate. This capability enables precise measurement of blood vessel diameters at multiple locations within the same vessel on a single image. Leveraging this technique, we investigated whether the propagation of flicker-induced vasodilation could be tracked by measuring the vessel diameter of the same artery at three different locations inside the field of view of the system.

In a typical acquisition of a flicker test from one of the subjects from the healthy subjects cohort, the same method as described in the previous section 5.1 was used to measure the lumen diameter of an artery at three distinct locations of the vessel. These locations were chosen to be as far apart from each other as possible (while keeping a well contrasted wall), as illustrated in figures 5.5. The distance between each location was approximately 2° (600 µm). The data used for this investigation was one of the flicker test from the previous section 5.1. However, the post processing pipeline was slightly modified in a way that instead of averaging the recorded images by groups of 10, the images were averaged by groups of 4 to increase temporal resolution. This was done to increase the temporal resolution in order to increase our chance of seeing a propagation of the response.

In figure 5.6, the three curves corresponding to the three locations are represented and on figure 5.7 the three moving average plots were superposed on the same figure. The first observation that can be made is that the amplitude of the dilation is not the same on the three locations.

The measured dilation at three distinct locations along the vessel exhibits significant differences, as illustrated in figure 5.7. A 7% maximum dilation can be measured for the two sections of the vessel in the middle of the image and on the temporal side of the image whereas only a 5% maximum dilation can be measured for the section on the nasal side of the imaged vessel.

These findings suggest that flicker-induced dilation of the vessel is non-uniform, with some sections of the vessel exhibiting greater dilation than others. One possible explanation for this phenomenon is the baseline size of the artery, as discussed in the previously presented article 5.1. Indeed, the nasal side of the imaged artery is wider than the other two sections which may explain why it shows lower dilation.

Regarding the propagation of neurovascular coupling, no obvious delay between the three curves can be observed on figure 5.7. The lumen diameter of the imaged artery measured on the temporal side (represented in blue in figure 5.7) seems to rise before the nasal side (represented in green in figure 5.7) which would indicate a propagation of the vasodilation from the fovea towards the optic disk. However if we look at the maximum dilation (at t=32 seconds approximately) we notice that no delay between the three curves can be observed. Overall, these results are quite inconclusive and more investigation is required. One issue with this experiment is the fact that we are using a wide field flicker, this means that the region around the imaged artery is stimulated, therefore the observed dilation might be due to local effect and not to a backward propagation of the vessel dilation. An improved protocol for investigating the propagation of flicker induced vasodilation would be to only stimulate near the fovea.

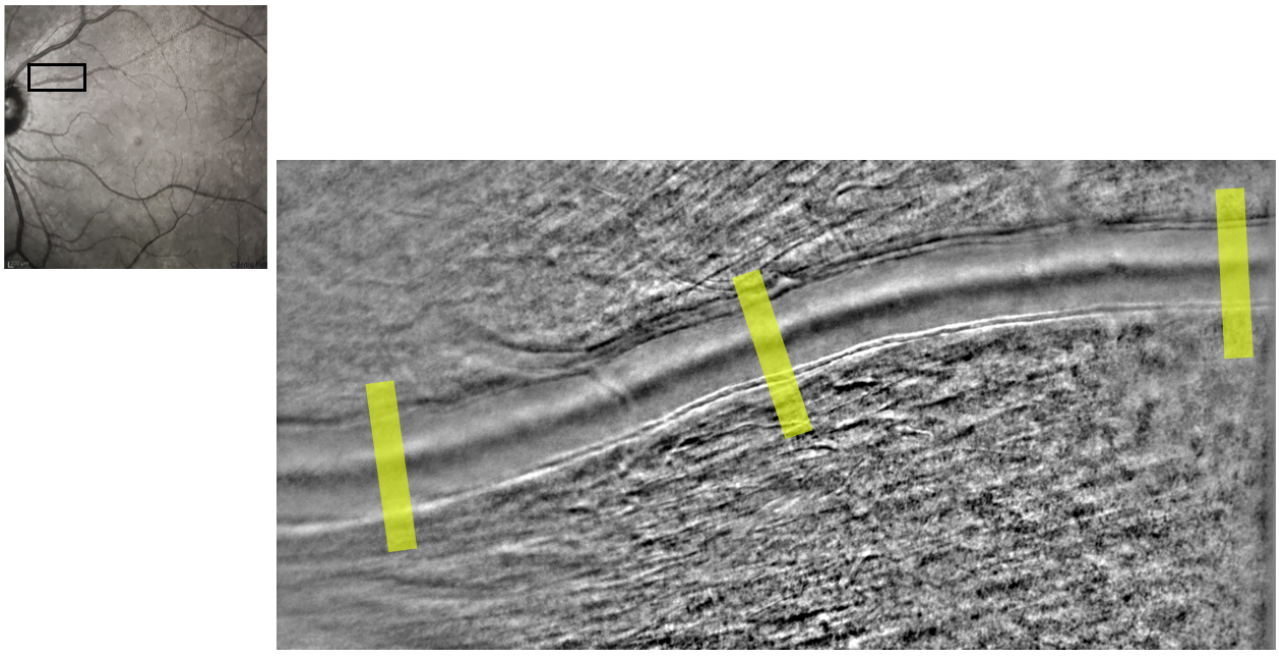

Figure 5.5: Image of the artery that was used to study the dilation of the vessels at three different locations. The three yellow rectangles indicate the three locations where the lumen diameter was measured.

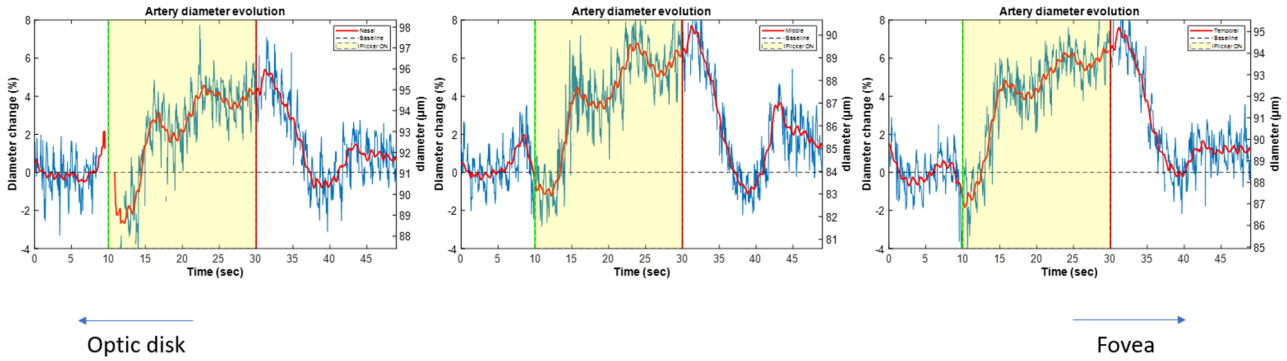

Figure 5.6: Measured lumen diameter of the artery at each location. The three locations are represented with yellow rectangles on figure 5.5.

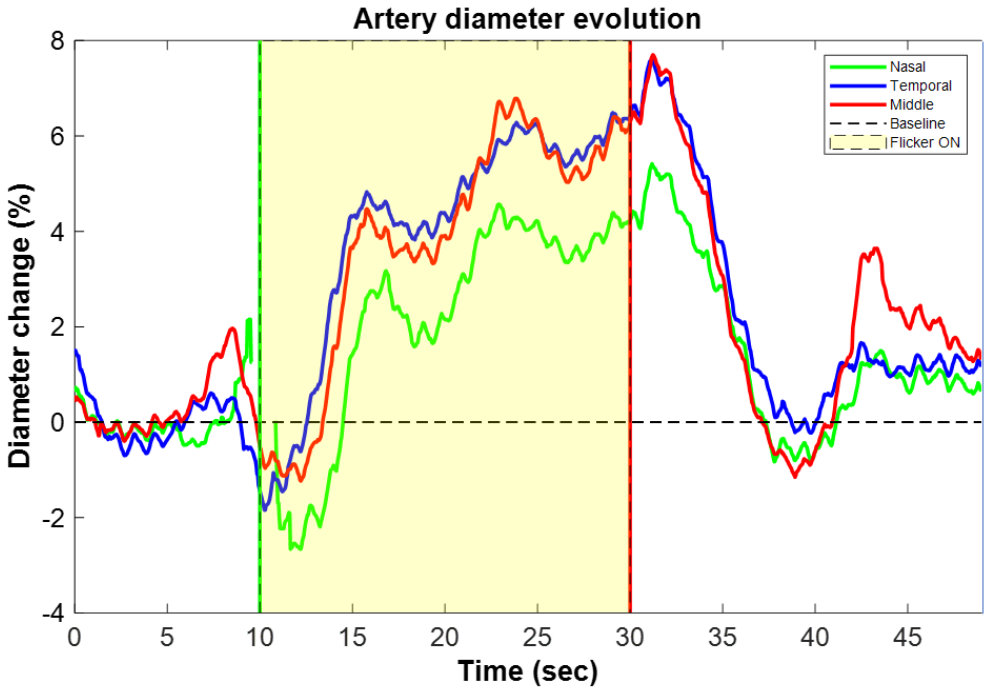

Figure 5.7: Moving average of lumen diameter for each location, represented on the same figure.

5.2.5 Symmetry of dilation of retinal vessel during a flicker test

Given our system's ability to resolve the vessel walls, the individual movements of both sides of the vessel could be observed. Figure 5.8 presents an example of a flicker test where the movements of the two inner walls of the vessel were measured.

By examining the moving average of the measured positions of the right and left walls, shown in red in figure 5.8, we can see that the dilation in response to flicker stimulation is relatively symmetrical in this case. However, we noted some differences in the dynamics of the two walls during light stimulation. Specifically, the right wall reached its final position 7 seconds after the onset of stimulation, whereas the left wall continued to expand throughout the entire stimulation period.

Interestingly, the blue curve in figure 5.8 suggests that the cardiac cycle affects the right side of the vessel more than the left side in this specific case. One possible explanation for this observation could be the curvature of the vessel. Each pulse of the cardiac cycle exerts pressure on the artery, and in the case of a curved artery, the outer side of the curve experiences greater force with each pulse. This differential pressure could explain the observed asymmetry in wall movements with each heartbeat.

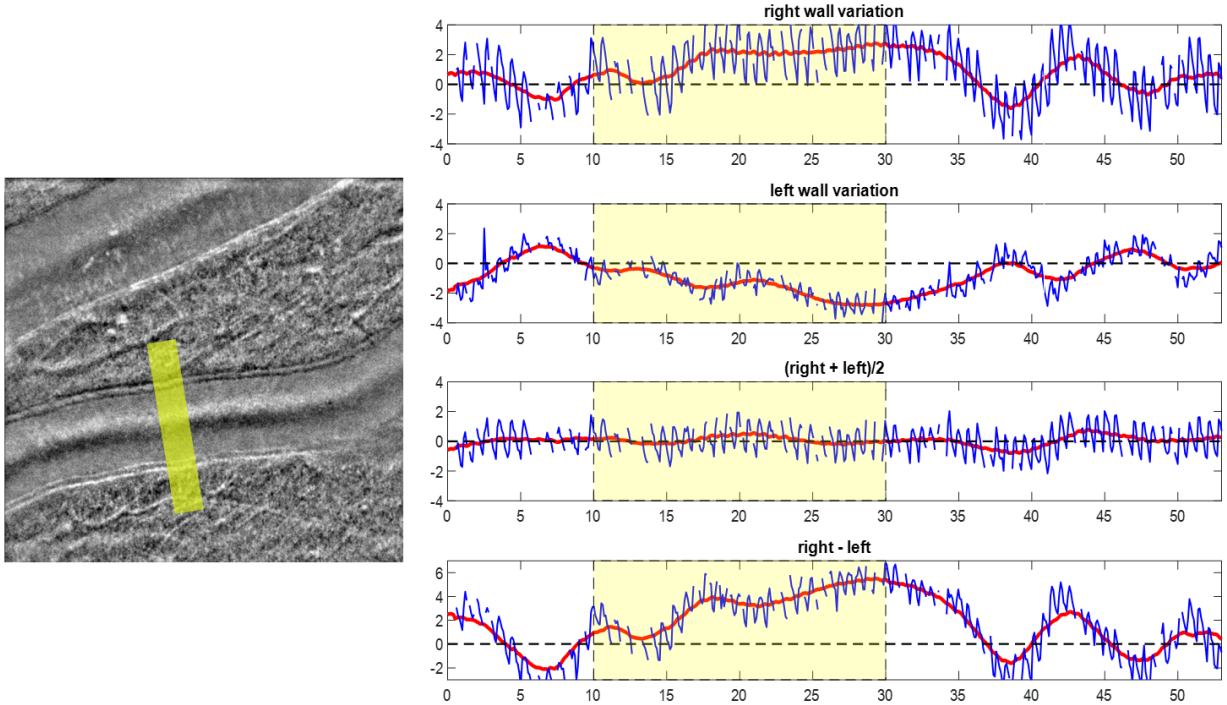

Figure 5.8: Measurement of the movements of the right wall and the left wall during a flicker test. The first and second graphs depict the displacement of the right and left walls of the artery, the 3 rd graph represent the overall movement of the vessel and the last graph represents the measured lumen diameter of the vessel.

5.2.6 Discussion

5.2.6.1 The importance of continuously assessing the vessel's diameter

Employing high spatial and temporal resolution methods to measure blood vessel diameter, both with and without flicker stimulation, reveals the limitations of relying on single-image measurements taken before, during, or after stimulation. Such single-point measurements can introduce errors due to the influence of the cardiac cycle and vasomotion. The influence of the cardiac cycle can be accounted for relatively easily by synchronizing image acquisition with a heart rate monitor. However, accounting for vasomotion presents a greater challenge. We have observed considerable variability in both the amplitude and frequency of vasomotion across different subjects.

This issue is illustrated in figure 5.9, which presents an example with and without stimulation in a subject exhibiting pronounced vasomotion. For instance, attempting to determine the baseline diameter by measuring only once at t=23 s or t=27 s would yield a 3.5% variation in diameter. When assessing blood flow, such discrepancies can lead to significant inaccuracies. A similar issue arises when measuring vessel diameter during stimulation. The observed dilation results from both flicker-induced hyperemia and the slow modulation caused by vasomotion. As demonstrated in figure 5.9, taking a single measurement at t=25 s would result in an underestimation of the true effect of the flicker stimulation on vessel dilation.

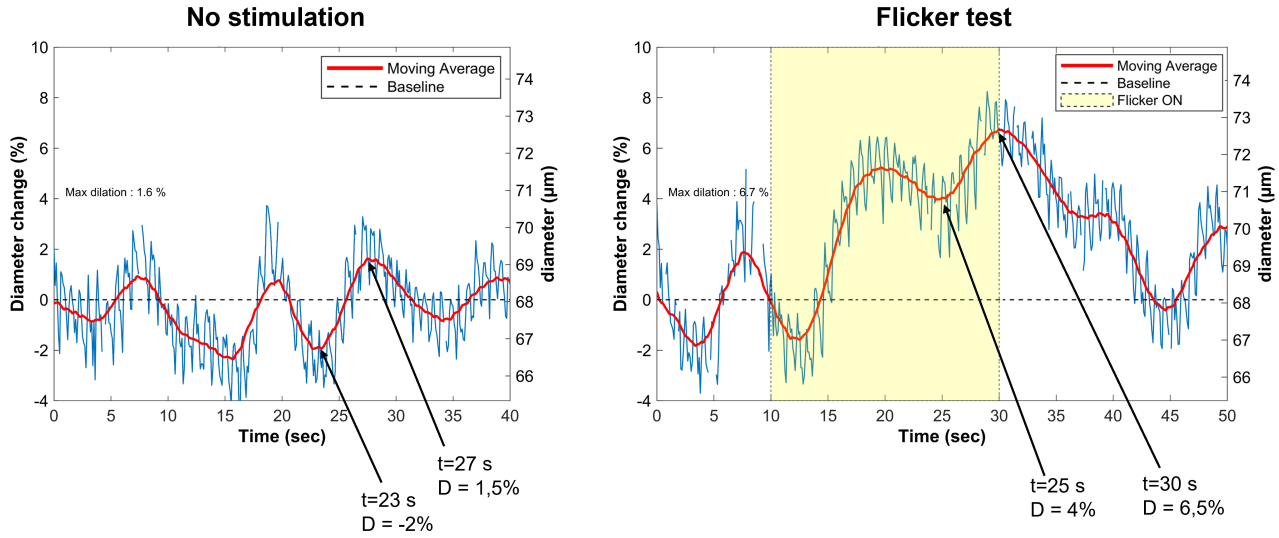

Figure 5.9: Example of one acquisition without stimulation and a flicker test on a subject exhibiting a high amplitude of vasomotion. In the absence of stimulation, the vasomotion amplitude is approximately 3.5% ($\approx$ 2.5µm). This vasomotion is also present during the flicker test acquisition, where it modulates the vessel diameter both during and after the stimulation.

5.2.6.2 Limitations of the method

The first limitation of this method arises from the vertical scanning of the retina using a horizontal thin illumination line with the AO-CRSO imaging system. This means that the phase contrast of blood vessels is better on horizontal vessels than it is on vertical vessels. Due to the layout of vessels in the retina, this is was not much of an issue for imaging large arteries in the 60-100 µm diameter range because it was easy to find horizontal sections of these vessels. However, this could be a limitation when attempting to image larger vessels located above or below the optic disk or smaller venules, arterioles, and capillaries in the parafoveal region.

Another limitation comes from the simplicity of the image processing method to measure the lumen diameter from an image of the vessel. The method averages the vessel cross-section over a 30 µm length, which requires the selected portion of the vessel to be straight. This limitation could be an issue if we tried to apply this method on some pathologies characterized by high vessel tortuosity. A better processing method, using vessel segmentation would be beneficial in addressing this limitation.

Finally, due to the high frame rate of the system, each acquisition generates a substantial amount of data (32 GB for a 50 sec video). As a result, extensive data processing is required for each acquisition, which can be time-consuming. Developing more efficient processing workflows could help mitigate this issue.

Conclusion of the chapter:

We demonstrated our method's capability to measure flicker-induced vasodilation at high spatial and temporal resolution in a cohort of healthy subjects. With our approach, we were able to visualize the full dynamics of retinal blood vessels, providing a comprehensive view of how the heartbeat, vasomotion and the flicker stimulation impact the diameter of blood vessels in the retina.

We measured a maximum vessel dilation of 5.2% ± 1.6% (4.4 µm ± 1.3 µm) when the subjects were exposed to flicker stimulation and 2.5% ± 1% (2.1 µm ± 0.9 µm) without stimulation. This dilation without stimulation was attributed to vasomotion. Additionally, within our cohort, we identified a correlation between artery size and maximum flicker induced dilation, with smaller arteries exhibiting greater maximum dilation than larger arteries.

We also employed the system in an exploratory manner, investigating the effects of varying stimulation durations, consecutive stimulation sessions, and the impact of subject anticipation on the vascular response. By modifying system parameters, stimulation settings, and image processing pipelines, we demonstrated the flexibility of this system and its potential for advancing our understanding of both vascular dynamics and neurovascular coupling.

General conclusion and future work

Conclusion

The eye offers a unique opportunity to investigate neurovascular coupling. As such, developing specialized imaging systems for studying neurovascular coupling in the eye, could significantly advance the diagnosis, prevention, and understanding of both ocular and systemic diseases. Throughout this thesis, my goal was to study neurovascular coupling in the human retina at a high spatial and temporal resolution. Achieving this goal required substantial instrumental development, which is detailed in Part I of this manuscript.

To both achieve high spatial and temporal resolution on a camera-based adaptive optics system, the main challenge is to increase image contrast. To address this challenge, the DMD-integrated AO-FIO, a system able to project illumination patterns onto the retina, was used as a pathfinder to understand how to elicit and maximize phase contrast specifically for blood vessels and red blood cells on a camera-based system. We developed a strategy to achieve phase contrast imaging by scanning the field of view with a thick line illumination and by numerically stitching the neighboring non illuminated area of the illumination to reconstruct the entire field of view. Using this method, we demonstrated full-field phase contrast imaging of vessel walls, capillaries, and red blood cells. However, achieving full-field imaging came at the expense of imaging speed.

To improve the speed of this method, a more efficient system based on the same principle was implemented: the AO-CRSO. By projecting a thin illumination line concentrating all the power of the source into the retina and using a 2D camera in rolling shutter mode for the detection, we demonstrated that high speed enhanced bright field contrast and phase contrast imaging on a wide field of view. A differential offset mode was also implemented, further increasing the contrast translucent structures with a final imaging speed of 100 Hz for a 2.5°x4.5° field of view. Additionally, we demonstrated its capability to image blood vessel walls and resolve individual red blood cells within capillaries, enabling blood flow measurement.

The AO-CRSO system offers new possibilities for studying neurovascular coupling at a high spatial and temporal resolution. Therefore in part II of this manuscript, I presented the work that I carried out in order to use this system to study the effect of a flicker stimulation on the diameter of blood vessels of the retina in healthy subjects.

To apply this system on human subjects for investigating neurovascular coupling, a stimulation channel designed to project flicker test into the retina was first implemented into the system. Then, building on the empirical insights gained from the DMD-integrated AO-FIO system, we optimized the exposure time and offset parameters of the AO-CRSO system to maximize vessel walls contrast. Furthermore, we developed an image processing pipeline to semi automatically process recorded images of blood vessels to measure their lumen diameter. With this method, we demonstrated the ability to measure vessel lumen diameters in large

vessels (60–100 µm) with a precision of 0.1 µm, every 0.1 seconds, over continuous acquisitions of up to four minutes.

Finally, using the previously proposed method, we studied flicker induced vasodilation on 8 healthy subjects by continuously imaging blood vessels, either without stimulation or while exposing the retina to a wide field flicker stimulation. For the first time, the dynamics of retinal blood vessels was measured at a high spatial and temporal resolution, offering a view of how the heartbeat, vasomotion, and flicker stimulation influence the size of blood vessels in the retina. By varying the settings of the flicker stimulus, we further demonstrated the flexibility of this method, highlighting its potential for advancing our understanding of retinal neurovascular coupling in both healthy and pathological conditions.

Perspectives

Given the AO-CRSO capabilities to provide phase contrast images at a high spatial and temporal resolution, there are many different paths for further research into neurovascular coupling with this system. During this first clinical investigation of neurovascular coupling, I chose to focus on quite large arteries (60-100 µm in diameter). An interesting follow up study would be to study neurovascular coupling in smaller vessels down to capillaries. This would provide additional insights into microvascular dynamics and their role in neurovascular coupling.

Another possible area of exploration is the impact of diseases on the flicker-induced response. Studying subjects with retinal or systemic vascular conditions could reveal alterations in vascular reactivity and contribute to early diagnosis and monitoring of disease progression.

To fully use the system's wide field of view and high frame rate, another exciting direction would be to try measuring the propagation of neurovascular coupling. A possible experimental protocol would involve local flicker stimulation around the fovea while imaging a horizontal artery perfusing the fovea at the system's maximum frame rate (800 Hz). This could help determine if backward propagation of dilation can be detected, shedding light on the spatial dynamics of neurovascular coupling.

Another area of exploration would be to measure blood flow, this could be done with the AO-CRSO in small vessels where red blood cells can be resolved. In addition, a promising system to measure blood flow is the Laser Doppler Holography system that I worked on during my thesis. The team of Michael Atlan is now able to provide quantitative measurements of blood flow from LDH images which could offer new applications for studying neurovascular coupling in both healthy and pathological retinas.

The AO-CRSO system's ability to image vascular dynamics in-vivo also opens opportunities to explore vasomotion, its role in retinal blood flow, and its potential as a biomarker for disease. Furthermore, the system's high spatio-temporal resolution offers a unique opportunity to study the effects of the cardiac cycle on retinal blood vessels. By imaging the effect of the heartbeat on blood vessels in high-resolution videos, we may be able to infer mechanistic properties of the broader vascular system, potentially leading to new biomarkers for assessing vascular health.

Finally, as part of Ines Loukili's thesis work, the AO-CRSO system is being adapted for optoretinography (ORG), a technique with which the photoreceptor's response is probed with short intense flashes of visible light. Pairing neurovascular coupling with optoretinography to link photoreceptor activity with neurovascular mechanisms could be a very interesting path for further research with this system.

Appendix A

Foveolar drusen decrease fixation stability in pre-symptomatic AMD

Foveolar Drusen Decrease Fixation Stability in Pre-Symptomatic AMD

Jimmy Murari,[1] Josselin Gautier,[2,3] Joël Daout,[1] Léa Krafft,[4] Pierre Senée,[4,5] Pedro Mecê,[4,6] Kate Grieve,[1,2] William Seiple,[7] Denis Sheynikhovich,[1] Serge Meimon,[4] Michel Paques,[2] and Angelo Arleo[1]

[1]Sorbonne Université, INSERM, CNRS, Institut de la Vision, Paris, France
[2]CHNO des Quinze-Vingts, INSERM-DGOS CIC, Paris, France
[3]LTSI, Inserm UMR 1099, University of Rennes, Rennes, France
[4]Office National d'Etudes et de Recherches Aérospatiales (ONERA), Hauts-de-Seine, France
[5]Quantel Medical SA, Cournon d'Auvergne, France
[6]Institut Langevin, CNRS, ESPCI, Paris, France
[7]Lighthouse Guild, New York, New York, United States

Correspondence: Denis Sheynikhovich, Sorbonne Université, INSERM, CNRS, Institut de la Vision, 21 r Ecole de Medecine, Paris 75006, France; denis.sheynikhovich@sorbonne-universite.fr.

JM and JG contributed equally to this work.
SM, MP, and AA equally supervised this work.

Received: March 29, 2024
Accepted: June 2, 2024
Published: July 8, 2024

Citation: Murari J, Gautier J, Daout J, et al. Foveolar drusen decrease fixation stability in pre-symptomatic AMD. *Invest Ophthalmol Vis Sci.* 2024;65(8):13. https://doi.org/10.1167/iovs.65.8.13

Purpose. This study aims at linking subtle changes of fixational eye movements (FEM) in controls and in patients with foveal drusen using adaptive optics retinal imaging in order to find anatomo-functional markers for pre-symptomatic age-related macular degeneration (AMD).

Methods. We recruited 7 young controls, 4 older controls, and 16 patients with presymptomatic AMD with foveal drusen from the Silversight Cohort. A high-speed research-grade adaptive optics flood illumination ophthalmoscope (AO-FIO) was used for monocular retinal tracking of fixational eye movements. The system allows for sub-arcminute resolution, and high-speed and distortion-free imaging of the foveal area. Foveal drusen position and size were documented using gaze-dependent imaging on a clinical-grade AO-FIO.

Results. FEM were measured with high precision (RMS-S2S = 0.0015 degrees on human eyes) and small foveal drusen (median diameter = 60 µm) were detected with high contrast imaging. Microsaccade amplitude, drift diffusion coefficient, and ISOline area (ISOA) were significantly larger for patients with foveal drusen compared with controls. Among the drusen participants, microsaccade amplitude was correlated to drusen eccentricity from the center of the fovea.

Conclusions. A novel high-speed high-precision retinal tracking technique allowed for the characterization of FEM at the microscopic level. Foveal drusen altered fixation stability, resulting in compensatory FEM changes. Particularly, drusen at the foveolar level seemed to have a stronger impact on microsaccade amplitudes and ISOA. The unexpected anatomo-functional link between small foveal drusen and fixation stability opens up a new perspective of detecting oculomotor signatures of eye diseases at the presymptomatic stage.

Keywords: age-related macular degeneration (AMD), drusen, fixational eye movements, fovea

Age-related macular degeneration (AMD) is the main cause of vision loss in developed countries, affecting 180 million people in 2020 with an expected prevalence of 288 million by 2040.[1] AMD starts with the accumulation of extracellular deposits, called drusen, in between the Bruch's membrane and the retinal pigment epithelium (RPE). Multiplication and expansion of drusen is associated with late stages of AMD, which are classified into exudative (wet-AMD) and/or atrophic (dry-AMD).[2] Wet-AMD is caused by irregular blood vessel growth (i.e. neovascularization) at the macular level, and it affects approximately 10 to 20% of patients with AMD.[3] Although macular neovascularization can be successfully treated using anti-VEGF therapies, these treatments do not prevent the development of atrophy, which causes sight loss in the long term.[4] Geographic atrophy or dry-AMD is the irreversible loss of photoreceptors caused either by drusen development or neovascular growth, and it accounts for about 80% to 90% of the cases.[2] No effective treatment currently exists for this form of AMD. The absence of efficient treatment strategies for the late-stage AMD is exacerbated by the fact that patients frequently remain unaware of their AMD condition,[5] so that they typically receive a diagnosis only upon the emergence of clinical indications, often at a stage too advanced for effective implementation of preventive strategies. There is therefore an urgent need to characterize anatomo-functional rela-

tionships associated with the earliest asymptomatic AMD stages aiming at complementing existing medical imaging techniques with functional measures of retinal anomalies that can serve as biomarkers of future disease onset. If indeed the presymptomatic structural anomalies are associated with functional, for example, oculomotor, changes, their timely detection may also incite the individuals with a risk of developing AMD to engage in risk mitigation strategies to delay AMD onset and progression.[6–8]

The objective of the present study is to test the novel hypothesis that the appearance of drusen, an early structural anomaly in presymptomatic AMD, is associated with detectable changes in microscopic eye movements during ocular fixation. Even though the development of early-to-late stages of confirmed AMD has already been associated with changes in fixation stability, decreased visual acuity, reduced visual field, slower reading speed, lower contrast sensitivity, and an overall deterioration of functional vision useful for daily activities,[9–11] these previous studies did not explore fixational eye movements in presymptomatic stages, nor did they characterize the link between retinal structure changes and fixational eye movements. In patients with central scotomas, fixation stability as assessed by retinal motion compensation strategies has been shown to worsen with AMD progression.[12] Moreover, advanced geographic atrophies were reported to affect different components of fixational eye movements, such as microsaccades (small saccades of amplitude below 1 degree) and ocular drift[13,14] (random Brownian-walk-like eye movements between microsaccades). More specifically, these studies report higher microsaccade amplitudes associated with macular lesions[13] and lower spectral whitening of natural scenes by ocular drift in patients with long-lasting macular disease, compared to age-matched controls.[14] Given the significant changes in fixational stability in advanced forms of AMD, it is important to test whether even the first signs of potential future disease can induce changes in eye movement statistics.

The hypothesis was tested by simultaneously performing (i) high-resolution retina imaging to visualize and characterize small asymptomatic alterations of the foveal structure, and (ii) high-speed retina tracking to detect fixational eye movements. We studied the relationship between subtle structural retinal anomalies and fixational eye movement characteristics by examining healthy controls and participants with foveal drusen, but no scotoma or atrophy according to conventional measures. If the appearance of first drusen indeed leads to fixation instability, as the current study shows, such a structure-function relationship provides the possibility to use fine oculomotor measurements to predict the appearance of retinal anomalies and therefore contribute to the development of early anatomo-functional biomarkers for urgently needed screening approaches in presymptomatic AMD.

Methods

Participants

A cohort of 39 participants were recruited for the study as part of 1 of 3 groups: young controls ($n = 7$, [2 women], age = 31 ± 7 years old), older controls ($n = 20$, [14 women], age = 75 ± 4 years old), and drusen participants ($n = 12$, [8 women], age = 79 ± 3 years old). The initial assignment of participants to the groups relied on the detection of drusen by standard spectral-domain optical coherence tomography (SD-OCT) imaging (Spectralis OCT, Heidelberg Engineering, Heidelberg, Germany). All participants were recruited from the SilverSight cohort,[15] and they were fully screened and ascertained not to suffer from any age-related sensory, cognitive, or motor pathology.

Prior to the beginning of the experiment, older controls and drusen participants were screened using a novel imaging method, developed previously in our laboratory using Adaptive Optics Flood Illumination Ophthalmoscope (AO-FIO, rtx1; Imagine Eyes), which is capable of detecting foveal

Table. Age, Visual Acuity and Drusen Properties of Study Participants

Participant ID	Age, Years Old	Tested Eye	Visual Acuity	Number of Drusen	Mean Drusen Area ± SD (Arcmin^2)	Total Drusen Area (Arcmin^2)	Mean Drusen Eccentricity ± SD (Arcmin)
DI1	79	OD	1.2	7	79 ± 14	556	27 ± 22
DI2	78	OD	1	7	169 ± 66	1182	28 ± 23
DI3	80	OD	1	5	75 ± 18	376	30 ± 25
DI4	84	OS	1.2	7	143 ± 32	998	37 ± 29
DI5	80	OD	1.2	32	339 ± 147	10861	42 ± 31
DI6	83	OS	1	12	176 ± 50	2121	42 ± 26
DI7	76	OS	1	9	131 ± 72	1184	45 ± 27
DI8	74	OD	1	2	106 ± 29	212	45 ± 14
DI9	75	OD	1.2	6	178 ± 40	1069	56 ± 32
DO1	73	OD	0.8	5	148 ± 78	741	62 ± 22
DO2	84	OS	1	13	177 ± 48	2313	63 ± 25
DO3	70	OS	1	15	180 ± 70	2710	62 ± 32
DO4	80	OD	0.7	6	128 ± 49	766	68 ± 19
DO5	81	OD	1.2	20	139 ± 39	2791	69 ± 42
DO6	74	OS	0.8	14	59 ± 15	826	76 ± 25
DO7	76	OD	1.2	28	189 ± 75	5311	92 ± 34
Mean ± SD for drusen group ($n = 16$)	**78 ± 4**	/	**1 ± 0.2**	**11 ± 8**	**133 ± 59**	**2126 ± 2000**	**53 ± 27**
Mean for older controls ($n = 4$)	**72 ± 2**	/	**>1**	/	/	/	/
Mean for young controls ($n = 7$)	**31 ± 7**	/	**>1**	/	/	/	/

Investigative Ophthalmology & Visual Science

drusen not visible in standard SD-OCT or fundus imaging[16] (see the next section). As a consequence, nine participants that had initially been recruited as older controls were actually found to have drusen in the foveal region, and they were thus moved into the drusen group. In addition, a total of 12 participants had to be excluded from study: 3 because of too blurry retina images on the rtx1; 3 due to poor signal-to-noise ratio during the fixation task; 2 because they were not fixating the right target; 3 because of excessive tiredness and discomfort during the experiment; and 1 because she exhibited fixation patterns typical of another disease. As a result, a total of 27 participants were kept for the analyses: 7 young controls ([2 women], age = 31 ± 7 years old), 4 older controls ([1 woman], age = 72 ± 2 years old), and 16 drusen patients ([10 women], age = 78 ± 4 years old). Their demographic and ophthalmological characteristics are given in the Table.

All clinical, experiment, and data management procedures were approved by the Ethical Committee "CPP Ile de France V" (ID RCB 2015-A01094-45, n. CPP: 16122 MSB), and they adhered to the tenets of the Declaration of Helsinki. A signed consent was obtained by each participant to be included in the study as well as for the inclusion in the Multimodal Ophthalmologic Imaging protocol (IMA-MODE, ID_RCB 2019-A00942-55 CPP: Sud Est III 2019-021-B) of the Quinze-Vingts National Ophthalmology Hospital.

Drusen Detection by Gaze-Dependent Imaging

In order to reliably detect the presence of even the smallest drusen, gaze-dependent fundus imaging of all older participants' central retina was performed using a commercial clinical-grade AO-FIO (rtx1; Imagine Eyes) following the method and protocol described by Rossi et al.[16] Compared to direct single-shot retinal flood imaging, gaze dependent imaging computes the local contrast maxima across a stack of 5 images whose gaze direction has been sequentially shifted: one 4 degrees × 4 degrees fovea-centered image of the retina, focused on the photoreceptors, and four horizontally and vertically displaced images (±1 degree with respect

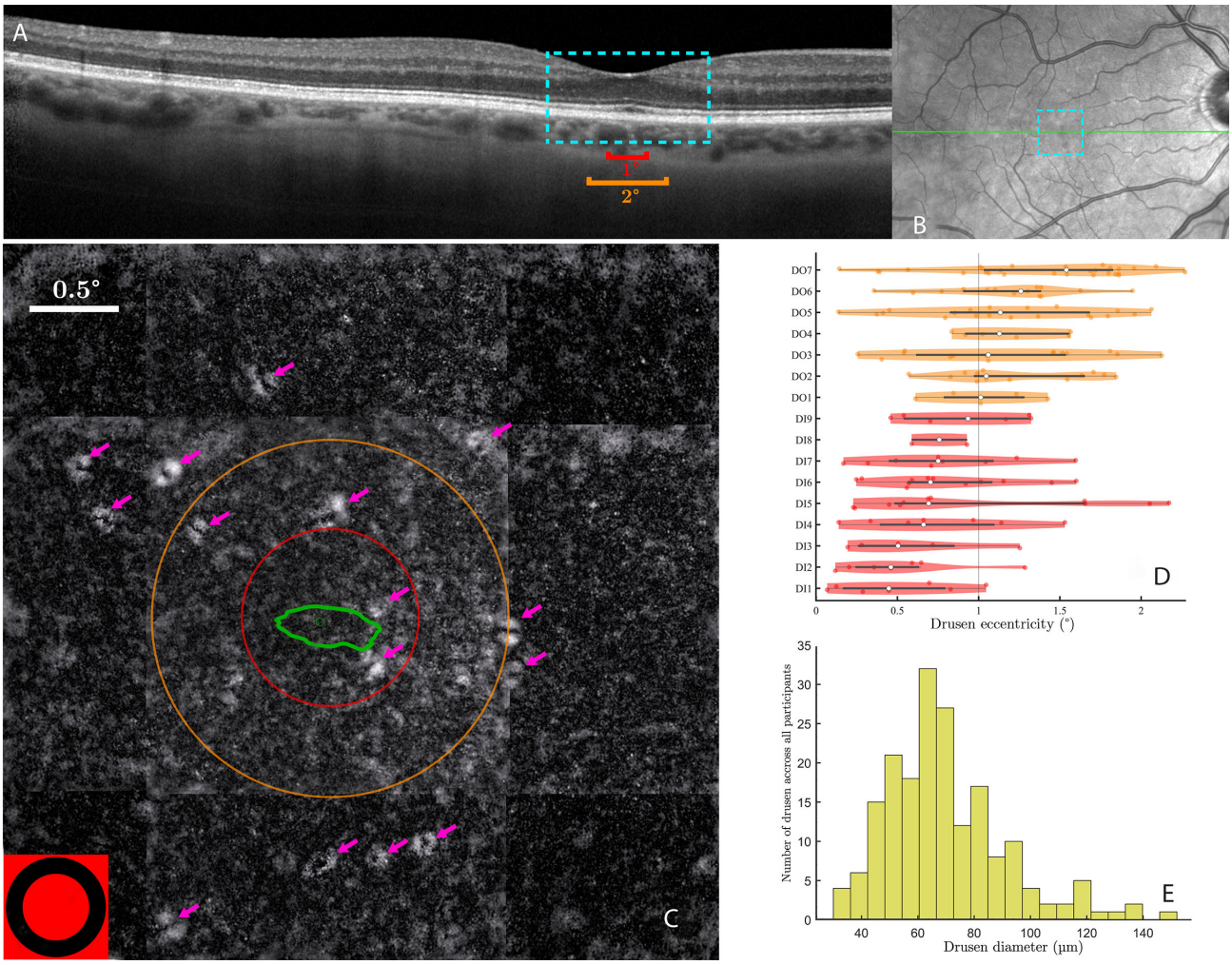

Figure 1. Drusen visualization and identification. (**A**) SD-OCT image of a patient. A 2 times zoom on the 4 degrees center area is shown in *blue*. The *red and orange lines* are the same size as the circle diameters in (**C**). (**B**) Fundus image with the OCT cut of (**A**) in *green* and the *blue dotted* area showing the 4 degrees zone where gaze-dependent imaging is performed. (**C**) Gaze-dependent image of the 4 degrees × 4 degrees zone around the fovea of the same patient. The *pink arrows* indicate the drusen: the *white ring* is the slope of the bump caused by the druse, and the *black center* part is the tip. The *red and orange circles* are, respectively, of 0.5 degrees and 1 degree of the radius. The *green line* is the ISOA 86%. On the *bottom left corner*, is the fixation target to scale. (**D, E**) Distribution of drusen eccentricities (**C**) and diameters (**D**) across all participants.

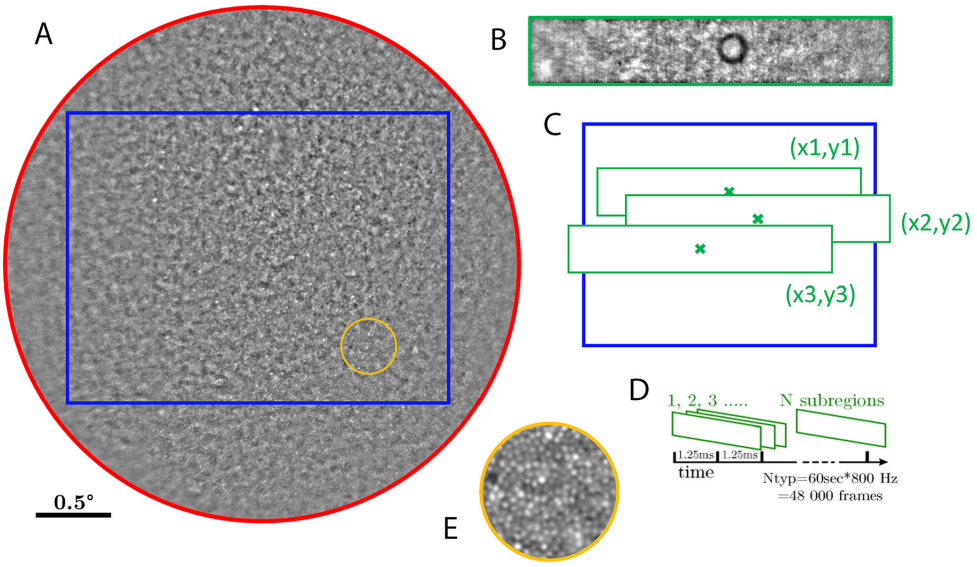

Figure 2. Principle of the AOFIO retinal tracking. (**A**) The 4 degrees of full field obtained after initial phase of the fixation task (5 seconds at 100 Hz, in *red*). Only the rectangular sub-part (in *blue*) was used as a reference image for subsequent eye movement analysis, as it is enough to track and monitor eye movements during central fixation (typically less than 2 degrees in amplitude). During the experimental phase of the task, the 2 × 0.5 degrees subregion (in *green*) is tracked at very high speed (800 Hz, 16 bits). (**B**) An actual frame recorded at this frequency. (**C**) Eye displacement is obtained by phase-correlation over the reference image. (**D**) Custom eye tracking software processes large sequences of up to 5 Mbits/frame. (**E**) A 3 times zoom on an area 1 degree away from the fovea with clearly visible photoreceptor mosaic.

to the center image). After image registration, the maximum of the standard deviation for each x and y pixel of the five-image stack is computed to make the gaze-varying structure visible. In the resulting contrast image, drusen and their delineation are clearly visible (Fig. 1C). This gaze-dependent retina imaging method allows for the detection of foveal drusen less than 25 µm in diameter that are not detected by standard imaging methods and it also visualizes much more reliably drusen 25 to 60 µm in diameter, providing more precise information about their size and position.[16] In a final step, drusen were manually annotated as ellipses by two experts in medical images, followed by a validation by two ophthalmologists (including author M.P.). All the image filtering, registration, and processing were performed using custom software written in MATLAB (Mathworks, USA, 2023).

Ocular Fixation Task

Following drusen assessment, all participants were tested in an ocular fixation experiment in order to see whether the presence of drusen affects fixational eye movements. In order to precisely detect even the smallest eye movements, video recordings of the fovea during fixation were performed using the PARIS AO-FIO (ONERA)[17] located at the Quinze-Vingts National Ophthalmology Hospital in Paris, France. Both the PARIS AO-FIO retinal imaging setup and retinal motion tracking process are described in the following sections. Before the ocular fixation task, the dominant eye was dilated with a drop of 1% tropicamide (mydriaticum, tropicamide 0.5%). The recordings were performed in a dark room with minimal stray light and with the participant's head fixed on a chinrest. The fixation task consisted of two phases. In the initial phase, participants were required to fixate a central cross for 5 seconds. This phase served to initialize the retinal motion tracking procedure. In the experimental phase, the participants were asked to fixate on a circle (outer diameter = 17 arcmin [0.28 degrees], inner diameter = 11 arcmin [0.18 degrees]) for 30 seconds, across 5 trials. The instructions were "Please, fixate on the circle for 30 seconds. Do not speak and try not moving your head. Do not hesitate to blink if you need to.," and a vocal indication about time progression was provided after 15 seconds.

Retina Imaging Setup

High-resolution structural imaging of the fovea was performed using the PARIS AO-FIO,[17] through video recordings focused on the photoreceptor layer. Concurrently with retina imaging, the Paris AO-FIO allowed for the projection of NIR illumination patterns (i.e. stimuli) onto the retina via a deformable digital micromirror device (DMD)[18] as well as for partial-field illumination.[19] The stimulus projection with the DMD was controlled using a custom-made Python code and the ALP4Lib python library wrapper. The PARIS AO-FIO system consists of two optical channels: the Wavefront correction channel, and the illumination and imaging channel, combined with the stimulation channel. A fibered SuperLuminescent Diode (Exalos, Switzerland) with nominal center wavelength of 750 nm measures optical aberrations, and an 850 nm LED source (Thorlabs, USA) coupled with a liquid fiber homogeneously illuminate the retina over a 4 degrees diameter field of view (Fig. 2A). The adaptive optics compensated for the spherical, cylindrical, and some higher order aberrations of the eye's optics before the stimulus reached the retina. The backscattered light from the eye was reflected back on the deformable mirror before reaching the imaging camera. The adaptive optics loop was controlled with a LabVIEW program and image acquisition was monitored via the Holovibes software.[20]

Investigative Ophthalmology & Visual Science

Retina Motion Tracking

During the initial phase of the ocular fixation task (5 seconds), a full field sequence of images covering a 4 degrees diameter field of participants' retina was recorded at 100 Hz (2048 × 2048 pixel frames). The recorded full field retinal images were first stabilized and then averaged into a unique squared full field reference image of the center of the retina (see Fig. 2A). Then, during the experimental phase of the task, only a sub-band (2 degrees × 0.5 degrees, 1400 × 256 pixel, with the black circle target at the center) was recorded at 800 Hz to be used for retina motion tracking (Fig. 2B). Retinal motion was tracked using a phase-correlation registration method[21,22] (Fig. 2C) after bandpass filtering the image sequences. The algorithm consisted in finding the position that best fitted each frame of the high-speed video onto the reference image. The best fit was considered as the peak value coordinates of the correlation map computed in the Fourier domain (see Clip 1).

Even if the maximum sampling frequency of the camera was only limited by vertical pixel resolution, we found that 1400 pixels horizontally offered a good tradeoff between field coverage and video bandwidth. The resulting 0.684 MB/frame (16 bits) led to a very large 547 MB/s video bandwidth that could only be recorded with solid state hard drives and ad hoc recording software (Holovibes). Videos were recorded on a separate computer than the one used for stimulus presentation.

Detection of Retina Motion Related Events

Processing of the raw pixel displacement of each frame relative to the reference images to ocular movement in arcminutes with annotated events was made with a MATLAB custom program (based on the work of Bowers and Gautier[23]). Microsaccades were detected using an acceleration threshold inspired by Engbert.[24] An acceleration, rather than velocity, threshold (factor $N = 3$ standard deviation of the median) was used in order to differentiate fast ocular drift epochs from small and slower microsaccades, which can have similar velocities but distinct accelerations. The acceleration was computed for the 30 seconds fixation, and smoothed using running average with an approximately 70 ms window. This adaptive algorithm allowed for thresholds that fitted the participants who had relatively small microsaccades and stable ocular drift, as well as the participants with larger microsaccade and drift amplitudes. In addition, to ensure that microsaccades were all entirely detected and that some parts of ocular drift were not mislabeled as microsaccades, all traces were manually verified after the automatic annotation. Blinks were detected automatically as sudden drops in mean frame pixel intensity, which corresponded to the closed eye reflecting less light back to the camera. Rejected data were epochs of ocular coordinates marked by the user as false data due to failures in the imaging or the tracking (to the exclusion of blinks). They accounted for 0% to 3% of the fixation data for each participant. Everything in between the three types of events – microsaccades, blinks, or rejected data – was automatically marked as drift.

Root mean square sample to sample (RMS-S2S) deviation was calculated to measure the precision of the retina tracking method. A given RMS-S2S of an eye-tracker quantifies the average movement due to noise between successive data is its squared value.[25,26] Filtering ocular traces can have a strong effect on RMS-S2S and skews the results.[27] However, in this tracking method, ocular traces were used raw, and RMS-S2S appeared to be the right metric to measure precision.

Estimation of Fixation Stability

The Bivariate Contour Ellipse Area (BCEA) and, more recently, the ISOline Area (ISOA) metrics have been used to clinically measure fixation stability of patients with central vision loss, including AMD.[28] ISOA is more robust than BCEA as it can delineate non-ellipsoidal fixation patterns[29] and it can be used to detect possible multiple retinal fixation loci (PRLs), such as in patients with AMD. The choice of the bandwidth and the extent (i.e. number of standard deviations) to compute the ISOA is relatively arbitrary and open to criticism.[29–31] The choice of a 1 degree window for kernel density estimation, which subtends ISOA calculation, has been shown to be robust and appropriate with respect to the classical definition of the 1 degree foveola.[30,31] Concerning the ISOA contour extent, we used both the standard 68% ISOA (i.e. encompassing 68% of the data points) and the 86% ISOA (i.e. computed over 2 standard deviations in the 2D space defined from the center of the fixation distribution).[32] The rationale was that the 86% ISOA contour would provide complementary insights on the global fixation pattern that might better differentiate healthy controls from participants with foveal drusen.

Drift Diffusion Coefficient and Amplitude Spectrum Computation

In the framework of the Brownian motion,[33,34] the eye movement during drift epochs can be modeled by a random walk, and motion statistics can be measured by the diffusion coefficient D. We computed the diffusion coefficient D by least square best fit to the measurements of the empirical standard deviation of the eye displacement as a function of time.[35] The motion amplitude spectra of the ocular drift segments were analyzed by using a multitaper spectral analysis. This analysis was carried separately on the horizontal and vertical components of eye motion,[36,37] on overlapping segments of 1 second. The time half-bandwidth product was fixed at 2.5, and the last taper was dropped to maximize the spectral concentration ratios in the Slepian sequences.

Statistical Analysis

Linear mixed-effect model fit by maximum likelihood (*fitlme* function on MATLAB) was used to compare FEM components between groups with the Formula (1). $FEM_{component}$ were microsaccade amplitudes, ISOAs, or drift coefficients.

$$FEM_{component} \sim groups + (1|trial) \quad (1)$$

Results

Detection and Characterization of Foveal Drusen

Figure 1 shows foveal drusen detected in one participant by using gaze-dependent retinal fundus imaging protocol[16] (see Fig. 1C), as well as the corresponding region in an SD-OCT cut across the fovea (Figs. 1A, 1B). Overall, in 9 out

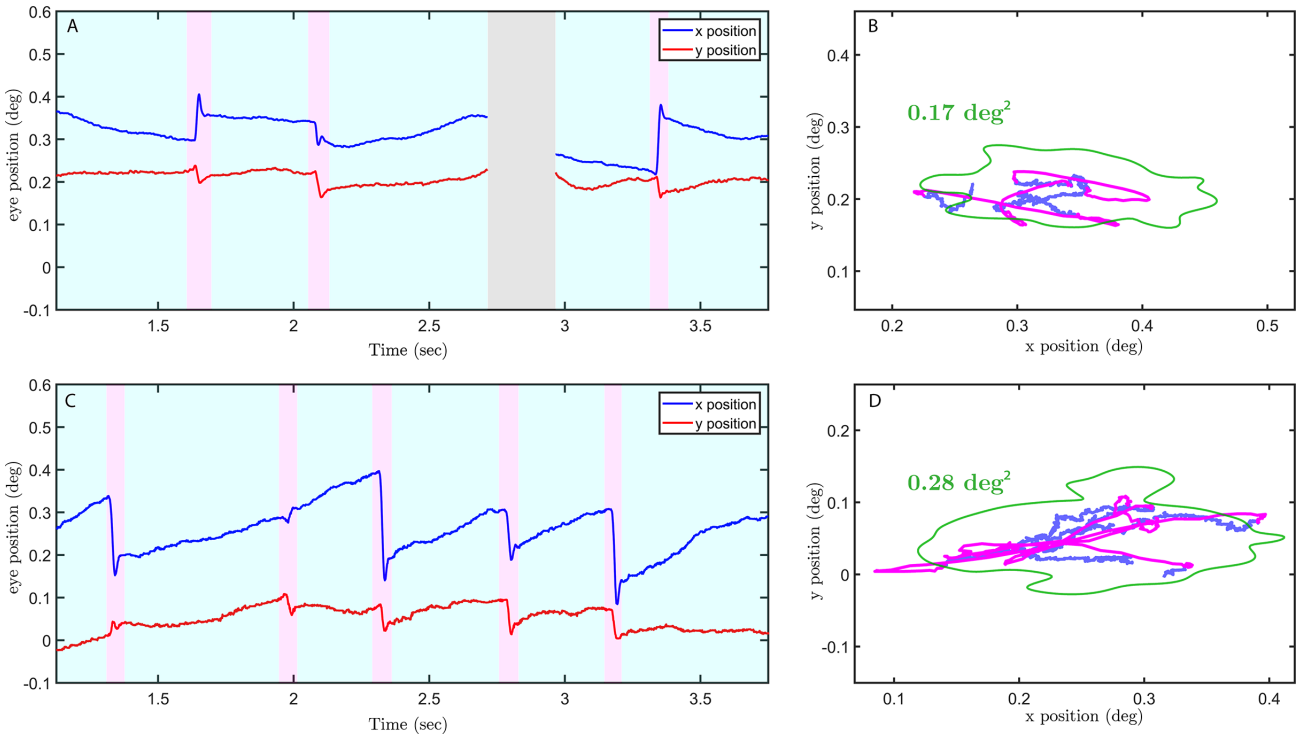

Figure 3. Retina motion traces of a healthy young subject (**A, B**) versus a subject with drusen (**C, D**) with the corresponding movement in the visual field. The eye traces are shown for 3 seconds. Microsaccades are annotated in *pink* and drift in *light blue*. Eye position is shown in degrees. The *green line* is the ISOA 86%.

of 20 participants (45%), initially deemed to have no drusen and therefore assigned to the control group based on SD-OCT images, the presence of foveal drusen was detected using the gaze-dependent detection procedure. These participants were therefore re-assigned to the drusen group (see Methods). Across all participants of the drusen group, we quantified the number of foveal drusen, their eccentricity with respect to the center of the fovea, their areas, their diameters (i.e. computed as the average diameter of the ellipses), and the total area covered by all drusen (see the Table). The median drusen diameter in the study was 60 µm (0.2 degrees; see Fig. 1E).

Precision and Robustness of Retinal Motion Tracking

Retinal tracking during ocular fixation was performed using the Paris AO-FIO,[17] as described in the Methods section. Figure 3 shows the example traces recorded during 4 seconds of the ocular fixation task in one control participant and one participant with ocular drusen. Our retinal tracking method allowed both microsaccades (shown in magenta) and ocular drift (shown in blue) to be easily visualized and detected in both control and drusen participants.

The precision of the tracking procedure was quantified by the average RMS-S2S and achieved 0.0015 degrees, as measured on unfiltered data across all participants. This value is an order of magnitude lower than what is deemed sufficient to detect microsaccades[25] (0.03 degrees). The method allowed for the detection of numerous small microsaccades down a few arcminutes (see microsaccadic amplitude distribution in Fig. 4). A low standard deviation of the tracking error (σ = 0.0006 degrees) suggests that the method is very robust from participant to participant. Finally, in order to assess possible noise sources stemming from either mechanical vibration of the Paris AO-FIO setup or defects of the tracking algorithm, as well as to get a standard RMS-S2S value, we quantified the precision of the tracking method on a non-moving artificial eye (OEMI-7 Ocular Imaging Eye Model). We found an RMS-S2S of 0.00019 degrees (σ = 0.00009 degrees over 4 recordings). The precision found on human eyes and the artificial eye is equal or better than any reported values in literature (0.0069 degrees on a DPI Gen5.5 with an non-moving artificial eye[38] and 0.012 degrees on a human eye[39]; 0.0012 to 0.0045 on the EWET1 prototypes on human eyes[39]) without being affected by lens-wobble artifacts, such as in a DPI or distortion artifacts, such as in an AO-SLO system (no RMS-S2S values found for AO-SLO in literature).

The sensitivity to noise was additionally assessed by power spectrum analysis. Power spectra were only weakly affected by noise across all subject groups, even at higher frequencies (above 100 Hertz [Hz]; Figs. 5C, 5D). The power spectrum of the still model eye was one to two orders of magnitude below human participants (Supplementary Fig. S1), suggesting negligible setup-related noise.

An addition to be very precise, the method was also found to be resistant to variations in lens transparency (Supplementary Fig. S2). More specifically, in 11 participants (41%), classified by orthoptists as having corticonuclear lens opacities, the mean RMS-S2S was 0.0018 degrees, only slightly superior to the mean RMS-S2S of all other participants (0.0014 degrees).

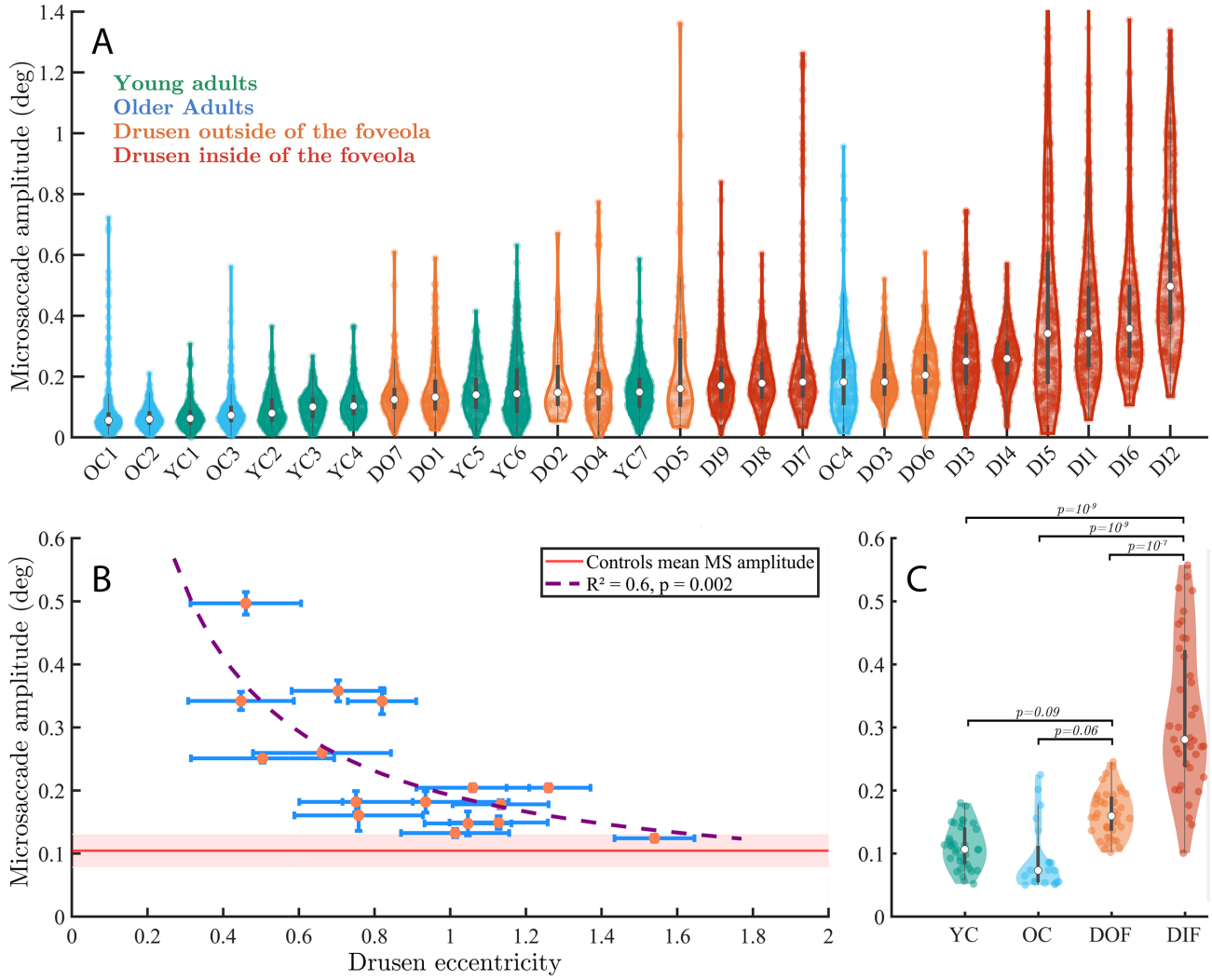

Figure 4. Microsaccade characteristics across individuals and groups. (**A**) Violin plots of individual distributions of microsaccade amplitudes across all participants, color-coded by group and sorted with respect to the mean microsaccade amplitudes. Each *dot* is one microsaccade during the fixation task. (**B**) Microsaccade mean amplitude with respect to drusen eccentricity from the center of the fovea. Standard errors are shown in *blue bars*. (**C**) Microsaccade amplitudes across all four groups. Each *dot* is the average microsaccade amplitude for 30 seconds (one trial).

Effect of Eccentricity of Foveal Drusen on Microsaccades

To see whether the presence of foveal drusen is associated with changes in eye movements, we plotted individual distributions of microsaccade amplitudes sorted from lowest to highest mean amplitude (Fig. 4A). The distributions of young and older participants from the control group were shifted toward the lowest amplitudes, whereas those from the drusen group toward the highest ones, suggesting a link between drusen properties and FEM characteristics. Strikingly, we also noted that the highest microsaccade amplitudes were associated with the presence of drusen mainly inside the foveola (the 0.4-0.6 degrees foveal pit),[40] suggesting that drusen eccentricities may play an important role in oculomotor changes induced by the presence of drusen.

To quantify this effect, we computed Pearson's correlation coefficients between the measured drusen characteristics (i.e. their number, area, and eccentricity) and microsaccade sizes. We found a significant negative correlation between the participants' drusen eccentricities and their microsaccade amplitudes ($r = -0.74$, $P = 0.001$). Hence, the closer drusen were to the center of the fovea, the larger were microsaccades. Conversely, the more eccentric were the drusen in a particular participant, the more similar this participant was to the control subjects in terms of the microsaccade amplitude. No significant correlation was found among the number of drusen, the mean drusen area, or the total drusen area and microsaccade amplitude ($r = -0.003$, $P = 0.99$; $r = 0.16$, $P = 0.53$; and $r = 0.13$, $P = 0.61$, respectively. The results in Figure 4B show that microsaccade amplitudes start increasing exponentially when drusen are located closer than 0.8 degrees to 1 degree with respect to the center of the fovea.

To further characterize the role of drusen eccentricity, participants from the drusen group were subsequently

Investigative Ophthalmology & Visual Science

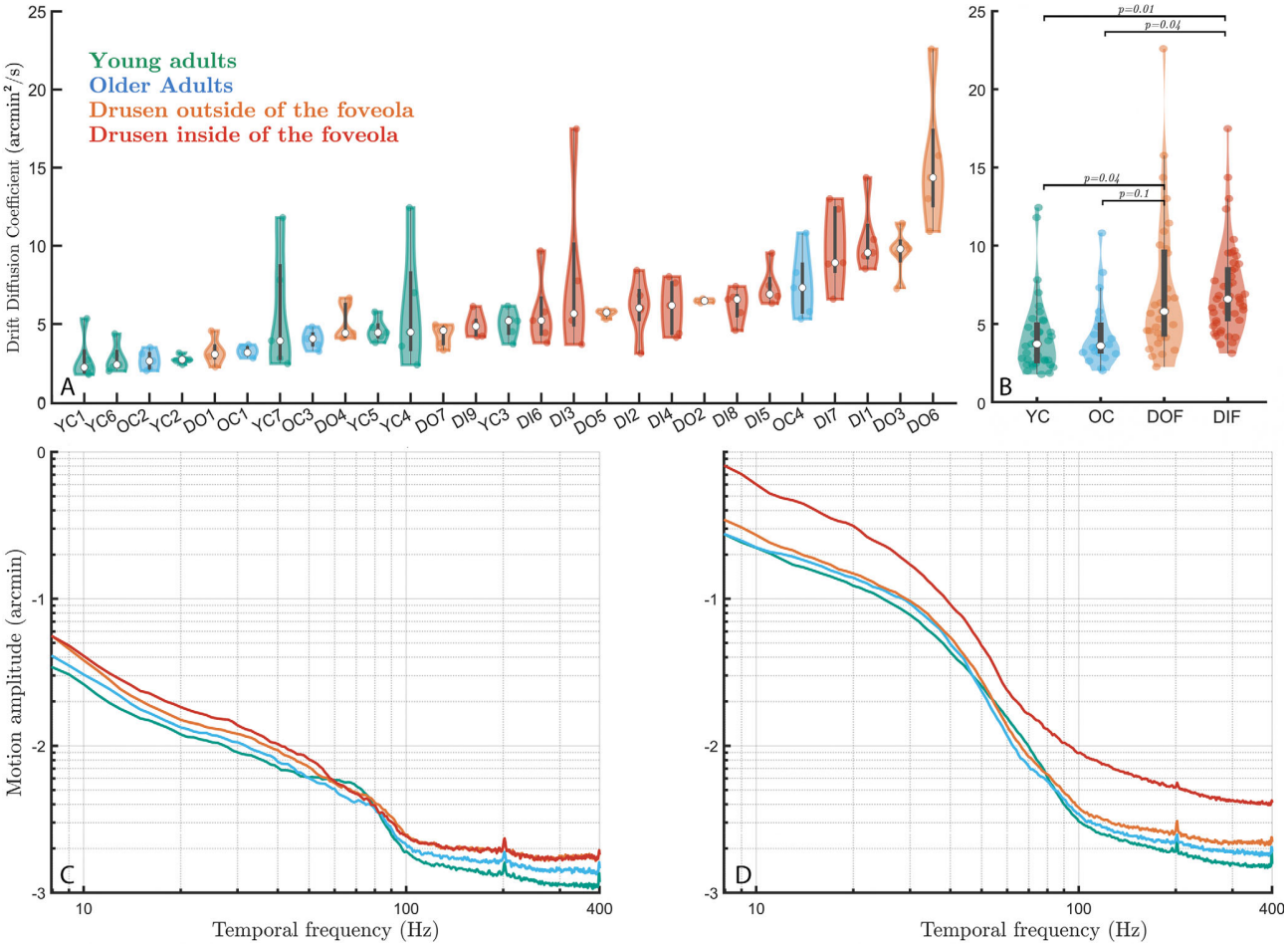

Figure 5. Drift dynamics and motion spectra across groups – horizontal motion. (**A**) Drift diffusion coefficient distribution across all participants, sorted from lowest to highest. Each *dot* is one trial. (**B**) Drift diffusion coefficient across groups. (**C**) Motion spectrum of drifts only across the four groups. (**D**) Whole motion spectrum (drifts + microsaccades) across the four groups. An increase in dynamics across most frequencies is visible with age, and even further with the presence of foveal or foveolar drusen. This progressive increase is particularly visible in the mid-frequency (10–40 Hz, *top left inset*) and very-high frequency range (100–400 Hz, *top-right inset*).

classified into two subgroups. The classification took into account the approximate diameter of the foveola (0.4–0.6 degrees[40]), of the stimulus (0.28 degrees), and of the median foveal druse (0.2 degrees). The first subgroup (named DIF, for "drusen inside the foveola") included the participants with drusen mainly located in the foveola (i.e. mean drusen eccentricity less than 1 degree with respect to the center of the fovea, $n = 8$). The other subgroup (named DOF, for "drusen outside the foveola") consisted of participants with drusen located mainly outside their foveola ($n = 8$).

Statistical analysis using linear mixed effects model revealed significant differences between the microsaccade amplitude in the DIF group and the three other groups (Fig. 4C; DIF versus young controls: $|t| = 6.5$, $P = 10^{-9}$; DIF versus older controls: $|t| = 6$, $P = 10^{-9}$; DIF versus DOF: $|t| = 5$, $P = 10^{-7}$). The group with drusen outside the foveola (DOF) tended to have larger microsaccades than young controls ($|t| = 1.7$, $P = 0.09$) and older controls ($|t| = 1.8$, $P = 0.06$). There was no difference between young and older controls ($|t| = 0.4$, $P = 0.66$).

Although no significant differences were found between groups in terms of the average drusen area, we hypothesized that large drusen closer to the center of the fovea should have an even stronger effect on microsaccade amplitude. The rapid drop-off of both cone density and acuity in the fovea suggest that both the drusen area and eccentricity can have tremendous effect on foveal vision. We therefore computed the correlation between the drusen area divided by eccentricity (that we called drusen density) and measured FEM characteristics. This new measure was indeed stronger correlated with microsaccade amplitude ($r = 0.82$, $P = 0.0001$) than the eccentricity alone. There were no statistical differences in the rate of microsaccades between groups and all participants produced approximately 1 to 3 microsaccades per second.

The above results show that drusen eccentricity, a simple property of retinal structure associated with the presymptomatic stage of AMD, is a crucial factor explaining the difference in microsaccade size between control participants and subjects with a relatively elevated risk of developing the disease. The quality of this simple structural measure in

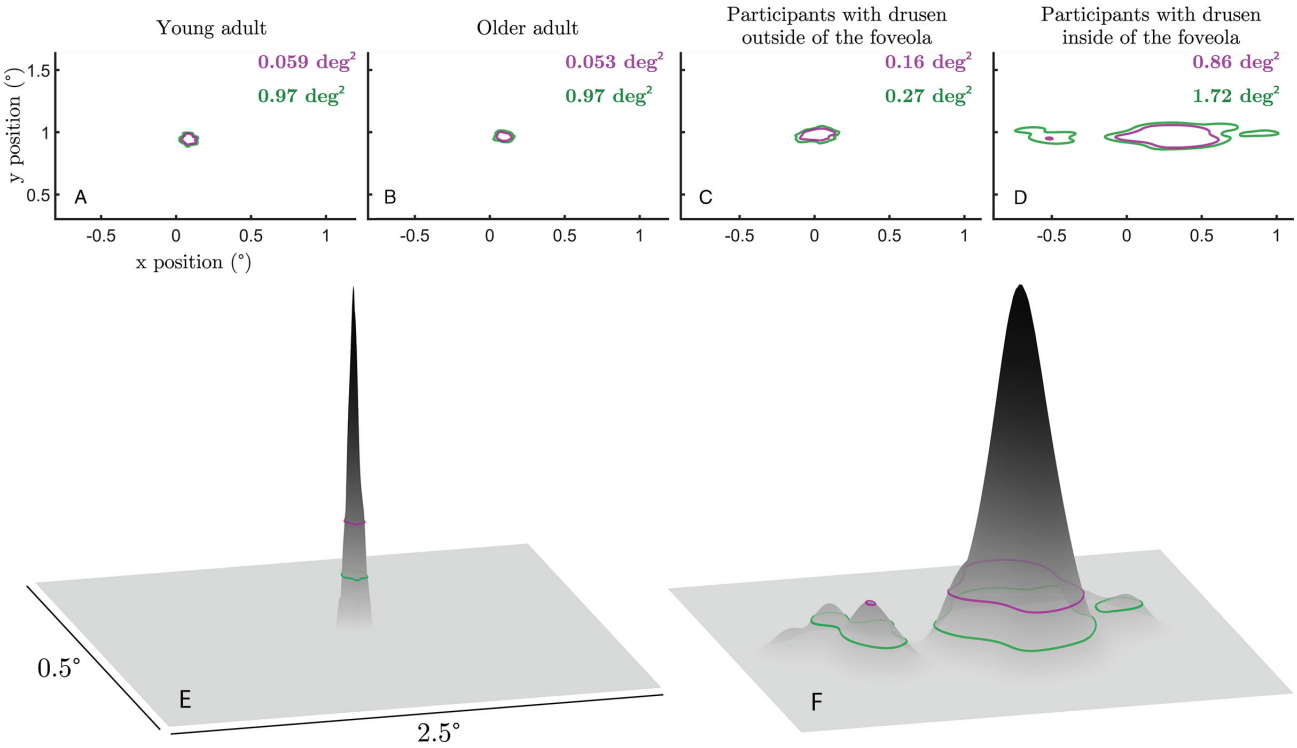

Figure 6. Impact of drusen on fixation stability. The top row shows sample data respectively from a young adult (**A**), an older adult (**B**), a participant with foveal drusen (**C**), and a participant with foveolar drusen (**D**). The bottom row show the probability density of the young adult participant of (**A**) on the *left* (**E**) and the foveolar participant of (**D**) on the *right* (**F**). ISOA contours encompassing 68% (*purple*) and 86% (*green*) of the eye position data.

explaining functional changes can be further improved by taking into account the drusen area.

Impact of Foveal Drusen on Ocular Drift and Eye Motion Spectrum

Apart from microsaccades, the ocular drift component of FEM (see Fig. 3) was also affected by the presence of foveal drusen, but to a lesser extent. Indeed, the analysis of ocular drift in the four participant groups defined in the previous section revealed significant differences in drift diffusion coefficients between participants with drusen in the foveola and control subjects (Figs. 5A, 5B; DIF versus young controls: $|t| = 2.5$, $P = 0.01$; DIF versus older controls: $|t| = 2$, $P = 0.04$). Statistical pairwise comparisons between all other groups have shown that the DOF group was significantly different from young controls ($|t| = 2$, $P = 0.04$), but not from older controls ($|t| = 1.7$, $P = 0.1$). No differences were found between young and older controls ($|t| = 0.1$, $P = 0.93$, the absence of statistical differences here should be taken with caution considering the low sample size of older controls). Individual diffusion coefficient revealed larger variability within groups but less between groups (see Figs. 5A, 5B) when compared to the mean microsaccade amplitude (see Fig. 4A). No significant correlations were found between drift diffusion coefficient and drusen properties across all subjects (eccentricity: $r = 0.09$, $P = 0.72$; drusen number: $r = -0.003$, $P = 0.99$; mean drusen area: $r = -0.1$, $P = 0.69$; and total drusen area: $r = -0.05$, $P = 0.85$).

A different way to analyze FEM changes induced by drusen presence is to look at the motion spectrum across the subject groups. The spectral analysis of ocular drift revealed a progressive increase in motion amplitude both with age and drusen centrality (see Fig. 5C), marked in the middle frequency range (10–40 Hz). No difference in motion amplitude was observed at high frequencies (100–400 Hz) between the two drusen groups, in contrast to an age-related difference in control subjects (see Fig. 5C). When accounting for the spectral changes caused by microsaccades (see Fig. 5D), the foveolar drusen group clearly stood out across all motion frequencies, potentially impeding later-stage neural processing of the visual input.[35] The differences between the two motion spectra (see Figs. 5C, 5D) reflect the statistical differences in drift diffusion coefficient between subjects groups presented above and highlight the more important role of microsaccades, compared to ocular drift, in FEM changes induced by the presence of the central drusen.

Foveolar Drusen Impair Fixation Stability

Fixational movements of the eye, including microsaccades and drift, are the primary determinants of fixational stability, a functional measure of ocular stability at the macroscopic level usually evaluated by such measures as the ISOline area[28,29] (see the Methods section). The discovered relationship between central drusen and microsaccade size, described in the previous section, suggests that a similar relationship should exist between drusen eccentricity and ocular stability in the fixation task. Indeed, we found a strong and significant negative correlation between ISOA (at 86% level) and drusen eccentricity ($r = -0.72$, $P = 0.001$) as well

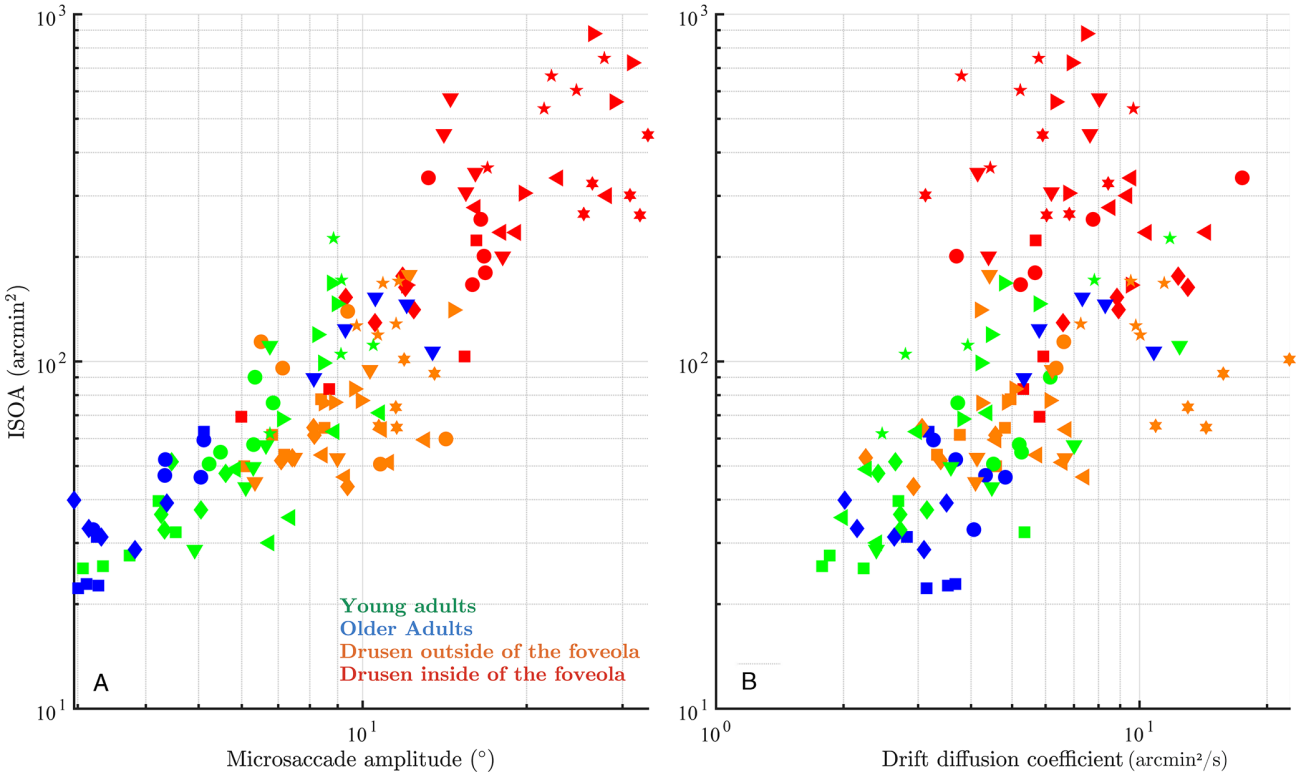

Figure 7. Contribution of microsaccade amplitude and drift coefficient to fixation stability. (**A**) Microsaccade amplitude versus 86% ISOA. (**B**) Drift coefficient versus ISOA on the *right*. One symbol represents one trial of a participant from its colored group.

as highly significant positive correlation between ISOA and drusen density ($r = 0.72$, $P = 0.0004$ across all subjects. We checked that there were no significant differences between participants in terms of microsaccade frequencies that could explain changes in fixation stability. In order to better understand the effect of drusen on fixation stability and its topological characteristics, we quantitatively compared average ISOA values across the four groups of subjects using the linear mixed modeling approach and visualized average ISOA contours (Fig. 6). The participants with drusen mainly in the foveola had the largest ISOA as compared to the other three groups (DIF versus young controls: $|t| = 5.5$, $P = 10^{-7}$; DIF versus older controls: $|t| = 4.9$, $P = 10^{-6}$; and DIF versus DOF: $|t| = 5.4$, $P = 10^{-7}$). ISOAs remained similar between the DOF group and young controls ($|t| = 0.24$, $P = 0.81$) or older controls ($|t| = 0.24$, $P = 0.67$), and between young and older controls ($|t| = 0.2$, $P = 0.83$). These results extend our conclusion from the previous section by showing that impaired fixation stability in subjects with drusen in foveola is primarily mediated by the increase in microsaccade size and not by other FEM properties, such as ocular drift.

Given the consistent and strong effect of foveal drusen on both fixation stability and microsaccade amplitude, it is not surprising that there was a strong correlation between the ISOA 86% values and microsaccade amplitudes across the entire study population (Fig. 7A; $r^2 = 0.85$, $P = 0.001$). Interestingly, when looking at Figure 7, in all groups except DIF, higher values for ISOA seemed to come with both proportional increases in microsaccade amplitude and drift diffusion coefficient at the same time. However, for the DIF group, drift diffusion coefficient appeared to lose its correlation with ISOA compared to the rest of the study population.

Discussion

The objective of the present study was to see whether structural retinal changes in presymptomatic AMD can have detectable consequences on functional aspects of vision. More specifically, we tested the hypothesis that FEM abnormalities are associated with early structural retinal anomalies, such as the appearance of small central drusen.

The primary finding of this study is that participants with foveal drusen exhibit significantly larger microsaccades and higher fixation instability (measured by ISOA) as compared with healthy controls, while maintaining equivalent microsaccade rates. Strikingly, drusen eccentricity with respect to the center of the fovea appears to be the main determinant factor associated with larger microsaccades and ISOAs. Indeed, we found that the more central the drusen were, the more unstable the fixation was; conversely, the further from the center of the fovea the drusen were, the more the participants tended to behave like controls, with minimal to no changes in fixation stability. We propose the following quantification criterion to assess the point after which drusen eccentricity strongly affect fixation characteristics: microsaccade amplitude starts increasing exponentially when average drusen eccentricity is less than 1 degree with respect to the center of the fovea. Considering the size of the typical drusen and of the fixation target, the threshold point approximately corresponds to the size of

the foveola, that is, the 350 µm foveal pit, as defined by Kolb.[40] Our results further suggest that quantification of microsaccade amplitude and ISOA in a simple ocular fixation test could in principle be sufficient to discriminate healthy participants from those with retinal anomalies in the foveola, such as drusen. Previous studies in patients with central scotomas suggest that these patients may develop one or more eccentric areas of fixation (referred to as preferred retinal locus or PRL),[41] giving rise to an extended overall fixation area. We therefore checked in our presymptomatic subjects from the DIF group whether they express increased and possibly multipeaked fixation densities (as opposed to Gaussian-like distributions expected for the other groups). This was indeed the case, as only in the DIF group the ISOA contours exhibited multiple islands of fixation (see Fig. 6). In this study, we also evaluated the impact of foveal drusen density and eccentricity on the ocular diffusion drift coefficient, which provides a displacement estimator reflecting the randomness and stability of visual fixation.[35] The motion spectrum of drift epochs without microsaccades appeared, however, impacted by the presence of drusen and their centrality, especially in the middle frequency range. The dynamics of the complete eye movements (i.e. microsaccades included) during fixation appears successively altered with age, with the presence of foveal and further with foveolar drusen. This confirms the impact of drusen on microsaccade dynamics, and the importance to finely characterize them. Further research is needed to understand the role and implication of drusen on visual sampling and perception.

Another interesting observation stemming from this study concerns the definition of healthy older adults from an ophthalmological point of view. Twenty participants of this study were initially recruited as healthy controls based on the fact that (i) no visible foveal drusen were found using standard SD-OCT imaging analyzed by ophthalmologists, and (ii) no visual symptoms (in terms of visual acuity, contrast sensitivity, and so on) were observed during inclusion to the Silversight cohort. Subsequently, using AO-FIO-based gaze-dependent retina imaging, 45% of these participants were found to actually have small drusen in their fovea. This experimental observation, made with the use of more advanced imaging technique, aligns with early studies suggesting that drusen are more prevalent than previously assumed.[42,43] It also emphasizes the utmost importance of the development of sensitive measurement techniques that can be applied at presymptomatic stages to detect the presence of small drusen. Whereas recent progress in retinal imaging resulted in retromode[44] or gaze-dependent[16] methods, which can both detect drusen invisible in standard SD-OCT images, this study opens up a new avenue in drusen detection research by showing that the appearance of small drusen can be detected based on simple functional measures, that is, by looking at the FEM. Moreover, the discovered link between central drusen and fixation stability can explain the discrepancy present in the literature regarding the differences in fixation stability between young and healthy older adults, with some studies reporting an age-related decrease in stability[45–47] and other studies, including ours, reporting no effect of age.[48–50] If the presence of foveal drusen is a common trait among older participants and these drusen do affect fixation stability, as we observe in our experiment, then the putative effect of age on fixation stability in the above studies can in fact be explained by the presence of participants with undetected central drusen in the sample of older adults (because virtually all previous studies used standard retina fundus imaging or SD-OCT). In conclusion, a combination of imaging methods and functional oculomotor measures, with a potential addition of subjective patient-reported measures of retinal health[50] can be part of the general strategy for multifactor screening for retinal diseases, including AMD, in the general population. DIF participants were clearly clustered together around higher values of both ISOA and microsaccade amplitudes, suggesting the possibility of an automatic detection procedure for the existence of foveolar drusen that could, for instance, use both ISOA and microsaccade amplitude values. Although it is currently impossible to know whether or not existing drusen will develop into severe forms of AMD,[51] detection of drusen at the earliest possible stage will allow to monitor their progression and take the necessary precautions (e.g. apply anti-VEGF treatment[4]) before critical and irreversible damage occurs. Health style changes might help slow down their growth, and new drugs are currently being clinically tested to prevent the formation and evolution of drusen.[7]

To the best of our knowledge, alterations of fine oculomotor control in relation to small, asymptomatic changes of retinal structure have never been previously reported, whereas the assessment of eye movements to identify noninvasive biomarkers of a number of diseases is not new.[52] Research on eye movements has indeed existed for more than a century, and infrared video eye trackers capabilities, accuracy, and accessibility have renewed the interest on eye movements to clinicians and psychologists. FEMs have been explored in neurological disorders, such as amblyopia,[53,54] schizophrenia,[55] Parkinson's disease,[56] and others.[57] There have also been attempts to reveal new FEM-based biomarkers to predict multiple sclerosis and follow its progression.[58] However, when it comes to detecting subtle retinal structural anomalies by means of FEM analysis, it is key to be able to record the whole spectrum of microsaccade amplitudes, down to 1 arcminute. The recent use of adaptive optics retinal imaging instruments has made it possible to reach this resolution. The AO-FIO used in this study allowed us to observe an average healthy microsaccade amplitude of 6.3 arcminutes, whereas participants with drusen had an average microsaccade amplitude of 13.8 arcminutes. In the past 20 years, FEM studies using pupil-based eye trackers have defined a microsaccade with amplitudes up to 1 to 2 degrees,[25,59–61] and basic fixation tasks often showed average microsaccade amplitudes of 20 to 60 arcminutes. It is thus possible that the differences between controls and drusen participants found in our study would not have been detected using these less precise eye trackers and/or a fixation target larger than ours, because microsaccade amplitude is known to be target-dependent.[23] Further studies are being conducted in our team to confirm such hypotheses. This study, like many in the past decade, shows that FEMs reveal a lot of unique information about patients. The system we use is probably too advanced and complex for immediate clinical use but the study is paving the road toward future FEM analysis in ophthalmologic testing with future accessible tracking methods that are starting to become available in the market.

Whereas general functional significance of microsaccades is still a matter of debate, many researchers agree that microsaccades play an important functional role in the presence of foveolar stimuli, and the foveola size is even considered as a reference to define microsaccades.[59,62] As discussed in Poletti's review on attention and eye move-

ments at the foveal scale,[59] any stimuli in the foveola can be attention-grabbing and whether it is voluntary or not, it is possible to have microsaccade directed toward different stimuli as close as 20 arcminutes from each other. It would not be correct to consider foveal drusen as inputs to the visual system, but our data suggest that they might change retinal processing in specific retinal locations. Drusen appears to distort foveal vision but the exact role of or consequence on the oculomotor system remains to be determined. Fixation instability could be the result of the oculomotor system adaptation to avoid drusen locally (as can be seen in Clip 2). The second hypothesis consists in a more widespread RPE/photoreceptor dysfunction and degraded foveal sensory integration which would in turn impair motor control. The local compensatory versus global oculomotor deficiency hypotheses require further investigation. The relative impact of each eye's drusen on binocular vision is another open subject of research to supplement these findings.

In conclusion, by combining state-of-the-art retinal imaging techniques and a novel retinal motion tracking approach, we report an association between the presence of foveal drusen and fixation instability, hence linking structural and functional changes during aging. By demonstrating a strong association between foveal drusen properties and oculomotor behavior in a simple ocular fixation task our results suggest that FEM can be considered as a functional biomarker for innovative AMD screening approaches. More generally, our results suggest a possibility that the presence of even small drusen may affect visual perception. Thus, further studies are required to test potential effects of drusen on performance in tasks requiring high visual acuity, contrast sensitivity, and photoreceptor function.

Acknowledgments

Supported by the IHU FOReSIGHT (ANR-18-IAHU-01), SilverSight (ANR-18-CHIN-0002), OPTORETINA ERC (101001841), and UNADEV/Aviesan 2020.

Disclosure: **J. Murari**, None; **J. Gautier**, None; **J. Daout**, None; **L. Krafft**, None; **P. Senée**, None; **P. Mecê**, None; **K. Grieve**, None; **W. Seiple**, None; **D. Sheynikhovich**, None; **S. Meimon**, None; **M. Paques**, None; **A. Arleo**, None

References

1. Wong WL, Su X, Li X, et al. Global prevalence of age-related macular degeneration and disease burden projection for 2020 and 2040: a systematic review and meta-analysis. *Lancet Glob Health*. 2014;2(2):e106–e116.
2. Danis RP, Lavine JA, Domalpally A. Geographic atrophy in patients with advanced dry age-related macular degeneration: current challenges and future prospects. *Clin Ophthalmol*. 2015;9:2159–2174.
3. Pugazhendhi A, Hubbell M, Jairam P, Ambati B. Neovascular macular degeneration: a review of etiology, risk factors, and recent advances in research and therapy. *Int J Mol Sci*. 2021;22(3):1170.
4. Rofagha S, Bhisitkul RB, Boyer DS, Sadda SR, Zhang K. Seven-year outcomes in ranibizumab-treated patients in ANCHOR, MARINA, and HORIZON: a multicenter cohort study (SEVEN-UP). *Ophthalmology*. 2013;120(11):2292–2299.
5. Cervantes-Castañeda RA, Banin E, Hemo I, Shpigel M, Averbukh E, Chowers I. Lack of benefit of early awareness to age-related macular degeneration. *Eye*. 2008;22(6):777–781.
6. Schultz NM, Bhardwaj S, Barclay C, Gaspar L, Schwartz J. Global burden of dry age-related macular degeneration: a targeted literature review. *Clin Ther*. 2021;43(10):1792–1818.
7. Fleckenstein M, Keenan TDL, Guymer RH, et al. Age-related macular degeneration. *Nat Rev Dis Primers*. 2021;7(1):1–25.
8. Seddon JM. Macular degeneration epidemiology: nature-nurture, lifestyle factors, genetic risk, and gene-environment interactions – The Weisenfeld Award Lecture. *Invest Ophthalmol Vis Sci*. 2017;58(14):6513–6528.
9. Verghese P, Vullings C, Shanidze N. Eye movements in macular degeneration. *Ann Rev Vis Sci*. 2021;7(1):773–791.
10. Pondorfer SG, Wintergerst MWM, Gorgi Zadeh S, et al. Association of visual function measures with drusen volume in early stages of age-related macular degeneration. *Invest Ophthalmol Vis Sci*. 2020;61(3):55.
11. Calabrese A, Bernard JB, Hoffart L, et al. Wet versus dry age-related macular degeneration in patients with central field loss: different effects on maximum reading speed. *Invest Ophthalmol Vis Sci*. 2011;52(5):2417–2424.
12. Macedo AF, Crossland MD, Rubin GS. Investigating unstable fixation in patients with macular disease. *Invest Ophthalmol Vis Sci*. 2011;52(3):1275–1280.
13. Kumar G, Chung STL. Characteristics of fixational eye movements in people with macular disease. *Invest Ophthalmol Vis Sci*. 2014;55(8):5125–5133.
14. Ağaoğlu MN, Chung STL. Exploration of the functional consequences of fixational eye movements in the absence of a fovea. *J Vision*. 2020;20(2):12.
15. LAGRENE K, Bécu M, Seiple WH, et al. Healthy and pathological visual aging in a French follow-up cohort study. *Invest Ophthalmol Vis Sci*. 2019;60(9):5915.
16. Rossi EA, Norberg N, Eandi C, et al. A new method for visualizing drusen and their progression in flood-illumination adaptive optics ophthalmoscopy. *Transl Vis Sci Technol*. 2021;10(14):19.
17. Gofas-Salas E, Mecê P, Petit C, et al. High loop rate adaptive optics flood illumination ophthalmoscope with structured illumination capability. *Appl Opt*. 2018;57(20):5635–5642.
18. Krafft L, Senée P, Gofas-Salas E, et al. Multimodal high-resolution retinal imaging using camera-based DMD-integrated adaptive optics flood-illumination ophthalmoscope. *Opt Lett*. 2023;48(14):3785–3788.
19. Krafft L, Gofas-Salas E, Lai-Tim Y, et al. Partial-field illumination ophthalmoscope: improving the contrast of a camera-based retinal imager. *Appl Opt*. 2021;60(31):9951–9956.
20. Atlan M. Ultrahigh-throughput rendering of digital holograms. In: *Imaging and Applied Optics 2018 (3D, AO, AIO, COSI, DH, IS, LACSEA, LS&C, MATH, pcAOP) (2018), Paper DM5F.4*. Washington, DC: Optica Publishing Group; 2018:DM5F.4, doi:10.1364/DH.2018.DM5F.4.
21. Mecê P. *4D Exploration of the Retina for Adaptive Optics-Assisted Laser Photocoagulation*. PhD Thesis. These de doctorat, Paris, France: Sorbonne Paris Cité; 2018.
22. Mece P, Chen A, Petit C, Mugnier L, Paques M, Meimon S. Real-time optical stabilization of retinal motion at micrometer precision using adaptive optics flood-illumination ophthalmsocope. *Optica Open*. Preprint. Published online December 28, 2023, https://doi.org/10.1364/opticaopen.24907464.v1.
23. Bowers NR, Gautier J, Lin S, Roorda A. Fixational eye movements in passive versus active sustained fixation tasks. *J Vision*. 2021;21(11):16.
24. Engbert R. Microsaccades: a microcosm for research on oculomotor control, attention, and visual perception. In: Martinez-Conde S, Macknik SL, Martinez LM, Alonso JM, Tse PU, Eds. *Progress in Brain Research*. Vol. 154. Visual Perception. New York, NY: Elsevier; 2006:177–192, doi:10.1016/S0079-6123(06)54009-9.

25. Holmqvist K, Nyström M, Andersson R, Dewhurst R, Jarodzka H, Van de Weijer J. *Eye Tracking: A Comprehensive Guide to Methods and Measures*. Oxford, England, UK: OUP Oxford; 2011.
26. Holmqvist K, Örbom SL, Hooge ITC, et al. Eye tracking: empirical foundations for a minimal reporting guideline. *Behav Res*. 2023;55(1):364–416.
27. Niehorster DC, Zemblys R, Beelders T, Holmqvist K. Characterizing gaze position signals and synthesizing noise during fixations in eye-tracking data. *Behav Res Methods*. 2020;52:2515–2534.
28. Whittaker SG, Budd J, Cummings RW. Eccentric fixation with macular scotoma. *Invest Ophthalmol Vis Sci*. 1988;29(2):268–278.
29. Castet E, Crossland M. Quantifying eye stability during a fixation task: a review of definitions and methods. *Seeing Perceiving*. 2012;25(5):449–469.
30. Martinez-Conde S, Macknik SL, Troncoso XG, Dyar TA. Microsaccades counteract visual fading during fixation. *Neuron*. 2006;49(2):297–305.
31. Otero-Millan J, Troncoso XG, Macknik SL, Serrano-Pedraza I, Martinez-Conde S. Saccades and microsaccades during visual fixation, exploration, and search: Foundations for a common saccadic generator. *J Vision*. 2008;8(14):21.
32. Wang B, Shi W, Miao Z. Confidence analysis of standard deviational ellipse and its extension into higher dimensional euclidean space. *PLoS One*. 2015;10(3):e0118537.
33. Intoy J, Rucci M. Finely tuned eye movements enhance visual acuity. *Nat Commun*. 2020;11(1):795.
34. Engbert R, Kliegl R. Microsaccades keep the eyes' balance during fixation. *Psychol Sci*. 2004;15:431–436, https://journals.sagepub.com/doi/abs/10.1111/j.0956-7976.2004.00697.x.
35. Kuang X, Poletti M, Victor JD, Rucci M. Temporal encoding of spatial information during active visual fixation. *Curr Biol*. 2012;22(6):510–514.
36. Thomson DJ. Spectrum estimation and harmonic analysis. *Proceedings of the IEEE*. 1982;70(9):1055–1096.
37. Babadi B, Brown EN. A review of multitaper spectral analysis. *IEEE Trans Biomed Eng*. 2014;61(5):1555–1564.
38. Holmqvist K, Blignaut P. Small eye movements cannot be reliably measured by video-based P-CR eye-trackers. *Behav Res*. 2020;52(5):2098–2121.
39. Holmqvist K, Orbom SL, Miller M, Kashchenevsky A, Shovman MM, Greenlee MW. Validation of a prototype hybrid eye-tracker against the DPI and the Tobii Spectrum. In: *ACM Symposium on Eye Tracking Research and Applications*. ACM; 2020:1–9.
40. Kolb H, Nelson RF, Ahnelt PK, Ortuño-Lizarán I, Cuenca N. The Architecture of the Human Fovea. In: Kolb H, Fernandez E, Nelson R, eds. *Webvision: The Organization of the Retina and Visual System*. Salt Lake City, UT: University of Utah Health Sciences Center; 1995. Accessed October 23, 2023, http://www.ncbi.nlm.nih.gov/books/NBK554706/.
41. Duret F, Issenhuth M, Safran AB. Combined use of several preferred retinal loci in patients with macular disorders when reading single words. *Vision Res*. 1999;39(4):873–879.
42. Klein R, Klein BEK, Linton KLP. Prevalence of age-related maculopathy: The Beaver Dam Eye Study. *Ophthalmology*. 1992;99(6):933–943.
43. Bressler NM, Bressler SB, West SK, Fine SL, Taylor HR. The grading and prevalence of macular degeneration in Chesapeake Bay Watermen. *Arch Ophthalmol*. 1989;107(6):847–852.
44. Cozzi M, Monteduro D, Airaldi M, et al. Retromode imaging technology for detecting drusen-like deposits in healthy adults. *Ophthalmol Retina*. 2023;7:1051–1058.
45. Cutini A, Fragiotta S, Spadea L, et al. Normal values and repeatibility of bivariate contour ellipse area (BCEA) with Microperimeter Mp-1. *Invest Ophthalmol Vis Sci*. 2014;55(13):169.
46. Agathos CP, Bernardin D, Huchet D, Scherlen AC, Assaiante C, Isableu B. Sensorimotor and cognitive factors associated with the age-related increase of visual field dependence: a cross-sectional study. *AGE*. 2015;37(4):67.
47. Morales MU, Saker S, Wilde C, et al. Reference clinical database for fixation stability metrics in normal subjects measured with the MAIA microperimeter. *Transl Vis Sci Technol*. 2016;5(6):6.
48. Kosnik W, Fikre J, Sekulerf R. Visual fixation stability in older adults. *Invest Ophthalmol Vis Sci*. 1986;27(12):1720–1725.
49. González EG, Mandelcorn MS, Mandelcorn ED, Tarita-Nistor L. Effect of visual feedback on the eye position stability of patients with AMD. *Vision*. 2019;3(4):59.
50. Bécu M. *Impact of Healthy Aging on Spatial Cognition. Spatial Navigation and Gaze Dynamics in Ecological Conditions*. Phdthesis. Paris, France: Sorbonne Université; 2018. Accessed October 2, 2023, https://theses.hal.science/tel-02862784.
51. Ferris FL, Wilkinson CP, Bird A, et al. Clinical classification of age-related macular degeneration. *Ophthalmology*. 2013;120(4):844–851.
52. Marandi RZ, Gazerani P. Aging and eye tracking: in the quest for objective biomarkers. *Future Neurology*. 2019;14(4):FNL33.
53. Shaikh AG, Otero-Millan J, Kumar P, Ghasia FF. Abnormal fixational eye movements in amblyopia. Martinez-Conde S, ed. *PLoS One*. 2016;11(3):e0149953.
54. Ghasia F, Wang J. Amblyopia and fixation eye movements. *J Neurol Sci*. 2022;441:120373.
55. Egaña J, Devia C, Mayol R, et al. Small saccades and image complexity during free viewing of natural images in schizophrenia. *Front Psychiatry*. 2013;4:37. Accessed October 2, 2023, https://www.frontiersin.org/articles/10.3389/fpsyt.2013.00037.
56. Kaski D, Bronstein AM. Ocular tremor in Parkinson's disease: discussion, debate, and controversy. *Front Neurol*. 2017;8:134. Accessed May 24, 2022, https://www.frontiersin.org/article/10.3389/fneur.2017.00134.
57. Alexander RG, Macknik SL, Martinez-Conde S. Microsaccade characteristics in neurological and ophthalmic disease. *Front Neurol*. 2018;9:144. Accessed July 18, 2023, https://www.frontiersin.org/articles/10.3389/fneur.2018.00144.
58. Sheehy CK, Bensinger ES, Romeo A, et al. Fixational microsaccades: a quantitative and objective measure of disability in multiple sclerosis. *Mult Scler*. 2020;26(3):343–353.
59. Poletti M. An eye for detail: eye movements and attention at the foveal scale. *Vis Res*. 2023;211:108277.
60. Steinman RM, Cunitz RJ, Timberlake GT, Herman M. Voluntary control of microsaccades during maintained monocular fixation. *Science*. 1967;155(3769):1577–1579.
61. Collewijn H, Kowler E. The significance of microsaccades for vision and oculomotor control. *J Vis*. 2008;8(14):20.
62. Martinez-Conde S, Otero-Millan J, Macknik SL. The impact of microsaccades on vision: towards a unified theory of saccadic function. *Nat Rev Neurosci*. 2013;14(2):83–96.

Investigative Ophthalmology & Visual Science

Appendix B

Implementation of a Laser Doppler Holography setup to study neurovascular coupling

B.0.1 Motivation

At the beginning of my thesis, three systems showed significant potential for studying neurovascular coupling. The DMD-integrated AO-FIO, the AO-CRSO and a Laser Doppler Holography (LDH) setup. My interest in LDH for studying neurovascular coupling was motivated by the work of Michael Atlan's group, which demonstrated the capability of Laser Doppler Holography for blood flow imaging in the retina [106, 107]. The ability of this system to generate blood flow contrasted images with a wide field of view and high temporal resolution is particularly promising for studying neurovascular coupling, as it could provide a detailed view of blood flow changes in the retina in response to flicker stimulation.

My goal was to replicate the LDH setup, adapt it for studying neurovascular coupling and investigate how to improve the transverse resolution and sensitivity of this system as capillaries, small venules and arterioles are not currently visible with the system used by Michael Atlan's team. The initial goal was the development of a computational adaptive optics correction to improve the transverse resolution of the system.

During my PhD thesis, I worked concurrently on both the AO-CRSO system and the LDH. However, the AO-CRSO system showed promising results early on, particularly in observing blood vessel dilation during flicker tests. Given that arterial dilation is a key driver of functional hyperemia, I decided to prioritize my efforts on the AO-CRSO system as my research progressed. While I did replicate an LDH setup at ONERA and took initial steps to adapt it for studying neurovascular coupling, I did not pursue improvements to the system's transverse resolution, choosing instead to focus on the AO-CRSO system. The preliminary work that I have done with this system is presented in this appendix.

B.0.2 System description

Laser Doppler Holography (LDH) operates on the principle of digital holography, where an interference pattern is created between a wave scattered by an object and a reference wave. This pattern is imaged by a 2D camera. By numerically reconstructing the recorded hologram

using wave propagation formulas derived from Fourier optics theory, the object wave field can be retrieved [108].

In Doppler holography, the optical field backscattered by the retina is frequency shifted due to the movement of red blood cells. When this Doppler-shifted light interferes with the non-Doppler-shifted reference wave on the camera, the resulting interferogram is temporally modulated at a frequency corresponding to the Doppler shift caused by the moving red blood cells [106]. By recording these interferograms with a high-speed camera and applying a short-time Fourier transform analysis, the Doppler frequency shift can be measured, allowing for the reconstruction of motion contrast images that reveal the blood vessels of the retina. (More details in image processing section).

B.0.3 Optical setup

The optical setup of the system is represented in figure B.1 A), it similar to an interferometer in a Mach-Zehnder configuration. The light from a 785 nm single-mode fiber laser diode is split into two beams, one going to the eye (object arm) and one going directly to the camera (reference arm). A Polarizing Beam Splitter (PBS) cube is used in the object arm to illuminate the eye and collect the light backscattered by the retina. The light sent to the eye is linearly polarized, but only the cross-polarized component of the light backscattered by the retina is transmitted by the polarizing beam splitter. This is done to reduce stray light and to favor multiply scattered photons which have lost their initial polarization but also carry the Doppler broadened signal [106]. The object and reference waves are combined using a non-polarizing beam splitter cube and interfere on the sensor of the camera. The recorded interferogram are then processed to give the final angiographic images.

A picture of the optical setup that I used during my PhD thesis is shown in figure B.1 B). The optical elements are the same as the ones described in figure B.1 A) with two exceptions: instead of a converging lens at L1, a diffuser is used. This modification prevents the illumination beam from being focused on the cornea, thereby improving ocular safety. Furthermore instead of using two cameras, I am only using one fast camera. The camera used in my setup is the Phantom S710 (Ametek), which is capable of recording 512x512 pixel images at a rate of 20 kHz. A high frame rate is crucial for LDH, as the largest Doppler frequency shifts caused by the movement of red blood cells can reach 30-40 kHz at the central retinal artery [109]. According to the Nyquist theorem, a camera with a frame rate of around 70 kHz would be required to sample these frequencies. However, except for large arteries close the the central retinal artery, blood flow is slow enough in most vessels of the retina to be sampled with our camera.

In terms of ocular safety, the system conformed to the ISO 15004-2:2007 standard, which sets illumination limits for ophthalmic instruments. A total optical power of 1.5 mW was directed toward the eye while ensuring that the illuminance remained within the permissible limit across the entire cornea.

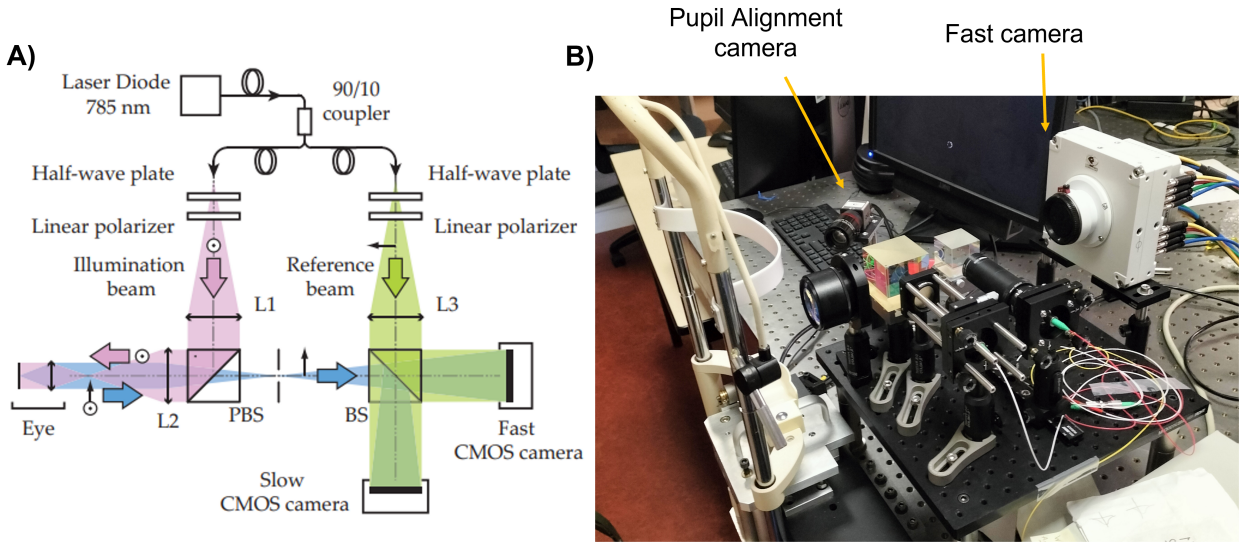

Figure B.1: A) Schematics of the Laser Doppler Holography setup, from Leo Puyo et al. [106] B) Image of my LDH setup at ONERA

B.0.4 Image processing

In Laser Doppler Holography, the optical setup is rather simple, all the complexity relies in the image processing to get from the recorded interferogram to a final angiographic image. To process the images, I used the software Holovibes [96] developed by Michael Atlan. It is an open source software enabling high speed image rendering of laser doppler holography images. The different steps of the image processing pipeline are detailed in Leo Puyo's thesis [110] and can be roughly described in the following few steps schematically described in the diagram represented in figure B.2.

- **Hologram rendering:** The camera records interferograms between the object wave and the reference wave in the sensor plane. To achieve a final image of the retina, the object wave is first numerically propagated in the plane of the retina. To achieve this numerical propagation, different methods can be used. In Holovibes two methods are available: The Fresnel method, relying on the Fresnel-Huygens principle and the angular spectrum method, relying on the Fourier decomposition of the electrical field [108].
- **Hologram to power spectral density:** In LDH, the Doppler frequency shift is measured from the hologram beat frequency [106]. Therefore, the power spectral density of the recorded hologram stream is measured. This is done either by Short Time Fourier Transform (STFT) or by Principal Component Analysis (PCA) [111].
- **Spectral density to final image:** To get the final angiographic image, the measured power spectral density is integrated over the frequency corresponding to the red blood cells' Doppler frequency shift. By eliminating low frequencies, static features and slow moving features can be removed, with only the blood vessels remaining on the final images.

In addition, because the wave field is numerically propagated, all sorts of numerical manipulation of the wave field are possible, for instance the use of computational adaptive optics [112].

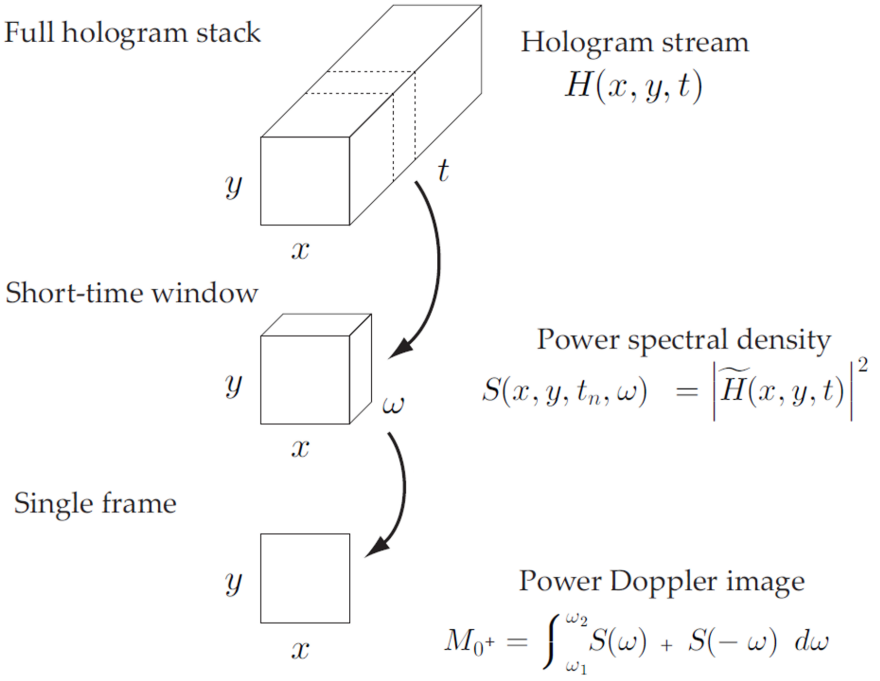

Figure B.2: Schematic Representation of a Power Doppler Image Formation from a Hologram stream. Adapted from Puyo et al. [106]

B.0.5 First image with my setup

The optical setup illustrated in figure B.1 B) was assembled, and preliminary images were acquired from a healthy subject. An example of an image captured using this setup is shown in figure B.3. The image, centered on the optic disc, reveals the largest veins and arteries of the retina. Additionally, some pulsativity (variations in contrast of the arteries with each heartbeat) could be observed in the recorded videos. The field of view is relatively wide ($\approx$ 20° x 20°) and vessels with diameters of 10-15 µm or larger can be resolved, smaller vessels and capillaries are not visible on our setup.

B.0.6 Future work

Preliminary steps were taken in order to explore neurovascular coupling using laser Doppler holography. A stimulation channel to make flicker tests was implemented into the system by positioning a screen in front of the second beam splitter cube (See figure B.4 below). Given the large field of view of the system, it presents a compelling opportunity to investigate variations in retinal blood flow in response to flicker stimulation. Such changes should be visible in LDH images as thickening and increased intensity of the retinal vessels. Furthermore, work is in progress in Michael Atlan's team to derive quantitative measurements in terms of blood velocity and blood flow from LDH images. This improvement would provide quantitative assessment of the increase in blood flow during a flicker test, allowing for instance, the identification of specific arteries responsible for localized changes in blood flow when a region of the retina is exposed to flicker stimulation.

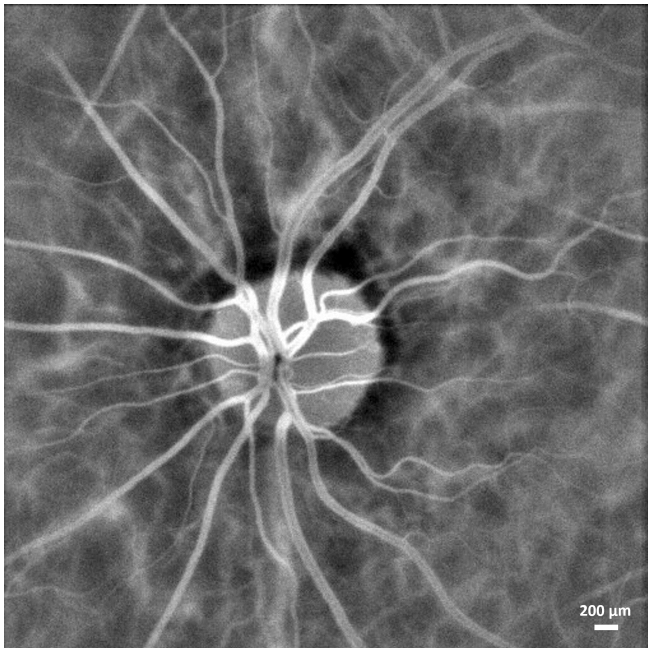

Figure B.3: Average image, centered on the optical disc, taken with my Laser Doppler Holography setup

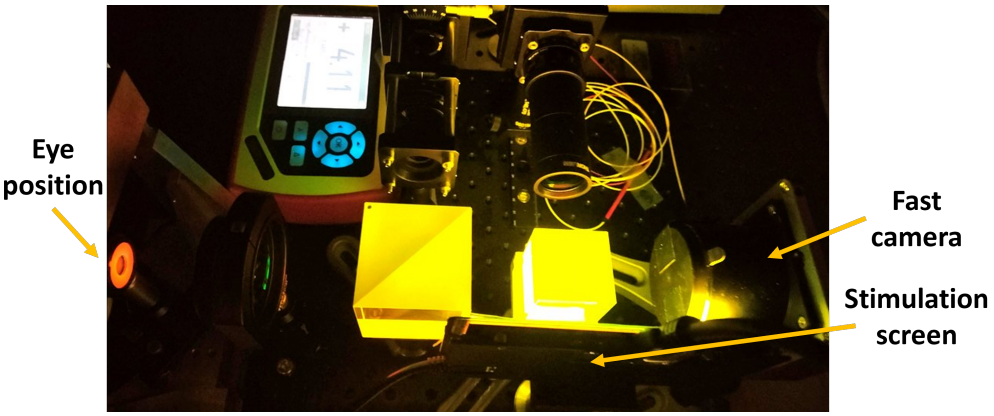

Figure B.4: A stimulation screen was placed in front of the second beam splitter cube to enable flicker stimulation with the LDH setup

Bibliography

[1] Suzana Herculano-Houzel. The Human Brain in Numbers: A Linearly Scaled-up Primate Brain. *Frontiers in Human Neuroscience*, 3:31, November 2009.

[2] C. S. Roy and C. S. Sherrington. On the Regulation of the Blood-supply of the Brain. *The Journal of Physiology*, 11(1-2):85–158.17, January 1890.

[3] S Ogawa, T M Lee, A R Kay, and D W Tank. Brain magnetic resonance imaging with contrast dependent on blood oxygenation. *Proceedings of the National Academy of Sciences*, 87(24):9868–9872, December 1990.

[4] Costantino Iadecola. The Neurovascular Unit Coming of Age: A Journey through Neurovascular Coupling in Health and Disease. *Neuron*, 96(1):17–42, September 2017.

[5] Gary H. Glover. Overview of Functional Magnetic Resonance Imaging. *Neurosurgery clinics of North America*, 22(2):133–139, April 2011.

[6] C. W. Leffler, D. W. Busija, R. Mirro, W. M. Armstead, and D. G. Beasley. Effects of ischemia on brain blood flow and oxygen consumption of newborn pigs. *American Journal of Physiology-Heart and Circulatory Physiology*, 257(6):H1917–H1926, December 1989. Publisher: American Physiological Society.

[7] Helene Girouard and Costantino Iadecola. Neurovascular coupling in the normal brain and in hypertension, stroke, and Alzheimer disease. *Journal of Applied Physiology*, 100(1):328–335, January 2006. Publisher: American Physiological Society.

[8] Monica R. Metea and Eric A. Newman. Glial Cells Dilate and Constrict Blood Vessels: A Mechanism of Neurovascular Coupling. *The Journal of Neuroscience*, 26(11):2862–2870, March 2006.

[9] Eric A. Newman. Functional hyperemia and mechanisms of neurovascular coupling in the retinal vasculature. *Journal of Cerebral Blood Flow and Metabolism: Official Journal of the International Society of Cerebral Blood Flow and Metabolism*, 33(11):1685–1695, November 2013.

[10] Kassandra Kisler, Amy R. Nelson, Axel Montagne, and Berislav V. Zlokovic. Cerebral blood flow regulation and neurovascular dysfunction in Alzheimer's disease. *Nature reviews. Neuroscience*, 18(7):419–434, July 2017.

[11] G Garhöfer, C Zawinka, H Resch, P Kothy, L Schmetterer, and G T Dorner. Reduced response of retinal vessel diameters to flicker stimulation in patients with diabetes. *The British Journal of Ophthalmology*, 88(7):887–891, July 2004.

[12] Amir H. Kashani, Samuel Asanad, Jane W. Chan, Maxwell B. Singer, Jiong Zhang, Mona Sharifi, Maziyar M. Khansari, Farzan Abdolahi, Yonggang Shi, Alessandro Biffi, Helena Chui, and John M. Ringman. Past, present and future role of retinal imaging in neurodegenerative disease. *Progress in Retinal and Eye Research*, 83:100938, July 2021.

[13] F. Formaz, C. E. Riva, and M. Geiser. Diffuse luminance flicker increases retinal vessel diameter in humans. *Current Eye Research*, 16(12):1252–1257, December 1997.

[14] Kaija Polak, Leopold Schmetterer, and Charles E. Riva. Influence of flicker frequency on flicker-induced changes of retinal vessel diameter. *Investigative Ophthalmology and Visual Science*, 43(8):2721–2726, August 2002.

[15] Edgar Nagel, Walthard Vilser, and Ines Lanzl. Age, blood pressure, and vessel diameter as factors influencing the arterial retinal flicker response. *Investigative Ophthalmology and Visual Science*, 45(5):1486–1492, May 2004.

[16] C. E. Riva, S. Harino, B. L. Petrig, and R. D. Shonat. Laser Doppler flowmetry in the optic nerve. *Experimental Eye Research*, 55(3):499–506, September 1992.

[17] C. E. Riva, S. Harino, R. D. Shonat, and B. L. Petrig. Flicker evoked increase in optic nerve head blood flow in anesthetized cats. *Neuroscience Letters*, 128(2):291–296, July 1991.

[18] Charles E. Riva, Martial Geiser, Benno L. Petrig, and Beijing 100193, PR China Ocular Blood Flow Research Association. Ocular blood flow assessment using continuous laser Doppler flowmetry. *Acta Ophthalmologica*, 88(6):622–629, September 2010.

[19] Junzhong Liang, David R. Williams, and Donald T. Miller. Supernormal vision and high-resolution retinal imaging through adaptive optics. *JOSA A*, 14(11):2884–2892, November 1997. Publisher: Optica Publishing Group.

[20] Austin Roorda, Fernando Romero-Borja, William J. Donnelly III, Hope Queener, Thomas J. Hebert, and Melanie C.W. Campbell. Adaptive optics scanning laser ophthalmoscopy. *Opt. Express*, 10(9):405–412, May 2002.

[21] Yusufu N. Sulai, Drew Scoles, Zachary Harvey, and Alfredo Dubra. Visualization of retinal vascular structure and perfusion with a nonconfocal adaptive optics scanning light ophthalmoscope. *JOSA A*, 31(3):569–579, March 2014. Publisher: Optica Publishing Group.

[22] Toco Y. P. Chui, Dean A. VanNasdale, and Stephen A. Burns. The use of forward scatter to improve retinal vascular imaging with an adaptive optics scanning laser ophthalmoscope. *Biomedical Optics Express*, 3(10):2537–2549, October 2012. Publisher: Optica Publishing Group.

[23] Drew Scoles, Yusufu N. Sulai, and Alfredo Dubra. In vivo dark-field imaging of the retinal pigment epithelium cell mosaic. *Biomedical Optics Express*, 4(9):1710–1723, August 2013.

[24] Elena Gofas Salas. *Manipulation of the illumination of an Adaptive Optics Flood Illumination Ophthalmoscope for functional imaging of the retina in-vivo*. These de doctorat, Sorbonne université, January 2019.

[25] Léa Krafft. *Spatial filtering for flood illumination ophthalmoscope*. These de doctorat, université Paris-Saclay, October 2022.

[26] Léa Krafft, Elena Gofas-Salas, Yann Lai-Tim, Michel Paques, Laurent Mugnier, Olivier Thouvenin, Pedro Mecê, and Serge Meimon. Partial-field illumination ophthalmoscope: improving the contrast of a camera-based retinal imager. *Applied Optics*, 60(31):9951–9956, November 2021. Publisher: Optica Publishing Group.

[27] Mark B. Vestergaard, Jette L. Frederiksen, Henrik B. W. Larsson, and Stig P. Cramer. Cerebrovascular Reactivity and Neurovascular Coupling in Multiple Sclerosis—A Systematic Review. *Frontiers in Neurology*, 13:912828, June 2022.

[28] Martin Prince, Gemma-Claire Ali, Maëlenn Guerchet, A. Matthew Prina, Emiliano Albanese, and Yu-Tzu Wu. Recent global trends in the prevalence and incidence of dementia, and survival with dementia. *Alzheimer's Research & Therapy*, 8:23, July 2016.

[29] World Alzheimer Report 2015, The Global Impact of Dementia: An analysis of prevalence, incidence, cost and trends.

[30] Ying Zhang, Yanjiang Wang, Ce Shi, Meixiao Shen, and Fan Lu. Advances in retina imaging as potential biomarkers for early diagnosis of Alzheimer's disease. *Translational Neurodegeneration*, 10:6, February 2021.

[31] Konstantin Kotliar, Christine Hauser, Marion Ortner, Claudia Muggenthaler, Janine Diehl-Schmid, Susanne Angermann, Alexander Hapfelmeier, Christoph Schmaderer, and Timo Grimmer. Altered neurovascular coupling as measured by optical imaging: a biomarker for Alzheimer's disease. *Scientific Reports*, 7(1):12906, October 2017.

[32] Vision impairment and blindness.

[33] Lauren K. Wareham and David J. Calkins. The Neurovascular Unit in Glaucomatous Neurodegeneration. *Frontiers in Cell and Developmental Biology*, 8:452, June 2020.

[34] Amélie Lecleire-Collet, Isabelle Audo, Mounir Aout, Jean-François Girmens, Rénata Sofroni, Ali Erginay, Jean-François Le Gargasson, Saddek Mohand-Saïd, Taly Meas, Pierre-Jean Guillausseau, Eric Vicaut, Michel Paques, and Pascale Massin. Evaluation of Retinal Function and Flicker Light-Induced Retinal Vascular Response in Normotensive Patients with Diabetes without Retinopathy. *Investigative Ophthalmology and Visual Science*, 52(6):2861–2867, May 2011.

[35] Yi Stephanie Zhang, Ilda Mucollari, Changyow C. Kwan, Gianna Dingillo, Jaspreet Amar, Gregory W. Schwartz, and Amani A. Fawzi. Reversed Neurovascular Coupling on Optical Coherence Tomography Angiography Is the Earliest Detectable Abnormality before Clinical Diabetic Retinopathy. *Journal of Clinical Medicine*, 9(11):3523, November 2020. Number: 11 Publisher: Multidisciplinary Digital Publishing Institute.

[36] Adrian Glasser and Melanie C. W. Campbell. Presbyopia and the optical changes in the human crystalline lens with age. *Vision Research*, 38(2):209–229, January 1998.

[37] David A. Atchison and George Smith. Chapter 1 - The human eye: an overview. In David A. Atchison and George Smith, editors, *Optics of the Human Eye*, pages 3–10. Butterworth-Heinemann, Edinburgh, 2000.

[38] Pablo Artal. Optics of the eye and its impact in vision: a tutorial. *Advances in Optics and Photonics*, 6(3):340–367, September 2014. Publisher: Optica Publishing Group.

[39] Fuensanta A. Vera-Díaz, Nathan Doble, Fuensanta A. Vera-Díaz, and Nathan Doble. The Human Eye and Adaptive Optics. In *Topics in Adaptive Optics*. IntechOpen, January 2012.

[40] A. Roorda, C. A. Garcia, J. A. Martin, S. Poonja, H. Queener, F. Romero-Borja, R. Sepulveda, K. Venkateswaran, and Y. Zhang. What can adaptive optics do for a scanning laser ophthalmoscope ? *Bulletin De La Societe Belge D'ophtalmologie*, (302):231–244, 2006.

[41] Jason Porter, Antonio Guirao, Ian G. Cox, and David R. Williams. Monochromatic aberrations of the human eye in a large population. *JOSA A*, 18(8):1793–1803, August 2001. Publisher: Optica Publishing Group.

[42] Larry N. Thibos, Xin Hong, Arthur Bradley, and Xu Cheng. Statistical variation of aberration structure and image quality in a normal population of healthy eyes. *Journal of the Optical Society of America. A, Optics, Image Science, and Vision*, 19(12):2329–2348, December 2002.

[43] Luis Diaz-Santana, Cristiano Torti, Ian Munro, Paul Gasson, and Chris Dainty. Benefit of higher closed-loop bandwidths in ocular adaptive optics. *Optics Express*, 11(20):2597–2605, October 2003.

[44] P. A. Howarth and A. Bradley. The longitudinal chromatic aberration of the human eye, and its correction. *Vision Research*, 26(2):361–366, 1986.

[45] Robert J. Noll. Zernike polynomials and atmospheric turbulence*. *JOSA*, 66(3):207–211, March 1976. Publisher: Optica Publishing Group.

[46] Susana Martinez-Conde, Stephen L. Macknik, and David H. Hubel. The role of fixational eye movements in visual perception. *Nature Reviews Neuroscience*, 5(3):229–240, March 2004. Publisher: Nature Publishing Group.

[47] Pedro Mecê, Jessica Jarosz, Jean-Marc Conan, Cyril Petit, Kate Grieve, Michel Paques, and Serge Meimon. Fixational eye movement: a negligible source of dynamic aberration. *Biomedical Optics Express*, 9(2):717–727, January 2018.

[48] Roy M. Pritchard. Stabilized Images on the Retina. *Scientific American*, 204(6):72–79, 1961. Publisher: Scientific American, a division of Nature America, Inc.

[49] Jing Lu, Boyu Gu, Xiaolin Wang, and Yuhua Zhang. High-speed adaptive optics line scan confocal retinal imaging for human eye. *PLOS ONE*, 12(3):e0169358, March 2017. Publisher: Public Library of Science.

[50] Elena Gofas-Salas, Pedro Mecê, Cyril Petit, Jessica Jarosz, Laurent M. Mugnier, Aurélie Montmerle Bonnefois, Kate Grieve, José Sahel, Michel Paques, and Serge Meimon. High loop rate adaptive optics flood illumination ophthalmoscope with structured illumination capability. *Applied Optics*, 57(20):5635–5642, July 2018.

[51] Simple Anatomy of the Retina by Helga Kolb – Webvision.

[52] Richard H. Masland. The Neuronal Organization of the Retina. *Neuron*, 76(2):266–280, October 2012.

[53] Marianthi Karali and Sandro Banfi. Inherited Retinal Dystrophies: The role of gene expression regulators. *The international journal of biochemistry & cell biology*, 61, February 2015.

[54] Robert S. Molday and Orson L. Moritz. Photoreceptors at a glance. *Journal of Cell Science*, 128(22):4039–4045, November 2015.

[55] Heidi Hofer, Joseph Carroll, Jay Neitz, Maureen Neitz, and David R. Williams. Organization of the human trichromatic cone mosaic. *The Journal of Neuroscience: The Official Journal of the Society for Neuroscience*, 25(42):9669–9679, October 2005.

[56] Austin Roorda and David R. Williams. The arrangement of the three cone classes in the living human eye. *Nature*, 397(6719):520–522, February 1999. Publisher: Nature Publishing Group.

[57] Debarshi Mustafi, Andreas H. Engel, and Krzysztof Palczewski. Structure of cone photoreceptors. *Progress in Retinal and Eye Research*, 28(4):289–302, July 2009.

[58] D. A. Baylor, B. J. Nunn, and J. L. Schnapf. Spectral sensitivity of cones of the monkey Macaca fascicularis. *The Journal of Physiology*, 390:145–160, September 1987.

[59] Joanna Kur, Eric A. Newman, and Tailoi Chan-Ling. Cellular and physiological mechanisms underlying blood flow regulation in the retina and choroid in health and disease. *Progress in Retinal and Eye Research*, 31(5):377–406, September 2012.

[60] Raymond E. *Physiology of the Human Eye and Visual System*. Harper & Row, 1979.

[61] B Anand-Apte and JG Hollyfield. Encyclopedia of the eye, 2010.

[62] J. P. Campbell, M. Zhang, T. S. Hwang, S. T. Bailey, D. J. Wilson, Y. Jia, and D. Huang. Detailed Vascular Anatomy of the Human Retina by Projection-Resolved Optical Coherence Tomography Angiography. *Scientific Reports*, 7(1):42201, February 2017. Publisher: Nature Publishing Group.

[63] Stéphane Fouquet, Ophélie Vacca, Florian Sennlaub, and Michel Paques. The 3D Retinal Capillary Circulation in Pigs Reveals a Predominant Serial Organization. *Investigative Ophthalmology and Visual Science*, 58(13):5754–5763, November 2017.

[64] Shelley Mo, Erika Phillips, Brian D. Krawitz, Reena Garg, Sarwat Salim, Lawrence S. Geyman, Eleni Efstathiadis, Joseph Carroll, Richard B. Rosen, and Toco Y. P. Chui. Visualization of Radial Peripapillary Capillaries Using Optical Coherence Tomography Angiography: The Effect of Image Averaging. *PLoS ONE*, 12(1):e0169385, January 2017.

[65] Danuta M. Sampson, Adam M. Dubis, Fred K. Chen, Robert J. Zawadzki, and David D. Sampson. Towards standardizing retinal optical coherence tomography angiography: a review. *Light: Science & Applications*, 11(1):63, March 2022. Publisher: Nature Publishing Group.

[66] Peter L. Nesper and Amani A. Fawzi. Human Parafoveal Capillary Vascular Anatomy and Connectivity Revealed by Optical Coherence Tomography Angiography. *Investigative Ophthalmology and Visual Science*, 59(10):3858–3867, August 2018.

[67] Peter Nesper, Hee Lee, Alaa Fayed, Greg Schwartz, Fei Yu, and Amani Fawzi. Hemodynamic response of the three macular capillary plexuses in dark adaptation and flicker stimulation using optical coherence tomography angiography. *Investigative Opthalmology and Visual Science*, 60:694, 02 2019.

[68] Dafna Goldenberg, Jonathan Shahar, Anat Loewenstein, and Michaella Goldstein. Diameters of retinal blood vessels in a healthy cohort as measured by spectral domain optical coherence tomography. *Retina (Philadelphia, Pa.)*, 33(9):1888–1894, October 2013.

[69] Luis Alarcon-Martinez, Yukihiro Shiga, Deborah Villafranca-Baughman, Nicolas Belforte, Heberto Quintero, Florence Dotigny, Jorge L. Cueva Vargas, and Adriana Di Polo. Pericyte dysfunction and loss of interpericyte tunneling nanotubes promote neurovascular deficits in glaucoma. *Proceedings of the National Academy of Sciences*, 119(7):e2110329119, 2022.

[70] R N Frank, T J Turczyn, and A Das. Pericyte coverage of retinal and cerebral capillaries. *Investigative Ophthalmology and Visual Science*, 31(6):999–1007, 06 1990.

[71] Hatem Jouda, Luis Murillo, and Tao Wang. Current progress in vascular engineering and its clinical applications. *Cells*, 11:493, 01 2022.

[72] Rebekka Heitmar and Robert J. Summers. The Time Course of Changes in Retinal Vessel Diameter in Response to Differing Durations of Flicker Light Provocation. *Investigative Ophthalmology and Visual Science*, 56(12):7581–7588, November 2015.

[73] G. Garhöfer, C. Zawinka, H. Resch, K. H. Huemer, G. T. Dorner, and L. Schmetterer. Diffuse luminance flicker increases blood flow in major retinal arteries and veins. *Vision Research*, 44(8):833–838, April 2004.

[74] Moe H. Aung, Tomas S. Aleman, Arielle S. Garcia, Brendan McGeehan, Gui-Shuang Ying, and Robert A. Avery. Stimulus type and duration affect magnitude and evolution of flicker-induced hyperemia measured by laser speckle flowgraphy at the optic disc and peripapillary vessels. *Scientific Reports*, 14(1):6659, March 2024. Publisher: Nature Publishing Group.

[75] Charles E. Riva, Eric Logean, and Benedetto Falsini. Visually evoked hemodynamical response and assessment of neurovascular coupling in the optic nerve and retina. *Progress in Retinal and Eye Research*, 24(2):183–215, March 2005.

[76] Kaiyuan Liu, Tiepei Zhu, Mengqin Gao, Xiaoting Yin, Rong Zheng, Yan Yan, Lei Gao, Zhihua Ding, Juan Ye, and Peng Li. Functional OCT angiography reveals early retinal neurovascular dysfunction in diabetes with capillary resolution. *Biomedical Optics Express*, 14(4):1670–1684, March 2023.

[77] Angelina Duan, Phillip A. Bedggood, Bang V. Bui, and Andrew B. Metha. Evidence of Flicker-Induced Functional Hyperaemia in the Smallest Vessels of the Human Retinal Blood Supply. *PLOS ONE*, 11(9):e0162621, September 2016. Publisher: Public Library of Science.

[78] Anja I. Srienc, Zeb L. Kurth-Nelson, and Eric Newman. Imaging retinal blood flow with laser speckle flowmetry. *Frontiers in Neuroenergetics*, 2, 2010.

[79] Zhangyi Zhong, Gang Huang, Toco Yuen Ping Chui, Benno L. Petrig, and Stephen A. Burns. Local flicker stimulation evokes local retinal blood velocity changes. *Journal of Vision*, 12(6):3, June 2012.

[80] Ameer A. Haider, Tonia S. Rex, and Lauren K. Wareham. cGMP Signaling in the Neurovascular Unit—Implications for Retinal Ganglion Cell Survival in Glaucoma. *Biomolecules*, 12(11):1671, November 2022. Number: 11 Publisher: Multidisciplinary Digital Publishing Institute.

[81] Gerhard Garhofer, Toke Bek, Andreas G. Boehm, Doina Gherghel, Juan Grunwald, Peter Jeppesen, Hélène Kergoat, Konstantin Kotliar, Ines Lanzl, John V. Lovasik, Edgar Nagel, Walthard Vilser, Selim Orgul, Leopold Schmetterer, and Ocular Blood Flow Research Association. Use of the retinal vessel analyzer in ocular blood flow research. *Acta Ophthalmologica*, 88(7):717–722, November 2010.

[82] David Huang, Eric A. Swanson, Charles P. Lin, Joel S. Schuman, William G. Stinson, Warren Chang, Michael R. Hee, Thomas Flotte, Kenton Gregory, Carmen A. Puliafito, and James G. Fujimoto. Optical Coherence Tomography. *Science (New York, N.Y.)*, 254(5035):1178–1181, November 1991.

[83] Talisa E. de Carlo, Andre Romano, Nadia K. Waheed, and Jay S. Duker. A review of optical coherence tomography angiography (OCTA). *International Journal of Retina and Vitreous*, 1(1):5, April 2015.

[84] Charles E. Riva, Eric Logean, and Benedetto Falsini. Temporal dynamics and magnitude of the blood flow response at the optic disk in normal subjects during functional retinal flicker-stimulation. *Neuroscience Letters*, 356(2):75–78, February 2004.

[85] Stephen A. Burns, Ann E. Elsner, Kaitlyn A. Sapoznik, Raymond L. Warner, and Thomas J. Gast. Adaptive optics imaging of the human retina. *Progress in Retinal and Eye Research*, 68:1–30, January 2019.

[86] Clément Viard, Kiyoko Nakashima, Barbara Lamory, Michel Pâques, Xavier Levecq, and Nicolas Château. Imaging microscopic structures in pathological retinas using a flood-illumination adaptive optics retinal camera. In *Ophthalmic Technologies XXI*, volume 7885, pages 66–75. SPIE, February 2011.

[87] Bing Zhang, Ni Li, Jie Kang, Yi He, and Xiao-Ming Chen. Adaptive optics scanning laser ophthalmoscopy in fundus imaging, a review and update. *International Journal of Ophthalmology*, 10(11):1751–1758, November 2017.

[88] Daniela Castro Farías, Carlo Lavia, Florence Rossant, and Michel Paques. Neurovascular coupling in the human retina evaluated by adaptive optics ophthalmoscopy. *Investigative Ophthalmology and Visual Science*, 62(8):20, June 2021.

[89] Céline Faure, Cindy Castrale, Anaïs Benabed, Pauline Cognard, Romain Lezé, Daniela Castro-Farias, Marion Gérard, Céline Louapre, and Michel Paques. Structural and functional analysis of retinal vasculature in HANAC syndrome with a novel intronic COL4A1 mutation. *Microvascular Research*, 145:104450, January 2023.

[90] Michel Paques, Valérie Krivosic, Daniela Castro-Farias, Cédric Dulière, Dominique Hervé, Céline Chaumette, Florence Rossant, Abbas Taleb, Jessica Lebenberg, Eric Jouvent, Ramin Tadayoni, and Hugues Chabriat. Early remodeling and loss of light-induced dilation of retinal small arteries in CADASIL. *Journal of Cerebral Blood Flow and Metabolism: Official Journal of the International Society of Cerebral Blood Flow and Metabolism*, 44(7):1089–1101, July 2024.

[91] Engin Akyol, Ahmed M. Hagag, Sobha Sivaprasad, and Andrew J. Lotery. Adaptive optics: principles and applications in ophthalmology. *Eye (London, England)*, 35(1):244–264, January 2021.

[92] Toco Y. P. Chui, Thomas J. Gast, and Stephen A. Burns. Imaging of Vascular Wall Fine Structure in the Human Retina Using Adaptive Optics Scanning Laser Ophthalmoscopy. *Investigative Ophthalmology and Visual Science*, 54(10):7115–7124, October 2013.

[93] Raymond L. Warner, Alberto de Castro, Lucie Sawides, Tom Gast, Kaitlyn Sapoznik, Ting Luo, and Stephen A. Burns. Full-field flicker evoked changes in parafoveal retinal blood flow. *Scientific Reports*, 10(1):16051, September 2020. Publisher: Nature Publishing Group.

[94] Yann Lai-Tim. *Imagerie haute résolution de la rétine humaine par illumination structurée assistée par optique adaptative*. These de doctorat, Université Paris sciences et lettres, November 2020.

[95] Jessica Jarosz. *Vers la conception d'un système d'optique adaptative pour la photocoagulation laser de la rétine*. These de doctorat, Paris 6, December 2015.

[96] Holovibes, https://holovibes.com/.

[97] Ethan A. Rossi, Nathaniel Norberg, Chiara Eandi, Celine Chaumette, Saloni Kapoor, Laura Le, Valerie C. Snyder, Joseph N. Martel, Josselin Gautier, Kiyoko Gocho, Kunal K. Dansingani, Jay Chhablani, Angelo Arleo, Sarah Mrejen, José-Alain Sahel, Kate Grieve, and Michel Paques. A New Method for Visualizing Drusen and Their Progression in Flood-Illumination Adaptive Optics Ophthalmoscopy. *Translational Vision Science & Technology*, 10(14):19, December 2021.

[98] Karine LAGRENE, Marcia Bécu, William H Seiple, Marine Raphanel Bataille, Sonia Combariza, Michel Paques, Anne Aubois, Bertrand Duclos, Chiara Eandi, Jean-François Girmens, Saddek Mohand-Said, and Angelo Arleo. Healthy and pathological visual aging in a French follow-up cohort study. *Investigative Ophthalmology and Visual Science*, 60(9):5915, July 2019.

[99] A. Guevara-Torres, D. R. Williams, and J. B. Schallek. Origin of cell contrast in offset aperture adaptive optics ophthalmoscopy. *Opt. Lett.*, 45(4):840–843, Feb 2020.

[100] Tim N. Ford, Kengyeh K. Chu, and Jerome Mertz. Phase-gradient microscopy in thick tissue with oblique back-illumination. *Nature Methods*, 9(12):1195–1197, December 2012.

[101] Matthew S. Muller, Jason J. Green, Karthikeyan Baskaran, Allen W. Ingling, Jeffrey L. Clendenon, Thomas J. Gast, and Ann E. Elsner. Non-mydriatic confocal retinal imaging using a digital light projector. *Proceedings of SPIE–the International Society for Optical Engineering*, 9376:93760E, February 2015.

[102] Ungsoo Samuel Kim, Omar A. Mahroo, John D. Mollon, and Patrick Yu-Wai-Man. Retinal Ganglion Cells—Diversity of Cell Types and Clinical Relevance. *Frontiers in Neurology*, 12:661938, May 2021.

[103] Timothy Q. Duong, Shing-Chung Ngan, Kamil Ugurbil, and Seong-Gi Kim. Functional Magnetic Resonance Imaging of the Retina. *Investigative Ophthalmology and Visual Science*, 43(4):1176–1181, April 2002.

[104] Anja I. Srienc, Zeb L. Kurth-Nelson, and Eric Newman. Imaging Retinal Blood Flow with Laser Speckle Flowmetry. *Frontiers in Neuroenergetics*, 2, September 2010. Publisher: Frontiers.

[105] Pedro Mece, Antoine Chen, Cyril Petit, Laurent Mugnier, Michel Paques, and Serge Meimon. Real-time optical stabilization of retinal motion at micrometer precision using Adaptive Optics Flood-Illumination Ophthalmsocope, December 2023.

[106] L. Puyo, M. Paques, M. Fink, J.-A. Sahel, and M. Atlan. In vivo laser Doppler holography of the human retina. *Biomedical Optics Express*, 9(9):4113–4129, September 2018. Publisher: Optica Publishing Group.

[107] Léo Puyo, Michel Paques, Mathias Fink, José-Alain Sahel, and Michael Atlan. Waveform analysis of human retinal and choroidal blood flow with laser Doppler holography. *Biomedical Optics Express*, 10(10):4942–4963, October 2019. Publisher: Optica Publishing Group.

[108] Joseph W Goodman. Introduction to fourier optics. *Introduction to Fourier optics, 3rd ed., by JW Goodman. Englewood, CO: Roberts & Co. Publishers, 2005*, 1, 2005.

[109] Charles Riva. *Laser Doppler Techniques for Ocular Blood Velocity and Flow*, pages 123–146. 03 2012.

[110] Léo Puyo. *Application clinique de l'holographie laser Doppler en ophtalmologie*. Phd thesis, Paris Sciences et Lettres (ComUE), September 2019.

[111] Leo Puyo, Loic Bellonnet-Mottet, Antoine Martin, Francois Te, Michel Paques, and Michael Atlan. Real-time digital holography of the retina by principal component analysis, 2020.

[112] Dierck Hillmann, Hendrik Spahr, Carola Hain, Helge Sudkamp, Gesa Franke, Clara Pfäffle, Christian Winter, and Gereon Hüttmann. Aberration-free volumetric high-speed imaging of in vivo retina. *Scientific Reports*, 6(1):35209, October 2016. Publisher: Nature Publishing Group.